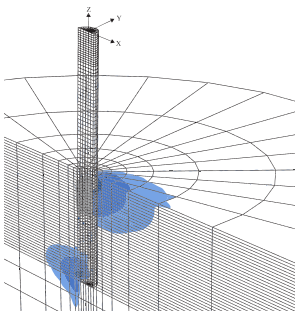
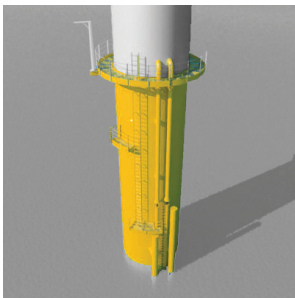


Evaluation of Load-Displacement Relationships for Large-Diameter Piles



Candidate Project
2008-2009:

Søren P. H. Sørensen
Kristian T. Brødbæk
Martin Møller

LONG CANDIDATE PROJECT

Evaluation of Load-Displacement Relationships for Large-Diameter Piles

Authors:

Søren P. H. Sørensen
Kristian T. Brødbæk
Martin Møller

Supervisors:

Anders H. Augustesen
Christian LeBlanc

Aalborg University

Faculties of Engineering, Science and Medicine

June 11, 2009

Number of pages: 239

Number of copies: 7

Preface

This thesis, "Evaluation of Load-Displacement Relationships for Large-Diameter Piles", is the product of a long candidate project carried out in the period of September 2008 to June 2009 at the Faculties of Engineering, Science and Medicine, Aalborg University, Denmark.

The thesis consists of three papers and a number of related appendices, a list of references is situated after each paper/appendix. Besides the three main papers an accepted conference paper is enclosed in the end of the thesis. The appendices are numbered by letters. Figures, tables, and equations are presented with consecutive numbers in each paper/appendix. Cited references are marked with author specifications and year of publication.

A pdf-script of the thesis and the produced computational programs are included on the enclosed compact disc.

The project is associated with the EFP programme "Physical and numerical modelling of monopile for offshore wind turbines", journal no. 033001/33033-0039. The funding is sincerely acknowledged. We, the authors would like to thank our supervisors, Assistant Professor at Aalborg University, Anders Hust Augustesen, and Dr. Christian LeBlanc, Dong Energy. Their assistance during the project is greatly appreciated. Finally, the support and technical advice from Professor MSO Lars Bo Ibsen, Dr. Morten Liingaard, Ph.d. Student Thomas S. Pedersen, and Assistant Engineers Kurt S. Sørensen and Nicholas Flint have been vital for the project to succeed.

Aalborg, June 11, 2009

Søren P. H. Sørensen

Kristian T. Brødbæk

Martin Møller

Summary

There is no approved design procedure for the design of large-diameter laterally loaded monopiles in sand, e.g. monopiles used as foundations for offshore wind turbines. Recently installed monopiles have diameters of 4–6 m and embedded pile lengths of 18–30 m. The p - y curve method, given in offshore design regulations, is usually employed for the design of monopiles. However, this method was developed for slender piles with diameters much less than 6 m and it is based on a limited number of tests.

The aim of the present work is to extend the p - y curve method to large-diameter non-slender piles by considering the effects of the pile diameter on the soil-pile interaction. The main focus is the initial stiffness of the p - y curves which, according to the current offshore design regulations, is governed by the initial modulus of subgrade reaction, k , multiplied with the depth measured from the soil surface. The initial modulus of subgrade reaction is according to the design regulations determined on basis of the relative density I_D or the angle of internal friction φ_{tr} , hence, it is considered independent of the pile properties.

The evaluation of the soil-pile interaction for large-diameter piles is based on experimental work as well as three-dimensional numerical analyses. Prior to the analyses, a consistent review concerning shortcomings and advantages of the currently recommended p - y curves was conducted. Considering the effect of diameter to the initial stiffness of the p - y curves contradictory conclusions has been drawn through time. A predominant part of researchers conclude that the effects of diameter are negligible. However, most of the analyses are conducted on diameters far smaller than the diameters employed for offshore wind turbine foundations. Furthermore, it is found that the non-slender monopiles behave as almost rigid objects when subjected to lateral loads. Hence, the failure mode is different from the one presumed in the existing p - y curve method. These findings are employed as basis for the experimental work and numerical analyses.

The numerical analyses are made by means of the commercial programs

FLAC^{3D} and *Plaxis 3D Foundation*. In both models a Mohr–Coulomb material model is employed. The numerical models are validated through six small-scale tests of heavily instrumented piles with diameters varying between $D = 60 - 80$ mm subjected to lateral loads acting with a given vertical eccentricity. Both test piles have a slenderness ratio of $L/D = 5$ implying embedded pile lengths of $L = 300 - 400$ mm. The tests are successfully carried out in a pressure tank at different effective stress levels in order to overcome sources of error, such as; small non-measurable strains, non-linear failure criterion, and excessive angles of internal friction. After validating the models to small-scale tests the numerical models are extended to full-scale offshore wind turbine foundations with diameters of $D = [2,3,5,7]$ m. The results are compared to results obtained from a traditional p – y curve design based on a Winkler model approach.

Major findings of the analyses are:

- The laboratory tests, as well as the numerical analyses, show that the non-slender piles behave almost rigidly when subjected to lateral loads. The non-slender piles have a single point of zero deflection implying a negative deflection at the pile-toe.
- Both the laboratory tests and the numerical analyses show that the initial stiffness of the p – y curves increases with increasing pile diameter.
- Through the numerical analyses it is found that the initial modulus of subgrade reaction, given by the offshore design regulations, is overestimated for large-diameter non-slender piles.
- Through the numerical analyses a linear variation of the initial stiffness with depth is found to be a non-conservative estimation at large depths.
- A non-linear variation of initial stiffness with depth was implemented in a Winkler model approach and the obtained load-displacement relationships were in good agreement with the results obtained by means of *FLAC^{3D}*.

Resumé - Summary in Danish

For horisontalt belastede monopæle med stor diameter installeret i sand findes på nuværende tidspunkt ingen anerkendt design procedure. Nyligt installerede monopæle, brugt til fundering af havvindmøller, har pælediameter på $D = 4 - 6$ m og rammedybder på $L = 18 - 30$ m. Disse pælefundamenter er som angivet i normerne for offshore konstruktioner designet efter p - y kurve metoden. Denne metode er oprindeligt udviklet på baggrund af forsøg på lange slanke pæle, og verificeringen af metoden for pæle med stor diameter og lavt slankhedsforhold, L/D , er mangelfuld.

Med fokus på diametereffekten på jord-pæl interaktionen er formålet med denne rapport at udvide den eksisterende p - y kurve metode til at være anvendelig for monopæle med store diameter. Hovedvægten er lagt på initialstivheden af p - y kurverne. Ifølge de gældende normer for offshore konstruktioner er initialstivheden af p - y kurverne styret af parameteren k samt dybden målt fra jordoverfladen. Ifølge anbefalingerne kan k bestemmes ud fra jordens relative densitet, I_D , eller friktionsvinklen, φ_{tr} . Hermed er det antaget, at initialstivheden af p - y kurverne er uafhængig af pæleens egenskaber, herunder pælediameteren.

Evalueringen af jord-pæl interaktionen er baseret på laboratorieforsøg, tredimensionelle numeriske analyser samt et gennemgribende litteraturstudie. Gennem litteraturstudiet bearbejdes fordele og begrænsninger ved p - y kurve metoden. Modstridende konklusioner med hensyn til pælediameterens betydning for initialstivheden af p - y kurverne er fundet i forbindelse med litteraturstudiet. Hovedparten af forskerne konkluderer, at diameterens betydning på initialstivheden er negligeabel. Det skal dog påpeges at langt størstedelen af analyserne er baseret på pæle med diameter langt mindre end nyligt installerede offshore monopæle. Yderligere er det fundet, at pæle med et lavt slankhedsforhold deformerer som næsten stive legemer, hvorfor brudfiguren antaget ved brug af p - y kurve metoden er fejlagtig. Disse konklusioner ligger til grund for laboratorieforsøgene samt de numeriske analyser.

De numeriske analyser er udført ved brug af de kommercielle programmer

FLAC^{3D} og *Plaxis 3D Foundation*. I begge programmer er en Mohr-Coulomb materiale model benyttet. De numeriske modeller er valideret i forhold til seks laboratorieforsøg udført på instrumenterede pæle med diametre på 60 og 80 mm. Længden af pælene er hhv. 300 og 400 mm svarende til et konstant slankhedsforhold på $L/D = 5$. Laboratorieforsøgene er udført i en tryktank for at kunne øge de effektive spændinger i jorden. Hermed minimeres usikkerheder som; ikke målbare tøjninger, et ikke-lineært brudkriterium samt ekstreme friktionsvinkler observeret ved 1-g forsøg. Forsøgsmetoden er udviklet løbende gennem projektet og fungerer efter hensigten. Efter valideringen af de numeriske modeller er disse udvidet til analyse af fuldskala vindmøllefundamenter med diametre på $D = [2; 3; 5; 7]$ m. Resultaterne sammenlignes med en Winkler model som traditionelt anvendes ved design af horisontalt belastede pæle.

Væsentlige konklusioner er som følger:

- Laboratorieforsøgene såvel som de numeriske analyser viser, at pæle med et lavt slankhedsforhold deformerer som næsten stive legemer under horisontal belastning. Pælene deformerer dermed omkring et rotationspunkt, hvilket giver anledning til en stor modsatrettet deformation ved pæletåen.
- Både laboratorieforsøgene og de numeriske analyser viser, at initialstivheden af p - y kurverne er afhængig af pælediameteren og stiger ved stigende diameter.
- Gennem de numeriske analyser er det fundet, at k bestemt i henhold til normerne for offshore konstruktioner er overestimeret for pæle med stor diameter og lavt slankhedsforhold.
- En lineær variation af p - y kurvernes initialstivhed med dybden er gennem de numeriske analyser fundet til at være en ikke-konservativ betragtning ved store dybder.
- En sammenligning af kraft-flytningskurverne for Winkler modellen og de opnåede resultater ved en *FLAC^{3D}* simulering viste god overensstemmelse, i så fald en ikke-lineær variation af initialstivheden med dybden blev implementeret i Winkler modellen.

Contents

1	Offshore wind turbine foundations	1
1.1	Foundation concepts	4
1.1.1	Gravity based	5
1.1.2	Monopile	6
1.1.3	Suction caisson	6
1.1.4	Tripod	7
1.2	Delimitations of the study	8
1.3	Aims of thesis	8
1.4	Thesis outline	10
2	Review of p-y Relationships in Cohesionless Soil	13
3	Evaluation of Load-Displacement Relationships for Non-Slender Monopiles in Sand	43
4	Numerical Evaluation of Load-Displacement Relationships for Non-Slender Monopiles in Sand	63
5	Concluding remarks	89
5.1	Major findings	91
5.1.1	Experimental work	92
5.1.2	Numerical models	92

5.1.3	Lateral pile deflection	93
5.1.4	Variation of initial stiffness, E_{py}^* , with depth	94
5.1.5	Initial modulus of subgrade reaction, k	95
5.1.6	Sensitivity of E_{py}^* to varying embedded pile length and pile bending stiffness	95
5.1.7	Improved Winkler model approach	96
5.2	Directions for future research	97
5.2.1	Experimental work	97
5.2.2	Numerical work	98
6	References	99
	Appendices	107
A	Test setup	109
A.1	Pressure tank	109
A.2	Measuring system	114
A.3	Soil characteristics	115
A.4	Interpretation of strain gauge measurements	118
A.5	Calibration of test piles	121
A.6	Test programme	121
B	Soil preparation and derivation of soil parameters	125
B.1	Pile installation	125
B.2	Preparation of soil	125
B.2.1	Preparation prior to all testing	127
B.2.2	Re-compaction of soil near the pile after installation	127
B.2.3	Re-compaction of the material between two tests	128

B.3	Cone penetration tests	128
B.4	Interpretation of CPT's	131
C	Material properties employed in the numerical analyses	135
D	Winkler model approach	137
D.1	Element geometry	138
D.2	Iterative procedures for solving the non-linear set of equations	139
D.2.1	Force controlled approach	140
D.2.2	Displacement controlled approach	141
D.3	Overburden pressure	141
D.4	Convergence analysis	143
D.5	Choice of beam theory	143
E	<i>FLAC^{3D}</i>	147
E.1	Numerical formulation	148
E.1.1	Discretisation of medium	148
E.2	Interfaces	149
E.2.1	Interface properties	151
E.3	Numerical stability	151
E.4	Numerical damping	152
F	<i>Plaxis 3D Foundation</i>	153
F.1	Numerical formulation	154
F.1.1	Discretisation of medium	154
F.2	Interfaces	155
F.3	Numerical stability	156
G	Mohr-Coulomb failure criterion	161

H Calibration of test piles	163
I Test 1: $D = 0.08$ m, $L = 0.4$ m, $P_0 = 0$ kPa	167
J Test 2: $D = 0.08$ m, $L = 0.4$ m, $P_0 = 100$ kPa	173
K Test 3: $D = 0.08$ m, $L = 0.4$ m, $P_0 = 50$ kPa	179
L Test 4: $D = 0.06$ m, $L = 0.3$ m, $P_0 = 0$ kPa	185
M Test 5: $D = 0.06$ m, $L = 0.3$ m, $P_0 = 50$ kPa	191
N Test 6: $D = 0.06$ m, $L = 0.3$ m, $P_0 = 100$ kPa	197
O Calibration of $FLAC^{3D}$ to laboratory test results	203
P Evaluation of the Load-Displacement Relationships for Large-Diameter Piles in Sand	205

CHAPTER 1

Offshore wind turbine foundations



Offshore wind turbine foundations

It is a predominating opinion that the greatest environmental threat against our planet, is the climate changes observed in the last decades. According to the UN's Intergovernmental Panel on Climate Change¹, the average temperatures around the world will increase by up to 5.8% in the coming century. According to leading scientists within the environmental area there is a close correlation between the global heating and the increasing emission of greenhouse gasses. In order to avoid the worst ravages caused by climate changes, the emission of greenhouse gasses must therefore be decreased. Fossil fuels such as coal, gas and oil are major emitters of carbon dioxide, which is considered to be the main greenhouse gas contributing to climate changes. In order to decrease the emission of carbon dioxide the percentage of renewable energy sources like wind energy must be raised.

Wind power is the most developed renewable energy source in Denmark, besides from biomass. In 2007 Denmark achieved 19.7 % of the total national electrical consumption from wind energy resources, according to The Danish Energy Agency². Denmark has been leading in the development of wind energy since the early 1980s. Due to this the level of knowledge in the area is high. Combining this knowledge with the favorable sea and wind conditions near the Danish coast, Denmark has significant wind energy potential and on behalf of a strong political backup the percentage of total national electrical consumption from wind energy resources are to be raised in the years to come. The wind power has traditionally been based on onshore wind turbines, but due to the size of the turbines and the increasing knowledge about offshore wind conditions, sea conditions and installation methods the market for offshore wind turbines is growing. As of January 1st 2006, Denmark had a total wind capacity of 3135 MW of which 423 MW was located offshore at eight offshore windfarms. During the years of 2009 and 2010 three new parks are commissioning; Horns Rev 2, Rødsand 2, and Sprogø, contributing with 224 MW, 207 MW, and 21 MW, respectively. Figure 1 outlines

¹www.gwec.net

²<http://www.energistyrelsen.dk>

the windfarms located offshore in Denmark. Furthermore, the Danish government has given permission to the commission of several other offshore wind turbine farms. According to Offshore Center Denmark³ the following parks are planned or under consideration, cf. fig. 1: Djursland/Anholt (400 MW), Frederikshavn 2, Kriegers Flak 1 (455 MW), Kriegers Flak 2 (600-700 MW), Rønland 2, Rønland 3, Rønne Bakke (70 MW). The capacities of Frederikshavn 2, Rønland 2, and Rønland 3 are not provided.

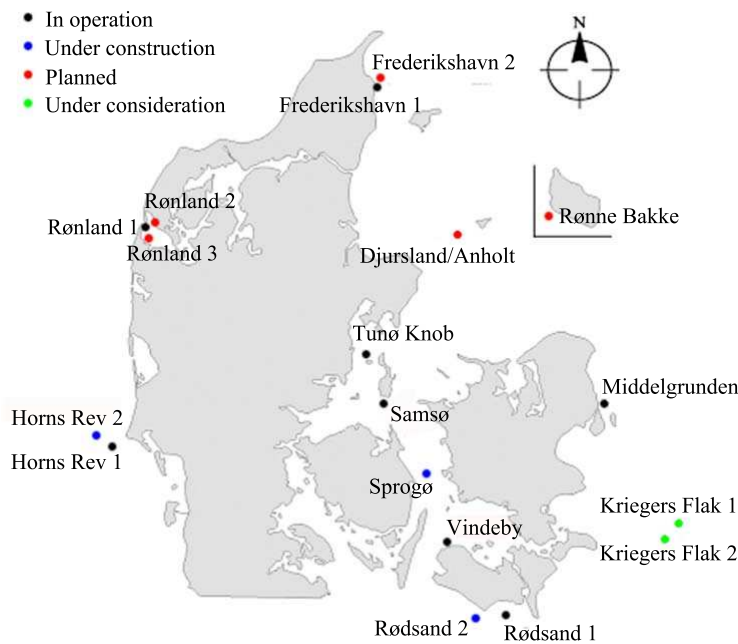


Figure 1: Danish windfarms in operation, under construction, planned, and under consideration.

1.1 Foundation concepts

Several foundation concepts for offshore wind turbines exist. The selection of type of foundation is governed by multiple factors; water depth, soil conditions, environmental conditions, type of loading, and economy. Traditionally the most cost-efficient solution is to be employed.

The main design parameters for the foundation are most often the rotation of the flange and the stiffness of the entire wind turbine system. The criteria are set by the wind turbine manufacturer. Traditionally the rotation due to plastic deformation at the flange is not allowed to exceed 0.5° in the service

³<http://www.offshorecenter.dk/offshorewindfarms.asp>

life of the foundation. In order to avoid resonance of the structure the first natural frequency needs to be between $1P$ and $3P$, where P denotes the frequency corresponding to one rotor rotation.

At relatively shallow water depths the dominant types of foundation is the gravity based foundation and the monopile. At suitable soil conditions, e.g. soil layers without chalk and hard till, the suction caisson is an alternative as well as the tripod foundation might be an alternative at water depths of 20 – 50 m. The four foundation concepts are illustrated in fig. 2. The four concepts are presented in the following subsections.

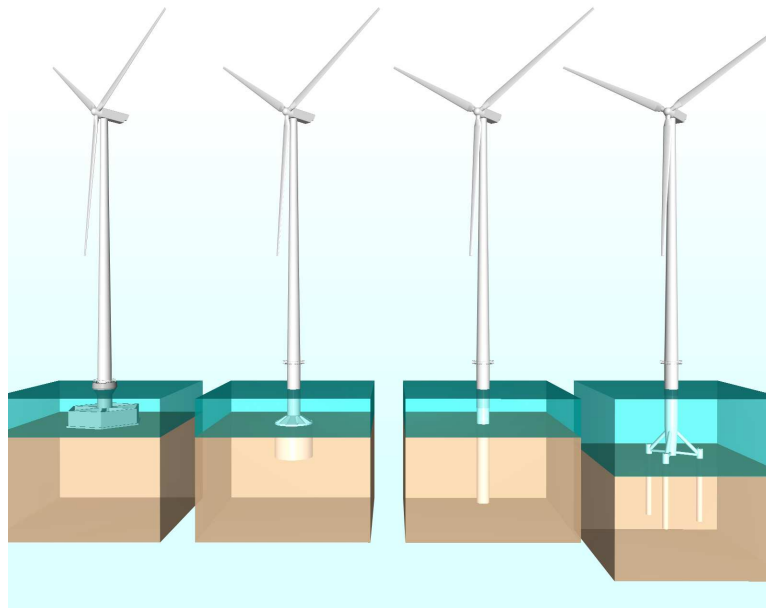


Figure 2: Common used foundations concepts at relatively shallow waters. From left to right: Gravity based, suction caisson, monopile and tripod foundation. After Liingaard (2006).

At water depths larger than 40–50 m jackets or floating foundations might be the most suitable solution. The deep water foundation concepts are however still in the state of development for offshore wind turbines.

Most of the concepts are originally developed to the oil and gas industry and are later employed to the offshore wind turbine industry. Due to this, foundation concepts are still to be developed and improved.

1.1.1 Gravity based

The gravity based foundation is designed to have enough weight and base area, so that tensile forces between the foundation and seabed are avoided.

Besides from uplifting and tilting the dead load of the foundation has to be sufficient to prevent sliding. The foundation is efficient if the dead load is high compared to the bending moment at the seabed level. However, the soil must have sufficient strength as well as settlements must be of an absolute minimum. The seabed most often needs preparation prior to the installation in terms of substitution of organic or soft soils. The foundation itself, is made of either a massive concrete construction or a caisson type foundation with additional ballast. When employing the caisson type foundation the foundation can be floated out to the location. Hereby, the cost of a crane vessel is reduced. Scour protection is most often necessary for cohesionless sea bed conditions.

1.1.2 Monopile

The monopile foundation consist of a large-diameter, pipe pile made of welded steel, and driven into the seabed by means of a hydraulic hammer or by vibration. The wind turbine is connected to the foundation through a transition piece. Most often the transition piece has a diameter fitting the outside of the pile. After placing the transition piece on top of the pile the joint is fixed by means of grouting. Recently installed monopile foundations have diameters of $D = 4 - 6$ m. The embedded length of a monopile foundation is most often $L = 18 - 30$ m. The bearing capacity of an axially loaded pile comprises shaft friction and resistance at the pile-toe. In case of hollow piles the soil inside the pile contributes to the bearing capacity by friction against the inner wall, or by point resistance of the soil plug at the pile tip, whichever is less. The lateral loads and bending moments are transferred to the surrounding soil by lateral earth pressures acting against the pile wall. The monopiles may be driven without any preparation of the seabed. Scour protection may though be needed in case of friction materials at the soil surface. Installation of the monopile foundations demands heavy duty piling or some times even drilling equipment. In addition to this, the monopile is sensitive to large boulders. However, due to the easy production and minimum of requirements to the conditions of the seabed, monopiles are commonly used.

1.1.3 Suction caisson

Suction caisson has for years been used for anchoring floating platforms within the oil and gas industry. After successful installation of a full scale wind turbine at Frederikshavn Harbour, cf. Ibsen et al. (2005), and recently a measuring mast at the Horns Rev 2 site, both with suction caisson foundations, the concept has shown useful in the wind turbine industry. The

suction caissons, or bucket foundation when employed for wind turbines, are made of a large-diameter pipe pile closed at the top. The lateral loads and bending moments are transferred to the subsoil by means of skin friction at the inside and outside of the bucket and by the dead load of the caisson. For installation the water inside the bucket is pumped out creating a negative pressure which together with the dead load of the bucket drives the skirts into the seabed. To ease the installation in dense soils, the soil material is loosened up by means of skirt tip injection. The bucket foundation is sensitive to the soil conditions at the site. In order to establish the negative pressure within the bucket the permeability of the soil must not be too high. On the other hand the bucket can not be installed in cohesive soils as the skirt friction will be predominating. Also, the concept is sensitive to large boulders in the subsoil.

The advantages of suction caissons are considerable. In the installation phase the foundation and the transition piece may be floated assembled to the site. The installation demands only a minimum of preparation of the seabed. Furthermore, the decommissioning of the foundation requires a minimum of time and equipment. At large water depths the monopod concept might be combined with the tripod concept as described in section 1.1.4 in order to spread the area of the footing.

1.1.4 Tripod

The main advantages of the tripod foundation are the installation and the material costs for wind turbines at deep water. The concept deals with a center piece or transition pipe supported by three legs each consisting of a pile, a pile sleeve and two braces. The piles, which are most often steel pipe piles, may be driven, jacked or bored. It is possible to incline the piles in order to optimise the design. The length of the piles are dependent on the soil conditions. In order to utilise the ability to transfer bending moments as tensile and compression forces in the piles, the tripod concept is most cost-efficient for foundation at water depths between 20 – 50 m. The concept requires a minimum of preparation of the seabed before installation. However, as for monopiles the concept is sensitive to large boulders in the subsoil. Further, due to the complexity of the structure the tripod requires extensive structural analyses as well as a demanding production phase.

A study performed by Feld et. al. (1999)⁴ suggest a beneficial combination of the tripod concept and the suction caissons at relatively large water depths. The investigation concerns an evaluation of a centre piece sucked into the seabed and supported by two perpendicular legs each attached to suction

⁴www.ramboll-wind.com/PDF/OMAE99.pdf

caissons. The concept indicated large economical savings for the Rødsand project due to the soft soils at the site. However, the savings at Horns Rev were small due to hard soil conditions favouring other foundation concepts.

1.2 Delimitations of the study

Focus is entirely paid to non-slender monopiles installed in sand subjected to static lateral loads.

1.3 Aims of thesis

Laterally loaded monopiles are traditionally designed based on a Winkler model approach, i.e. a beam supported by elastic foundations representing the soil. The soil is considered to consist of a series of uncoupled non-linear springs with stiffness' E_{py} acting on an elastic beam as shown in fig. 3. The spring stiffness E_{py} , traditionally denoted modulus of subgrade reaction, is given by the p - y curves as the secant modulus, cf. fig 3. A p - y curve describes the non-linear relationship between the soil pressure acting against the pile wall, p , and the lateral deflection of the pile, y . The p - y curve formulation for sand employed in the offshore design regulations, e.g. API (1993) and DNV (1992), is given by:

$$p(y) = Ap_u \tanh\left(\frac{kx}{Ap_u}y\right) \quad (1)$$

where $p(y)$ is the soil resistance acting in a given depth, x , beneath the soil surface, A is a factor accounting for static or cyclic loading conditions, p_u is the ultimate soil resistance, and k is the initial modulus of subgrade reaction. k is determined in terms of the angle of internal friction or the relative density of the soil.

The p - y curve for sand is governed by the ultimate soil resistance and the initial stiffness, E_{py}^* ($E_{py}^* = kx = E_{py}$ for $y = 0$). Due to the strict demands to stiffness and deformations in the serviceability mode, this initial part of the p - y curves is vital in the design of wind turbine foundations. The initial stiffness of the p - y curves is in the offshore design regulations assumed independent of pile properties including the pile diameter, which seems questionable. The current p - y curve formulations are based on the testing of two identical steel pipe piles with a slenderness ratio of $L/D = 34.4$, as described

by Cox et al. (1974). Currently installed monopiles have $L/D < 10$, implying a rather rigid pile behaviour. This contradicts the flexible behaviour as assumed in the design regulations.

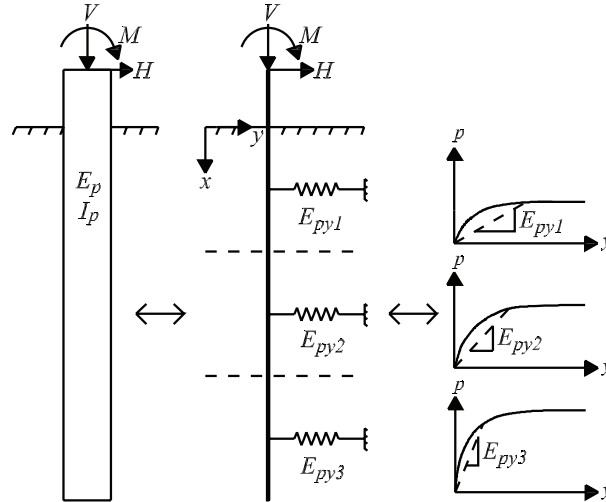


Figure 3: Winkler model approach and definition of p - y curves.

The aim of this thesis is to investigate the effects of pile diameter on the p - y curves for homogenous sand, cf. (1), with main focus on the initial part of the curves. The following is desired:

- A review of the current p - y curve method and the research conducted within the area is to be produced, whereas the limitations and advantages of the method is to be presented.
- It is desired to develop an experimental model where the downside effects of small-scale tests, e.g. non-linear Coulomb failure criterion due to small stress levels and scale effects as encountered in centrifuge test, are minimised.
- The laboratory tests should be possible to simulate in three-dimensional numerical programs, in order to validate the durability of these. By means of the numerical models calibrated to the laboratory tests, large-scale simulations are to be conducted with varying pile diameter in order to examine (1) and the correspondingly parameters E_{py}^* and k . Finally, the results of these simulations are to be compared with results by means of a Winkler model approach.

1.4 Thesis outline

The thesis contains five chapters and sixteen appendices. The chapters 2–4 are written as independent papers concerning individual issues related to the topics presented in section 1.3. Appendix P features a paper accepted for presentation at *The Twelfth International Conference on Civil, Structural and Environmental Engineering Computing, Portugal, 2009*.

Chapter 2 is an outline of the base concept of the p – y curves. A presentation is made of how the first p – y curves were derived and how they are employed as state-of-the-art design procedure for offshore wind turbine foundations. As presented in section 1.3 the p – y curve method has due to its simplicity some shortcomings. Especially, the method was derived for long slender piles which are seldom used for offshore wind turbine foundations. Here the piles are shorter and stiffer causing the piles to move as almost rigid objects when subjected to lateral loading. Although a lot of research has been conducted within this field in order to modify the p – y curve method to the present needs, there is no analysis which gives a definitive solution to the complex problem. In order to continue the work performed within this field chapter 2 contains a consistent review of the current relevant research.

Chapter 3 is a description and evaluation of six laboratory test conducted on two different pile diameters. The objective of the tests is to substantiate the numerical part of the thesis and experimentally investigate the problems in consideration. The tests are conducted in a pressure tank with a sealed elastic membrane separating the soil from the upper part of the pressure tank. In this way the effective stresses in the soil can be increased by increasing the pressure in the upper part of the tank. When increasing the effective stresses in the soil, problems with a non-linear yield surface, as for small stress levels, are overcome. The employed piles are heavily instrumented with strain gauges in order to determine bending moment distributions in the piles as well as p – y curves along the piles. Relationships between the lateral load and the pile displacement are obtained by three displacement transducers and a force transducer. The soil parameters are determined by several cone penetration tests.

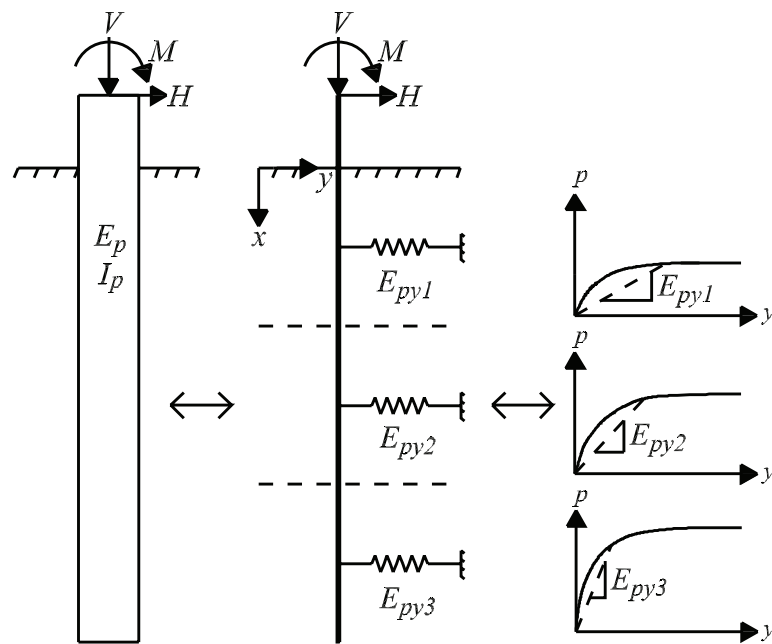
In chapter 4 three-dimensional numerical models conducted by means of *FLAC^{3D}* and *Plaxis 3D Foundation* are presented and employed to examine the validity of $E_{py}^* = kx$ and the magnitude of k , for non-slender large-diameter monopiles subjected to static horizontal loads. A Mohr–Coulomb material model with tension cut-off is employed in the analyses. Analyses with pile diameters varying between $D = 2 - 7$ m and embedded pile lengths of 20 m and 30 m are presented. Hereby, the effects of pile diameter and embedded pile length on the E_{py}^* are evaluated. Furthermore, the influence of

different pile bending stiffness' on the p - y curves is examined. The obtained results are compared to a traditional Winkler model approach employing the p - y curves recommended by the offshore design regulations, e.g. DNV (1992) and API (1993).

Chapter 5 concerns concluding remarks of the thesis, and directions for future work, based on the findings in this thesis.

CHAPTER 2

Review of p - y Relationships in Cohesionless Soil



Review of p - y Relationships in Cohesionless Soil

K. T. Brødbæk¹; M. Møller¹; and S. P. H. Sørensen¹

Aalborg University, January 2009

Abstract

Monopiles are an often used foundation concept for offshore wind turbine converters. These piles are highly subjected to lateral loads and thereby bending moments due to wind and wave forces. To ensure enough stiffness of the foundation and an acceptable pile-head deflection, monopiles with diameters at 4 to 6 m are typically necessary. In current practice these piles are normally designed by use of the p - y curve method although the method is developed and verified for small-diameter, slender piles with a diameter up to approximately 2 m. In the present paper a review of existing p - y curve formulations for piles in sand under static loading is presented. Based on numerical and experimental studies presented in the literature, advances and limitations of current p - y curve formulations are outlined.

1 Introduction

It is a predominating opinion that the global warming is caused by the emission of greenhouse gasses. According to United Nations (1998) there is a strong political interest to raise the percentage of renewable energy, and reduce the use of fossil fuels, in the years to come. Wind energy plays a major role in attaining these goals both onshore and offshore which is why a further development is of interest.

Several concepts for offshore wind turbine foundations exist. The choice of foundation concept primarily depends on site conditions and the dominant type of loading. At great water depths the most common foundation principle is monopiles, which are single steel pipe piles. The foundation should be designed to have enough ultimate resistance against vertical and lateral loads. Moreover, the defor-

mation criteria and stiffness of the foundation should be acceptable under lateral loading which is normally the primary design criterion for this type of foundation. In order to avoid resonance the first natural frequency of the structure needs to be between $1P$ and $3P$, where P denotes the frequency corresponding to one rotor rotation. According to LeBlanc et al. (2007) monopiles installed recently have diameters around 4 to 6 m and a pile slenderness ratio, L/D , around 5 where L is the embedded pile length and D is the outer pile diameter.

In current design of laterally loaded offshore monopiles, p - y curves are normally used. A p - y curve describes the non-linear relationship between the soil resistance acting against the pile wall, p , and the lateral deflection of the pile, y . Note that there in present paper is distinguished between soil resistance, p , and ultimate soil resistance, p_u . The soil resistance is given as the reaction force per unit length acting on the pile. The ultimate soil resistance is given as the maximum value of

¹Graduate Student, Dept. of Civil Engineering, Aalborg University, Sohngaardsholmsvej 57, 9000 Aalborg, Denmark.

soil resistance.

Several formulations of p - y curves exist depending on the type of soil. These formulations are originally formulated to be employed in the offshore oil and gas sector. However, they are also used for offshore wind turbine foundations, although piles with significantly larger diameter and significantly smaller slenderness ratio are employed for this type of foundation.

In this paper the formulation and implementation of p - y curves proposed by Reese et al. (1974) and API (1993) for piles in sands due to static loading will be analysed. However, alternative methods for designing laterally loaded piles have been proposed in the literature. According to Fan and Long (2005) these alternative approaches can generally be classified as follows:

- The limit state method.
- The subgrade reaction method.
- The elasticity method.
- The finite element method.

Simplest of all the methods are the limit state methods, e.g. Broms (1964), considering only the ultimate soil resistance.

The simplest method for predicting the soil resistance due to a given horizontal deflection is the subgrade reaction method, e.g. Reese and Matlock (1956) and Matlock and Reese (1960). In this case the soil resistance is assumed linearly dependent on the pile deflection. Full-scale tests though substantiate a non-linear relationship between soil resistance and pile deflection. The subgrade reaction method must therefore be considered too simple and highly inaccurate. In addition the subgrade reaction method is not able to predict the ultimate lateral resistance. The p - y curve method assumes a non-linear dependency between soil resistance and pile

deflection and is therefore able to produce a more accurate solution. Furthermore, the ultimate lateral resistance can be estimated by using the p - y curve method.

In both the p - y curve method and the subgrade reaction method the Winkler approach, cf. section 2, is employed to calculate the lateral deflection of the pile and internal forces in the pile. When employing the Winkler approach the pile is considered as a beam on an elastic foundation. The beam is supported by a number of uncoupled springs with spring stiffness' given by p - y curves. When using the Winkler approach the soil continuity is not taken into account as the springs are considered uncoupled.

The elasticity method, e.g. Banerjee and Davis (1978), Poulos (1971), and Poulos and Davis (1980), includes the soil continuity. However, the response is assumed to be elastic. As soil is more likely to behave elasto-plastically, this elasticity method is not to be preferred unless only small strains are considered. Hence, the method is only valid for small strains and thereby not valid for calculating the ultimate lateral resistance.

Another way to deal with the soil continuity and the non-linear behaviour is to apply a three-dimensional finite element model, e.g. Abdel-Rahman and Achmus (2005). When applying a three-dimensional finite element model both deformations and the ultimate lateral resistance can be calculated. Due to the complexity of a three-dimensional model, substantial computational power is needed and calculations are often very time consuming. Phenomena such as liquefaction, due to non-appropriate kinematic models, and gaps between soil and pile are at present hard to handle in the models. Hence, a finite element approach is a useful method but the accuracy of the results is highly dependent on the applied constitutive soil models as well as the calibration

of these models.

2 p - y curves and Winkler approach

As a consequence of the oil and gas industry's expansion in offshore platforms in the 1950s, models for designing laterally loaded piles were required. The key problem is the soil-structure interaction as the stiffness parameters of the pile, E_p , and the soil, E_s , may be well known but at the soil-pile interface the combined parameter E_{py} is governing and unknown. In order to investigate this soil-pile interaction a number of full-scale tests on fully instrumented piles have been conducted and various expressions depending on the soil conditions have been derived to predict the soil pressure acting on a pile subjected to lateral loading.

Historically, the derivation of the p - y curve method for piles in sand is as follows:

- Analysing the response of beams on an elastic foundation. The soil is characterised by a series of linear-elastic uncoupled springs, introduced by Winkler (1867).
- Hetenyi (1946) presents a solution to the beam on elastic foundation problem.
- McClelland and Focht (1958) as well as Reese and Matlock (1956) suggest the basic principles in the p - y curve method.
- Investigations by Matlock (1970) indicates that the soil resistance in one point is independent of the pile deformation above and below that exact point.
- Tests on fully instrumented test piles in sand installed at Mustang Island

are carried out in 1966 and reported by Cox et al. (1974).

- A semi-empirical p - y curve expression is derived based on the Mustang Island tests, cf. Reese et al. (1974). The expression becomes the state-of-the-art in the following years.
- Murchison and O'Neill (1984) compare the p - y curve formulation proposed by Reese et al. (1974) with three simplified expressions (also based on the Mustang Island tests) by testing the formulations against a database of relatively well-documented lateral pile load tests. A hyperbolic form is found to provide better results compared to the original expressions formulated by Reese et al. (1974).

Research has been concentrated on deriving empirical (e.g. Reese et al. 1974) and analytical (e.g. Ashour et al. 1998) p - y curve formulations for different types of soil giving the soil resistance, p , as a function of pile displacement, y , at a given point along the pile. The soil pressure at a given depth, x_t , before and during a static excitation is sketched in fig. 1b. The passive pressure on the front of the pile is increased as the pile is deflected a distance y_t while the active pressure at the back is decreased.

An example of a typical p - y curve is shown in fig. 2a. The curve has an upper horizontal limit denoted by the ultimate soil resistance, p_u . The horizontal line implies that the soil has an ideal plastic behaviour meaning that no loss of shear strength occurs with increasing strain. The subgrade reaction modulus, E_{py} , at a given depth, x , is defined as the secant modulus p/y . E_{py} is thereby a function of both lateral pile deflection, y , and depth, x , as well as the physical properties and load conditions. E_{py} does not uniquely represent a soil property, but is simply a convenient

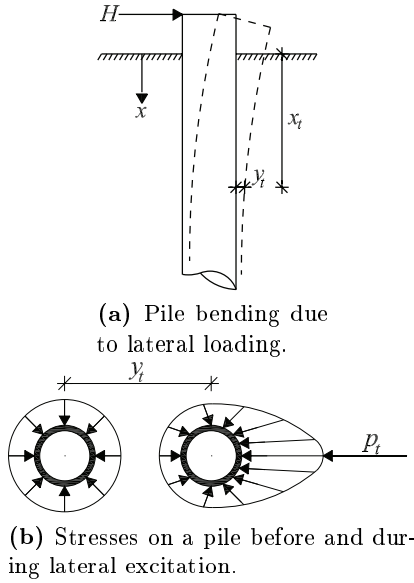


Figure 1: Distribution of stresses before and during lateral excitation of a circular pile. p_t denotes the net force acting on the pile at the depth x_t , after Reese and Van Impe (2001).

parameter that describes the soil-pile interaction. E_{py} is constant for small deflections for a particular depth, but decreases with increased deflection, cf. fig. 2b. A further examination of the shape of p - y curves is to be found in section 3, and an overview of the used parameters in this paper are given in tab. 1.

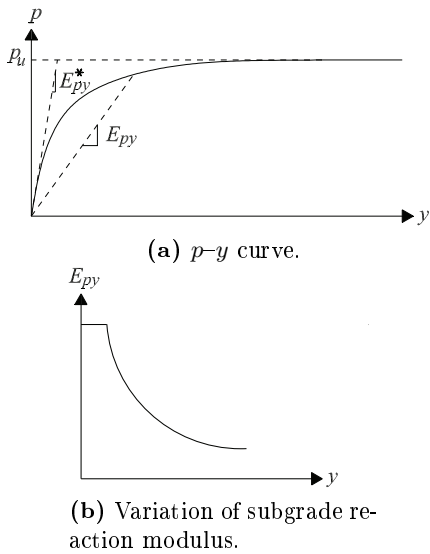


Figure 2: Typical p - y curve and variation of the modulus of subgrade reaction at a given point along the pile, after Reese and Van Impe (2001).

Since the pile deflection is non-linear a convenient way to obtain the soil resistance along the pile is to apply the Winkler approach where the soil resistance is modelled as uncoupled non-linear springs with stiffness K_i acting on an elastic beam as shown in fig. 3. K_i is a non-linear load transfer function corresponding to E_{py} . By employing uncoupled springs layered soils can conveniently be modelled.

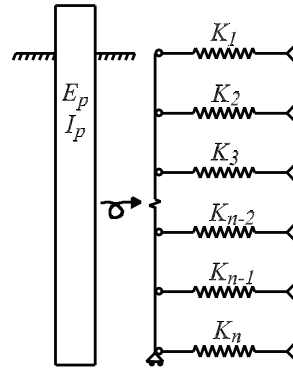


Figure 3: The Winkler approach with the pile modelled as an elastic beam supported by non-linear uncoupled springs. K is the stiffness corresponding to E_{py} .

The governing equation for beam deflection was stated by Timoshenko (1941). The equation for an infinitesimal small element, dx , located at depth x , subjected to lateral loading, can be derived from static equilibrium. The sign convention in fig. 4 is employed. N , V , and M defines the axial force, shear force and bending moment in the pile, respectively. The axial force, N , is assumed to act in the cross-section's centre of gravity.

Equilibrium of moments and differentiating with respect to x leads to the following equation where second order terms have been neglected:

$$\frac{d^2 M}{dx^2} + \frac{dV}{dx} - N \frac{d^2 y}{dx^2} = 0 \quad (1)$$

Table 1: Definition of parameters and dimensions used in the present paper.

Description	Symbol	Definition	Dimension
Pile diameter	D		L
Embedded pile length	L		L
Soil resistance	p		F/L
Ultimate soil resistance	p_u		F/L
Soil pressure	P	$P = p/D$	F/L^2
Pile deflection	y		L
Depth below soil surface	x		L
Second moment of inertia	I_p		L^4
Young's modulus of elasticity of the pile	E_p		F/L^2
Modulus of subgrade reaction	E_{py}	$E_{py} = p/y$	F/L^2
Initial stiffness	E_{py}^*	$E_{py}^* = \frac{dp}{dy}, y = 0$	F/L^2
Initial modulus of subgrade reaction	k	$k = E_{py}^*/x$	F/L^3

Following relations are used:

$$M = E_p I_p \kappa \quad (2)$$

$$\frac{dV}{dx} = -p \quad (3)$$

$$p(y) = -E_{py}y \quad (4)$$

E_p and I_p are the Young's modulus of elasticity of the pile and the second moment of inertia of the pile, respectively. κ is the curvature strain of the beam element.

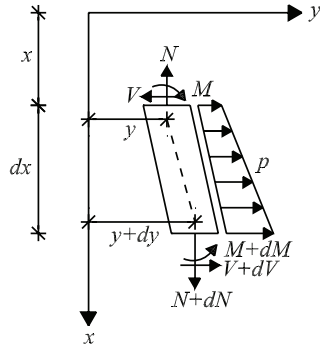


Figure 4: Sign convention for infinitesimal beam element.

With use of (2)–(4) and the kinematic assumption $\kappa = \frac{d^2y}{dx^2}$ which is valid in Bernoulli-Euler beam theory the governing fourth-order differential equation for determination of deflection is obtained:

$$E_p I_p \frac{d^4y}{dx^4} - N \frac{d^2y}{dx^2} + E_{py}y = 0 \quad (5)$$

In (5) the shear strain, γ , in the beam is neglected. This assumption is only valid

for relatively slender beams. For short and rigid beams the Timoshenko beam theory, that takes the shear strain into account, is preferable. The following relations are used:

$$V = G_p A_v \gamma \quad (6)$$

$$\gamma = \frac{dy}{dx} - \omega \quad (7)$$

$$\kappa = \frac{d\omega}{dx} \quad (8)$$

G_p and A_v are the shear modulus and the effective shear area of the beam, respectively. ω is the cross-sectional rotation as defined in fig. 5. In Timoshenko beam theory the shear strain and hereby the shear stress is assumed to be constant over the cross section. However, in reality the shear stress varies parabolic over the cross section. The effective shear area is defined so the two stress variations give the same shear force. For a pipe the effective shear area can be calculated as:

$$A_v = 2(D - t)t \quad (9)$$

where t is the wall thickness of the pipe.

By combining (1)–(4) and (6)–(8) two coupled differential equations can be formulated to describe the deflection of the beam:

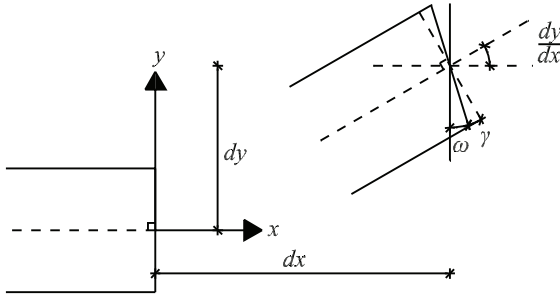


Figure 5: Shear and curvature deformation of a beam element.

$$GA_v \frac{d}{dx} \left(\frac{dy}{dx} - \omega \right) - E_{py}y = 0 \quad (10)$$

$$E_p I_p \frac{d^3 \omega}{dx^3} - N \frac{d^2 y}{dx^2} + E_{py}y = 0 \quad (11)$$

In the derivation of the differential equations the following assumptions have been used:

- The beam is straight and has a uniform cross section.
- The beam has a longitudinal plane of symmetry, in which loads and reactions lie.
- The beam material is homogeneous, isotopic, and elastic. Furthermore, plastic hinges do not occur in the beam.
- Young's modulus of elasticity of the beam material is similar in tension and compression.
- Beam deflections are small.
- The beam is not subjected to dynamic loading.

3 Formulations of p - y curves for sand

p - y curves describing the static behaviour of piles in cohesionless soils are presented

followed by a discussion of their validity and limitations, cf. section 4. Only the formulation made by Reese et al. (1974), hereafter denoted Method A, and the formulation proposed by API (1993), Method B, will be described. Both p - y curve formulations are empirically derived based on full-scale tests on free ended piles at Mustang Island.

3.1 Full-scale tests at Mustang Island

Tests on two fully instrumented, identical piles located at Mustang Island, Texas as described by Cox et al. (1974), are the starting point for the formulation of p - y curves for piles in sand. The test setup is shown in fig. 6.

To install the test- and reaction piles a Delmag-12 diesel hammer was used. The test piles were steel pipe piles with diameters of 0.61 m (24 in) and wall thickness' of 9.5 mm (3/8 in). The embedded length of the piles were 21.0 m (69 ft) which corresponds to a slenderness ratio of $L/D = 34.4$. The piles were instrumented with a total of 34 active strain gauges mounted from 0.3 m above the mudline to 9.5 m (32 ft) below the mudline. The strain gauges were bonded directly to the inside of the pile in 17 levels with highest concentration of gauges near the mudline. The horizontal distance between the centre of the two test piles was 7.5 m (24 ft and 8 in), cf. fig. 6. Between the piles the load cell was installed on four reaction piles. The minimum horizontal distance from the centre of a reaction pile to the centre of a test pile was 2.8 m (9 ft and 4 in). The water table was located at the soil surface, implying fully saturated soil.

Prior to pile installation, two soil borings were made, each in a range of 3.0 m (10 ft) from a test pile. The soil samples showed a slight difference between the two areas where the piles were installed, as

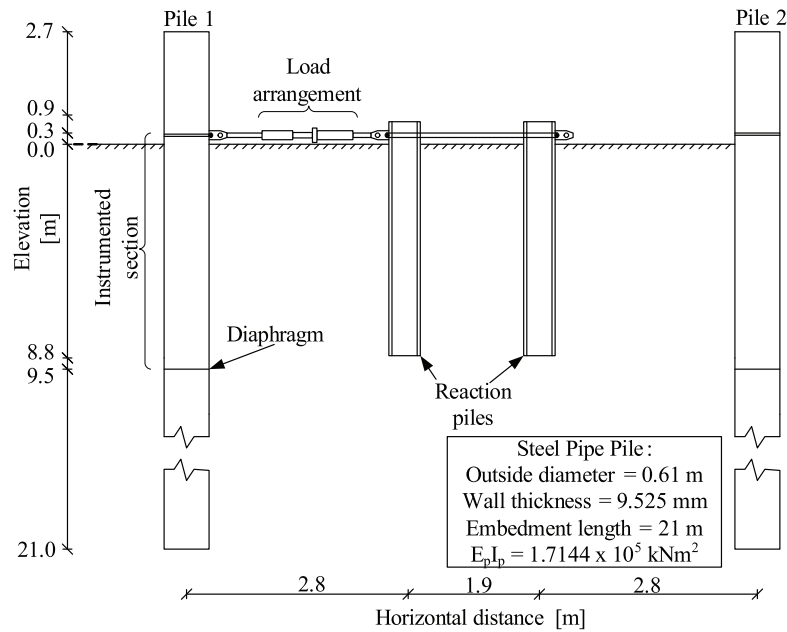


Figure 6: Setup for Mustang Island tests, after Cox et al. (1974).

one boring contained fine sand in the top 12 m and the other contained silty fine sand. The strength parameters were derived from standard penetration tests according to Peck et al. (1953). The standard penetration tests showed large variations in the number of blows per ft. Especially in the top 40 ft of both borings the number of blows per ft varied from 10 to 80. From 40 to 50 ft beneath the mudline clay was encountered. Beneath the clay layer the strength increased from 40 to 110 blows per ft. From 60 ft beneath the mudline to the total depth the number of blows per ft decreased from 110 to 15.

The piles were in total subjected to seven horizontal load cases consisting of two static and five cyclic. Pile 1 was at first subjected to a static load test 16 days after installation. The load was applied in increments until a maximum load of 267 kN (60000 lb) was reached. The maximum load was determined as no failure occurred in the pile. After the static load test on pile 1 two cyclic load tests were conducted. 52 days after installation a pull-out test was conducted on pile 2. A maximum of

1780 kN (400000 lb) was applied causing the pile to move 25 mm (1 inch). After another week pile 2 was subjected to three cases of cyclic loading and finally a static load test. The static load case on pile 2 was performed immediately after the third cyclic load case which might affect the results. Reese et al. (1974) do not clarify whether this effect is considered in the analyses.

3.2 Method A

Method A is the original method based on the Mustang Island tests, cf. Reese et al. (1974). The p - y curve formulation consists of three curves: an initial straight line, p_1 , a parabola, p_2 , and a straight line, p_3 , all assembled to one continuous piecewise differentiable curve, cf. fig. 7. The last straight line from (y_m, p_m) to (y_u, p_u) is bounded by an upper limit characterised by the ultimate soil resistance, p_u .

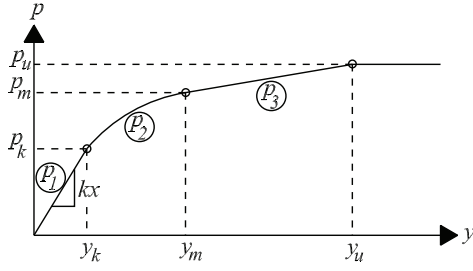


Figure 7: p - y curve for static loading using method A, after Reese et al. (1974).

Ultimate soil resistance

The total ultimate lateral resistance, F_{pt} , is equal to the passive force, F_p , minus the active force, F_a , acting on the pile. The ultimate resistance can be estimated analytically by means of either statically or kinematically admissible failure modes. At shallow depths a wedge will form in front of the pile assuming that the Mohr-Coulomb failure theory is valid. Reese et al. (1974) uses the wedge shown in fig. 8 to analytically calculate the passive ultimate resistance at shallow depths, p_{cs} . By using this failure mode a smooth pile is assumed, and therefore no tangential forces occur at the pile surface. The active force is also computed from Rankine's failure mode, using the minimum coefficient of active earth pressure.

At deep depths the sand will, in contrast to shallow depths, flow around the pile and a statical failure mode as sketched in fig. 9 is used to calculate the ultimate resistance. The transition depth between these failure modes occurs, at the depth where the ultimate resistances calculated based on the two failure modes are identical.

The ultimate resistance per unit length of the pile can for the two failure modes be

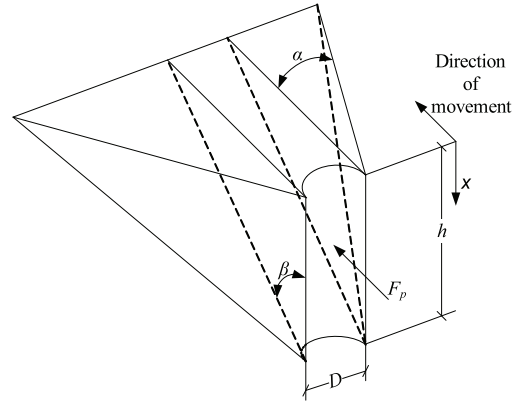


Figure 8: Failure mode at shallow depths, after Reese et al. (1974).

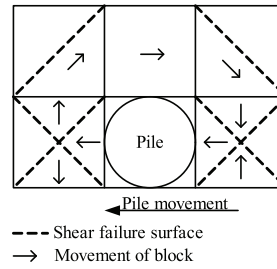


Figure 9: Failure mode at deep depths, after Reese et al. (1974).

calculated according to (12) and (13):

$$p_{cs} = \gamma' x \frac{K_0 x \tan \varphi_{tr} \sin \beta}{\tan(\beta - \varphi_{tr}) \cos \alpha} \quad (12)$$

$$+ \gamma' x \frac{\tan \beta}{\tan(\beta - \varphi_{tr})} (D - x \tan \beta \tan \alpha)$$

$$+ \gamma' x (K_0 x \tan \varphi_{tr} (\tan \varphi_{tr} \sin \beta - \tan \alpha) - K_a D)$$

$$p_{cd} = K_a D \gamma' x (\tan^8 \beta - 1) \quad (13)$$

$$+ K_0 D \gamma' x \tan \varphi_{tr} \tan^4 \beta$$

p_{cs} is valid at shallow depths and p_{cd} at deep depths, γ' is the effective unit weight, and φ_{tr} is the angle of internal friction based on triaxial tests. The factors α and β measured in degrees can be estimated by the following relations:

$$\alpha = \frac{\varphi_{tr}}{2} \quad (14)$$

$$\beta = 45^\circ + \frac{\varphi_{tr}}{2} \quad (15)$$

Hence, the angle β is estimated according to Rankine's theory which is valid if the

pile surface is assumed smooth. The factor α depends on the friction angle and load type. However, the effect of load type is neglected in (14). K_a and K_0 are the coefficients of active horizontal earth pressure and horizontal earth pressure at rest, respectively:

$$K_a = \tan^2\left(45 - \frac{\varphi_{tr}}{2}\right) \quad (16)$$

$$K_0 = 0.4 \quad (17)$$

The value of K_0 depends on several factors, e.g. the friction angle, but (17) does not reflect that.

The theoretical ultimate resistance, p_c , as function of depth is shown in fig. 10. As shown, the transition depth increases with diameter and angle of internal friction. Hence, for piles with a low slenderness ratio the transition depth might appear far beneath the pile-toe.

By comparing the theoretical ultimate resistance, p_c , with the full-scale tests at Mustang Island, Cox et al. (1974) found a poor agreement. Therefore, a coefficient A is introduced when calculating the actual ultimate soil resistance, p_u , employed in the p - y curve formulations:

$$p_u = Ap_c \quad (18)$$

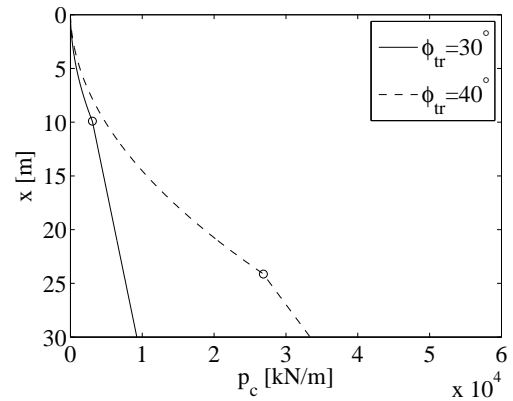
The variation of the coefficient A with non-dimensional depth, x/D , is shown in fig. 11a. The deformation causing the ultimate soil resistance, y_u , cf. fig. 7, is defined as $3D/80$.

p - y curve formulation

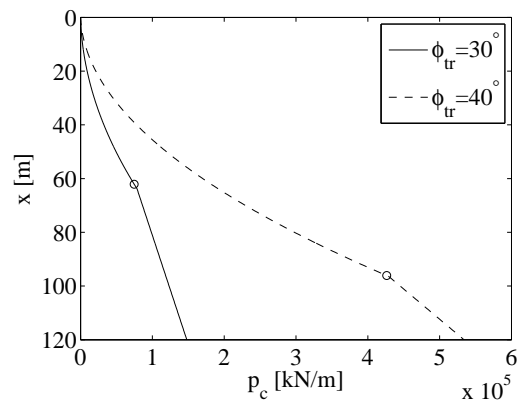
The soil resistance per unit length, p_m , at $y_m = D/60$, cf. fig. 7, can be calculated as:

$$p_m = Bp_c \quad (19)$$

B is a coefficient depending on the non-dimensional depth x/D , as plotted in fig. 11b.



(a) $D = 1.0$ m



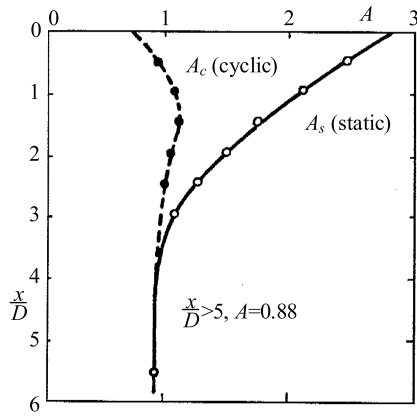
(b) $D = 4.0$ m

Figure 10: Theoretical ultimate resistance, p_c , as function of the depth. $\gamma' = 10$ kN/m³ has been used to plot the figure. The transition depths are marked with circles.

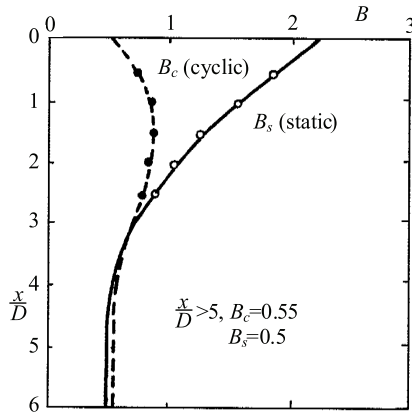
The slope of the initial straight line, p_1 as shown in fig. 7, depends on the initial modulus of subgrade reaction, k , cf. tab. 1, and the depth x . This is due to the fact that the in-situ Young's modulus of elasticity also increases with depth. Further, it is assumed that E_{py}^* increases linearly with depth since laboratory test shows, that the initial slope of the stress-strain curve for sand is a linear function of the confining pressure, cf. Terzaghi (1955). The initial straight line is given by:

$$p_1(y) = E_{py}^* y = kxy \quad (20)$$

Reese et al. (1974) suggest that the value of k only depends on the relative density/internal friction angle for the sand. On basis of full-scale experiments values



(a) Non-dimensional coefficient A for determining the ultimate soil resistance, p_u .



(b) Non-dimensional coefficient B for determining the soil resistance, p_m .

Figure 11: Non-dimensional variation of A and B , after Reese et al. (1974).

of k for loose sands, for medium sands, and for dense sands are 5.4 MN/m^3 (20 lbs/in^3), 16.3 MN/m^3 (60 lbs/in^3), and 34 MN/m^3 (125 lbs/in^3), respectively. The values are valid for sands below the water table. Earlier estimations of k has also been made, for example by Terzaghi (1955), but according to Reese and Van Impe (2001) these methods have been based on intuition and insight. Design regulations, e.g. API 1993 and DNV 1992, recommend the use of the curve shown in fig. 12. The curve only shows data for relative densities up to approximately 80 %, which causes large uncertainties in the estimation of k for very dense sands.

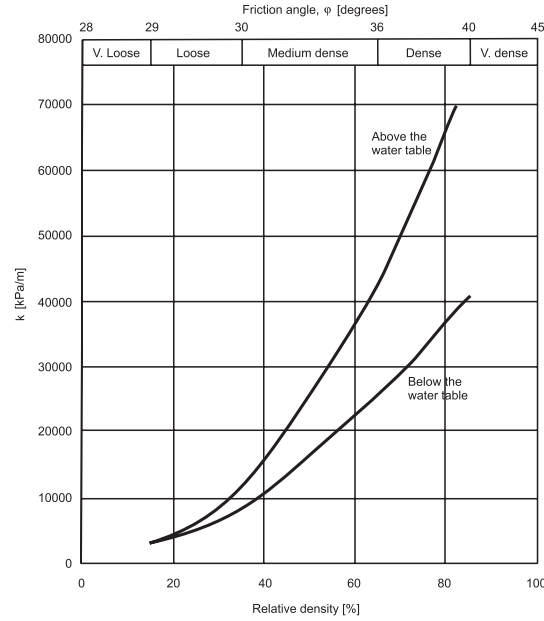


Figure 12: Variation of initial modulus of sub-grade reaction k as function of relative density, after API (1993).

The equation for the parabola, p_2 , cf. fig. 7, is described by:

$$p_2(y) = Cy^{1/n} \quad (21)$$

where C and n are constants. The constants and the parabola's start point (y_k, p_k) are determined by the following criteria:

$$p_1(y_k) = p_2(y_k) \quad (22)$$

$$p_2(y_m) = p_3(y_m) \quad (23)$$

$$\frac{\partial p_2(y_m)}{\partial y} = \frac{\partial p_3(y_m)}{\partial y} \quad (24)$$

The constants can then be calculated by:

$$n = \frac{p_m}{my_m} \quad (25)$$

$$C = \frac{p_m}{y_m^{1/n}} \quad (26)$$

$$y_k = \left(\frac{C}{kx}\right)^{n/(n-1)} \quad (27)$$

where m is the slope of the line, p_3 .

3.3 Method B

Design regulations, e.g. API (1993) and DNV (1992), suggest a modified formula-

tion of the p - y curves, in which the analytical expressions for the ultimate soil resistance, (12) and (13), are approximated using the dimensionless parameters C_1 , C_2 and C_3 :

$$p_u = \min \left(\begin{array}{l} p_{us} = (C_1x + C_2D)\gamma'x \\ p_{ud} = C_3D\gamma'x \end{array} \right) \quad (28)$$

The constants C_1 , C_2 and C_3 can be determined from fig. 13.

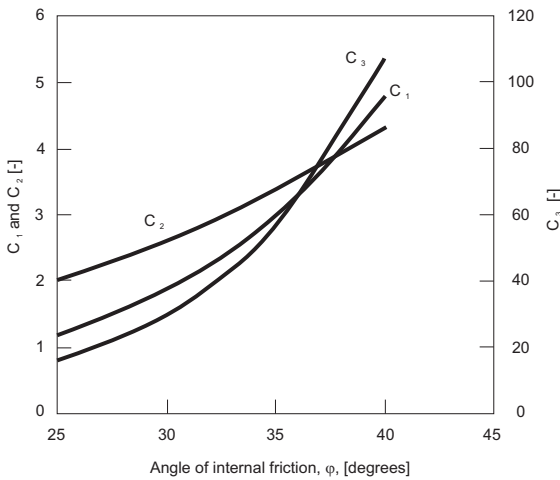


Figure 13: Variation of the parameters C_1 , C_2 and C_3 as function of angle of internal friction, after API (1993).

A hyperbolic formula is used to describe the relationship between soil resistance and pile deflection instead of a piecewise formulation as proposed by method A:

$$p(y) = Ap_u \tanh \left(\frac{kx}{Ap_u} y \right) \quad (29)$$

The coefficient A could either be determined from fig. 11a or by:

$$A = \left(3.0 - 0.8 \frac{H}{D} \right) \geq 0.9 \quad (30)$$

Since:

$$\frac{dp}{dy} \Big|_{y=0} = Ap_u \frac{\frac{kx}{Ap_u}}{\cosh^2 \left(\frac{kxy}{Ap_u} \right)} \Big|_{y=0} = kx \quad (31)$$

the p - y curve's initial slope is then similar using the two methods, cf. (20). Also the

upper bound of soil resistance will approximately be the same. However, there is a considerable difference in soil resistance predicted by the two methods when considering the pile deflection between y_k and y_u as shown in fig. 14. The soil parameters from tab. 2 has been used to construct the p - y curves shown in fig. 14.

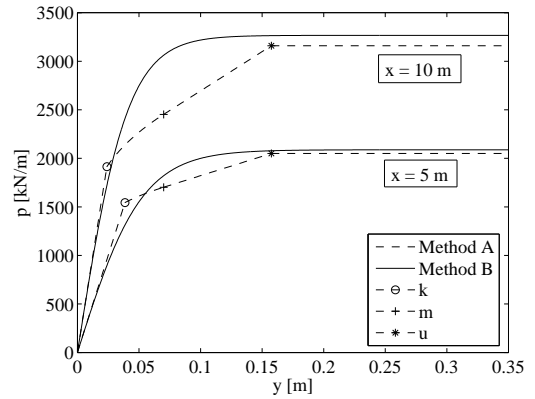


Figure 14: Example of p - y curves based on method A and B. The points k , m , and u refers to the points (y_k, p_k) , (y_m, p_m) , and (y_u, p_u) , respectively, cf. fig. 7.

Table 2: Soil parameters used for plotting the p - y curves in fig. 14.

γ' [kN/m ³]	ϕ_{tr} [°]	D [m]	k [kN/m ³]
10	30	4.2	8000

3.4 Comparison of methods

A comparison of both static and cyclic p - y curves has been made by Murchison and O'Neill (1984) based on a database of 14 full-scale tests on 10 different sites. The pile diameters varied from 51 mm (2 in.) to 1.22 m (48 in.). Both timber, concrete and steel piles were considered. The soil friction angles ranged from 23° to 42°. The test piles' slenderness ratio's are not provided.

Murchison and O'Neill (1984) compared the different p - y curve formulations with the full-scale tests using the Winkler approach. The predicted pile-head deflec-

tion, maximum moment, M_{max} , and the depth of maximum moment were compared according to the error, E :

$$E = \frac{|\text{predicted value} - \text{measured value}|}{\text{measured value}} \quad (32)$$

In the analysis it was desired to assess the formulations ability to predict the behaviour of steel pipe monopiles. Multiplication factors were therefore employed. The error, E , was multiplied by a factor of two for pipe piles, 1.5 for non-pipe driven piles and a factor of one for drilled piers. When predicted values were lower than the measured values the error was multiplied by a factor of two. By using these factors unconservative results are penalised and pipe piles are valued higher in the comparison. In tab. 3 the average value of E for static p - y curves are shown for the two methods. As shown, method B results in a lower average value of E for all the criteria considered in the comparison. The standard deviation of E was not provided in the comparison.

Table 3: Average values of the error, E . The methods are compared for pile-head deflection, maximum moment and depth to maximum moment.

	Pile-head deflection	M_{max}	Depth to M_{max}
Method A	2.08	0.75	0.58
Method B	1.44	0.44	0.40

Murchison and O'Neill (1984) analysed the sensitivity to parameter variation for method B. The initial modulus of subgrade reaction, k , the internal friction angle, φ , and the effective unit weight, γ' , were varied. They found that a 10 % increase in either φ or γ' resulted in an increase in pile-head deflection of up to 15 and 10 %, respectively. For an increase of 25 % in k an increase of up to 10 % of the pile-head deflection was found. The sensitivity analysis also shows that k has the greatest influence on pile-head deflection at small deflections and that φ has a great influence at large deflections. Murchison

and O'Neill (1984) state that the sizes of the errors in tab. 3 cannot be explained by parameter uncertainties. The amount of data included in the database was very small due to the unavailability of appropriately documented full-scale tests and Murchison and O'Neill (1984) therefore concluded that a further study of the soil-pile interaction was needed.

4 Limitations of p - y curves

The p - y curve formulations for piles in cohesionless soils are, as described, developed for piles with diameters much less than 4 to 6 m which is often necessary for nowadays monopiles. Today, there is no approved method for dealing with these large-diameter offshore piles, which is probably why the design regulations are still adopting the original p - y curves, cf. Reese et al. (1974), API (1993), and DNV (1992).

The p - y curve formulations are, as described, derived on basis of the Mustang Island tests which included only two identical piles and a total of seven load cases. Furthermore, the tests were conducted for only one pile diameter, one type of sand, only circular pipe piles etc. Taken into account the number of factors that might affect the behaviour of a laterally loaded pile and the very limited number of full-scale tests performed to validate the method, the influence of a broad spectra of parameters in the p - y curves are still to be clarified. Especially when considering offshore wind turbine foundations a validation of stiff piles with a slenderness ratio of $L/D < 10$ is needed as the Mustang Island test piles had a slenderness ratio of $L/D = 34.4$. It is desirable to investigate this as it might have a significant effect on the initial stiffness which is not accounted for in the p - y curve method. Briaud et al. (1984) postulate that the soil response depends on the flexibility of the pile. Cri-

teria for stiff versus flexible behaviour of piles have been proposed by various authors, for example Dobry et al. (1982), Budhu and Davies (1987), and Poulos and Hull (1989). The difference in deformation behaviour of a stiff and a flexible pile is shown in fig. 15. A pile behaves rigidly according to the following criterion, cf. Poulos and Hull (1989):

$$L < 1.48 \left(\frac{E_p I_p}{E_s} \right)^{0.25} \quad (33)$$

E_s is Young's modulus of elasticity of the soil. The criterion for a flexible pile behaviour is:

$$L > 4.44 \left(\frac{E_p I_p}{E_s} \right)^{0.25} \quad (34)$$

According to (33) a monopile with an outer diameter of 4 m, an embedded length of 20 m and a wall thickness of 0.05 m behaves rigidly if $E_s < 7.6$ MPa. In contrast, the pile exhibits a flexible behaviour if $E_s > 617$ MPa. Even dense sands have $E_s < 100$ MPa, so the recently installed monopiles behave, more like a rigid pile than a flexible.

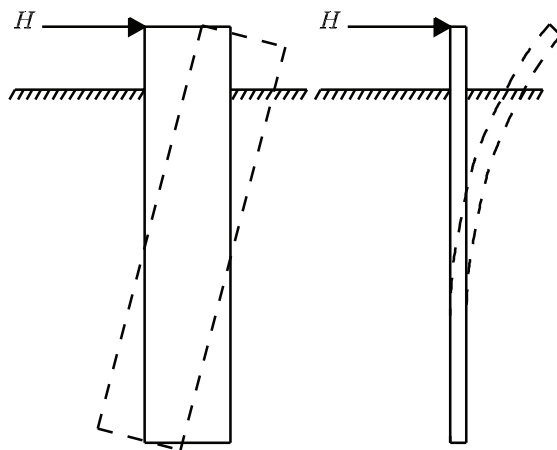


Figure 15: Rigid versus flexible pile behaviour.

For modern wind turbine foundations only small pile-head rotations are acceptable. Furthermore, the strict demands to the total stiffness of the system due to resonance in the serviceability mode increase the significance of the p - y curve's initial

slope and hereby the initial stiffness of the soil-pile system.

When using the p - y curve method the pile bending stiffness is employed when solving the beam on an elastic foundation problem. However, no importance is attached to the pile bending stiffness in the formulation of the p - y curves, hence E_{py} is independent of the pile properties. The validity of this assumption can be questioned as E_{py} is a parameter describing the soil-pile interaction.

When decoupling the non-linear springs associated with the Winkler approach another error is introduced since the soil in reality acts as a continuum.

In the following a number of assumptions and not clarified parameters related to the p - y curve method are treated separately. The treated assumptions and parameters are:

- Shearing force between soil layers.
- The ultimate soil resistance.
- The influence of vertical pile load on lateral soil response.
- Effect of soil-pile interaction.
- Effect of diameter on initial stiffness of p - y curves.
- Choice of horizontal earth pressure coefficient.
- Shearing force at the pile-toe.

4.1 Shearing force between soil layers

Employing the Winkler approach the soil response is divided into layers each represented by a non-linear spring. As the springs are uncoupled the layers are considered to be independent of the lateral

pile deflection above and below that specific layer, i.e. the soil layers are considered as smooth layers able to move relatively to each other without loss of energy to friction. Pasternak (1954) modified the Winkler approach by taking the shear stress between soil layers into account. The soil resistance per length of the pile is given by:

$$p(y) = -E_{py}^p y - G_s \frac{dy}{dx} \quad (35)$$

where G_s is the soil shear modulus. The subgrade reaction modulus E_{py} given in tab. 1 may indirectly contain the soil shear stiffness as the p - y curve formulation is fitted to full-scale tests. E_{py}^p , cf. (35), is a modulus of subgrade reaction without contribution from the soil shear stiffness.

Belkhir (1999) examines the significance of shear between soil layers by comparing the CAPELA design code, which takes the shear between soil layers into account, with the French PILATE design code, which deals with smooth boundaries. The two design codes are compared with the results of 59 centrifuge tests conducted on long and slender piles. Analyses show concordance between the two design codes when shear between soil layers is not taken into account. Furthermore, the analyses shows a reduction from 14 % to 5 % in the difference between the maximum moments determined from the centrifuge tests and the numerical simulations when taking the shear between the soil layers into account. However, it is not clear from the paper whether or not the shear between soil layers is dependent on pile diameter, slenderness ratio etc. Furthermore, it is not clarified whether the authors distinguish between E_{py} and E_{py}^p .

4.2 The ultimate soil resistance

The p - y curve formulations according to Method A and Method B, cf. (12) and (29), are both dependent on the ultimate

soil resistance. The method for estimating p_u is therefore evaluated in the following.

Failure modes

When designing large-diameter monopiles in sand, the transition between the presumed failure modes, cf. fig. 8 and fig. 9, will most often occur beneath the pile-toe, cf. fig. 10b. There are however several uncertainties concerning the ultimate soil resistance at shallow depths.

The prescribed method for calculating the ultimate soil resistance at shallow depths assumes that the pile is smooth, i.e. no skin friction appears and a Rankine failure mode will form. However, in reality a pile is neither perfectly rough nor perfectly smooth, and the assumed failure mechanism is therefore not exactly correct. According to Harremoës et al. (1984) a Rankine failure takes place for a perfectly smooth wall and a Prandtl failure for a perfectly rough wall, cf. fig. 16a and fig. 16b, respectively. Due to the fact that the pile is neither smooth nor rough a combination of a Rankine and Prandtl failure will occur. Furthermore, the failure modes are derived for a two-dimensional case.

In (12) the angle α , which determines the horizontal spread of the wedge, appears. Through experiments Reese et al. (1974) postulate that α depends on both the void ratio, friction angle, and the type of loading. However, the influence of void ratio and type of loading is neglected in the expression of α .

Nowadays monopiles are non-slender piles with high bending stiffness. The piles will therefore deflect as almost rigid piles and rather large deformations will occur beneath the point of zero deflection. However, when calculating the ultimate soil resistance according to method A and B the point of zero deflection is disregarded. For non-slender piles a failure mode as shown

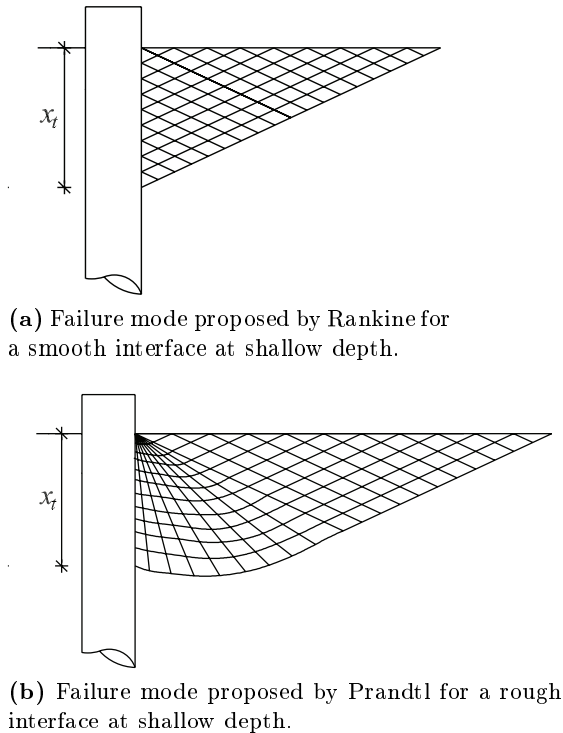


Figure 16: Rankine and Prandtl failure modes.

in fig. 17 could form. This failure mode is derived for a two-dimensional case and consists of stiff elastic zones and Rankine failures.

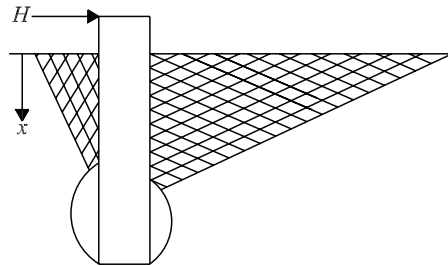


Figure 17: Possible failure mode for a non-slender pile at shallow depth.

Soil dilatancy

The effect of soil dilatancy is not included in method A and B, and thereby the effects of volume changes during pile deflection are ignored.

Fan and Long (2005) investigated the influence of soil dilatancy on the ultimate soil resistance by use of a three-

dimensional, non-linear finite element model. The constitutive model proposed by Desai et al. (1991) incorporating a non-associative flow rule was employed in the analyses. The finite element model was calibrated based on the full-scale tests at Mustang Island. The magnitudes of ultimate soil resistance were calculated for two compactions of one sandtype with similar friction angles ($\varphi_{tr} = 45^\circ$) but different angles of dilatancy. The dilatancy angles are not directly specified by Fan and Long (2005). Estimates have therefore been made by interpretation of the relation between volumetric strains and axial strains. Dilatancy angles of approximately 22° and 29° were found. An increase in ultimate soil resistance of approximately 50 % were found with the increase in dilatancy angle. In agreement with laboratory tests, where the dilatancy in dense sands contributes to strength, this makes good sense. However, as the dilatancy is increased and the friction angle is held constant extra shear strength is introduced to the material.

Alternative methods

Besides the prescribed method for calculating the ultimate soil resistance other formulations exist, see for example Broms (1964) and Hansen (1961). Fan and Long (2005) compared these methods with a finite element solution for various diameters, friction angles, and coefficients of horizontal earth pressure. Hansen's method showed the best correlation with the finite element model, whereas Broms' method resulted in conservative values of the ultimate soil resistance. Further, a significant difference between the finite element solution and the API method was found. The API method produces conservative results at shallow depths and non-conservative results at deep depths. The results of the comparison are shown in fig. 18.

When calculating the ultimate soil resis-

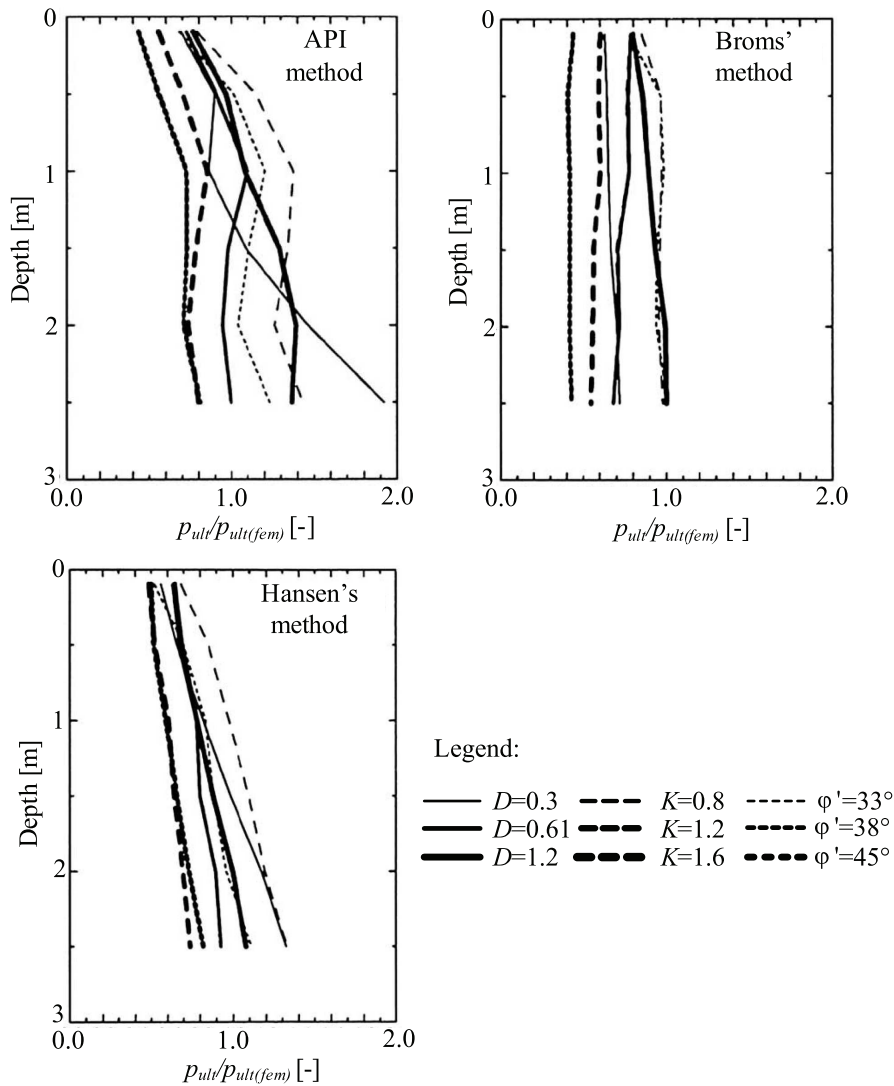


Figure 18: Comparison of the ultimate soil resistance estimated by Broms' method, Hansen's method and API's method with a finite element model, after Fan and Long (2005). $p_{ult}/p_{ult(fem)}$ defines the ratio of the ultimate soil resistance calculated by the analytical methods and the ultimate soil resistance calculated by the finite element model.

tance according to method A and B, the side friction as illustrated in fig. 19 is neglected. To take this into account Briaud and Smith (1984) has proposed a model where the ultimate soil resistance is calculated as the sum of the net ultimate frontal resistance and the net ultimate side friction. In the model both the net ultimate frontal resistance and the net ultimate side friction are taken to vary linearly with pile diameter. Zhang et al. (2005) refer to a comparison made by Barton and Finn (1983) of the model made by Briaud and Smith (1984) and lateral load tests per-

formed in a centrifuge. The circular piles, associated with the tests, have diameters of 9, 12, and 16 mm and a slenderness ratio larger than 20. The magnitude of the acceleration in the centrifuge is not provided. The ultimate soil resistance is compared for four depths and the error between measured and computed values is found to be less than 10 %. The methods proposed by Broms (1964) and Reese et al. (1974) are also compared with the model tests. Conclusions similar to Fan and Long (2005) are reached.

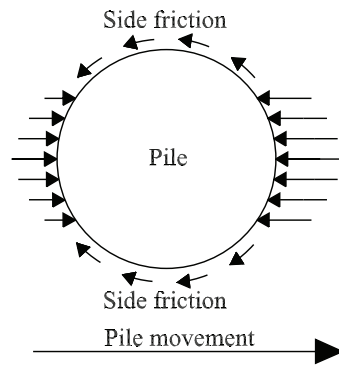


Figure 19: Side friction and soil pressure on the front and the back of the pile due to lateral deflection.

Side friction is due to the model proposed by Briaud and Smith (1984) unaffected by the diameter since both the ultimate frontal resistance and the net ultimate side friction vary linearly with diameter. However, the ultimate frontal resistance varies non-linearly with diameter in both the model proposed by Hansen (1961) and Reese et al. (1974). The importance of side friction might therefore be more significant for large-diameter monopiles. Furthermore, it should be emphasized that the normal resistance at the back of the pile is neglected in the analysis.

Summary

Several assumptions are employed when calculating the ultimate soil resistance according to Reese et al. (1974) and the design regulations, e.g. API (1993) and DNV (1992). These methods do not account for friction between pile and soil as the pile surface is assumed smooth. Furthermore, the failure modes do not consider deflections beneath the point of zero deflection. Thus, the assumed failure modes might be inaccurate.

The dilatancy of the soil affects the ultimate soil resistance, but it is neglected in the p - y curve formulations.

Several methods for determining the ultimate soil resistance exist. The method

proposed by Hansen (1961) were found to correlate better with a finite element model than the methods proposed by Reese et al. (1974) and Broms (1964). In order to take the effect of side friction into account a model was proposed by Briaud and Smith (1984). Predictions regarding the ultimate soil resistance correlate well with centrifuge tests using this model.

4.3 The influence of vertical load on lateral soil response

In current practice, piles are analysed separately for vertical and horizontal behaviour. Karthigeyan et al. (2006) investigated the influence of vertical load on the lateral response in sand through a three-dimensional numerical model. In the model they adopted a Drucker-Prager constitutive model with a non-associated flow rule.

Karthigeyan et al. (2006) calibrated the numerical model against two different kinds of field data carried out by Karasev et al. (1977) and Comodromos (2003). A concrete pile with a diameter of 0.6 m and a slenderness ratio of 5 were tested, cf. Karasev et al. (1977). The soil strata consisted of stiff sandy loam in the top 6 m underlain by sandy clay. Comodromos (2003) performed the tests in Greece. The soil profile consisted of silty clay near the surface with thin sublayers of loose sand. Beneath a medium stiff clay layer a very dense sandy gravel layer was encountered. A pile with a diameter of 1 m and a slenderness ratio of 52 were tested.

To investigate the influence of vertical load on the lateral response in sand Karthigeyan et al. (2006) made a model with a squared concrete pile (1200 × 1200 mm) with a length of 10 m. Two types of sand were tested, a loose and a dense sand with a friction angle of 30° and 36°, respectively. The vertical load was applied in two different ways, simultaneously with

the lateral load, SAVL, and prior to the lateral load, VPL. Various values of vertical load were applied. The conclusion of the analyses were that the lateral capacity of piles in sand increases under vertical load. The increase in lateral capacity depended on how the vertical load was applied as the highest increase was in the case of VPL. For the dense sand with a lateral deflection of 5 % of the side length the increase in lateral capacity was, in the case of SAVL, of up to 6.8 %. The same situation in the case of VPL resulted in an increase of up to 39.3 %. Furthermore, the analyses showed a large difference in the increase of lateral capacity between the two types of sand as the dense sand resulted in the highest increase. Due to vertical loads higher vertical soil stresses and thereby higher horizontal stresses occur, which also mobilise larger friction forces along the length of the pile. Therefore, the lateral capacity increases under the influence of vertical loading.

Although the analyses made by Karthigeyan et al. (2006) indicated a considerable increase in the lateral capacity at a relative high deflection, the improvement at small displacements are not as significant. Therefore the results might not be of importance for wind turbine foundations.

4.4 Effect of soil-pile interaction

No importance is attached to the pile bending stiffness, $E_p I_p$, in the formulation of the p - y curves. Hereby, E_{py} is independent of the pile properties, which seems questionable as E_{py} is a soil-pile interaction parameter. Another approach to predict the response of a flexible pile under lateral loading is the strain wedge (SW) model developed by Norris (1986), which includes the pile properties. The concept of the SW model is that the traditional parameters in the one-dimensional Winkler approach can be characterised in terms

of a three-dimensional soil-pile interaction behaviour.

The SW model parameters are related to a three-dimensional passive wedge developing in front of the pile subjected to lateral loading. The wedge has a form similar to the wedge associated with method A, as shown in fig. 8. However the angles α and β are given by:

$$\alpha = \varphi_m \quad (36)$$

$$\beta = 45^\circ + \frac{\varphi_m}{2} \quad (37)$$

where φ_m is the angle of mobilised internal friction.

The purpose of the method is to relate the stresses and strains of the soil in the wedge to the subgrade reaction modulus, E_{py} . The SW model described by Ashour et al. (1998) assumes a linear deflection pattern of the pile over the passive wedge depth, h , as shown in fig. 20. The dimension of the passive wedge depends on two types of stability, local and global, respectively. To obtain local stability the SW model should satisfy equilibrium and compatibility between pile deflection, strains in the soil and soil resistance. This is obtained by an iterative procedure where an initial horizontal strain in the wedge is assumed.

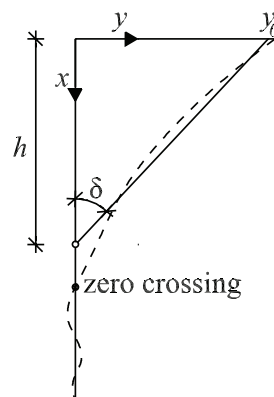


Figure 20: Linear deflection assumed in the SW-model, shown by the solid line. The dashed line shows the real deflection of a flexible pile. After Ashour et al. (1998).

After assuming a passive wedge depth the

subgrade reaction modulus can be calculated along the pile. Based on the calculated subgrade reaction modulus the pile-head deflection can be calculated from the one-dimensional Winkler approach. Global stability is obtained when concordance between the pile-head deflection calculated by the Winkler approach and the SW-model is achieved. The passive wedge depth is varied until global stability is obtained.

The pile bending stiffness influence the deflection calculated by the one-dimensional Winkler approach and hereby also the wedge depth. Hence, the pile bending stiffness influence the p - y curves calculated by the SW-model.

The equations associated with the SW model are based on the results of isotropic drained triaxial tests. Hereby an isotropic soil behaviour is assumed at the site. The SW model takes the real stresses into account by dealing with a stress level, defined as:

$$SL = \frac{\Delta\sigma_h}{\Delta\sigma_{hf}} \quad (38)$$

where $\Delta\sigma_h$ and $\Delta\sigma_{hf}$ are the mobilised horizontal stress change and the horizontal stress change at failure, respectively. The spread of the wedge is defined by the mobilised friction angle, cf. (36) and (37). Hence the dimensions of the wedge depends on the mobilised friction.

Although the SW model is based on the three-dimensional soil-pile interaction and it is dependent on both soil and pile properties there are still some points of criticism or doubt about the model. The model does not take the active soil pressure that occurs at the back of the pile into account. This seems to be a non-conservative consideration. Furthermore, the wedge only accounts for the passive soil pressure at the top front of the pile but neglects the passive soil pressure beneath the zero crossing point which will occur for a rigid pile, cf. section 4.2. The assumption of an isotropic behaviour of the soil in

the wedge seems unrealistic in most cases for sand. To obtain isotropic behaviour the coefficient of horizontal earth pressure, K , needs to be 1, which is not the case for most sands. Effects of cyclic loading are not implemented in the SW model which is a large disadvantage seen in the light of the strict demands for the foundation design.

Ashour et al. (2002) criticise the p - y curve method as it is based and verified through a small number of tests. However, the SW model, has according to Lesny et al. (2007) been verified only for conventional pile diameters, i.e. slender piles.

Ashour and Norris (2000) investigated by means of the SW model, the influence of pile stiffness on the lateral response for conditions similar to the Mustang Island tests. p - y curves at a depth of 1.83 m are shown in fig. 21 for different values of $E_p I_p$. The p - y curve proposed by Reese et al. (1974) is also presented in the figure. It is seen that there is a good concordance between the experimental test and the SW model for similar pile properties. Furthermore, the soil resistance increases with increasing values of $E_p I_p$.

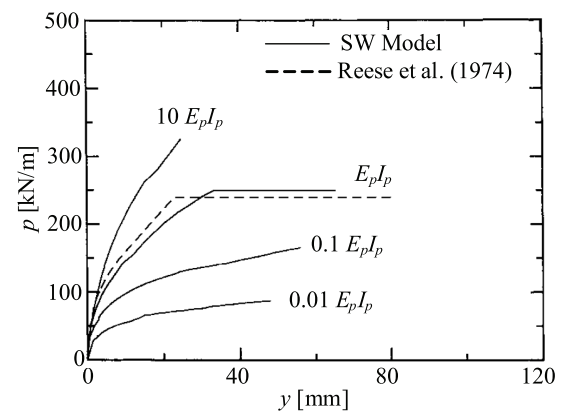


Figure 21: The influence of pile bending stiffness, after Ashour et al. (2000).

Changing the pile stiffness affects the p - y curves drastically according to the SW model. Fan and Long (2005) investigated the problem by changing the Young's modulus of elasticity of the pile while keeping

the diameter and the second moment of inertia constant in their three-dimensional finite element model. The results are shown in fig. 22. The investigation showed that the pile stiffness has neither significant influence on the ultimate bearing capacity nor on the initial stiffness of the soil-pile system. The effect of pile stiffness shown in fig. 21 and 22 has not been verified through experimental work.

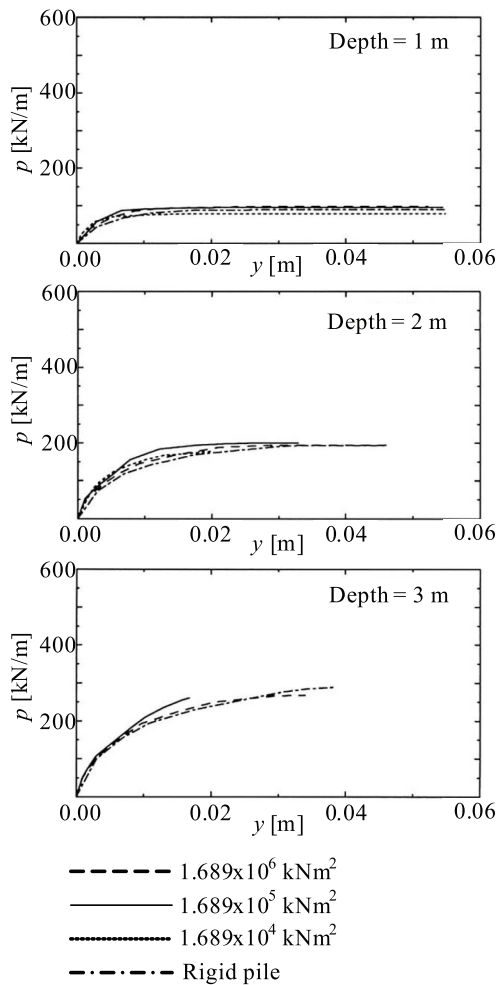


Figure 22: Effect of pile bending stiffness, after Fan and Long (2005).

4.5 Effect of diameter on initial stiffness of p - y curves

The initial modulus of subgrade reaction, k , is according to API (1993), DNV (1992), and Reese et al. (1974) only dependent on the relative density of the soil

as shown in fig. 12. Hence, the methods A and B do not include $E_p I_p$ and D in the determination of k , which might seem surprisingly. Different studies on the consequences of neglecting the pile parameters have been conducted over time with contradictory conclusions. Ashford and Juirnarongrit (2003) point out the following three conclusions.

The first significant investigation was the analysis of stress bulbs conducted by Terzaghi (1955). Terzaghi concluded that by increasing the pile diameter the stress bulb formed in front of the pile is stretched deeper into the soil. This results in a greater deformation due to the same soil pressure at the pile. Terzaghi found that the soil pressure at the pile is linearly proportional to the inverse of the diameter giving that the modulus of subgrade reaction, E_{py} , is independent on the diameter, cf. definitions in tab. 1.

Secondly, Vesic (1961) proposed a relation between the modulus of subgrade reaction used in the Winkler approach and the soil and pile properties. This relation showed that E_{py} is independent of the diameter for circular and squared piles.

Thirdly, Pender (1993) refers to two reports conducted by Carter (1984) and Ling (1988). Using a simple hyperbolic soil model they concluded that E_{py} is linear proportional to the pile diameter.

The conclusions made by Terzaghi (1955), Vesic (1961), and Pender (1993) concerns the subgrade reaction modulus, E_{py} . Their conclusions might also be applicable for the initial modulus of subgrade reaction, k , and the initial stiffness, E_{py}^* .

Based on the investigations presented by Terzaghi (1955), Vesic (1961), and Pender (1993), it must be concluded that no clear correlation between the initial modulus of subgrade reaction and the pile diameter has been realised. Ashford and Juirnarongrit (2005) contributed to the

discussion with their extensive study of the problem which was divided into three steps:

- Employing a simple finite element model.
- Analyses of vibration tests on large-scale concrete piles.
- Back-calculation of p - y curves from static load tests on the concrete piles.

The finite element analysis was according to Ashford and Juirnarongrit (2005) very simple and did not account very well for the soil-pile interaction since friction along the pile, the effect of soil confinement, and gaps on the back of the pile were not included in the model. In order to isolate the effect of the diameter on the magnitude of E_{py} , the bending stiffness of the pile was kept constant when varying the diameter. The conclusion of the finite element analysis were that the diameter has some effect on the pile-head deflection as well as the moment distribution. An increase in diameter leads to a decreasing pile-head deflection and a decreasing depth to the point of maximum moment. However, Ashford and Juirnarongrit (2005) concluded that the effect of increasing the diameter appears to be relatively small compared to the effect of increasing the bending stiffness, $E_p I_p$, which was not further investigated in the present case.

The second part of the work by Ashford and Juirnarongrit (2005) dealt with vibration tests on large-scale monopiles. The tests included three instrumented piles with diameters of 0.6, 0.9, and 1.2 m (12 m in length) and one pile with a diameter of 0.4 m and a length of 4.5 m. All piles were cast-in-drilled-hole and made up of reinforced concrete. They were installed at the same site consisting of slightly homogenous medium to very dense weakly cemented clayey to silty sand. The piles

were instrumented with several types of gauges, i.e. accelerometers, strain gauges, tiltmeters, load cells, and linear potentiometers. The concept of the tests were that by subjecting the piles to small lateral vibrations the soil-pile interaction at small strains could be investigated by collecting data from the gauges.

Based on measured accelerations the natural frequencies of the soil-pile system were determined. These frequencies were in the following compared to the natural frequencies of the system determined by means of a numerical model. Two different expressions for the modulus of subgrade reaction, E_{py} , were used, one that is linearly dependent and one that is independent on the diameter. The strongest correlation was obtained between the measured frequencies and the frequencies computed by using the relation independent of the diameter. Hence, the vibration tests substantiate Terzaghi and Vesic's conclusions. It is noticed that the piles were only subjected to small deflections, hence $E_{py} \approx E_{py}^*$.

Finally, Ashford and Juirnarongrit (2005) performed a back-calculation of p - y curves from static load cases. From the back-calculation a soil resistance was found at the ground surface. This is in contrast to the p - y curves for sand given by Reese et al. (1974) and the recommendations in API (1993) and DNV (1992) in which the initial stiffness, E_{py}^* , at the ground surface is zero. The resistance at the ground surface might be a consequence of cohesion in the slightly cemented sand.

Furthermore, a comparison of the results from the back-calculations for the various pile diameters indicated that the effects of pile diameter on E_{py}^* were insignificant. The three types of analyses conducted by Ashford and Juirnarongrit (2005) therefore indicate the same: the effect of the diameter on E_{py}^* is, insignificant.

Fan and Long (2005) investigated the influence of the pile diameter on the soil re-

response by varying the diameter and keeping the bending stiffness, $E_p I_p$, constant in their finite element model. The results are given as curves normalised by the diameter and vertical effective stress as shown in fig. 23. No significant correlation between diameter and initial stiffness is observed. It must be emphasised that the investigation considers only slender piles.

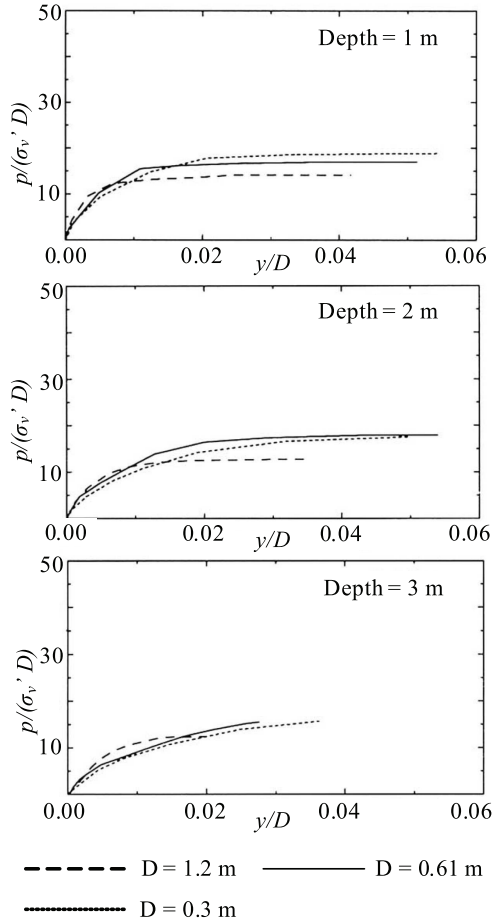


Figure 23: Effect of changing the diameter, after Fan and Long (2005).

For non-slender piles the bending stiffness might cause the pile to deflect almost as a rigid object. Therefore, the deflection at the pile-toe might be significant. Thus a correct prediction of the initial stiffness is important in order to determine the correct pile deflection.

Based upon a design criterion demanding the pile to be fixed at the toe, Lesny and Wiemann (2006) investigated by back-

calculation the validity of the assumption of a linearly increasing E_{py}^* with depth. The investigation indicated that E_{py}^* is overestimated for large-diameter piles at great depths. Therefore, they suggested a power function, to be used instead of a linear relation, cf. fig. 24. A finite element model was made in order to validate the power function. The investigations showed that employing the power function approach gave deflections more similar to the numerical modelling than by using the traditional linear approach in the p - y curve method. However, it was emphasised that the method should only be used for determination of pile length. The p - y curves still underestimates the pile-head deflections even though the parabolic approach is used.

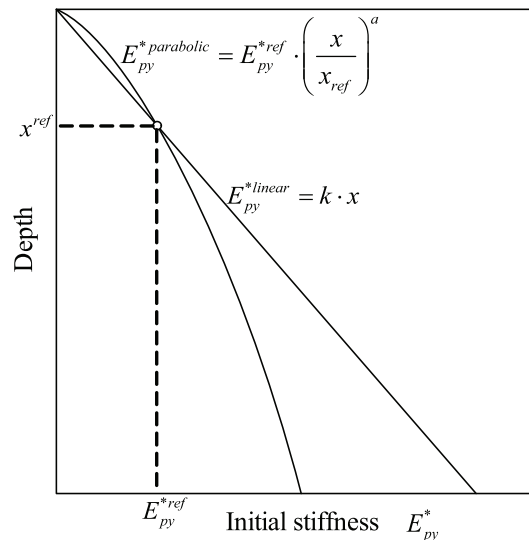


Figure 24: Variation of initial stiffness, E_{py}^* , as function of depth, after Lesny and Wiemann (2006). The linear approach is employed in Reese et al. (1974) and the design codes, e.g. API (1993) and DNV (1992). The exponent a can be set to 0.5 and 0.6 for dense and medium dense sands, respectively.

The above mentioned investigations all made by means of cohesionless soils are summarised in tab. 4. From this tabular it is obvious that more research is needed.

Looking at cohesion materials the tests are also few. According to Ashford and Juirnarongrit (2005) the most signif-

Table 4: Chronological list of investigations concerning the effects of diameter on the initial stiffness of the p - y curve formulations.

Author	Method	Conclusion
Terzaghi (1955)	Analytical	Independent
Vesic (1961)	Analytical	Independent
Carter (1984)	Analytical expression calibrated against full-scale tests	Linearly dependent
Ling (1988)	Validation of the method proposed by Carter (1984)	Linearly dependent
Ashford and Juirnarongrit (2005)	Numerical and large-scale tests	Insignificant influence
Fan and Long (2005)	Numerical	Insignificant influence
Lesny and Wiemann (2006)	Numerical	Initial stiffness is non-linear for long and large-diameter piles

icant findings are presented by Reese et al. (1975), Stevens and Audibert (1979), O'Neill and Dunnavant (1984), and Dunnavant and O'Neill (1985).

Reese et al. (1975) back-calculated p - y curves for a 0.65 m diameter pile in order to predict the response of a 0.15 m pile. The calculations showed a good approximation of the moment distribution, but the deflections however were considerably underestimated compared to the measured values associated with the 0.15 m test pile.

Based on published lateral pile load tests Stevens and Audibert (1979) found that deflections computed by the method proposed by Matlock (1970) and API (1987) were overestimated. The overestimation increases with increasing diameter leading to the conclusion that the modulus of subgrade reaction, E_{py} , increases for increasing diameter.

By testing laterally loaded piles with diameters of 0.27 m, 1.22 m, and 1.83 m in an overconsolidated clay, O'Neill and Dunnavant (1984) and Dunnavant and O'Neill (1985) found that there were a non-linear relation between deflection and diameter. They found that the deflection at 50 % of the ultimate soil resistance generally decreased with an increase in diameter. Hence, E_{py} increases with increasing pile

diameter.

4.6 Choice of horizontal earth pressure coefficient

When calculating the ultimate soil resistance by method A the coefficient of horizontal earth pressure at rest, K_0 , equals 0.4 even though it is well-known that the relative density/the internal friction angle influence the value of K_0 . In addition, pile driving may increase the coefficient of horizontal earth pressure K .

The influence of the coefficient of horizontal earth pressure, K , is evaluated by Fan and Long (2005) for three values of K and an increase in ultimate soil resistance were found for increasing values of K . The increase in ultimate soil resistance is due to the fact, that the ultimate soil resistance is primarily provided by shear resistance in the sand, which depends on the horizontal stress.

Reese et al. (1974) and thereby API (1993) and DNV (1992) consider the initial modulus of subgrade reaction k to be independent of K . Fan and Long (2005) investigated this assumption. An increase in K results in an increase in confining pressure implying a higher stiffness. Hence, k

is highly affected by a change in K ; k increases with increasing values of K .

4.7 Shearing force at the pile-toe

Recently installed monopiles have diameters around 4 to 6 m and a pile slenderness ratio around 5. Therefore, the bending stiffness, $E_p I_p$, is quite large compared to the pile length. The bending deformations of the pile will therefore be small and the pile will almost move as a rigid object as shown in fig. 25.

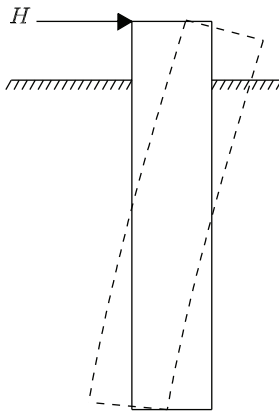


Figure 25: Deflection curve for non-slender pile.

As shown in fig. 25 there is a deflection at the pile-toe. This deflection causes shearing stresses at the pile-toe to occur, which increase the total lateral resistance. According to Reese and Van Impe (2001) a number of tests have been made in order to determine the shearing force at the pile-toe, but currently no results from these tests have been published and no methods for calculating the shearing force as a function of the deflection have been proposed.

5 Conclusion

Monopiles are an often used foundation concept for offshore wind energy converters and they are usually designed by use of the p - y curve method. The p - y curve

method is a versatile and practical design method. Furthermore, the method has a long history of approximately 50 years of experience.

The p - y curve method was originally developed to be used in the offshore oil and gas sector and has been verified with pile diameters up to approximately 2 m. However, nowadays monopiles with diameters of 4 to 6 m and a slenderness ratio around 5 are not unusual.

In the present review a number of the assumptions and not clarified parameters associated with the p - y curve method have been described. The analyses considered in the review state various conclusions, some rather contradictory. However most of the analyses are based on numerical models and concentrate on piles with a slenderness ratio much higher than 5. In order to extend the p - y curve method to nowadays monopiles further numerical and experimental work are needed. Important findings of this paper are summarised as follows:

- When employing the Winkler approach the soil response is assumed independent of the deflections above and below any given point. The effect of involving the shear stress between soil layers seems to be rather small, and from the analysis it is not clear whether the results are dependent on pile properties.
- The failure modes assumed when dealing with the ultimate soil resistance at shallow depth seems rather unrealistic. In the employed methods the surface of the pile is assumed smooth. Furthermore, the method does not take the pile deflection into account, which seems critical for rigid piles.
- Soil dilatancy affects the soil response, but it is neglected in the p - y curve formulations.

- Determining the ultimate soil resistance by the method proposed by Hansen (1961), seems to give more reasonable results than the method associated with the design codes. Moreover, side friction is neglected in the design codes.
- In current practice piles are analysed separately for vertical and horizontal behaviour. Taking into account the effect of vertical load seems to increase the lateral soil resistance. However, the effect is minor at small lateral deflections.
- Analyses of p - y curves' sensitivity to pile bending stiffness, $E_p I_p$, gives rather contradictory conclusions. According to the Strain Wedge model the formulations of p - y curves are highly affected by pile bending stiffness. This is in contradiction to the existing p - y curves and a numerical analysis performed by Fan and Long (2005).
- The initial stiffness is independent of pile diameter according to the existing p - y curves. This agrees with analytical investigations by Terzaghi (1955), and Vesic (1961). Similarly, Ashford and Juirnarongrit (2005) concluded that initial stiffness is independent of the pile diameter based upon an analysis of a finite element model and tests on large scale concrete piles. Carter (1984) and Ling (1988) however, found that the initial stiffness is linear proportional to pile diameter.
- Based upon a numerical model, Lesny and Wiemann (2006) found that the initial stiffness is over-predicted at the bottom of the pile when considering large-diameter piles.
- The initial stiffness of the p - y curve as well as the ultimate soil resistance increases with an increase in the coefficient of horizontal earth pressure.

This effect is not taking into consideration in the existing p - y curve formulations.

- A pile which behaves rigidly will have a deflection at the pile-toe. Taking this deflection into consideration might give an increase in net soil resistance.

References

- Abdel-Rahman K., and Achmus M., 2005. Finite element modelling of horizontally loaded Monopile Foundations for Offshore Wind Energy Converters in Germany. *International Symposium on Frontiers in Offshore Geotechnics*, Perth, Australia, Sept. 2005. Balkerna.
- API, 1993. Recommended practice for planning, designing, and constructing fixed offshore platforms - Working stress design, *API RP2A-WSD*, American Petroleum Institute, Washington, D.C., 21. edition.
- Ashford S. A., and Juirnarongrit T., March 2003. Evaluation of Pile Diameter Effect on Initial Modulus of Subgrade Reaction. *Journal of Geotechnical and Geoenvironmental Engineering*, **129**(3), pp. 234-242.
- Ashford S. A., and Juirnarongrit T., 2005. Effect of Pile Diameter on the Modulus of Subgrade Reaction. *Report No. SSRP-2001/22, Department of Structural Engineering, University of California, San Diego*.
- Ashour M., Norris G., and Pilling P., April 1998. Lateral loading of a pile in layered soil using the strain wedge model. *Journal of Geotechnical and Geoenvironmental Engineering*, **124**(4), paper no. 16004, pp. 303-315.
- Ashour M., and Norris G., May 2000. Modeling lateral soil-pile response based

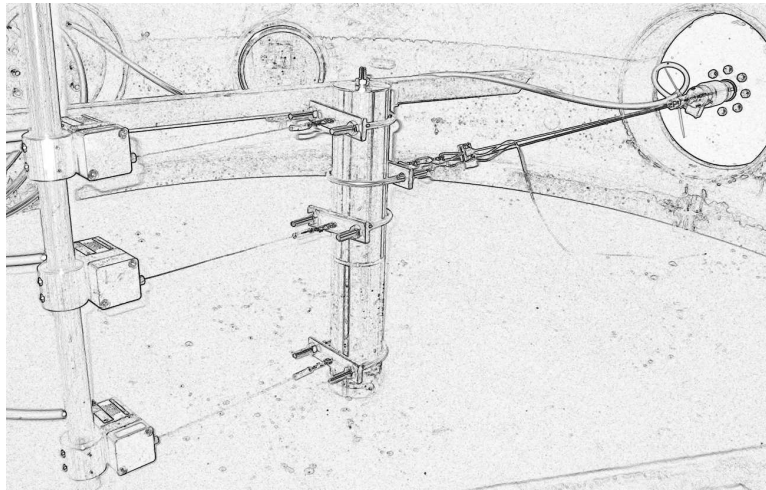
- on soil-pile interaction. *Journal of Geotechnical and Geoenvironmental Engineering*, **126**(5), paper no. 19113, pp. 420-428.
- Ashour M., Norris G., and Pilling P., August 2002. Strain wedge model capability of analyzing behavior of laterally loaded isolated piles, drilled shafts and pile groups. *Journal of Bridge Engineering*, **7**(4), pp. 245-254.
- Banerjee P. K., and Davis T. G., 1978. The behavior of axially and laterally loaded single piles embedded in non-homogeneous soils. *Geotechnique*, **28**(3), pp. 309-326.
- Barton Y. O., and Finn W. D. L., 1983. Lateral pile response and p - y curves from centrifuge tests. *Proceedings of the 15th Annual Offshore Technology Conference*, Houston, Texas, paper no. OTC 4502, pp. 503-508.
- Belkhir S., Mezazigh S., and Levacher, D., December 1999. Non-Linear Behavior of Lateral-Loaded Pile Taking into Account the Shear Stress at the Sand. *Geotechnical Testing Journal*, GTJODJ, **22**(4), pp. 308-316.
- Briaud J. L., Smith T. D., and Meyer, B. J., 1984. Using pressuremeter curve to design laterally loaded piles. *In Proceedings of the 15th Annual Offshore Technology Conference*, Houston, Texas, paper no. OTC 4501.
- Broms B. B., 1964. Lateral resistance of piles in cohesionless soils. *Journal of Soil Mechanics and Foundation Div.*, **90**(3), pp. 123-156.
- Budhu M., and Davies T., 1987. Nonlinear Analysis of Laterally loaded piles in cohesionless Soils. *Canadian geotechnical journal*, **24**(2), pp. 289-296.
- Carter D. P., 1984. A Non-Linear Soil Model for Predicting Lateral Pile Response. *Rep. No. 359, Civil Engineering Dept., Univ. of Auckland, New Zealand.*
- Comodromos E. M., 2003. Response prediction for horizontally loaded pile groups. *Journal of the Southeast Asian Geotechnical Society*, **34**(2), pp. 123-133.
- Cox W. R., Reese L. C., and Grubbs B. R., 1974. Field Testing of Laterally Loaded Piles in Sand. *Proceedings of the Sixth Annual Offshore Technology Conference*, Houston, Texas, paper no. OTC 2079.
- Desai C. S., Sharma K. G., Wathugala G. W., and Rigby D. B., 1991. Implementation of hierarchical single surface δ_0 and δ_1 models in finite element procedure. *International Journal for Numerical & Analytical Methods in Geomechanics*, **15**(9), pp. 649-680.
- DNV, 1992. Foundations - Classification Notes No 30.4, Det Norske Veritas, Det Norske Veritas Classification A/S.
- Dobry R., Vincente E., O'Rourke M., and Roesset J., 1982. Stiffness and Damping of Single Piles. *Journal of geotechnical engineering*, **108**(3), pp. 439-458.
- Dunnivant T. W., and O'Neill M. W., 1985. Performance analysis and interpretation of a lateral load test of a 72-inch-diameter bored pile in overconsolidated clay. *Report UHCE 85-4*, Dept. of Civil Engineering., University of Houston, Texas, p. 57.
- Fan C. C., and Long J. H., 2005. Assessment of existing methods for predicting soil response of laterally loaded piles in sand. *Computers and Geotechnics* **32**, pp. 274-289.
- Hansen B. J., 1961. *The ultimate resistance of rigid piles against transversal forces*. Danish Geotechnical Institute, Bull. No. 12, Copenhagen, Denmark, 5-9.
- Harremoës P., Ovesen N. K., and Jacobsen H. M., 1984. *Lærebog i geoteknik 2*, 4.

- edition, 7. printing. Polyteknisk Forlag, Lyngby, Danmark.
- Hetenyi M., 1946. *Beams on Elastic Foundation*. Ann Arbor: The University of Michigan Press.
- Karasev O. V., Talanov G. P., and Benda S. F., 1977. Investigation of the work of single situ-cast piles under different load combinations. *Journal of Soil Mechanics and Foundation Engineering*, translated from Russian, **14**(3), pp. 173-177.
- Karthigeyan S., Ramakrishna V. V. G. S. T., and Rajagopal K., May 2006. Influence of vertical load on the lateral response of piles in sand. *Computers and Geotechnics* **33**, pp. 121-131.
- LeBlanc C., Houlsby G. T., and Byrne B. W., 2007. Response of Stiff Piles to Long-term Cyclic Loading.
- Lesny K., and Wiemann J., 2006. Finite-Element-Modelling of Large Diameter Monopiles for Offshore Wind Energy Converters. *Geo Congress 2006, February 26 to March 1*, Atlanta, GA, USA.
- Lesny K., Paikowsky S. G., and Gurbuz A., 2007. Scale effects in lateral load response of large diameter monopiles. *Geo-Denver 2007 February 18 to 21*, Denver, USA.
- Ling L. F., 1988. Back Analysis of Lateral Load Test on Piles. *Rep. No. 460, Civil Engineering Dept., Univ. of Auckland, New Zealand*.
- Matlock H., and Reese L. C., 1960. Generalized Solutions for Laterally Loaded Piles. *Journal of the Soil Mechanics and Foundations Division*, **86**(5), pp. 63-91.
- Matlock H., 1970. Correlations for Design of Laterally Loaded Piles in Soft Clay. *Proceedings, Second Annual Offshore Technology Conference*, Houston, Texas, paper no. OTC 1204, pp. 577-594.
- McClelland B., and Focht J. A. Jr., 1958. Soil Modulus for Laterally Loaded Piles. *Transactions*. ASCE **123**: pp. 1049-1086.
- Murchison J. M., and O'Neill M. W, 1984. Evaluation of p - y relationships in cohesionless soils. *Analysis and Design of Pile Foundations. Proceedings of a Symposium in conjunction with the ASCE National Convention*, pp. 174-191.
- Norris G. M., 1986. Theoretically based BEF laterally loaded pile analysis. *Proceedings, Third Int. Conf. on Numerical Methods in offshore piling*, Editions Technip, Paris, France, pp. 361-386.
- O'Neill M. W., and Dunnavant T. W., 1984. A study of effect of scale, velocity, and cyclic degradability on laterally loaded single piles in overconsolidated clay. *Report UHCE 84-7*, Dept. of Civ. Engrg., University of Houston, Texas, p. 368.
- Pasternak P. L., 1954. On a New Method of Analysis of an Elastic Foundation by Means of Two Foundation Constants, *Gosudarstvennoe Izdatelstvo Liberatunni po Stroitelstvui Arkhitekture*, Moskow, pp. 355-421.
- Peck R. B., Hanson W. E., and Thornburn T. H., 1953. *Foundation Engineering*, John Wiley and Sons, Inc. New York.
- Pender M. J., 1993. Aseismic Pile Foundation Design Analysis. *Bull. NZ Nat. Soc. Earthquake Engineering.*, **26**(1), pp. 49-160.
- Poulos H. G., 1971. Behavior of laterally loaded piles: I - Single piles. *Journal of the Soil Mechanics and Foundations Division*, **97**(5), pp. 711-731.
- Poulos H. G., and Davis E. H., 1980. *Pile foundation analysis and design*, John Wiley & Sons.
- Poulos H., and Hull T., 1989. The Role of Analytical Geomechanics in Foundation

- Engineering. in *Foundation Eng.: Current principles and Practices*, **2**, pp. 1578-1606.
- Reese L. C., and Matlock H., 1956. Non-dimensional Solutions for Laterally Loaded Piles with Soil Modulus Assumed Proportional to Depth. *Proceedings of the eighth Texas conference on soil mechanics and foundation engineering*. Special publication no. 29.
- Reese L. C., Cox W. R., and Koop, F. D., 1974. Analysis of Laterally Loaded Piles in Sand. *Proceedings of the Sixth Annual Offshore Technology Conference*, Houston, Texas, **2**, paper no. OTC 2080.
- Reese L. C., and Welch R. C., 1975. Lateral loading of deep foundation in stiff clay. *Journal of Geotechnic Engineering*, Div., **101**(7), pp. 633-649.
- Reese L. C., and Van Impe W. F., 2001. *Single Piles and Pile Groups Under Lateral Loading*, Taylor & Francis Group plc, London.
- Stevens J. B., and Audibert J. M. E., 1979. Re-examination of p-y curve formulation. *Proceedings Of the XI Annual Offshore Technology Conference*, Houston, Texas, OTC 3402, pp. 397-403.
- Terzaghi K., 1955. Evaluation of coefficients of subgrade reaction. *Geotechnique*, **5**(4), pp. 297-326.
- Timoshenko S. P., 1941. Strength of materials, part II, advanced theory and problems, 2nd edition, 10th printing. New York: D. Van Nostrand.
- United Nations, 1998. Kyoto protocol. *United Nations framework convention on climate change*.
- Vesic A. S., 1961. Beam on Elastic Subgrade and the Winkler's Hypothesis. *Proceedings of the 5th International Conference on Soil Mechanics and Foundation Engineering*, Paris, **1**, pp. 845-850.
- Winkler E., 1867. Die lehre von elasticitat and festigkeit (on elasticity and fixity), Prague, 182 p.
- Zhang L., Silva F., and Grismala R., January 2005. Ultimate Lateral Resistance to Piles in Cohesionless Soils. *Journal of Geotechnical and Geoenvironmental Engineering*, **131**(1), pp. 78-83.

CHAPTER 3

Evaluation of Load-Displacement Relationships for Non-Slender Monopiles in Sand



Evaluation of Load-Displacement Relationships for Non-Slender Monopiles in Sand

S. P. H. Sørensen¹; M. Møller¹; and K. T. Brødbæk¹

Aalborg University, June 2009

Abstract

Monopiles are an often used foundation concept for offshore wind turbine converters. These piles are highly subjected to lateral loads and bending moments due to wind and wave forces. To ensure enough stiffness of the foundation and an acceptable pile-head deflection, monopiles with diameters of 4 to 6 m are typically necessary. In current practice these piles are normally designed by use of the p - y curve method although the method is developed and verified for small-diameter, slender piles with diameters up to approximately 2 m. This paper investigate the behaviour of two non-slender aluminium pipe piles subjected to lateral loads at a given vertical eccentricity. The piles are heavily instrumented with strain gauges in order to obtain p - y curves and bending moment distributions along the piles. In order to minimise scale effects the tests are successfully carried out in a pressure tank at varying stress levels. The tests are evaluated with the following main findings: The lateral pile deflection consists primarily of rotation as a rigid object; normalised load-displacement relationships indicate that the lateral load is proportional to the embedded length squared and the pile diameter; in current design the initial stiffness of the p - y curves is considered independent of the pile diameter. This recommendation is questionable as derived p - y curves indicate a strong dependency on pile diameter with a higher initial stiffness related to the largest pile diameter.

Keywords: Non-slender monopiles, Lateral load, Laboratory tests, Pressure tank, Varying stress levels, p - y curves, Sand.

1 Introduction

In current design of laterally loaded monopiles, used as foundation for offshore wind turbines, the p - y curve method is normally employed. Two of the non-clarified parameters related to the expression for the p - y curves for piles in cohesionless soil is, cf. chapter 2:

- Slenderness ratio L/D
- Initial stiffness of the p - y curves

Monopile foundations for modern offshore wind turbines have $L/D < 10$ and behave almost as rigid objects. In contrast the p - y curves employed in the design regulations, e.g. API (1993) and DNV (1992), are based on testing of two slender flexible piles with $L/D = 34.4$, cf. Cox et al. (1974).

The initial stiffness of the p - y curves is considered independent of the pile properties among these the pile diameter, which seems questionable. The research within the field of diameter effects gives contradictory conclusions, cf. chapter 2.

¹Graduate Student, Dept. of Civil Engineering, Aalborg University, Sohngaardsholmsvej 57, 9000 Aalborg, Denmark.

This paper evaluates the listed effects through tests. Since large-scale tests are expensive and time consuming, small-scale tests are conducted. Small-scale tests are however attached to significant scale effects. When conducting small-scale tests in sand at 1-g an often introduced source of error is the low stress levels causing the soil parameters and in specific the angle of internal friction to vary strongly with effective stresses. Therefore, it is an advantage to increase the effective stresses to a level where the angle of internal friction is independent of a possible stress variation during the tests. Furthermore, an increase in effective stress level minimise fluctuations on the measured signals.

The problem for low stress levels can be overcome by testing piles in a centrifuge or in a pressure tank as described in section 2.

This paper presents the results obtained by testing horizontally loaded piles in sand in a pressure tank, cf. fig. 1, at various stress levels. The conducted tests are quasi-static tests on two instrumented closed-ended aluminium pipe piles with outer diameters of 60 mm and 80 mm, respectively. The outline of the paper is:

- **Pressure tank:** The test setup, including the method for increasing the stress level.
- **Measuring system:** The employed measurement devices and the preparation of the test piles.
- **Soil conditions:** Material properties of the sand and preparation of the soil prior to testing.
- **Results:** Interpretation of strain gauge measurements and a discussion of the obtained results.

2 Pressure tank

The tests have been carried out in the pressure tank shown in fig. 1 at Aalborg University, Denmark. A cross sectional view of the test setup is illustrated in fig. 2. The pressure tank is manufactured by Bergla Maskinfabrik in Brønderslev, Denmark. The diameter and the height of the pressure tank are approximately 2.1 m and 2.5 m, respectively. The pressure tank is installed in a load-frame, cf. fig. 1, resting on a reinforced foundation independent of the floor in the laboratory. On top of the pressure tank a platform, cf. fig. 1, is installed in order to make access to the top and hereby the preparation for the tests more comfortable. The pressure tank has trap doors, which make the preparation prior to the testing possible. Furthermore, the tank contains openings, cf. fig. 3, where the measurement devices are lead out. At the top hatch, cf. fig. 1, a hydraulic piston is mounted in order to install the test piles. The pressure tank contains 0.69 m of fully saturated sand, cf. fig. 2. A high permeable layer of gravel is located underneath the sand. The instrumented piles are actuated by a hydraulic piston, cf. fig. 1, and due to displacement transducers and a force transducer the load-displacement relationships at three levels above soil surface is obtained.

The increase in effective stress level is created by separating the lower part of the tank, containing saturated soil, from the upper part by use of an elastic membrane. In this way the saturated soil is sealed from the air above. By increasing the pressure in the upper part of the tank, a homogenous increase in stresses is introduced at the soil surface by the elastic membrane comparable to a surface load. To ensure limited excessive pore pressure, the soil is connected to an ascension pipe, leaving the soil fully saturated but with stresses applied as effective stresses only.

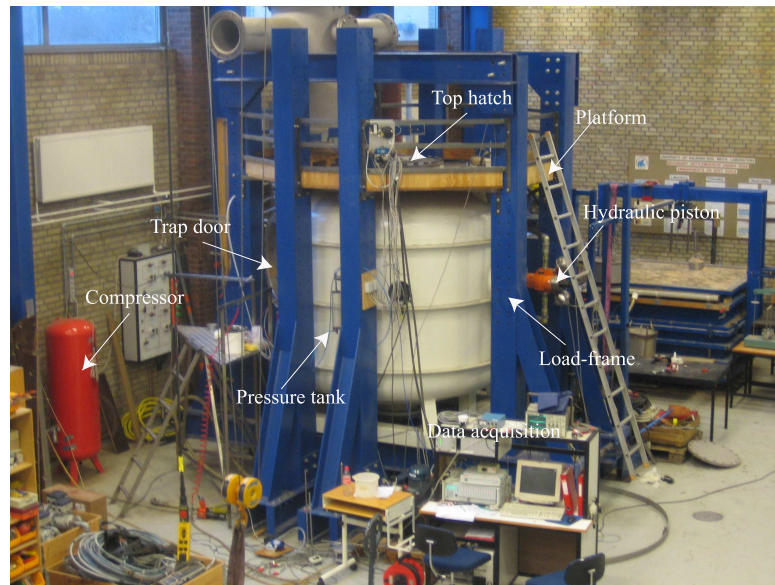


Figure 1: Pressure tank used for small-scale tests.

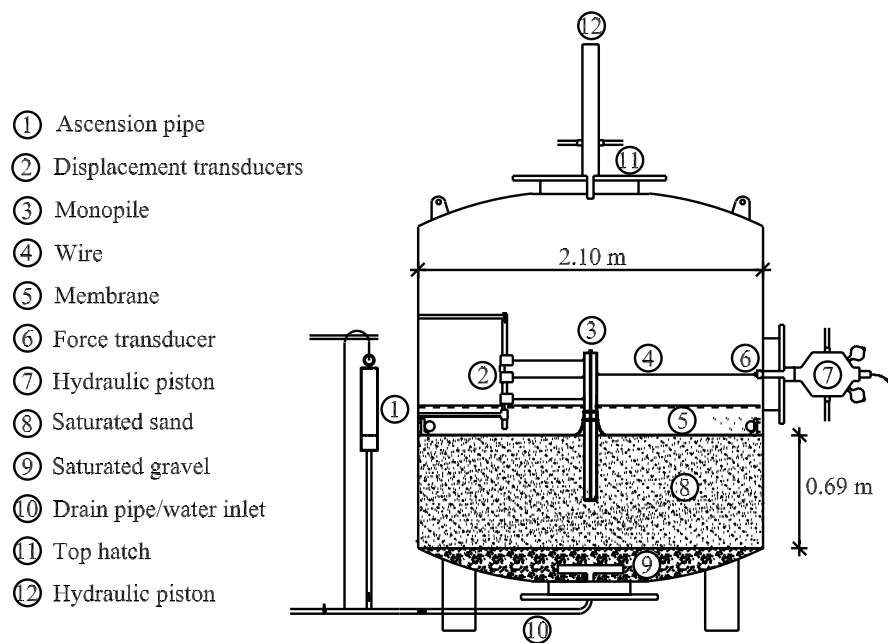


Figure 2: Test setup.

The pile is lead through a sealing in the elastic membrane allowing the pile to be extended above the soil surface. An example of the variation of effective vertical stresses is shown in fig. 4, where P_0 denote the magnitude of the overburden pressure.



Figure 3: Openings for the measurement devices.

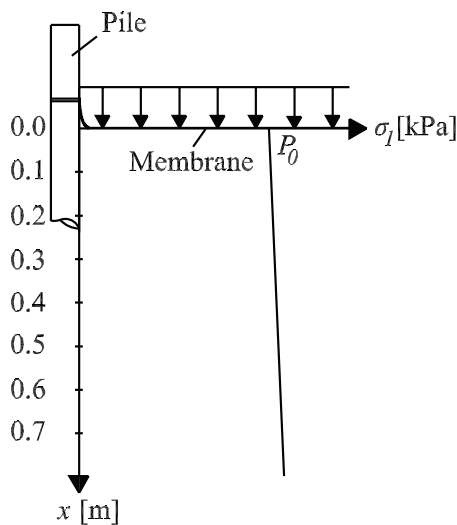


Figure 4: Variation of effective vertical stresses.

In the upper part of the pressure tank, approximately 16 cm of water is poured in, to ensure that the soil is fully saturated if leaks between the membrane and the pressure tank occurs. Further, the dynamic viscosity of water is about 55 times higher than in air², which minimise the flow through any potential gaps.

Due to the test setup, the maximum sand

depth is 0.69 m. In order to minimise effects of the boundaries, piles with diameters of 0.08 m and 0.06 m and embedded lengths of 0.4 m and 0.3 m, respectively, are employed.

Further information about the pressure tank and the elastic membrane is presented in appendix A.

3 Measuring system

A hydraulic piston, cf. ⑦ in fig. 2, actuates the test piles. The hydraulic piston is controlled by a prescribed displacement and acts with a vertical eccentricity in the range of 0.370 – 0.375 m above the soil surface, cf. fig. 5. In order to measure the force acting on the pile a force transducer of the type HBM U2B 10 kN connects in series the hydraulic piston and the wire. Lateral displacements at three levels above the soil surface are measured, cf. fig. 5. In addition the vertical displacement is measured for the pile with an outer diameter of 60 mm. In order to measure the lateral and vertical displacement, displacement transducers of the type WS10-1000-R1K-L10 from ASM GmbH are employed. A total number of 10 strain gauges are mounted on the pile beneath the soil surface. The tank pressure is measured by a HBM P6A 10 bar absolute pressure transducer. The sampling frequency is 10 Hz.

3.1 Test piles

Two instrumented aluminium piles with outer diameters of 80 mm (6082 AW-6082/T6) and 60 mm (6060 AW-6060/T6) respectively, have been tested. Both piles have a wall thickness of 5 mm and are closed-ended in order to protect the strain gauges and their corresponding cords against water. The pile with an

²<http://www.lmnoeng.com/fluids.htm>

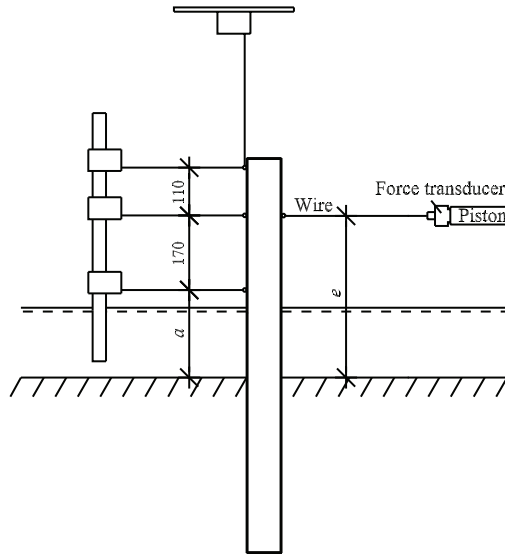


Figure 5: Measuring of lateral displacements at three levels, and measuring of the vertical displacement at the back of the pile. The distance a and the load eccentricity e are as listed in tab. 3.

outer diameter of 80 mm is shown in fig. 6.



Figure 6: Picture of the test pile with an outer diameter of 80 mm. The cords are lead out through the blue cable.

The strain gauges are mounted at five levels as shown in fig. 7. At each level two foil strain gauges are mounted on the pile with a mutual angle of 180° aligned in the plane of the horizontal load as illustrated in fig. 8. The strain gauges are mounted in vertical direction implying that the curvature strains in the axial direction of the pile are measured. Strain gauges of the type HBM K-LY43-3/120 are employed, which are encapsulated strain gauges produced to measure on aluminium alloys.

The strain gauges are installed in milled grooves in the aluminium profile and sealed with a waterproofed filler (HBM SG250). In order to make the surface area around the grooves smooth a two compo-

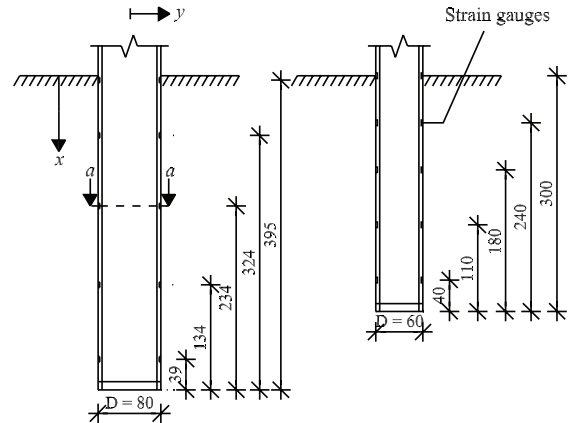


Figure 7: Strain gauge levels. Measures are in mm.

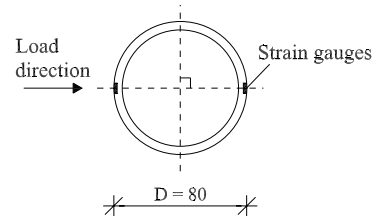


Figure 8: Cross section $a-a$. All measurement levels are identical. Measures are in mm.

nent fast curing adhesive (HBM X60) is employed on the outside of the protective coating. The depth, width, and length of the mill outs are approximately 2, 6, and 10 mm, respectively. The weakening of the profiles as a consequence of this is negligible compared to the bending stiffness of the remaining profile. The gauges are bonded to the piles with a two-part epoxy. The cables from the strain gauges are lead into the pile and through a hermetic packed hole in the pile-head, cf. fig. 6.

3.1.1 Calibration of test piles

In order to ensure a proper relation between the strain gauge output and the moment distribution, a calibration of the piles have been conducted by loading the piles transversely while supported as simply supported beams. In order to eliminate effects of stress concentrations, four load series with varying locations of the

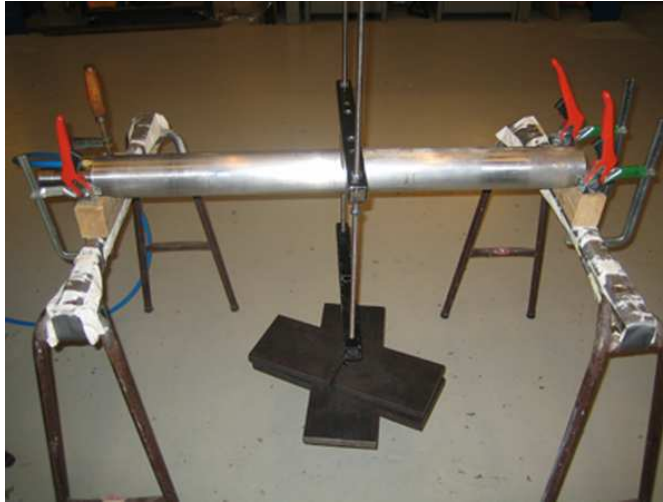


Figure 9: Test setup for calibration of pile bending stiffness, $E_p I_p$, and validation of strain gauges.

point load have been conducted at each pile. At each location load series consisting of seven load steps of 20 kg, from 0 – 120 kg have been applied. The setup is shown in fig. 9. An example of the test results is shown in fig. 10 for the upper strain gauge level. The remaining calibrations are given in appendix H. From Bernoulli–Euler beam theory the following relation between moment and strains is obtained:

$$E_p I_p = \frac{M r^*}{\bar{\varepsilon}} \quad (1)$$

$E_p I_p$ is the stiffness of the pile corresponding to the applied moment, M , and the mean value of the measured strains at a given strain gauge level, $\bar{\varepsilon}$. The slope of a linear regression to the points shown in fig. 10 is in accordance to (1) multiplied with the distance from the cross sectional centre to the gauge, $r^* = D/2 - t^*$, where D is the outer diameter of the pile and t^* is the depth of the mill out. Hereby, the pile bending stiffness, $E_p I_p$, is obtained. Similar interpretations have been made for each of the four other strain gauge levels. By taking the average of the bending stiffness' obtained at each strain gauge level the calibrated bending stiffness' of the piles are determined to $E I_{80,calibrated} = 52.4 \text{ kNm}^2$ and

$E I_{60,calibrated} = 24.9 \text{ kNm}^2$ for the two pile diameters, respectively. The standard deviation are $\sigma_{80} = 0.874$ and $\sigma_{60} = 0.585$. Due to the small strains obtained at the strain gauge level nearest to the pile-toe, large uncertainties are introduced. The results obtained at this level have been omitted in the calculation of $E_p I_p$.

4 Soil conditions

The tests are conducted on fully saturated Baskarp Sand no. 15, with the characteristics given in tab. 1. The distribution of grain size determined from sieve analysis is shown in fig. 11.

Table 1: Material properties for Baskarp Sand no. 15, after Larsen (2008).

Specific grain density d_s	2.64
Maximum void ratio e_{\max}	0.858
Minimum void ratio e_{\min}	0.549
$d_{50} = 50 \%$ - quantile	0.14 mm
$U = d_{60}/d_{10}$	1.78

The Baskarp sand nr. 15 contains uniformly graded small grains which makes a homogeneously compaction possible. The sand is permeable with the hydraulic conductivity $k \approx 6 \cdot 10^{-5} \text{ m/s}$ which allows drained conditions during the tests.

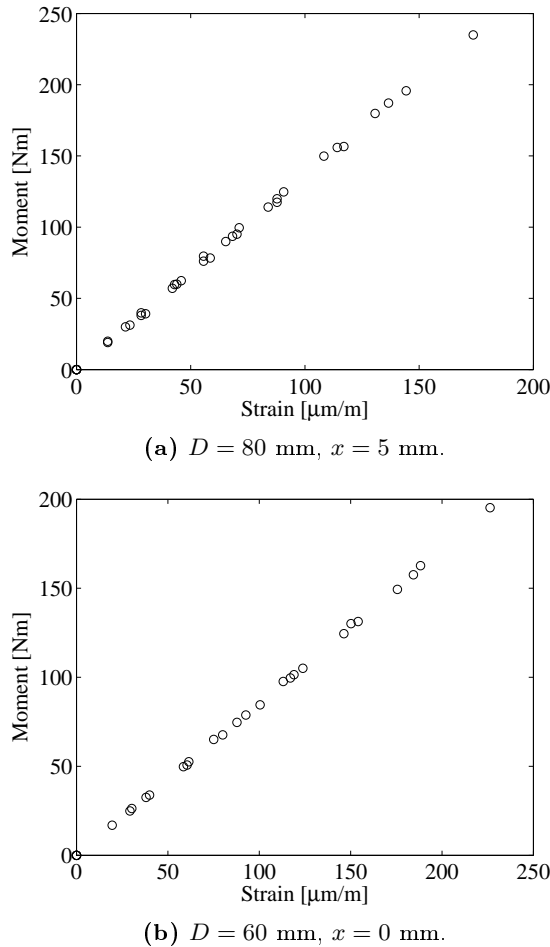


Figure 10: Measured strains versus applied moments at the upper strain gauge level.

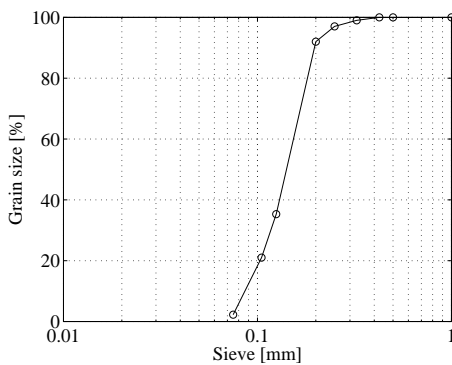


Figure 11: Distribution of grains for Baskarp Sand no. 15, after Larsen (2008).

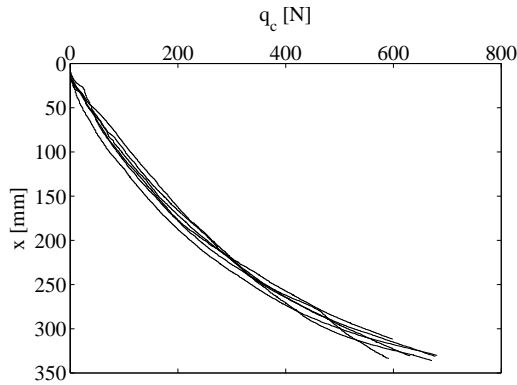
4.1 Preparation of soil

Between each test the soil is prepared by mechanical vibration. This ensures that the sand is fully saturated, and a homogeneous compaction of the material is obtained.

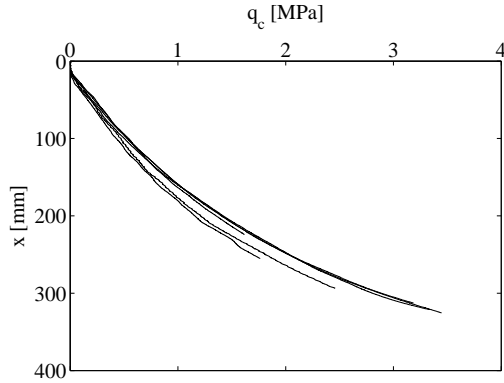
The piles are installed at the centre of the pressure tank, with the strain gauges aligned in the plane of the horizontal load. During installation an upward gradient of a magnitude of 0.9 has been applied in order to minimise the pressure at the closed pile-end and to protect the strain gauges. In this way the toe resistance and the skin friction along the pile are minimised during pile installation. After the installation of the pile the sand is mechanically vibrated minimising the disturbances from the pile installation, i.e. a homogeneous compaction of the sand is ensured. The pile is prevented from deforming from its upright position when vibrating with use of the hydraulic piston mounted on the top hatch, cf. (12) in fig. 2.

The compaction and homogeneity have been controlled by cone penetration tests (CPT). Four CPT's with a distance of 0.5 m from the centre of the pile and two at the neutral sides of the pile, i.e. the sides perpendicular to the load direction, with a distance of 0.16 m have been conducted. The employed CPT probe has a diameter of 15 mm.

A typical profile of the cone tip resistance, q_c , is shown in fig. 12a. The results from all tests are given in appendices I–N. As the profiles of q_c are without particular variation at the described six different locations in the pressure tank, the soil is considered homogeneously compacted. Figure 12b presents the mean values of each series of six CPT's conducted prior to each pile test. As shown the same compaction is reached prior to each test. For more details about the conducted CPT's see appendix B.3.



(a) Series of six CPT's prior to test nr. 2.



(b) Mean values of CPT's conducted prior to each test.

Figure 12: Output from CPT's.**Table 2:** Material properties. P_0 denote the magnitude of the overburden pressure.

	P_0 [kPa]	φ_{tr} [°]	I_D [-]	γ' [kN/m ³]
Test 1	0	52.6	0.79	10.2
Test 2	100	45.9	0.79	10.2
Test 3	50	48.5	0.79	10.2
Test 4	0	52.2	0.76	10.1
Test 5	50	48.3	0.78	10.1
Test 6	100	45.1	0.75	10.1

Soil parameters derived on the basis of the CPT's are presented in tab. 2. The parameters are derived in accordance to Ibsen et al. (2009) where the angle of internal friction is related to the stress level. The derivation of soil parameters are described in appendix B.4. A complete list of the derived soil parameters is presented in appendix C.

5 Results

The test programme, cf. tab. 3, is designed to investigate the soil resistance and its dependency on pile diameter at different stress levels.

During the tests, the soil is brought to failure, unloaded, and reloaded in order to estimate the ultimate soil resistance and the elastic behaviour of the soil. The applied displacements are of varying magnitudes due to different overburden pressures, P_0 , and pile diameters, D . Test results for the six laboratory tests are presented in appendix I–N.

Table 3: Test programme. The vertical distances a and e are illustrated in fig. 5.

	D [mm]	L/D	a [m]	e [m]	P_0 [kPa]
Test 1	80	5	0.200	0.370	0
Test 2	80	5	0.200	0.370	100
Test 3	80	5	0.200	0.370	50
Test 4	60	5	0.205	0.375	0
Test 5	60	5	0.205	0.375	50
Test 6	60	5	0.205	0.375	100

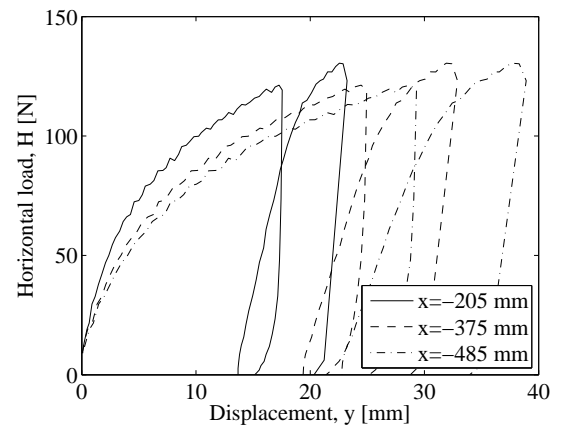
Figure 13a presents the load-displacement relationship for test 4, cf. tab. 3, while the normalised load-displacement relationships for test 4–6 are shown in fig. 13b. The horizontal load, cf. fig. 13b, is normalised as H/H_{max} where H_{max} denotes the ultimate load at each test and the horizontal displacement is normalised with outer pile diameter, y/D . A low-pass filter with a cutoff frequency at 0.1 Hz has been

employed. From fig. 13 it is seen that after the first unloading and reloading the load-displacement curves reaches the original curves. Furthermore, the upper displacement transducer produce the highest displacement and the lower displacement transducer produce the smallest displacement, which is as expected. The plastic behaviour of the soil is dependent on the amount of overburden pressure. After the first unloading the plastic deformation of the soil is determined to approximately 80% of the total deformation without overburden pressure, 60% of the total deformation when applying $P_0 = 50$ kPa, and 55% of the total deformation when applying $P_0 = 100$ kPa. However, it should be emphasised that the applied lateral deflection is larger for the tests without overburden pressure.

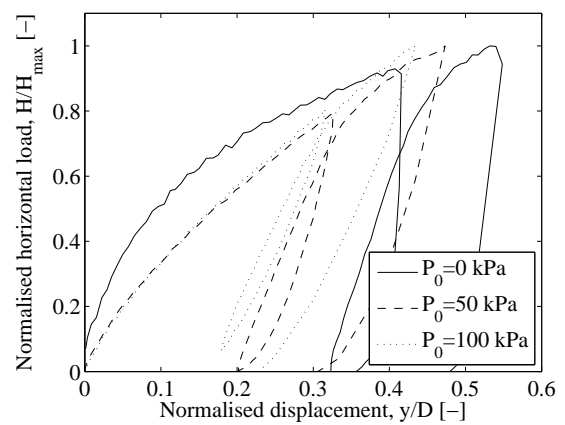
Figure 14 presents the dependency of overburden pressure on the lateral load. The required lateral loads in order to obtain a given pile displacement are, as expected, highly dependent of the magnitude of the overburden pressure. The lateral load at 10 mm deflection at the level of the hydraulic piston increases with a factor of approximately 20 and 13 for $D = 60$ and $D = 80$ mm, respectively at $P_0 = 50$ kPa. The factors increases to approximately 31 and 20 for $P_0 = 100$ kPa. These factors are determined in comparison with the loads without overburden pressure.

After a displacement of 20 mm, cf. fig. 14b, the load-displacement relationship for test 3 ($P_0 = 50$ kPa, $D = 80$ mm) is unrealistic as it recovers strength. This error might be caused by deviations in the pressure, cf. appendix K fig. K.2d, in the pressure tank. Hence, only the initial part of this test curve is valid. The deviations are only observed during test 3.

The vertical displacement versus time until the first unloading is presented in fig. 15 for the pile with an outer diameter of 60 mm without overburden pressure. The



(a) $P_0 = 0$ kPa.



(b) Normalised relationships between load (H/H_{max}) and displacement (y/D) measured at the height of the hydraulic piston.

Figure 13: Load-displacement relationships for the pile with an outer diameter of 60 mm.

vertical displacement are measured at the back of the pile with a wire transducer, cf. fig. 5. Hereby, both the rotation of the pile as a rigid object and the pile deformation contributes to the measured values of the vertical displacements. These contributions are deducted with use of the laws of trigonometry as presented in appendix A.2. From fig. 15 an interpreted maximum vertical displacement of 1.2 mm is observed. This corresponds to 0.4 % of the embedded pile length and the effect of this on the soil-pile interaction is negligible. When applying overburden pressures the upward displacement is of the same magnitude as outlined in fig. 15.

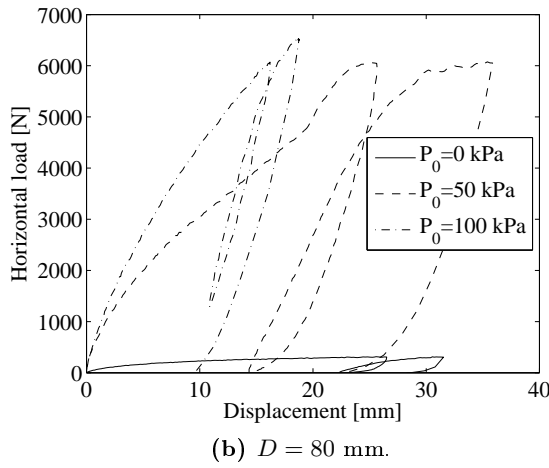
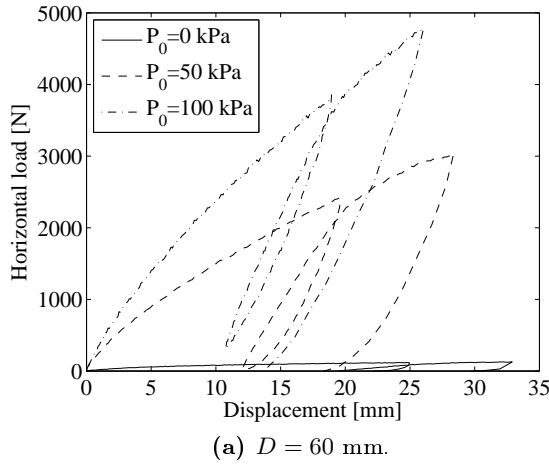


Figure 14: Load-displacement relationships at different overburden pressures measured at the height of the hydraulic piston.

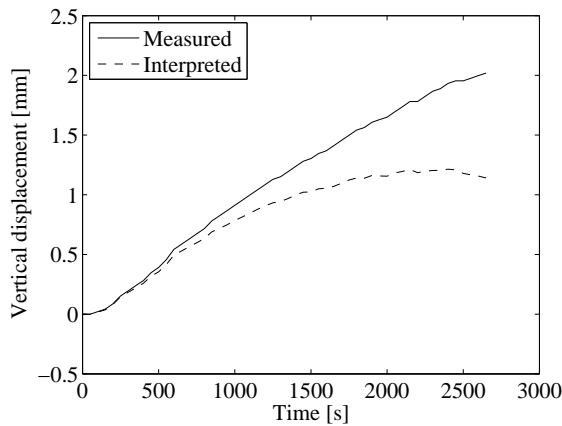


Figure 15: Vertical pile displacement versus time for $D = 60$ mm, and $P_0 = 0$ kPa. A positive vertical displacement indicate that the pile moves upward.

5.1 Interpretation of strain gauge measurements

The strain gauge measurements are interpreted in order to derive p - y curves and the moment distributions along the piles. A mean value, $\bar{\varepsilon}$, of the strains is calculated for each level, and the curvature, κ , and bending moments, M , are calculated by:

$$\kappa = \frac{\bar{\varepsilon}}{r^*} \quad (2)$$

$$M = E_p I_p \kappa \quad (3)$$

When interpreting the strain gauge measurements, zero curvature is assumed at the pile-toe. Hereby, the curvature is known in six levels of the piles. In order to calculate the pile deflection the discrete curvature measurements, κ , are fitted to a 5. order polynomial.

The deflection of the pile, y , and the soil resistance, p , are calculated from (4) and (5), respectively.

$$y(x) = \int \int \frac{M}{E_p I_p} dx dx \quad (4)$$

$$p(x) = \frac{d^2 M}{dx^2} \quad (5)$$

The double integration of moments with respect to depth, cf. (4), does not implement significant errors. However, double differentiation of the discrete moments results in an amplification of measurement errors. In order to minimise these errors the piecewise polynomial curve fitting method described by Yang and Liang (2006) is employed. The boundary conditions, cf. (4), for the pile deflection and rotation at the mudline are calculated based on displacements measured at the level of the hydraulic piston and 110 mm above, cf. fig. 5. For a more detailed description of the strain gauge interpretation see appendix A.4.

Figure 16 presents the bending moment distributions along the piles corresponding

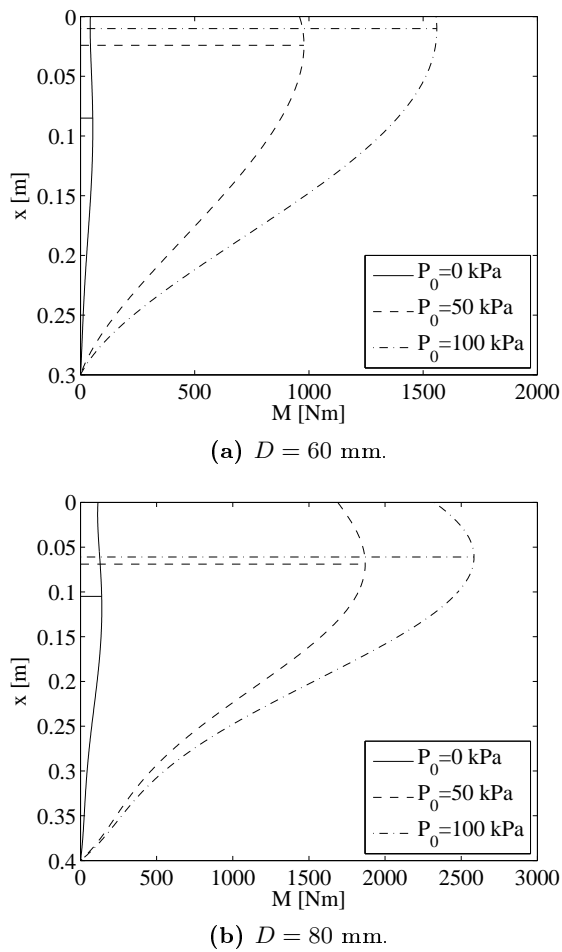


Figure 16: Bending moment distributions at different overburden pressures. The horizontal lines indicate the depth of maximum moment.

to the prescribed horizontal displacements listed in tab. 4. The maximum bending moment occurs at different locations depending on the magnitude of the overburden pressure. Without overburden pressure the depth of maximum bending moment is located at around $1/4$ of the embedded pile length determined from the soil surface. The maximum moment is situated between $1/8$ of the embedment length and the soil surface when applying overburden pressures. Therefore, it is concluded that the relative increase in soil resistance with overburden pressure is most significant at the soil surface.

Figure 17 presents the pile lateral displacements with depth at the three overburden

pressures for the two pile diameters. A prescribed displacement at the hydraulic piston of 10 mm has been applied. The lateral displacement can be separated into two components:

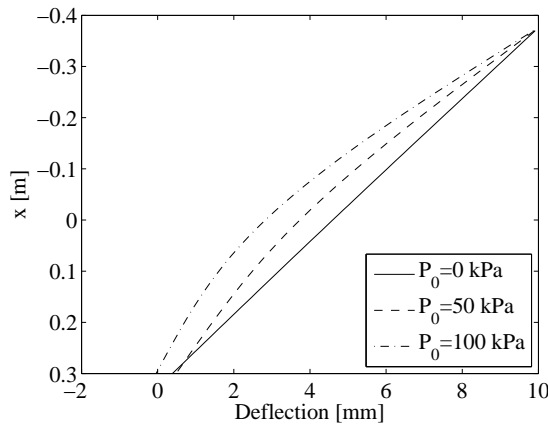
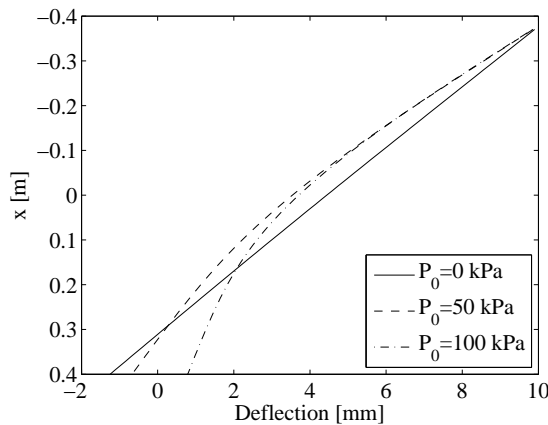
- Deformation of the pile due to bending moments.
- Rotation of the pile as a rigid body.

The pile deformation due to bending is determined in accordance to (4). The pile rotation above the hydraulic piston is obtained by the top two displacement transducers, cf. fig. 5. As shown in fig. 17, the pile exhibit an almost rigid body motion in the tests without overburden pressure. When applying overburden pressure the pile deformation caused by bending is more significant, but still with a pile deflection primarily depending on the rotation. Poulos and Hull (1989) proposed a criterion, cf. chapter 2, for the soil-pile interaction in which a high Young's modulus of elasticity for the soil in comparison with the stiffness of the pile material, leads to a flexible pile behaviour. When applying overburden pressure the effective stress level increases leading to an increase in Young's modulus of elasticity of the soil. Hereby, the more flexible pile behaviour for the tests with overburden pressure is as expected. Due to the rigid pile behaviour the deflection at the pile-toe must be negative which is not the case for most of the tests. This might be due to the relatively small vertical distance between the displacement transducers, cf. fig. 5, which leads to large uncertainties when determining the pile rotation.

Figure 18 presents normalised relationships between load, $H/L^2 D \gamma'$, and displacement, y/D , determined at the height of the hydraulic piston for the three stress levels. When overburden pressure is applied the initial part of the curves are very similar. This indicate that the lateral load is proportional to the embedded

Table 4: Applied displacements at the level of the hydraulic piston, and equivalent loads.

	D [mm]	P_0 [kPa]	Displacement [mm]	Load [N]
Test 1	80	0	30.7	311
Test 2	80	100	16.2	6071
Test 3	80	50	17.6	4457
Test 4	60	0	25.0	115
Test 5	60	50	19.6	2421
Test 6	60	100	18.9	3856

(a) $D = 60$ mm.(b) $D = 80$ mm.**Figure 17:** Lateral pile deflection at different overburden pressures.

length squared and the pile diameter. Figure 18a indicate that the lateral load might be proportional to the pile diameter with a factor larger than one. It should be emphasised that the slenderness ratio is constant during the tests implying that the lateral load might as well be proportional to the embedded length and the pile diameter squared.

5.2 Comparison of test results with a traditional Winkler model approach

A traditional Winkler model, cf. appendix D, has been constructed in order to compare the test results to the recommendations in the design regulations, e.g. API (1993) and DNV (1992). The Winkler model is made in *MATLAB* with use of the finite element toolbox *CALFEM*.

Figure 19 presents the load-displacement relationships for the tests without overburden pressure. Further, the relationships determined by means of the Winkler model are outlined in the figure. As expected the load increases with increasing pile diameter. The ultimate horizontal load given as the asymptotic horizontal value is overestimated, most significantly for $D = 80$ mm, when employing the recommendations in API (1993). However, for the initial part of the curves a good agreement between the Winkler model and the test results is observed until reaching a displacement of approximately 3 mm.

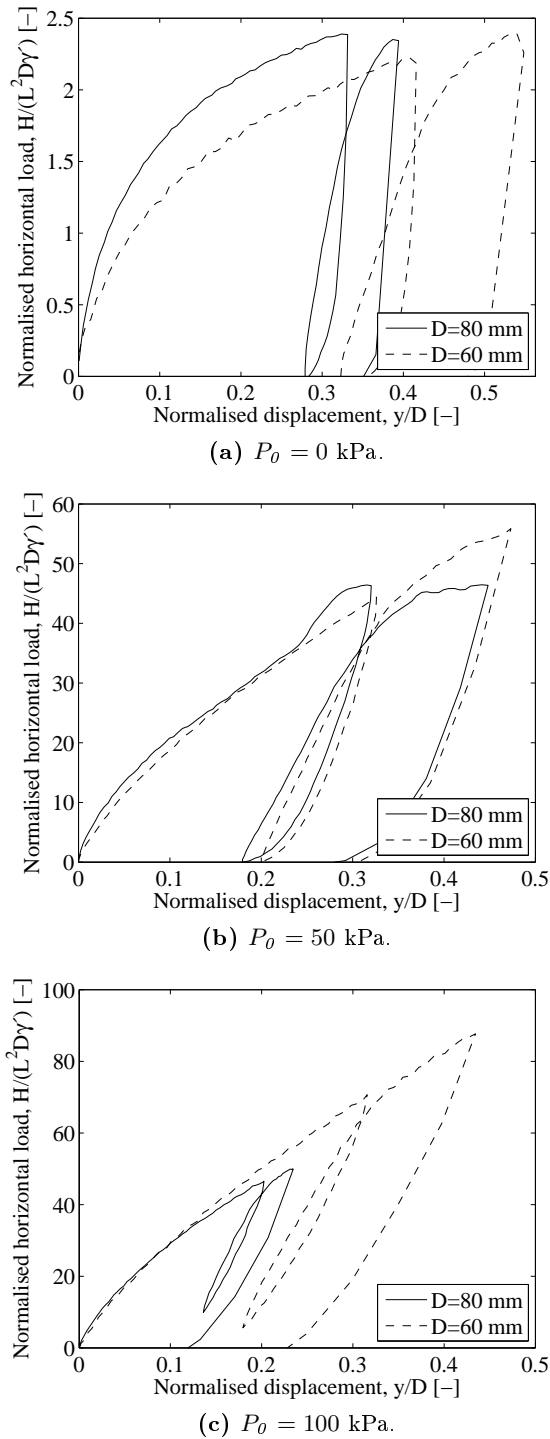


Figure 18: Normalised relationships between load ($H/L^2 D \gamma'$) and displacement (y/D) determined at the height of the hydraulic piston.

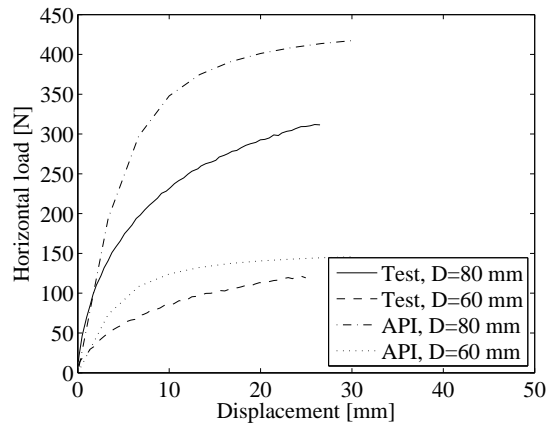


Figure 19: Comparison of measured load-displacement relationships at the height of the hydraulic piston with results obtained by means of a Winkler model approach. $P_0 = 0$ kPa. The initial modulus of subgrade reaction, k , is set to 40.000 kN/m^3 while the angles of internal friction are as listed in tab. 2.

In order to evaluate the ultimate soil resistance presented in API (1993), load-displacement relationships are calculated using an upper bound solution for the ultimate soil resistance, cf. Jacobsen and Gwizdala (1992), and the formulation proposed by Hansen (1961). The distinction between the three methods is the spreading of the wedge forming in front of the pile. Load-displacement relationships for the three methods incorporated in the Winkler model, and the test results are presented in fig. 20 for the pile with an outer diameter of 80 mm and $P_0 = 0$ kPa. From the figure it is observed that the upper bound solution overestimates the ultimate resistance and that the formulation by Hansen (1961) underestimates the ultimate resistance. The best agreement to the current study is the method proposed in the design regulations. Similar results have been observed for the pile with an outer diameter of 60 mm. This is in contradiction to chapter 2 where an investigation performed by Fan and Long (2005) is presented. This investigation indicates that Hansen's method is the best for estimating the ultimate soil resistance. However, the investigation by Fan and Long

(2005) considered only slender piles with diameters between 0.3-1.2 m modelled in a finite element program. Furthermore, the investigation considered the ultimate soil resistance of the p - y curves until a depth of 2.5 m while the analysis above considers the load-displacement relationship at the pile-head. On basis of the laboratory tests it is concluded that the determination of ultimate soil resistance in accordance to API (1993) is workable but non-conservative.

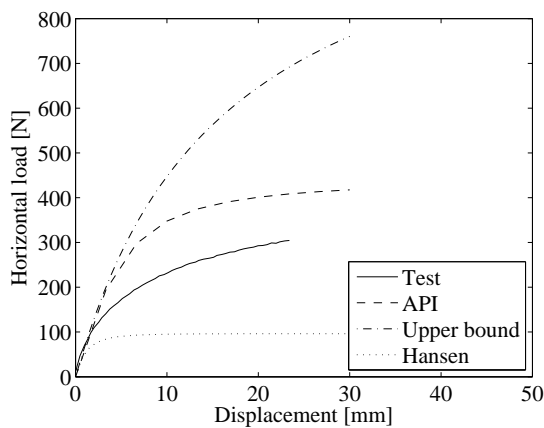


Figure 20: Load-displacement relationships determined at the height of the hydraulic piston versus three criteria, cf. API (1993), upper-bound, and Hansen (1961). $P_0 = 0$ kPa, $D = 80$ mm. The initial modulus of subgrade reaction, k , is set to 40.000 kN/m³ while the angle of internal friction is as listed in tab. 2.

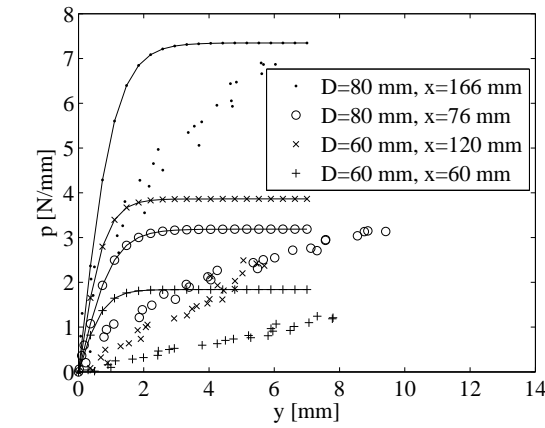
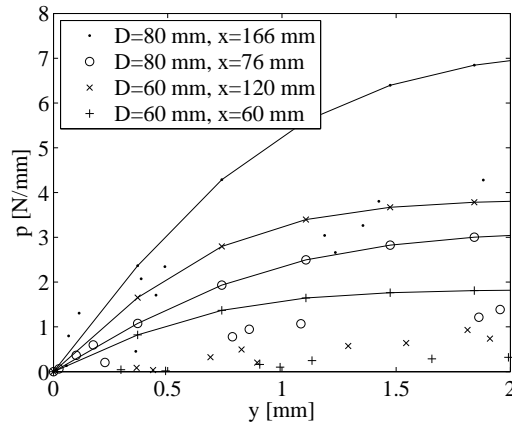
Figure 21 presents the derived p - y curves based on the tests and the p - y curves obtained by means of API (1993) at two strain gauge levels for each pile. The selected levels are located near the depth of the maximum moment and with strain gauge devices above and below. Hereby, the soil resistance is determined with good reliability for the chosen levels. In order to take the effect of overburden pressure, P_0 , into account the approach described by Georgiadis (1983) is employed. In accordance to this an equivalent system with a fictive depth, x' , is employed to describe the effect of the overburden pressure, cf. appendix D.3. The fictive depth varies between 0.41–0.71 m for the tests with over-

burden pressure. As shown in fig. 21c this method provides smaller variations of soil resistance than obtained by the tests. This is caused by the fact that x' is high compared to the distance between the single strain gauge levels. It should be emphasised that the employed method proposed by Georgiadis (1983) is for physically soil layers where friction between layers are taken into account. This is not the case when the overburden pressure is separated from the soil by the elastic membrane. Without overburden pressure the results obtained from the Winkler model approach, cf. fig. 21a, is closer to the test results, though with significant deviations.

Figure 22 presents normalised relationships between soil resistance, $p/D\sigma'$, and deflection, y/D , at two depths. The observations leads to the conclusion that the initial stiffness of the p - y curve is highly dependent on the pile diameter; the larger pile diameter the higher initial stiffness. In the case without overburden pressure the initial stiffness for the pile with an outer diameter of 80 mm is in the range of 3–4 times higher than the stiffness for the pile with an outer diameter of 60 mm. However, it should be emphasised that the p - y curves are obtained in different depths and at different embedded pile lengths. According to API (1993) the initial stiffness is independent on the pile diameter, cf. chapter 2. This seems questionable based on this analyses. In the normalised figures the initial slope decreases when overburden pressures is applied. The factor is in the range of 7–30% of the slope without overburden pressures. However, it should be emphasised that the vertical stress distribution, cf. fig. 4, is abnormal for the tests with overburden pressures.

6 Conclusion

The paper presents the results of six quasi-static tests on laterally loaded monopiles.


 (a) $P_0 = 0$ kPa.


(b) Initial part of fig. 21a.

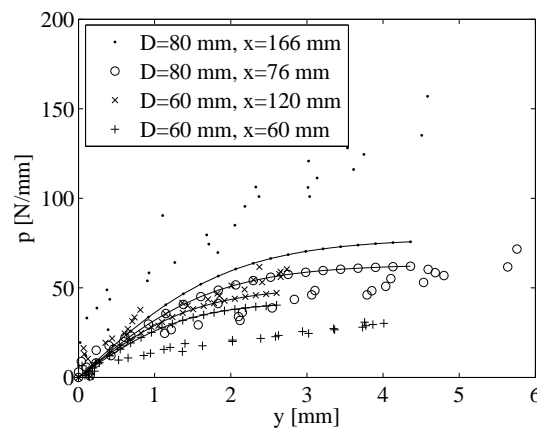

 (c) $P_0 = 100$ kPa.

Figure 21: Derived p - y curves compared to the p - y curves recommended in API (1993). The solid lines denotes the p - y curves determined by the recommendations in API (1993). The initial modulus of subgrade reaction, k , is set to 40.000 kN/m^3 while the angles of internal friction are as listed in tab. 2

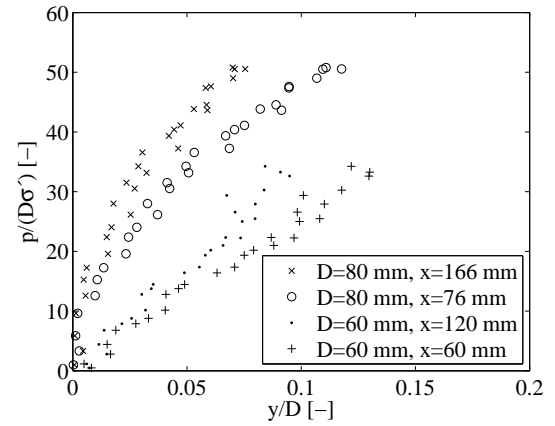
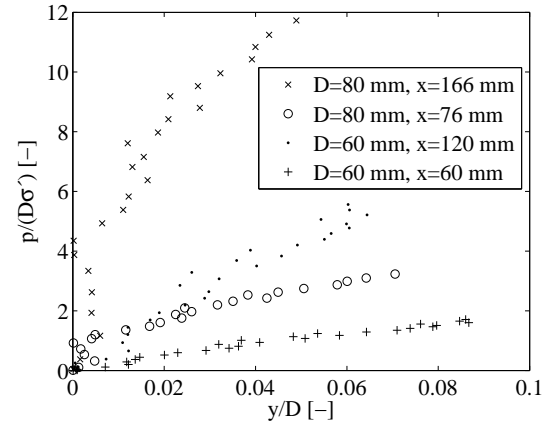
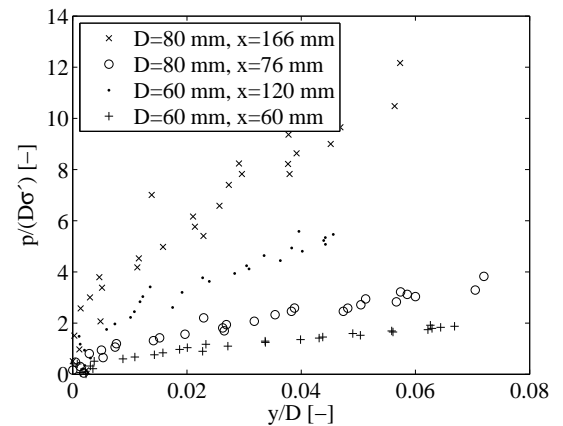

 (a) $P_0 = 0$ kPa.

 (b) $P_0 = 50$ kPa.

 (c) $P_0 = 100$ kPa.

Figure 22: Normalised relationships between soil resistance ($p/D\sigma'$) and deflection (y/D) at different overburden pressures. σ' denote the effective vertical stress.

The tests are carried out in a pressure tank at varying effective stress levels from 0–100 kPa. When increasing the effective stresses in the soil, problems with a non-linear yield surface, as for small stress levels, are overcome. The tests are conducted on two aluminium pipe piles with outer diameters of 80 mm and 60 mm. Both prototypes have a slenderness ratio, L/D , on 5. The piles are instrumented with a total of 10 strain gauges located at five levels along each pile.

The increase in effective stress level have been created by separating the lower part of the tank, containing saturated sand and pile, from the upper part by use of an elastic membrane. The test setup are working without any complications and the obtained results seems very reliable.

Based on the results obtained from the laboratory tests some conclusions may be drawn:

- The deflection of the piles consists primarily of a rigid body motion, i.e. the piles merely rotates around one point of zero deflection. This behaviour deviates from the behaviour of the slender piles tested at Mustang Island, which are the basis of the p - y relations employed in the design regulations, e.g. API (1993) and DNV (1992).
- When applying overburden pressures the soil resistance increases and as a consequence to this the piles exhibits a more flexible pile behaviour. Furthermore, the depth of the maximum moment moves closer to the soil surface when overburden pressure is applied.
- The tests indicate that the horizontal load acting at the pile-head is proportional to the embedded length squared and the pile diameter.
- The ultimate soil resistance determined by API (1993) provides a reasonable fit with the test results. The upper bound solution, cf. Jacobsen and Gwizdala (1992), and the method proposed by Hansen (1961) is not supported by the current study.
- The initial stiffness of the p - y curve is highly dependent on the pile diameter; the larger pile diameter the larger initial stiffness. This observation conflicts with the recommendations in the design regulations.

References

API, 1993. Recommended practice for planning, designing, and constructing fixed offshore platforms - Working stress design, *API RP2A-WSD*, American Petroleum Institute, Washington, D.C., 21. edition.

Cox W. R., Reese L. C., and Grubbs B. R., 1974. Field Testing of Laterally Loaded Piles in Sand. *Proceedings of the Sixth Annual Offshore Technology Conference*, Houston, Texas, paper no. OTC 2079.

DNV, 1992. Foundations - Classification Notes No 30.4, Det Norske Veritas, Det Norske Veritas Classification A/S.

Georgiadis M., 1983. Development of p - y curves for layered soils. *Proceedings of the Geotechnical Practice in Offshore Engineering*, ASCE, pp. 536-545.

Hansen B. J., 1961. *The ultimate resistance of rigid piles against transversal forces*. Danish Geotechnical Institute, Bull. No. 12, Copenhagen, Denmark, 5-9.

Ibsen L. B., Hanson M., Hjort T. H., and Thaarup M., 2009. MC-Parameter Calibration for Baskarp Sand No. 15. *DCE Technical Report No. 62*, Department of Civil Engineering, Aalborg University, Denmark.

Jacobsen M., and Gwizdala K., 1992. *Bearing Capacity and Settlements of Piles*. Centertrykkeriet, Aalborg University, Denmark.

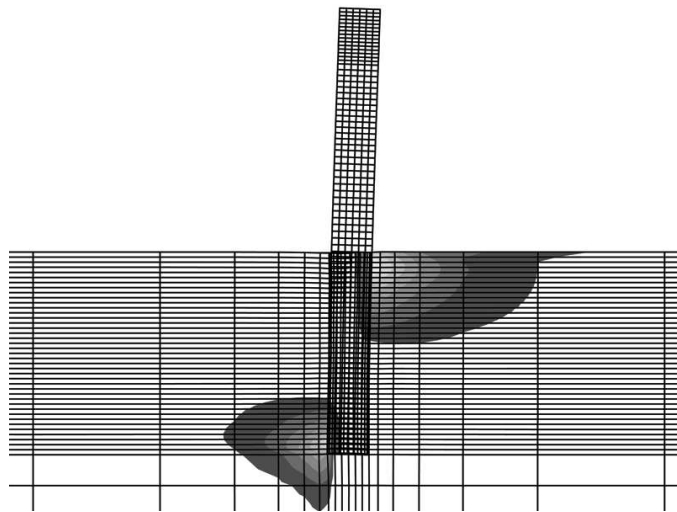
Larsen K. A., 2008. Static Behaviour of Bucket Foundations. *DCE Thesis no. 7*, Department of Civil Engineering, Aalborg University, Denmark.

Poulos H., and Hull T., 1989. The Role of Analytical Geomechanics in Foundation Engineering. *in Foundation Eng.: Current principles and Practices*, **2**, pp. 1578-1606.

Yang K., Liang R., 2006. Methods for Deriving p - y Curves from Instrumented Lateral Load Tests. *Geotechnical Testing Journal*, **30**(1), paper ID GTJ100317, pp. 31-38.

CHAPTER 4

Numerical Evaluation of Load-Displacement Relationships for Non-Slender Monopiles in Sand



Numerical Evaluation of Load-Displacement Relationships for Non-Slender Monopiles in Sand

M. Møller¹; K. T. Brødbæk¹; and S. P. H. Sørensen¹

Aalborg University, June 2009

Abstract

Monopiles are an often used foundation concept for offshore wind turbine converters. These piles are highly subjected to lateral loads and thereby bending moments due to wind and wave forces. To ensure enough stiffness of the foundation and an acceptable pile-head deflection, monopiles with diameters of 4 to 6 m are typically necessary. In current practice these piles are normally designed by use of the p - y curve method although the method is developed and verified for slender piles with diameters up to approximately 2 m. This paper treats numerical models constructed in the commercial programs *FLAC^{3D}* and *Plaxis 3D Foundation* with the objective to examine horizontally loaded, large-diameter piles in cohesionless soil. First, the models are calibrated to six small-scale tests conducted in a pressure tank. Hereafter, the models are extended to large-scale simulations. The large-scale simulations are evaluated with the following main findings: Non-slender piles behave almost rigidly when subjected to lateral loads implying a significant deflection at the pile-toe; the initial stiffness of the p - y curves is found to increase for an increase in diameter; the initial stiffness of the p - y curves is independent of the embedded length of the pile and the pile bending stiffness; the initial stiffness of the p - y curves does not vary linearly with depth as suggested in the offshore design regulations; the Winkler model approach is found to provide reasonable results for large-diameter, non-slender piles if the initial stiffness is updated to vary by means of a power function.

Keywords: Monopile, Lateral load, p - y curves, Modulus of subgrade reaction, Winkler model approach, Sand, *FLAC^{3D}*, *Plaxis 3D Foundation*.

1 Introduction

In current design of laterally loaded monopiles, used as foundation for offshore wind turbines, the p - y curve method is normally employed. Two of the non-clarified parameters related to the expression for the p - y curves for piles in cohesionless soil is, cf. chapter 2:

- Slenderness ratio L/D
- Initial stiffness of the p - y curves

Monopile foundations for modern offshore wind turbines have $L/D < 10$ and behave as almost rigid objects when subjected to lateral loads. In contrast the p - y curves employed in the design regulations, e.g. API (1993) and DNV (1992), are based on testing of two slender flexible piles with $L/D = 34.4$, cf. Cox et al. (1974).

The initial stiffness of the p - y curves is considered independent of the pile properties among these the pile diameter, which

¹Graduate Student, Dept. of Civil Engineering, Aalborg University, Sohngaardsholmsvej 57, 9000 Aalborg, Denmark.

seems questionable. The research within the field of effects of pile diameter on the initial stiffness gives contradictory conclusions as described in chapter 2.

As large-scale tests are expensive and time consuming a proper numerical model calibrated to small-scale tests is an important tool in the assessment of the p - y curve method. This paper describes numerical models constructed in the commercial programs *FLAC^{3D}* and *Plaxis 3D Foundation* with the objective to examine horizontally loaded, large-diameter piles in cohesionless soil. For offshore wind turbine foundations only small deformations are allowed. On this basis, the focus of the analysis is the initial stiffness of the p - y curves. The outline of the paper is as follows:

- **Laboratory test setup:** The test setup forming the basis for the calibration of the numerical models is presented. The tests are carried out in a pressure tank in order to minimise the scale effects attached to small-scale tests at 1-g.
- **Construction of 3D models:** The model conducted in *FLAC^{3D}* is first calibrated to the small-scale laboratory tests and hereafter extended to large-scale. In order to validate the results provided by *FLAC^{3D}* a comparable model is created in *Plaxis 3D Foundation*.
- **Calibration of numerical models:** The *FLAC^{3D}* model is successfully calibrated to the results obtained in the laboratory tests. From this calibration the interface properties are determined. The *Plaxis 3D Foundation* does not fit the test results satisfactory. The tendencies from varying the diameter however, are similar for the two numerical models.
- **Simulation of large-scale monopiles:** The calibrated numerical models are extended to simulate

large-scale offshore monopiles with diameters of $D = [2,3,5,7]$ m.

- **Comparison of *FLAC^{3D}* with a Winkler model approach:** The Winkler model approach incorporating the API p - y curves is evaluated against the soil-pile interaction obtained by means of *FLAC^{3D}*.

2 Laboratory test setup

Six quasi-static laboratory tests have been conducted on two instrumented closed-ended aluminium pipe piles with outer diameters, D , of 60 mm and 80 mm, respectively. The wall thickness is 5 mm. Both piles have a slenderness ratio $L/D = 5$ corresponding to an embedded length, L , of 0.3 and 0.4 m, respectively. The piles are subjected to a horizontal load applied 0.370 m above the soil surface. The piles are instrumented with strain gauges in five levels beneath the soil surface, cf fig. 1. Furthermore, displacement transducers are attached to the pile at 200 mm, 370 mm, and 480 mm above the soil surface.

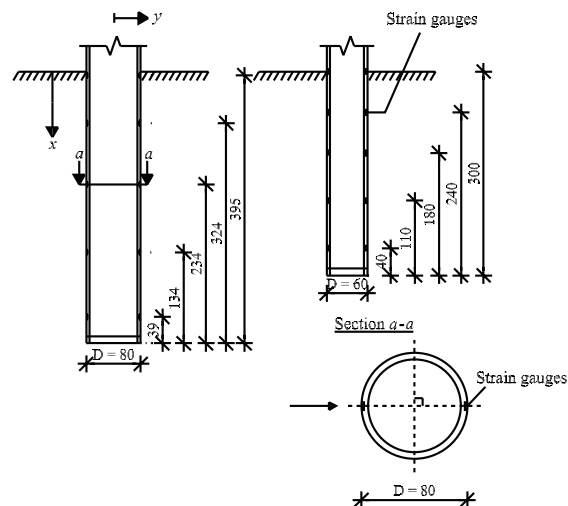


Figure 1: Strain gauge levels. Measures are in mm.

In order to overcome sources of error such as small non-measurable stresses, a non-linear failure criterion, and excessive an-

gles of internal friction, the piles are installed and tested in a pressure tank containing 0.69 m of fully saturated sand. The stress dependent angle of internal friction and Young's modulus of elasticity are determined from cone penetration tests, in accordance to Ibsen et al. (2009). A picture of the pressure tank is shown in fig. 2.

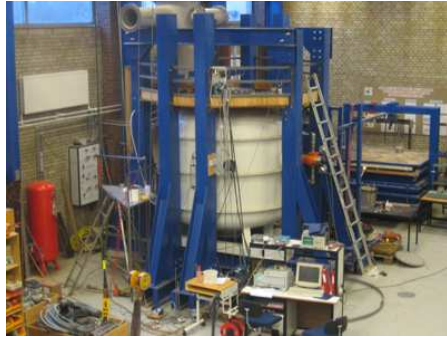


Figure 2: Pressure tank.

In the pressure tank an elastic membrane is placed on the soil surface, leaving the soil sealed from the top part of the tank. The pile is lead through a sealing in the elastic membrane allowing the pile to be extended above the soil surface. When increasing the air pressure in the upper part of the tank, the elastic membrane is pressed against the soil, by which the stresses in the soil are increased. The lower part of the tank, containing the saturated soil, is connected to an ascension pipe, leaving all the applied loads to pressure between the grains, i.e. an increase in effective stresses. The details of the laboratory tests are described in chapter 3. The material properties of the soil and the piles for the six tests are listed in appendix C.

3 Construction of 3D models

The numerical models are at first constructed to match the laboratory tests in scale 1:1 in order to calibrate the interface properties and validate the models. After

a calibration to the laboratory tests the models are extended to large-scale offshore wind turbine foundations, at which the effect of pile diameter on initial stiffness is analysed.

3.1 *FLAC*^{3D}

A three-dimensional numerical model is constructed in *FLAC*^{3D}, which is a commercial program based on a dynamic explicit finite difference solver. The theory behind *FLAC*^{3D} is described in appendix E. To simplify the model, symmetry of the test setup is utilised, so only one half of the pile and surrounding soil are modelled. Furthermore, the pile is modelled as a solid cylinder, in contrast to the closed-ended pipe piles employed in the laboratory tests. The geometry and the orientation of the coordinate system is shown in fig. 3. A finer mesh discretisation is employed in the soil near the pile, as large variations in strains and stresses occurs in this area.

The bending stiffness of the solid pile in the numerical model is given as an equivalent to the stiffness of the hollow test pile, resulting in a reduced Young's modulus of elasticity given as:

$$E_{solid} = \frac{E_{hollow} I_{hollow}}{I_{solid}} \quad (1)$$

The subscripts *hollow* and *solid* denote the parameters derived for the pipe piles, in this case the laboratory test piles and large-scale piles, and the parameters employed in the *FLAC*^{3D} model, respectively. The weight of the hollow and the solid piles are in the same way equivalent. Poisson's ratio of the pile material is not scaled, leading to an incorrect scaling of the shear modulus and bulk modulus. The effect of not scaling these parameters correctly is however considered negligible as the pile primarily is subjected to bending moments.

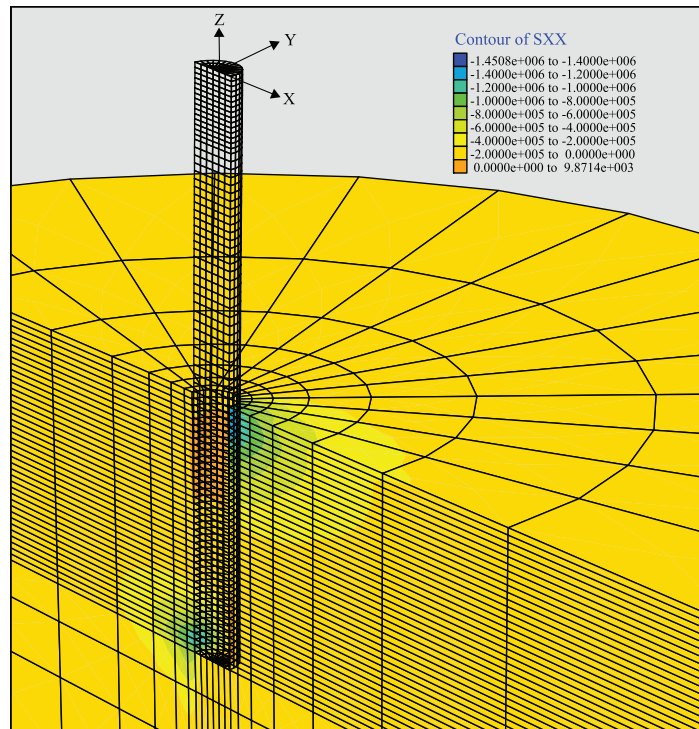


Figure 3: Three-dimensional mesh for the $FLAC^{3D}$ model and effective horizontal stresses in Pa, $SXX = \sigma'_{xx}$, (in the plane of symmetry) for a horizontal load at 5300 N, $D = 0.08$ m, $L = 0.4$ m, and an overburden pressure of $P_0 = 100$ kPa.

The grid is generated from simple zone elements. Each of these zones consist of five first order, constant rate of strain, tetrahedral subelements. The soil-pile interface is modelled by the standard $FLAC^{3D}$ interface consisting of triangular elements. By default two triangular interface elements are created for each zone face. The interfaces are one-sided and attached to the soil. For the constitutive relations of the interfaces a linear Coulomb shear-strength criterion is employed. See appendix E for further information on the $FLAC^{3D}$ element theory.

At the outer perimeter of the soil, the element nodes are restrained in the x and y directions. At the bottom surface the nodes are restrained in all directions while the surface at the symmetric line is restrained in the y direction. The outer boundaries are adjusted to each pile diameter and pile length as given in section 3.3.

The horizontal load is applied as horizontal node velocities acting with a given vertical eccentricity. The horizontal velocities are applied at the nodes corresponding to $x = 0$ at the pile-head acting in the positive x -direction. Hereby, no artificial bending moment is introduced at the pile-head. It should be emphasised that for $D = 2$ m the simulation did not reach equilibrium for the displacement controlled model. This might be due to the ratio between load eccentricity and pile diameter causing dynamic effects to influence the calculation. Instead the horizontal load was applied as nodal forces acting at the pile-head for $D = 2$ m. It has been validated that the two methods for applying the horizontal load produce similar results with only small deviations, cf. fig. 4.

Disagreement between the applied load and the bending moment of the pile at the soil surface has been observed when modelling the pile with only few elements

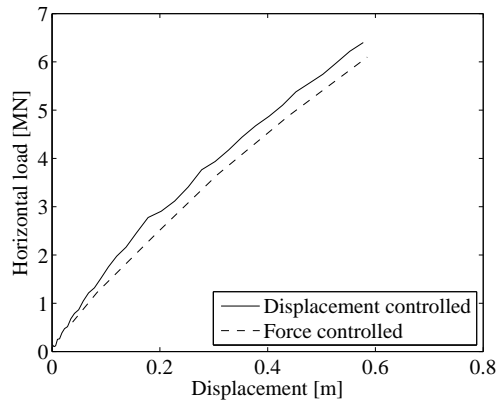


Figure 4: Load-displacement relationships for $D = 3$ m, and $L = 20$ m obtained from the displacement controlled and load controlled models, respectively.

in the vertical direction. A relatively fine discretisation is therefore employed for the pile to ensure convergence of the stresses. An example of the agreement between the applied load and the computed bending moment in the pile at the soil surface is shown in fig. 5.

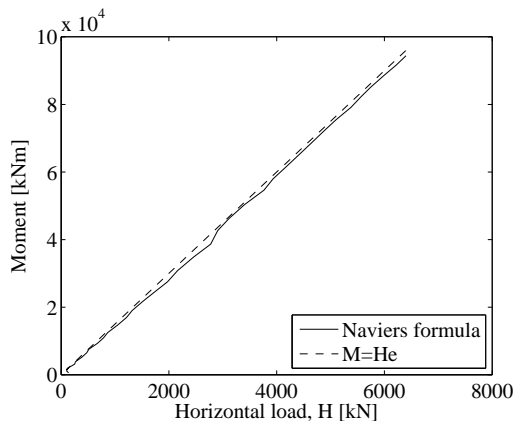


Figure 5: Comparison of the horizontal load, H , multiplied with the load eccentricity, e , with the bending moment at the soil surface calculated as presented in section 3.6 for $D = 3$ m, and $L = 20$ m. The pile has in the vertical direction been divided into 40 elements beneath the soil surface and 50 elements above the soil surface.

When creating the model, the soil elements are generated at first. Secondly, the interfaces are generated and attached to the soil elements. Thirdly, the pile is generated. The pile is generated above the soil surface and afterwards moved into the

soil. Hereby, it is possible to group the pile elements and to specify pile nodes for the computation of bending moment.

The calculations are executed in steps. Firstly, the initial stresses are generated using a K_0 -procedure. Secondly, an equilibrium state is calculated where the pile as well as the soil are assigned the properties of the soil. Furthermore, the pile is assumed smooth at this stage, all in order to prevent stress concentrations near the pile. After the first equilibrium state the correct pile and interface properties are assigned and the model is brought to a second equilibrium state. Additionally, overburden pressure is for the small-scale tests applied as an initial load before the second equilibrium state. After reaching the second equilibrium state, velocities are applied to the pile-head in small increments in order to minimise inertial forces in the system. Further, the combined damping model, cf. appendix E.4, is employed to the system.

3.2 *Plaxis 3D Foundation*

A three-dimensional model is constructed by means of the commercial program *Plaxis 3D Foundation*, which is based on the finite element method and developed to solve geotechnical problems. In contrast to *FLAC^{3D}* a full model is constructed as *Plaxis 3D Foundation* does not facilitate the symmetrical conditions to be utilised. The pile is modelled as a hollow pile with use of wall elements. Wall elements are predefined eighth-noded quadrilateral plate elements. The wall elements can deform by shearing, bending, and axial deformation. In order to apply the lateral load equally to the pile-head nodes a rigid top plate is employed. The lateral load is applied as a point load in the centre node of the top plate. In order to compare the results from the two numerical models a plate is applied at the bottom of the pile. Both the top plate and the bottom

plate is made of floor elements, which is a predefined plate element with six nodes. Similar to the wall element type, floor elements can deform by shearing, bending, and axial deformation. However, no interfaces are attached to the floor element type. Hereby, the footing of the pile and the soil are rigidly connected.

The soil is divided into clusters in order to employ a finer mesh in the area close to the pile. An example of the discretisation of a model is shown in fig. 6. Notice that the coordinate system differs from the coordinate system employed in *FLAC^{3D}*, cf. fig. 3. The soil is divided into 15-noded wedge elements. All the elements provide a second-order interpolation of the displacements and correspondingly a first-order interpolation of stresses and strains.

Interface elements with 16 nodes, corresponding to eight pairs of nodes, are applied between the soil and the wall elements. The thickness of the interfaces are set to zero, however a virtual thickness is applied in order to establish the stiffness of the interface. The Coulomb criterion is employed for the interfaces to distinguish between elastic and plastic behaviour. The stiffness and strength of the interface is governed by the factor, R_{inter} . The angle of internal friction of the interface, φ_i , is set to the angle of internal friction of the soil, φ_{tr} , multiplied with R_{inter} while the stiffness parameters, E_i and G_i , are scaled with R_{inter} squared. Poisson's ratio is by default set to $\nu_i = 0.45$ in the interface. For a perfectly rough soil-structure interface $R_{inter} = 1.0$. As the transition between a soil and a structure is normally weaker and more flexible than the associated soil layer, values of $R_{inter} < 1.0$ should be applied. For further information on the *Plaxis 3D Foundation* reference is made to appendix F.

The boundary conditions are similar to the ones employed in *FLAC^{3D}* except that no boundary restrictions are attached to the

plane of symmetry. The size of the soil mass at each simulation is presented in section 3.3.

When computing the equilibrium state the K_0 -procedure is employed. The equilibrium state is calculated in stages. Firstly, equilibrium is calculated for the model containing only soil. Secondly, a possible overburden pressure is applied as a vertical load. Thirdly, the pile is installed and a new equilibrium state is calculated. In order to obtain load-displacement relationships and p - y curves the total lateral load is applied in stages.

3.3 Outer boundaries

In order to avoid the outer boundaries from affecting the results, the volume of the soil is adjusted to each pile diameter. According to Abbas et al. (2008) the width of the soil mass should be $40D$ and the height of the soil mass should be $h = L + 20D$, where L denotes the embedded length of the pile and D denotes the pile diameter, cf. fig. 7. However, Abbas et al. (2008) investigated piles which were exposed to both horizontal and vertical loading. As only the behaviour due to lateral loading is examined in the simulations a smaller height of the soil mass is employed. For the large-scale simulations the width of the soil mass is set to $40D$ while the height is set to $L + 10$ m. The small-scale simulations are supposed to fit the laboratory tests. The outer boundaries are therefore given as the volume of the soil mass in the pressure tank, i.e. a diameter of 2.1 m and a soil depth of 0.69 m, cf. chapter 3. *FLAC^{3D}* allows a curved outer boundary, which is utilised in all models. On the opposite, *Plaxis 3D Foundation* allows only a squared outer boundary why the diameter of the models in *FLAC^{3D}* corresponds to the side length in *Plaxis 3D Foundation*.

For both the model in *FLAC^{3D}* and *Plaxis*

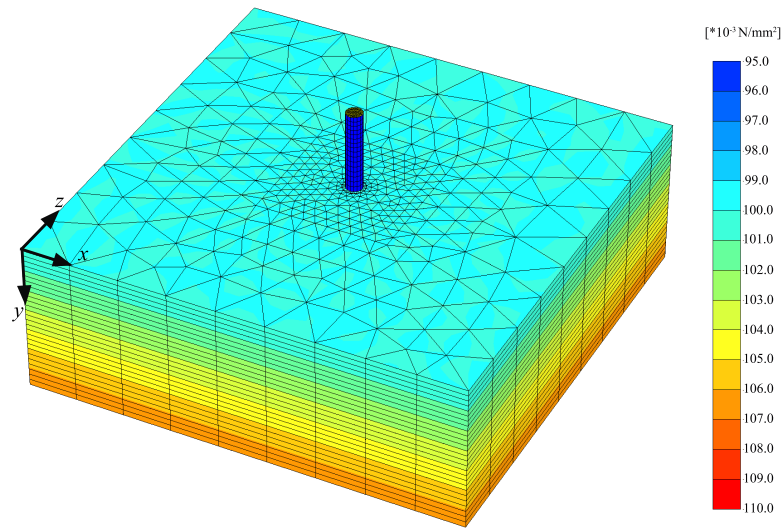


Figure 6: Three-dimensional mesh for the *Plaxis 3D Foundation* model and effective vertical stresses in MPa, σ'_{yy} , prior to the horizontal load is applied for $D = 0.08$ m, $L = 0.4$ m, and $P_0 = 100$ kPa.

3D Foundation it has been observed that the zone of failure does not reach the outer boundaries.

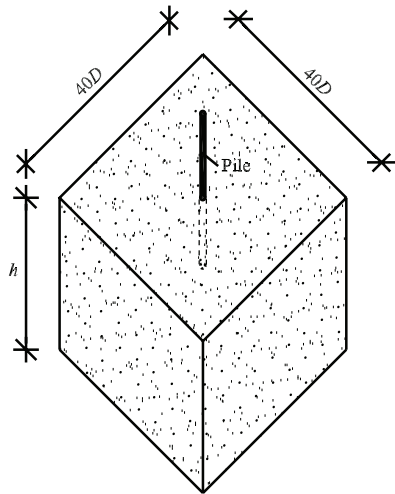


Figure 7: Dimensions of the soil volume. D is the outer diameter of the employed pile.

3.4 Material models

In both numerical models a traditional elasto-plastic Mohr–Coulomb model is employed to describe the constitutive relations. The yield function of the constitutive model is controlled by a non-associated flow rule. No tension forces are allowed in the soil, as a pure friction ma-

terial is considered, why tension cut-off is appointed. A brief description of the model is given in appendix G.

3.5 Young's modulus of elasticity, E_0

When calibrating the numerical models to the laboratory tests the soil parameters are assumed to remain constant with depth due to the small variations in effective stresses. Young's modulus of elasticity of the soil is however varied with respect to the stress level for the calculations on large-scale monopiles. The tangential Young's modulus of elasticity, E_0 , is assumed to vary with the minor principal stress, σ'_3 , on the basis of (2)-(3) as proposed by Ibsen et al. (2009). Equation (2)-(3) are valid for Baskarp Sand Nr. 15. The relative density, I_D , is inserted in % and σ_3^{ref} is a reference minor principal stress of 100 kPa.

$$E_0 = E_0^{ref} \left(\frac{c \cdot \cos(\varphi_{tr}) + \sigma'_3 \sin(\varphi_{tr})}{c \cdot \cos(\varphi_{tr}) + \sigma_3^{ref} \sin(\varphi_{tr})} \right)^{0.58} \quad (2)$$

$$E_0^{ref} = 1.82(0.6322I_D^{2.507} + 10920) [\text{kN/m}^2] \quad (3)$$

For the model in *Plaxis 3D Foundation* the variation of Young's modulus is approximated by three stepwise linear functions. The tangential Young's modulus of elasticity of the soil according to (2)-(3) and the approximated stepwise functions are illustrated in fig. 8.

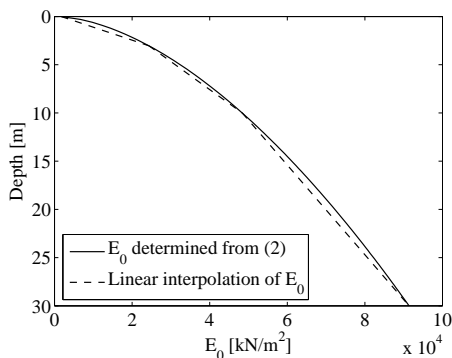


Figure 8: Variation of Young's modulus of elasticity of the soil, E_0 .

3.6 Computation of soil resistance and pile bending moment

The bending moment, M , at a given level of the pile is in *FLAC^{3D}* calculated by use of Naviers formula:

$$M = \frac{(\sigma_{zz,i} - \bar{\sigma}_{zz,i})I_{yy}}{x_i} \quad (4)$$

where $\sigma_{zz,i}$ is the vertical normal stresses at point i , I_{yy} is the second moment of inertia around the y -axis, x_i is the x -coordinate of point i , and $\bar{\sigma}_{zz,i}$ is the average vertical stress corresponding to the axial force acting in the pile. The bending moment is calculated from two points ($y = 0$, $x = \pm D/2$) at each level of the pile in order to eliminate the average vertical stress.

For the model in *Plaxis 3D Foundation* the bending moment is computed by a summation of the product of the nodal forces in the y -direction, $f_{y,i}$, and the x -coordinates, for all nodes at a given level

of the pile:

$$M = \sum_i^n f_{y,i}x_i \quad (5)$$

The soil resistance is for both numerical models calculated by differentiating the bending moment distribution along the pile twice. The double differentiation gives an amplification of errors in the bending moment distribution. In order to minimise these errors the piecewise polynomial curve fitting method described by Yang and Liang (2006) is employed. Hereby, the bending moment distribution is estimated by fitting five successive moment data points to 3. order polynomials. It is emphasised that (4) and (5) are related to the coordinate systems employed in the respective models. The piecewise polynomial curve fitting method is further treated in appendix A.4.

4 Calibration of numerical models

On the basis of the derived soil parameters given in appendix C the numerical models in *FLAC^{3D}* and *Plaxis 3D Foundation* have been calibrated. The soil parameters are assumed to be constant with depth.

4.1 *FLAC^{3D}*

In the calibration of the model constructed in *FLAC^{3D}* the obtained load-displacement relationship and bending moment distributions have been compared to the test results. As an example of the calibration the load-displacement relationship is shown in fig. 9 for $D = 80$ mm, and $P_0 = 100$ kPa. Figure 10 presents the calibrated and measured bending moment distribution at a horizontal load of 2100 N for the same test. As shown in fig. 9 and

fig. 10, the agreement between the experimental and computed values is relatively good. Similar analyses have been made for the five remaining tests with similar results. As the computed values by means of $FLAC^{3D}$, when employing the soil parameters obtained from CPT's, are rather similar to the measured values it is concluded that the numerical model produce realistic results. The difference between the calibrated and measured load-displacement relationships and bending moment distributions might be due to uncertainties from determination of the soil parameters rather than numerical errors. In the calibrations the wall friction angle, δ , has been set to 30° , and the dilatancy angle to $\psi = 10^\circ$. The shear stiffness, k_s , and the normal stiffness, k_n , of the interface has been set to $k_s = k_n = 100E_0$.

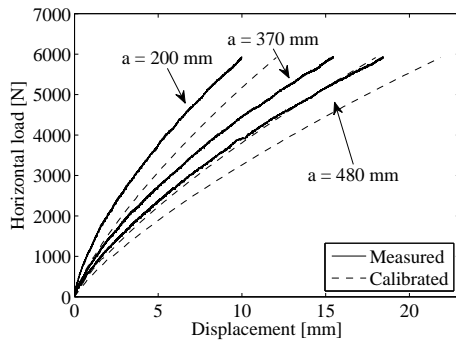


Figure 9: Calibrated load-displacement relationship determined by means of $FLAC^{3D}$ at three levels above soil surface, for the test with $D = 0.08$ m, $L = 0.4$ m, and $P_0 = 100$ kPa. a denotes the distance from the soil surface to the level of measuring.

4.2 *Plaxis 3D Foundation*

In order to validate the results obtained by means of *Plaxis 3D Foundation* the pile with $D = 80$ mm, and $P_0 = 100$ kPa have been simulated. The load-displacement relationships are shown in fig. 11.

The load-displacement relationship, cf. fig 11, does not fit the laboratory tests well. In *Plaxis 3D Foundation* a horizontal dis-

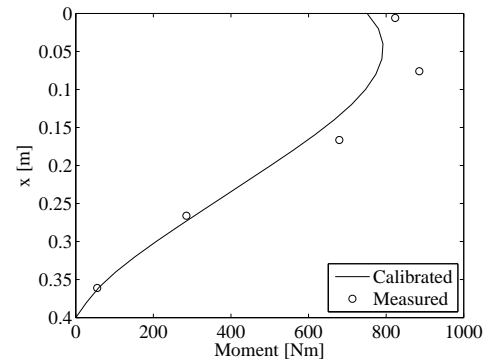


Figure 10: Bending moment distribution determined by means of $FLAC^{3D}$ and the laboratory test result at a horizontal load of 2100 N. $D = 0.08$ m, $L = 0.4$ m, and $P_0 = 100$ kPa.

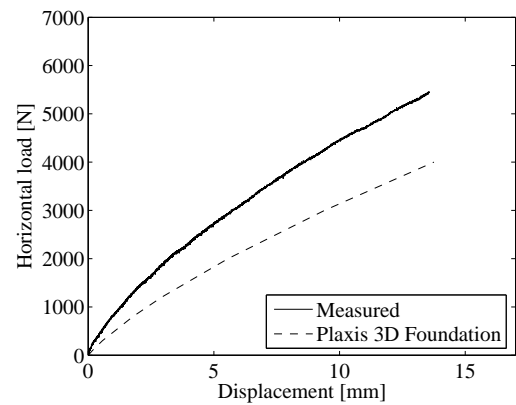


Figure 11: Load-displacement relationship determined by means of *Plaxis 3D Foundation* and laboratory tests, measured at the level of the hydraulic piston. $D = 0.08$ m, $L = 0.4$ m, and $P_0 = 100$ kPa.

placement measured in the level of the hydraulic piston is determined to $y = 13.8$ mm at a horizontal load of $H = 4000$ N. At the same horizontal load a displacement of $y = 8.5$ mm is measured at the laboratory. Hereby, the model in *Plaxis 3D Foundation* overestimates the displacement with approximately 60% compared to the test result.

The potential sources of error causing the large displacements in the *Plaxis 3D Foundation* model are several. The most obvious are the soil parameters including Young's modulus of elasticity of the soil, E_0 , and the interface properties. As E_0 governs the initial part of the curve, which

is the main focus of this paper, the influence of uncertainties concerning E_0 and the interface properties are evaluated.

The stiffness of the soil is determined from CPT's conducted without overburden pressure and extrapolated under the influence of stress level. If the Young's modulus of elasticity is correct and all other sources of error are negligible, a simulation with an elastic material model should form the tangent stiffness of the laboratory tests. As shown in fig. 12 this is not the case with a Young's modulus of elasticity of $E_0 = 41.0$ MPa as derived from the CPT's. In order to assess the sensitivity of the model with respect to the Young's modulus of elasticity, the impact of doubling the soil stiffness, i.e. $E_0 = 82.0$ MPa, is tested. The load-displacement relationship when doubling E_0 is shown in fig. 12.

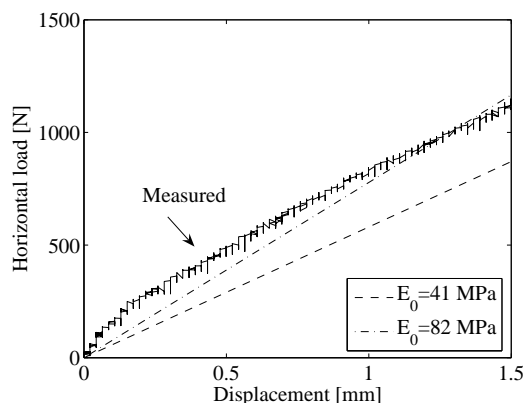


Figure 12: Initial part of load-displacement relationship determined by means of *Plaxis 3D Foundation* when employing an elastic material model. $D = 0.08$ m, $L = 0.4$ m, and $P_0 = 100$ kPa.

Even when doubling the Young's modulus of elasticity the tangent stiffness obtained by means of *Plaxis 3D Foundation*, cf. fig. 12, is underestimated compared to the laboratory test. By this it is concluded that the Young's modulus of elasticity is not the main reason for the difference between the results in *Plaxis 3D Foundation* and the laboratory tests.

The interface properties in *Plaxis 3D*

Foundation are governed by the parameter R_{inter} . In the simulation shown in fig. 11 a value of $R_{inter} = 0.69$ have been employed after the recommendations in *Plaxis 3D Foundation Manual* (2007). R_{inter} can maximally take the value $R_{inter} = 1.0$ corresponding to a perfectly rough connection between soil and structure. The effect on the load-displacement relationship of increasing R_{inter} from 0.69 to 1.0 is shown in fig. 13.

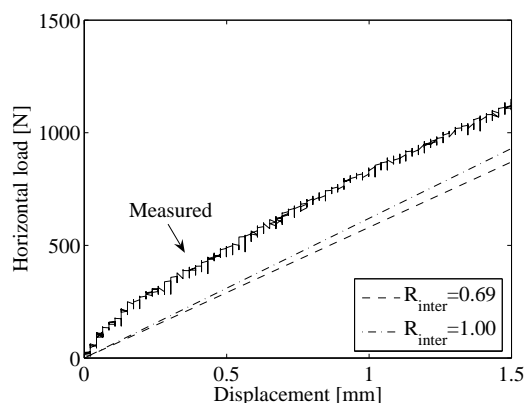


Figure 13: Initial part of load-displacement relationship determined by means of *Plaxis 3D Foundation* when employing R_{inter} of 0.69 and 1.00, respectively. $D = 0.08$ m, $L = 0.4$ m, and $P_0 = 100$ kPa. An elastic material model has been employed.

A perfectly rough interface between the soil and the pile is highly unlikely. However, the simulation with $E_0 = 41.0$ MPa and $R_{inter} = 1.0$ does not, as shown in fig. 13, result in sufficient stiffness.

The conclusion of the above analysis is that the simulations in *Plaxis 3D Foundation* do not meet an acceptable accuracy for the load-displacement relationship in comparison with the laboratory tests.

4.3 Comparison with a simulation of a Horns Rev monopile

As described, the model in *FLAC^{3D}* fits the laboratory tests well, which is in contrast to the model in *Plaxis 3D Foundation*. Kellezi and Hansen (2003) have

simulated a monopile foundation at Horns Rev subjected to static lateral load. The foundation is subjected to a horizontal load of 2503 kN and a bending moment of 84983 kNm, acting at seabed level. The analysis was performed by means of the three-dimensional numerical program *ABAQUS* assuming drained soil conditions. The soil conditions, cf. tab. 1, are primarily sand with a layer of low-strength organic sand located at a depth of 13.5 m. A Mohr-Coulomb material model incorporating isotropic hardening/softening has been employed by Kellezi and Hansen (2003). The simulation performed by Kellezi and Hansen (2003) is used as benchmark in order to determine whether the numerical model in *FLAC^{3D}* or the model in *Plaxis 3D Foundation* produce acceptable load-displacement relationships.

Figure 14 presents load-displacement relationships determined by means of *FLAC^{3D}* and *Plaxis 3D Foundation* compared with the results obtained by Kellezi and Hansen (2003). It should be emphasized that similar material parameters and interface properties are employed for the three numerical models. As shown in the figure *Plaxis 3D Foundation* produce a horizontal displacement approximately 99 % larger than *ABAQUS* at a horizontal load of 2503 kN. Hereby, the model in *Plaxis 3D Foundation* overestimates the horizontal displacement compared with both the laboratory tests and the results obtained by *ABAQUS* and *FLAC^{3D}*. The deviation of lateral displacement when comparing the results from *ABAQUS* and *FLAC^{3D}* are small, especially when considering displacements smaller than 0.02 m. The difference between the results obtained by *ABAQUS* and *FLAC^{3D}* at greater displacements might be due to various interface descriptions, and the lack of material hardening incorporated in the *FLAC^{3D}* model.

In order to make a reasonable fit be-

tween the load-displacement relationships obtained by means of *ABAQUS* and *Plaxis 3D Foundation* a study on the influence of Young's modulus of elasticity has been performed. When multiplying Young's modulus of elasticity with a factor of 2.5 for all soil layers the difference in pile-head displacement is lower than 2 %, cf. fig. 14, when comparing the results obtained by *ABAQUS* and *Plaxis 3D Foundation*.

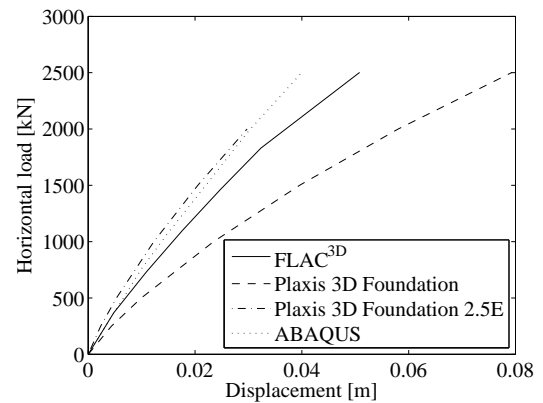


Figure 14: Comparison of load-displacement relationships calculated by means of *FLAC^{3D}* and *Plaxis 3D Foundation* with the results obtained by Kellezi and Hansen (2003) with use of *ABAQUS*.

5 Simulation of large-scale monopiles

In order to evaluate the effects of diameter on the initial stiffness of the p - y curves laterally loaded large-diameter monopiles are simulated by means of the commercial programs *FLAC^{3D}* and *Plaxis 3D Foundation*. In the calibration of the numerical models *Plaxis 3D Foundation* were found to overestimate the pile deflection in comparison with the laboratory tests. Furthermore, *Plaxis 3D Foundation* also produced a larger displacement when simulating the load-displacement relationship for a monopile at Horns Rev compared to numerical models in *ABAQUS* and *FLAC^{3D}*. Therefore, *Plaxis 3D Foundation* is not expected to produce realistic values of soil resistance and pile deflection. However, a re-

Table 1: Geometric and mechanical data for the soil, after Kellezi and Hansen (2003).

Soil type	Depth [m]	E [kN/m ²]	γ' [kN/m ³]	φ [°]	ψ [°]	ν [-]
Sand	1.0	31800	10	42.0	12.0	0.3
Sand	3.5	57100	10	43.5	13.5	0.3
Sand	5.5	52534	10	42.5	12.5	0.3
Sand	6.5	44100	10	41.7	11.7	0.3
Sand	7.0	58200	10	43.2	13.2	0.3
Sand	8.5	72170	10	44.3	14.3	0.3
Sand	10.0	52950	10	43.1	13.1	0.3
Sand	11.5	35400	10	40.3	10.3	0.3
Sand	12.5	23530	10	37.2	7.2	0.3
Sand	13.5	13600	10	33.8	3.8	0.3
Org. sand	20.0	3135	7	21.6	0.0	0.3
Org. sand	21.04	12950	7	31.2	1.2	0.3
Sand	41.8	36800	10	37.8	7.8	0.3

alistic variation of soil resistance with pile diameter and depth have been observed in the calibrations. The model is therefore employed in the simulation of large-scale monopiles in order to validate the tendencies observed in *FLAC^{3D}*. *Plaxis 3D Foundation* is much less time consuming than *FLAC^{3D}* implying the possibility of more simulations at a given time period.

In the evaluation of the effects of diameter on the initial stiffness of the p - y curves, four circular, closed-ended, pipe piles with diameters of 2 m, 3 m, 5 m, and 7 m are simulated in both *FLAC^{3D}* and *Plaxis 3D Foundation*. Furthermore, a slender monopile with a diameter of 1 m are simulated in *Plaxis 3D Foundation*. The pile with this diameter has not produced a realistic load-displacement relationship by means of *FLAC^{3D}* due to a high load eccentricity compared to the pile diameter. All piles have a wall thickness of 0.05 m and the horizontal load is applied with a vertical eccentricity of 15 m. The embedded length of the piles is 20 m, except for the analyses conducted in section 5.6. For all analyses drained soil conditions are employed.

5.1 Soil and pile properties at large-scale analyses

The material parameters for the soil and the piles employed in the simulations are given in tab. 2. The material properties of the large-scale piles corresponds to the properties of steel and are scaled in accordance to (1). The tangential Young's modulus of elasticity, E_θ , is varied with depth, cf. (2)-(3).

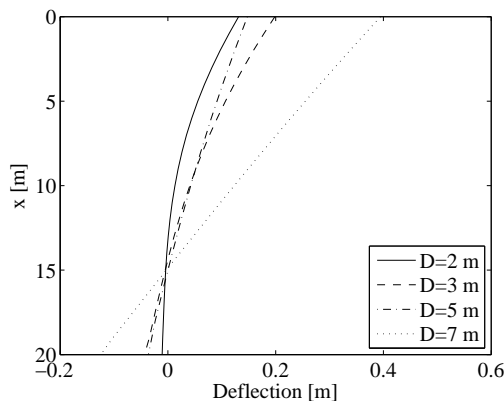
5.2 Effects of diameter on pile behaviour

Figure 15 presents the lateral pile deflection behaviour with respect to depth for the model incorporated in *FLAC^{3D}*. The applied displacements at the pile-head, corresponding lateral loads, and depth of maximum moments are outlined in tab. 3. As shown the lateral displacements at the pile-head and the horizontal loads are different in the four cases. The more rigid pile behaviour for increasing diameters, cf. fig. 15, is in good accordance with Poulos and Hull (1989) as the employed pile bending stiffness increases for increasing pile diameter. Due to the rigid pile behaviour, a significant negative de-

Table 2: Material properties employed for the large-scale analyses.

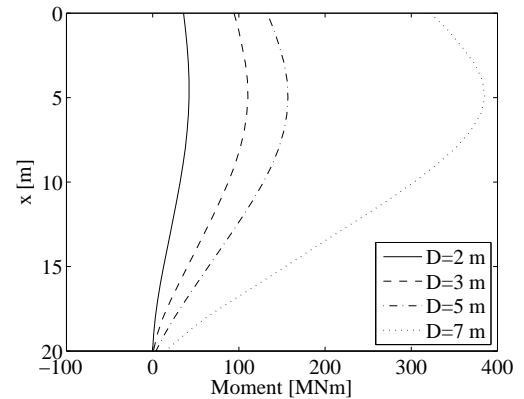
Unit weight of the soil γ'	10 kN/m ³
Angle of internal friction φ_{tr}	40°
Dilatancy angle ψ_{tr}	10°
Cohesion c	0.1 kN/m ²
Relative density I_D	80%
Poisson's ratio for the soil ν_s	0.23
Coefficient of horizontal earth pressure at rest K_0	1-sin(φ_{tr})
Young's modulus of elasticity for the hollow pile E_p	210 GPa
Poisson's ratio for the pile ν_p	0.3
Unit weight of the pile γ_p	78.5 kN/m ³

flexion is observed at the pile-toe. The magnitude of negative deflection increases with increasing pile bending stiffness. The point of zero deflection, cf. fig. 15, are for $D = 3 - 7$ m located at a depth of approximately $x = 15$ m at the applied displacements, cf. tab. 3. As the pile deflection for $D = 2$ m consists of a high amount of deformation due to bending the point of zero deflection is located nearer the soil surface at a depth of approximately $x = 13$ m. For all piles it has been observed that the location of the point of zero deflection depends on the applied displacement; the distance measured from soil surface to the depth of zero deflection increases with increasing displacement. This is caused by the fact that the zone of failure propagates downwards with increasing pile displacement.


Figure 15: Lateral pile deflection calculated by means of $FLAC^{3D}$.

The distribution of bending moments with depth simulated in $FLAC^{3D}$ are presented

in fig. 16. It is observed that the maximum bending moment is located at depths of approximately 5 m for $D = 3 - 7$ m. For $D = 2$ m the maximum bending moment is located at a depth of approximately 4.5 m. As the point of zero deflection for the pile with $D = 2$ m is located nearer the soil surface than for the other three piles, the maximum moment is also expected to be located nearest to the soil surface.


Figure 16: Bending moment distribution calculated by means of $FLAC^{3D}$.

A similar pile behaviour has been observed for the model constructed in *Plaxis 3D Foundation*. The pile with $D = 1$ m deflects primarily by bending resulting in almost zero horizontal displacement at the pile-toe.

Table 3: Applied displacements at the pile-head, equivalent loads, and depth of maximum moments for the analyses in $FLAC^{3D}$.

Outer pile diameter [m]	Displacement [m]	Load [MN]	Depth of max. moment [m]
2	0.49	2.5	4.5
3	0.58	6.4	4.8
5	0.24	8.8	5.0
7	0.84	21.4	4.9

5.3 Comparison of computed p - y curves with the design regulations

The distribution of soil resistance with depth for the model in $FLAC^{3D}$ is shown in fig. 17. It is observed that the soil resistance do not approach zero at the soil surface for all piles. However, it should be emphasized that the soil resistance at the soil surface is approximated from the bending moment at the soil surface and at four points below the soil surface. Hereby, uncertainties are attached to the determination of the soil resistance at the soil surface. These uncertainties also account for the calculated soil resistance at the pile-toe. Alternatively the soil resistance could have been computed by integrating the stresses in the interface elements along the circumference of the pile. Deviations in the soil resistance can be observed near the point of zero deflection, most significantly for $D = 7$ m. Small uncertainties in the bending moment distribution implies uncertainties when determining the soil resistance. Near the point of zero deflection the soil resistance is approximately zero and the effect of uncertainties on the distribution of soil resistance is therefore most significant at this depth.

Figure 18 presents the p - y curves obtained by means of $FLAC^{3D}$ at a depth of $x = 2$ m. Further, the p - y curves according to the design regulations, e.g. API (1993) and DNV (1992), are outlined in the figure. As expected the ultimate soil resistance increases with increasing pile diameter. Further, the initial part of the

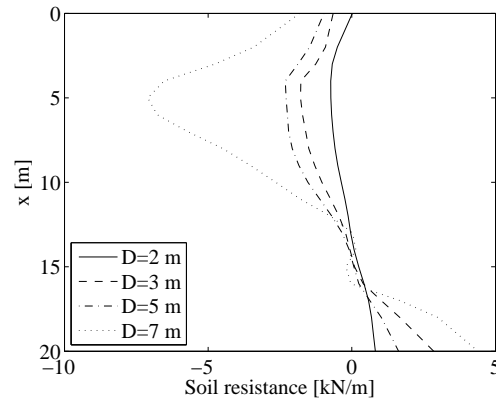


Figure 17: Soil resistance versus depth determined by means of $FLAC^{3D}$.

curves, is stiffer for the API p - y curves compared to the p - y curves obtained by means of $FLAC^{3D}$. The ultimate soil resistance of the API p - y curves has some degree of conservatism in the case of very large diameters. This is however, not observed for the piles with $D = 2 - 3$ m. Furthermore, the p - y curves obtained from the three-dimensional numerical model do not reach a steady state at the applied displacements. Although the load-displacement relationship obtained by a force and a displacement controlled approach are in agreement, cf. fig. 4, the p - y curve for $D = 2$ m has some degree of fluctuation.

5.4 Variation of initial stiffness with depth

The variation of initial stiffness with depth, $E_{py}^* = \frac{dp}{dy}$, $y = 0$, is presented in fig. 19a for the four pile diameters modelled in $FLAC^{3D}$. Figure 19b presents the va-

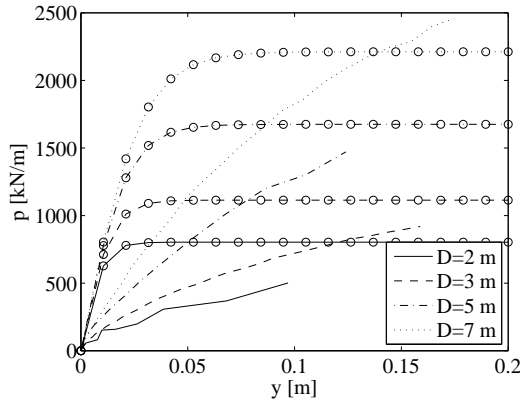
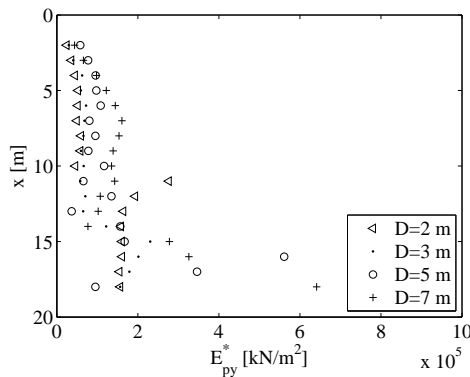
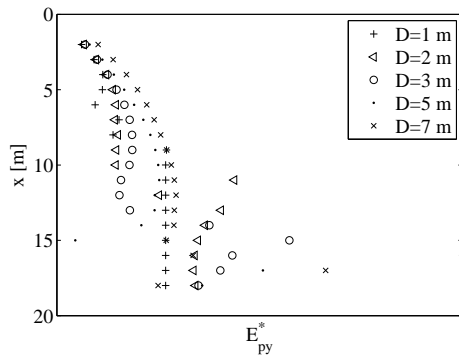


Figure 18: Comparison of API p - y curves marked with (o) and the p - y curves obtained by means of $FLAC^{3D}$ for the four piles, respectively.



(a) $FLAC^{3D}$.



(b) $Plaxis\ 3D\ Foundation$.

Figure 19: Initial stiffness, E_{py}^* , versus depth.

riation of E_{py}^* with depth for the analyses computed by means of *Plaxis 3D Foundation*. From the figures it is observed that the initial stiffness increases with increasing pile diameter. The offshore design regulations, e.g. DNV (1992) and API (1993), suggest that the initial modulus of subgrade reaction, k , and hereby also the initial stiffness $E_{py}^* = kx$:

$$\frac{dp}{dy} \Big|_{y=0} = Ap_u \frac{\frac{kx}{Ap_u}}{\cosh^2\left(\frac{kxy}{Ap_u}\right)} \Big|_{y=0} = kx \quad (6)$$

is independent of the pile diameter. This is in contrast to the variation of initial stiffness with depth shown in fig. 19a and fig. 19b. The p - y curves obtained near the point of zero deflection as well as at the pile-toe is characterised by a lot of scatter due to small deflections causing large uncertainties for the initial stiffness at large depths.

According to fig. 19a and fig. 19b E_{py}^* does not vary linearly with depth. Lesny and Wiemann (2006) propose a power function for the variation of E_{py}^* with depth:

$$E_{py}^* = E_{py,ref}^* \left(\frac{x}{x_{ref}} \right)^a \quad (7)$$

where $E_{py,ref}^*$ denotes the initial stiffness at a reference depth, x_{ref} , and a is a factor depending on the relative density of the sand. According to Lesny and Wiemann (2006) the factor a is to be set to 0.6 for medium dense sands.

Figure 20 presents the initial stiffness' obtained by means of *Plaxis 3D Foundation* and the variations based on (6) and (7) for $D = 7$ m. The two expressions, cf. (6) and (7), are identical when $a = 1$. As a reference initial stiffness, $E_{py,ref}^*$, the initial stiffness at $x_{ref} = 2$ m is employed. Figure 20 indicate that the linear expression employed in the design regulations fits the obtained E_{py}^* well until a depth of approximately 5 m. Beneath this depth the linear expression highly overestimates E_{py}^* , given that the soil response is non-conservative

at large depths. Equation (7) fits the obtained E_{py}^* very well until a depth of 14 m. Equation (6) is highly affected by the value of k while (7) produces a reasonable fit independent of the reference value due to the non-linear behaviour. E_{py}^* is not clearly defined beneath $x = 14$ m due to the influence of the point of zero deflection. For the remaining pile diameters a similar non-linear variation of E_{py}^* with depth is found, most significantly for $D = 3 - 7$ m. Hereby, the expression in the offshore design regulations overestimates the soil-pile interaction for large-diameter monopiles at large depth. The non-linear variation of initial stiffness is observed in connection with both the analyses in *FLAC^{3D}* and *Plaxis 3D Foundation*.

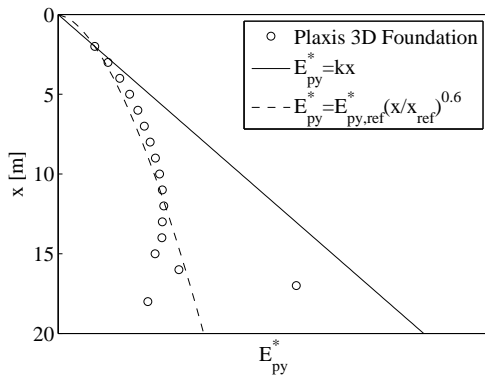


Figure 20: Variation of E_{py}^* as function of depth determined by means of *Plaxis 3D Foundation* for $D = 7$ m, and $x_{ref} = 2$ m.

5.5 Effect of diameter on initial modulus of subgrade reaction

The magnitudes of k in (6) obtained by means of *FLAC^{3D}* are outlined in tab. 4 at $x = 2 - 7$ m where the assumption of a linear variation of initial stiffness with depth is reasonable. As indicated in tab. 4, k is highly dependent on the pile diameter; increasing diameter results in an increase in k . This observation is most significant when comparing the results for the piles with $D = 2 - 5$ m. For dense sand

($\varphi_{tr} = 40^\circ$) the offshore design regulations recommend $k = 40000$ kN/m³. This does not agree with the analyses since k ranges between 7000–29000 kN/m³.

A power function of the form:

$$k = k_{ref} \left(\frac{D}{D_{ref}} \right)^b \quad (8)$$

is employed in order to describe the relation between k and D .

Figure 21 and 22 presents the normalised relationship based on (8) by means of the two numerical models, respectively. The exponent b is determined to 0.645 and 0.226 by means of *FLAC^{3D}* and *Plaxis 3D Foundation*, respectively. Hereby, there is a considerable difference between k/k_{ref} , cf. fig. 21 and 22, obtained by the two numerical models. This difference is most significant at diameters of $D = 5 - 7$ m implying a higher exponent b determined by means of *FLAC^{3D}*. However, both models highly indicates that there is a correlation between k and D . More research is needed in order to make a clear correlation between pile diameter and initial modulus of subgrade reaction. The fact that the initial modulus of subgrade reaction is affected by the pile diameter is substantiated by investigations of piles in clay, e.g. O'Neill and Dunnivant (1984) and Dunnivant and O'Neill (1985), as treated in chapter 2.

5.6 Effect of extra embedded length

The previous analyses have been based on varying diameters and a constant embedded pile length of 20 m. In order to eliminate the effect of embedded length on the initial stiffness of the p - y curves the embedded length has been extended to 30 m. The analyses have been made by means of *Plaxis 3D Foundation*. Figure 23 presents the variation of E_{py}^* with depth when varying the embedded length for $D = 3$ m and

Table 4: Initial modulus of subgrade reaction, k , obtained by means of $FLAC^{3D}$. k is specified in $[kN/m^3]$.

	$D = 2 \text{ m}$	$D = 3 \text{ m}$	$D = 5 \text{ m}$	$D = 7 \text{ m}$
$x = 2 \text{ m}$	12116	14799	28964	21891
$x = 3 \text{ m}$	11899	13550	25798	21846
$x = 4 \text{ m}$	11166	15663	23921	24547
$x = 5 \text{ m}$	10482	11881	19532	24440
$x = 6 \text{ m}$	8602	12045	18065	24077
$x = 7 \text{ m}$	7051	9747	11475	22963

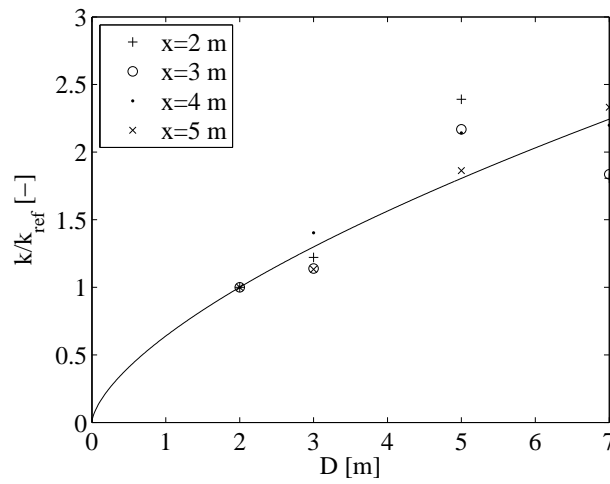


Figure 21: Normalised initial modulus of subgrade reaction versus pile diameter determined by means of $FLAC^{3D}$. As k_{ref} the value at $D = 2 \text{ m}$ have been employed. $b = 0.645$.

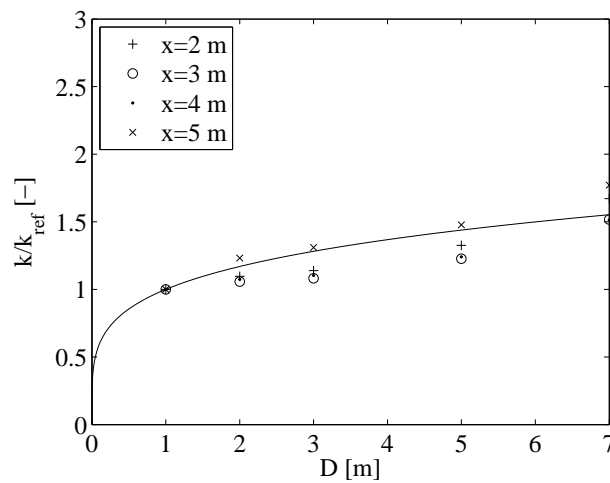


Figure 22: Normalised initial modulus of subgrade reaction versus pile diameter determined by means of *Plaxis 3D Foundation*. As k_{ref} the value at $D = 1 \text{ m}$ have been employed. $b = 0.226$.

$D = 5$ m, respectively. From fig. 23 it is observed that E_{py}^* is not significantly influenced by the embedded length. The point of zero deflection changes slightly with length. Due to an extra embedded length reasonable p - y curves beneath the point of zero deflection is obtained. Similar results have been obtained for the remaining pile diameters.

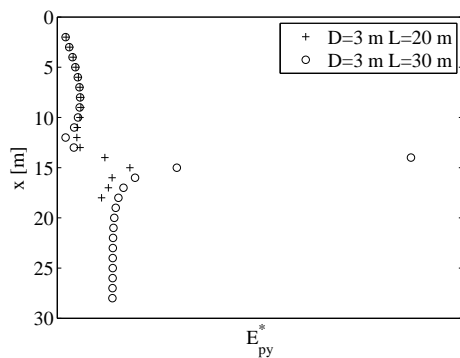
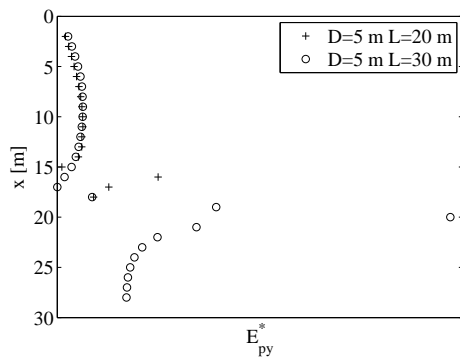
(a) $D = 3$ m.(b) $D = 5$ m.

Figure 23: Effect of embedded length on E_{py}^* determined by means of *Plaxis 3D Foundation*.

5.7 Variation of pile bending stiffness

According to Ashour and Norris (2000) the bending stiffness of the pile, $E_p I_p$, has significant influence on the p - y curves. In order to investigate whether the changes in E_{py}^* registered for different pile diameters are related to the bending stiffness of the pile, simulations have been performed in *Plaxis 3D Foundation* with varying values of $E_p I_p$. The evaluation has been

carried out for $D = 3$ m. The second moment of inertia, I_p , has, due to a constant geometry, been kept constant. Young's modulus of elasticity for the hollow pile has been varied between the values $E_p = 2.1 \cdot 10^7$ kPa, $E_p = 2.1 \cdot 10^8$ kPa, and $E_p = 2.1 \cdot 10^9$ kPa. Figure 24 presents derived p - y curves when varying the pile bending stiffness determined by means of *Plaxis 3D Foundation*. The figures outline the derived p - y curves at a depth of $x = 2$ m and $x = 10$ m, respectively.

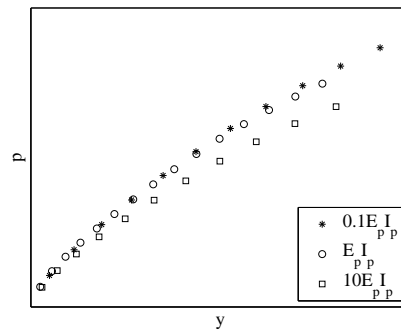
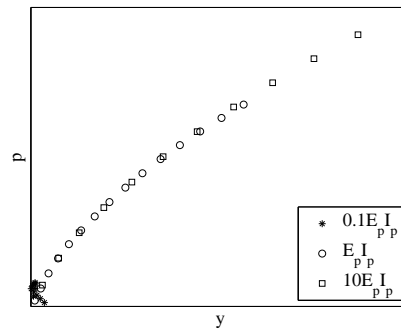
(a) $x = 2$ m(b) $x = 10$ m

Figure 24: p - y curves determined for different pile bending stiffness' by means of *Plaxis 3D Foundation*. $D = 3$ m.

As shown in fig. 24 the pile bending stiffness does not have significant influence on the p - y curves, neither on the initial stiffness nor on the ultimate soil resistance. This investigation is substantiated by the work performed by Fan and Long (2005). The point of zero deflection is situated nearer the soil surface when decreasing the pile bending stiffness. Due to this, the most slender pile is characterised by a lot

of scatter at $x = 10$ m, cf. fig. 24b.

5.8 Load-displacement relationships

Based on small-scale tests it is in chapter 3 indicated that the horizontal load is proportional to the embedded length squared and the pile diameter. However, it should be emphasised that the slenderness ratio, L/D , were kept constant for all tests.

Figure 25 presents normalised load-displacement relationships for various pile diameters and embedded lengths calculated by means of *Plaxis 3D Foundation*. The horizontal load is normalised as $H/L^2D\gamma$ and the pile displacement as y/D . A disagreement between the normalised load-displacement relationships for the various simulated piles can be observed.

As a constant slenderness ratio were employed for the small-scale tests, the lateral load might as well be proportional to the embedded length and the pile diameter squared. Figure 26 show the normalised relationships between load, $H/LD^2\gamma$, and displacement, y/D , at the pile-head for various pile diameters and embedded lengths. A good agreement can be observed for the normalised load-displacement relationships of the various piles. Hereby, the simulations in *Plaxis 3D Foundation* indicate a proportionality between the lateral load and the embedded length and the pile diameter squared.

6 Comparison of $FLAC^{3D}$ with a Winkler model approach

A traditional Winkler model, cf. appendix D, has been constructed in order to compare the results obtained from the three-dimensional numerical model in $FLAC^{3D}$

with the recommendations in the design regulations, e.g. API (1993) and DNV (1992). The nonlinear soil-pile interaction is modelled using the API (1993) $p-y$ curves. Bernoulli-Euler beam theory is employed for the pile even though a more rigid than flexible pile behaviour has been observed for the large-scale piles, cf. fig. 15. Hence, Timoshenko beam theory could preferably be applied. However, only minor errors are observed when using Bernoulli-Euler beam theory, cf. appendix D.5. The comparison between the results obtained by means of $FLAC^{3D}$ and the Winkler model approach is performed, with the same pile geometry, and soil conditions as listed in tab. 2. In fig. 27 the pile deflection with depth obtained by means of $FLAC^{3D}$ and the Winkler model, respectively, is compared for an applied horizontal load at the pile-head of 6.4 MN for $D = 3$ m. The lateral pile deflection determined by means of $FLAC^{3D}$ indicate a very stiff pile behaviour compared to the pile behaviour obtained by the Winkler model approach incorporating API $p-y$ curves, cf. fig. 27. Further, some conclusions can be drawn:

- The deflection at the soil surface determined by means of the Winkler model approach is 37 % of the deflection computed by means of $FLAC^{3D}$.
- The deflection at the pile-toe determined by means of the Winkler model approach is 4 % of the deflections computed by means of $FLAC^{3D}$.
- The point of zero deflection is situated at a depth of approximately 11.0 m for the Winkler model approach. By means of $FLAC^{3D}$ the point of zero deflection is situated in a depth of approximately 14.4 m.

The large disagreement for the pile deflection at the pile-toe indicates that the soil resistance is highly overestimated in the

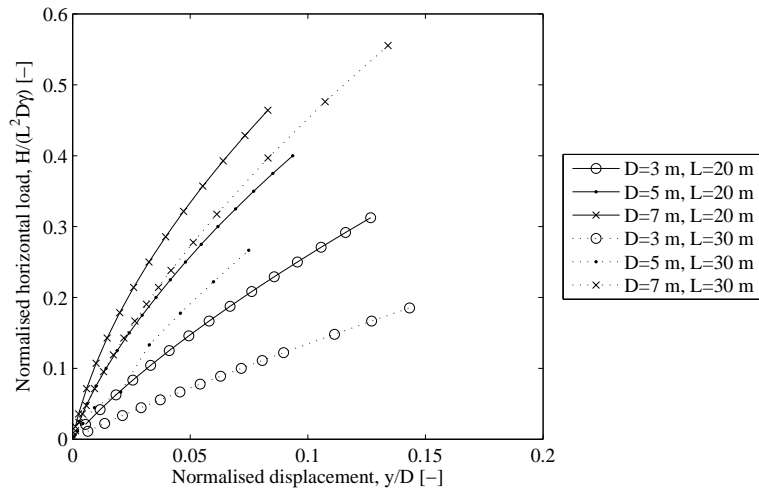


Figure 25: Normalised relationships between load ($H/L^2 D \gamma$) and displacement (y/D) determined at the pile-head at various pile diameters and embedded lengths by means of *Plaxis 3D Foundation*.

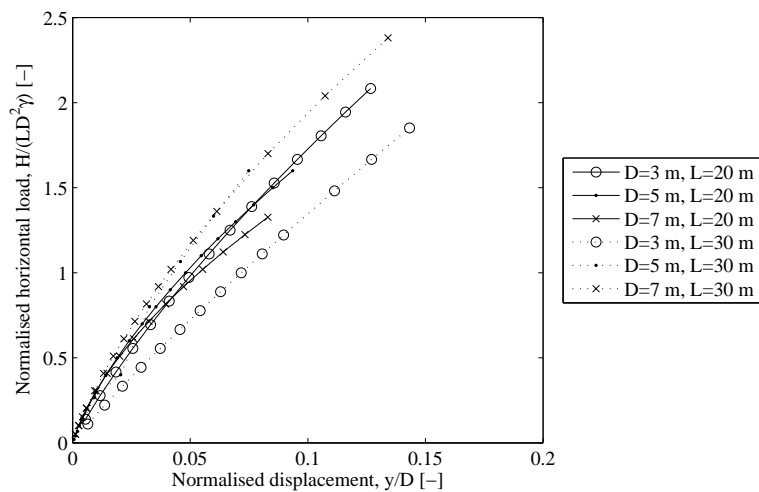


Figure 26: Normalised relationships between load ($H/L D^2 \gamma$) and displacement (y/D) determined at the pile-head at various pile diameters and embedded lengths by means of *Plaxis 3D Foundation*.

design regulations at large depths. The overestimation of soil resistance at large depths also causes the disagreement in the location of the point of zero deflection.

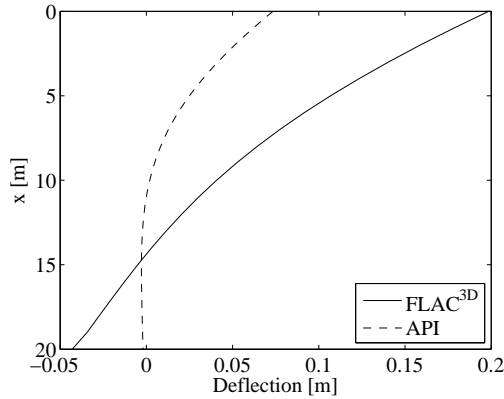


Figure 27: Comparison of lateral pile deflection calculated by means of $FLAC^{3D}$ with the Winkler model approach employing API p - y curves for $D = 3$ m.

In fig. 28 the bending moment distribution along the pile obtained by means of $FLAC^{3D}$ and the Winkler model, respectively, is compared for an applied horizontal load of 6.4 MN for $D = 3$ m. A reasonable agreement between the distribution of bending moment for the model in $FLAC^{3D}$ and the Winkler model can be observed. The depth of maximum bending moment is for both models located at a depth of approximately 5 m. The Winkler model approach overestimates the size of the maximum bending moment with 5 % compared to $FLAC^{3D}$. Near the pile-toe the bending moment computed by means of $FLAC^{3D}$ varies almost linearly with depth. This is in contrast to the bending moment calculated by means of the Winkler model approach, where a significantly non-linear variation of bending moment with depth is observed. As the soil resistance is determined as the 2. order derivative of the bending moment the significant non-linear variation of bending moment at large depths indicate a large soil resistance. Hereby, the distribution of bending moment substantiate the observations in fig. 27.

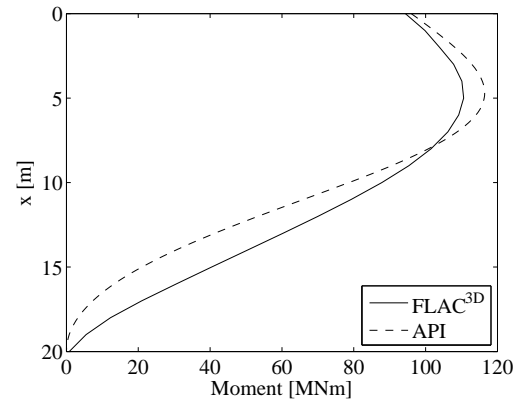


Figure 28: Comparison of bending moment distribution calculated by means of $FLAC^{3D}$ with the Winkler model approach employing API p - y curves for $D = 3$ m.

Figure 29 presents the load-displacement relationships at the pile-head located 15 m above seabed ($D = 3$ m) obtained by means of $FLAC^{3D}$ and the Winkler model approach. The power function, cf. (7), and the recommendations in API (1993), with $k = 40000$ kN/m³ and $k = k_{ref}$ at $x = 2$ m, respectively have in turn been implemented in the Winkler model approach. Figure 29 indicate that the expression employed in API (1993) highly overestimates the strength of the soil at all deflections compared to $FLAC^{3D}$. This is expected in accordance with tab. 4 since the initial modulus of subgrade reaction, k , recommended by API (1993) is overestimated compared to the values calculated by means of $FLAC^{3D}$. The linear expression, cf. (6), with k_{ref} as the value obtained at $x_{ref} = 2$ m produces reasonable results until a deflection of approximately 0.1 m. At greater deflections there is a considerable difference between the deflections determined by $FLAC^{3D}$ and the linear expression. When employing the power function, cf. (7), in the Winkler model approach the initial part of the load-displacement relationship fits very well until a deflection of 0.2 m. At greater deflections an overestimation of the horizontal load is observed compared to $FLAC^{3D}$. However, the difference is much smaller

than obtained by employing the linear expression in the Winkler model. Similar load-displacement behaviour has been observed for the remaining pile diameters.

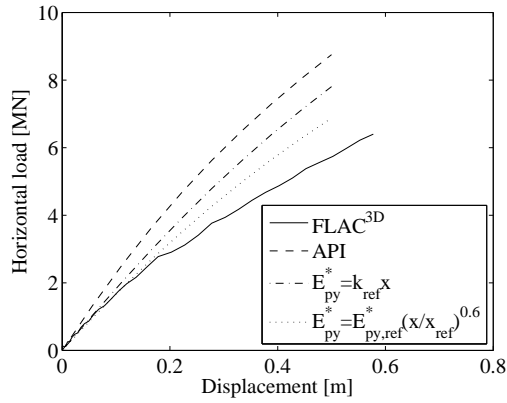


Figure 29: Load-displacement relationships at the pile-head calculated by means of $FLAC^{3D}$ compared with the Winkler model approach incorporating API ($k = 40000 \text{ kN/m}^3$), API (k_{ref}), and the power function, cf. Lesny and Wiemann (2006), respectively.

For modern wind turbine foundations only small deformations/rotations are allowed. Therefore, it is desirable that the initial part of the curves fits the pile behaviour well, which is the case for the power function employed in the Winkler model approach. Hence, it can be concluded that the Winkler model approach is useful when a proper variation of the initial stiffness associated with the p - y curves is employed.

7 Conclusion

A numerical study of the behaviour of laterally loaded large-diameter monopiles in sand is presented in this paper. The evaluation is made by means of the three-dimensional numerical programs $FLAC^{3D}$ and *Plaxis 3D Foundation*. The numerical models are calibrated against well-defined small-scale tests and hereafter extended to large-scale monopiles with pile diameters varying between $D = 2 - 7 \text{ m}$. During the calibration process, *Plaxis 3D Foundation*

were found to overestimate the pile deflection in comparison with the laboratory tests. Therefore, *Plaxis 3D Foundation* does not produce realistic values of soil resistance and pile deflection. However, a realistic variation of soil resistance with pile diameter and depth were observed. The model were therefore employed in the simulation of large-scale monopiles in order to validate the tendencies observed in $FLAC^{3D}$. The conclusions that can be drawn are:

- Non-slender piles deflect as almost rigid objects resulting in only one point of zero deflection. Hence, significant negative deflections at the pile-toe are observed.
- The initial modulus of subgrade reaction, k , is highly affected by the pile diameter; increasing diameter results in an increase in k . This is observed in both $FLAC^{3D}$ and *Plaxis 3D Foundation* simulations. This contradicts the recommendations in the offshore design regulations. k is varying between $7000\text{--}29000 \text{ kN/m}^3$ at small depths when increasing the diameter from $2\text{--}7 \text{ m}$.
- The initial stiffness of the p - y curves, E_{py}^* , is independent of both the embedded length of the pile and the pile bending stiffness, $E_p I_p$. According to this, the main parameter affecting E_{py}^* is the pile diameter.
- The design regulations recommends a linear variation of initial stiffness with depth. This recommendation is non-conservative at large depths. Here, the soil response is overestimated. A non-linear variation of initial stiffness with depth proposed by Lesny and Wiemann (2006) provides a good agreement when compared to the results from the three-dimensional numerical analyses.

- The numerical analyses indicate that the horizontal load acting at the pile-head is proportional to the pile diameter squared and the embedded pile length.

References

Abbas J. M., Chik Z. H., and Taha M. R., 2008. Single Pile Simulation and Analysis Subjected to Lateral Load. *Electronic Journal of Geotechnical Engineering*, **13E**, pp. 1-15.

API, 1993. Recommended practice for planning, designing, and constructing fixed offshore platforms - Working stress design, *API RP2A-WSD*, American Petroleum Institute, Washington, D.C., 21. edition.

Ashour M., and Norris G., May 2000. Modeling lateral soil-pile response based on soil-pile interaction. *Journal of Geotechnical and Geoenvironmental Engineering*, **126**(5), paper no. 19113, pp. 420-428.

Cox W. R., Reese L. C., and Grubbs B. R., 1974. Field Testing of Laterally Loaded Piles in Sand. *Proceedings of the Sixth Annual Offshore Technology Conference*, Houston, Texas, paper no. OTC 2079.

DNV, 1992. Foundations - Classification Notes No 30.4, Det Norske Veritas, Det Norske Veritas Classification A/S.

Fan C. C., and Long J. H., 2005. Assessment of existing methods for predicting soil response of laterally loaded piles in sand. *Computers and Geotechnics* **32**, pp. 274-289.

FLAC^{3D} 3.1 manual, 2006. Fast Lagrangian Analysis of Continua in 3 Dimensions, Itasca Consulting Group Inc., Minneapolis, Minnesota, USA.

Ibsen L. B., Hanson M., Hjort T. H., and Thaarup M., 2009. MC-Parameter Calibration for Baskarp Sand No. 15. *DCE Technical Report No. 62*, Department of Civil Engineering, Aalborg University, Denmark.

Kellezi L., and Hansen P. B., 2003. Static and dynamic analysis of an offshore mono-pile windmill foundation. *Proceedings of the BGA International Conference on Foundations: Innovations, observations, design and practice*, Dundee, UK, pp. 401-410.

Lesny K., and Wiemann J., 2006. Finite-Element-Modelling of Large Diameter Monopiles for Offshore Wind Energy Converters. *Geo Congress 2006, February 26 to March 1*, Atlanta, GA, USA.

Plaxis 3D Foundation Manual Version 2, Brinkgreve R. B. J., and Swolfs W. M. (edt.), 2007.

Poulos H., and Hull T., 1989. The Role of Analytical Geomechanics in Foundation Engineering. *in Foundation Eng.: Current principles and Practices*, **2**, pp. 1578-1606.

Yang K., Liang R., 2006. Methods for Deriving *p-y* Curves from Instrumented Lateral Load Tests. *Geotechnical Testing Journal*, **30**(1), paper ID GTJ100317, pp. 31-38.

CHAPTER 5

Concluding remarks



Concluding remarks

The purpose of this thesis has been to evaluate the initial stiffness of the existing p - y curves, with respect to the design of monopile foundations for offshore wind turbines installed in homogeneous cohesionless soil. The evaluation has been carried out in three stages:

- **Review:** A consistent review concerning shortcomings and advantages of current recommended p - y curves.
- **Experimental work:** Existing p - y curves for sand has been evaluated through six laboratory tests. In addition, the laboratory tests are employed to calibrate numerical models. The tests are carried out at small-scale. However, a new test method has successfully been developed with the main purpose to minimise the scale effects that are often introduced in small-scale tests.
- **Numerical simulations:** Laterally loaded monopiles have been simulated by means of the commercial three-dimensional numerical programs *FLAC^{3D}* and *Plaxis 3D Foundation*. The models have been calibrated to the laboratory test piles and afterwards extended to large-scale monopile foundations with varying diameters.

Based on the results obtained in the three stages some conclusions can be drawn. These conclusions are summarised and compared in the following. In addition to this, directions of future research are given.

5.1 Major findings

The following conclusions are stated with respect to the aim of the thesis as presented in section 1.3.

5.1.1 Experimental work

Through the project, a new test method and appurtenant test setup was developed. The objective of the new method was to develop a method allowing the soil-pile interaction to be examined for varying confining pressures. The tests were conducted in a pressure tank in order to control the confining pressure. In the pressure tank an elastic membrane were placed on the soil surface, leaving the saturated soil sealed from the top part of the tank. When increasing the air pressure in the upper part of the tank, the elastic membrane were pressed against the soil, by which the stresses in the soil were increased. The lower part of the pressure tank were connected to an ascension pipe, leaving all the applied loads to pressure between the grains, i.e. an increase in effective stresses. When increasing the effective stresses in the soil, problems with a non-linear yield surface, as for small stress levels, were overcome. The conducted tests were quasi-static tests on two instrumented closed-ended aluminium pipe piles with outer diameters of 60 mm and 80 mm and a wall thickness of 5 mm. Both piles had a slenderness ratio of 5 corresponding to an embedded pile length of 0.3 m and 0.4 m, respectively. The piles were subjected to a horizontal load acting 0.37 m above the soil surface. The piles were instrumented with strain gauges in five levels beneath the soil surface and displacement transducers were attached to the piles at three points above the soil surface.

The test setup proved to work successfully. The conducted tests showed realistic results, which could be reproduced by means of *FLAC^{3D}* within acceptable margins of error. From the strain gauge measurements the p - y curves were derived by means of the piecewise polynomial curve fitting method developed by Yang and Liang (2006). The obtained p - y curves were acceptable however, clearly influenced by the uncertainties of the strain gauge devices and in particular the number of measurement levels.

5.1.2 Numerical models

Numerical simulations were conducted by means of *FLAC^{3D}* and *Plaxis 3D Foundations* with the objective to examine the behaviour of large-diameter monopile foundations subjected to lateral loads. At first the laboratory test results were reproduced in order to calibrate the numerical models. The simulations conducted by means of *FLAC^{3D}* showed very good results with only small deviations from the laboratory tests in the pile-head displacement and bending moment distribution. Furthermore, the model was successfully calibrated to a typical Horns Rev monopile, cf. Kellezi and Hansen (2003), installed in a multilayered soil.

The *Plaxis 3D Foundations* model however, did not simulate the results of the laboratory tests well. The displacements obtained by means of *Plaxis 3D Foundations* were highly overestimated compared to *FLAC^{3D}*, the laboratory tests, and the Horns Rev monopile modelled by Kellezi and Hansen (2003). Therefore, the model should not, in its current state, be employed in the design of large-scale monopile foundations. Even though *Plaxis 3D Foundations* overestimated the displacements, a realistic variation of soil resistance with pile diameter and depth was observed. The model was employed in the simulation of large-scale monopiles in order to validate the tendencies predicted by *FLAC^{3D}*.

In the large-scale simulations piles with outer diameters of 2, 3, 5, and 7 m and a wall thickness of 0.05 m were employed. The embedded length of the piles varied from 20–30 m.

5.1.3 Lateral pile deflection

The literature review revealed that the existing state-of-the-art procedure is based on very few large-scale tests. Additionally the frame of reference has changed since the current design of monopiles is based on testing of long and slender piles supporting offshore oil and gas platforms. Recently installed offshore wind turbine monopile foundations have a slenderness ratio $L/D < 10$ causing the piles to behave as almost rigid objects when subjected to lateral loads. However, the current recommended design procedure was derived for piles with a slenderness ratio $L/D = 34.4$, causing the piles to bend when exposed to lateral loads and hereby causing a completely different failure mode.

Poulos and Hull (1989) proposed a relation between the stiffness of the pile and the stiffness of the soil. Through this relation it was found that even for very dense sand, $E_s > 100$ MPa, monopiles for offshore wind turbines behave almost rigidly when subjected to lateral loads. This conclusion was substantiated by both the numerical simulations conducted by means of *FLAC^{3D}* and *Plaxis 3D Foundations*. It was found that the non-slender piles had a single point of rotation implying a negative deflection at the pile-toe. Also the piles tested in the laboratory behaved rigidly when subjected to lateral loads. The slenderness ratio of these piles were $L/D = 5$ and even when applying an overburden pressure of 1 bar at the soil surface the piles exhibited an almost rigid behaviour. The pile bending, however, became more distinguished for increasing overburden pressure which is in accordance to Poulos and Hull (1989).

The numerical simulations as well as the laboratory tests indicated that the horizontal load might be proportional to the embedded pile length and the

pile diameter squared.

5.1.4 Variation of initial stiffness, E_{py}^* , with depth

According to the offshore design regulations, e.g. API (1993) and DNV (1992), E_{py}^* increases proportionally with depth. This assumption was not validated through the numerical simulations. The values of E_{py}^* obtained by means of *FLAC^{3D}* and *Plaxis 3D Foundations* fitted, however, a power function, as proposed by Lesny and Wiemann (2006), reasonably, cf. fig. 1. Hence, the design regulations overestimate the initial stiffness of the p - y curves at large depths implying an overestimation of the net soil resistance. This is in agreement with analyses performed by Lesny and Wiemann (2006) as well as Augustesen et al. (2009) which document that the stiffness of the p - y curves are, in general, significantly overestimated with depth. Figure 2 presents the pile lateral deflection computed by means of *FLAC^{3D}* for $D = 3$ m compared to a Winkler model approach incorporating the p - y curves recommended by API (1993). From fig. 2 it is observed that the horizontal deflection at seabed level determined by means of the API method is highly underestimated compared to *FLAC^{3D}*. Further, the deflection at the pile-toe is much smaller by means of the API method compared to the results from *FLAC^{3D}*. The difference in deflection pattern for the two methods is caused by the overestimation of E_{py}^* at large depths when employing the recommendations in the design regulations. Hereby, the Winkler model approach employing p - y curves recommended by API (1993) is highly non-conservative for non-slender monopiles.

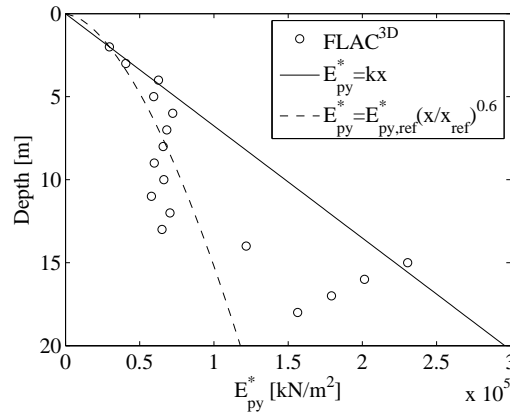


Figure 1: Variation of E_{py}^* as function of depth by means of *FLAC^{3D}*. $D = 3$ m, $x_{ref} = 2$ m, $E_{py,ref}^* = 17330$ kN/m², and $\varphi_{tr} = 40^\circ$.

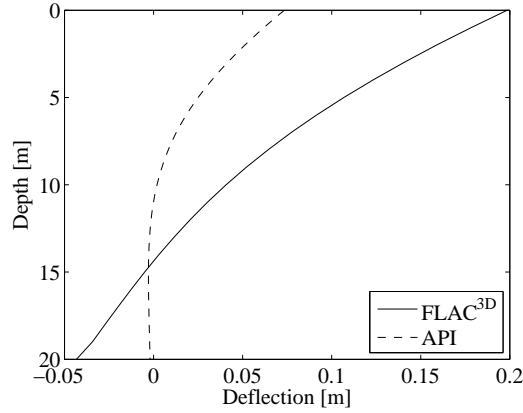


Figure 2: Comparison of pile lateral deflection calculated by means of $FLAC^{3D}$ with the Winkler model approach employing API p - y curves for $D = 3$ m, $\varphi_{tr} = 40^\circ$, $H = 6.4$ MN, and $M = 96.0$ MNm acting at seabed level.

5.1.5 Initial modulus of subgrade reaction, k

According to the design regulations, e.g. API (1993) and DNV (1992), the initial modulus of subgrade reaction, k , is determined from either the angle of internal friction in the soil or the relative density of the soil. Through the numerical simulations and laboratory tests it was found that k is highly dependent on the diameter of the pile. The values of k proposed in the design regulations were found to be non-conservative. The deviations between the obtained values of k and the recommended values in the design regulations was found to vary between approximately 27.5–82.5% for the piles with outer diameters of $D = 2 - 7$ m.

5.1.6 Sensitivity of E_{py}^* to varying embedded pile length and pile bending stiffness

In figure 3 the variation of E_{py}^* with depth is shown for $D = 3$ m and embedded lengths of 20 m and 30 m, respectively. As shown no significant influence of the embedded length was observed on E_{py}^* . Similarly no effect was observed on E_{py}^* when varying the pile bending stiffness in the range of $0.1E_pI_p - 10E_pI_p$ where E_pI_p denotes the pile bending stiffness determined for a steel pipe pile with an outer of $D = 3$ m and a wall thickness of $t = 0.05$ m. Hence, the main pile parameter affecting E_{py}^* is the pile diameter.

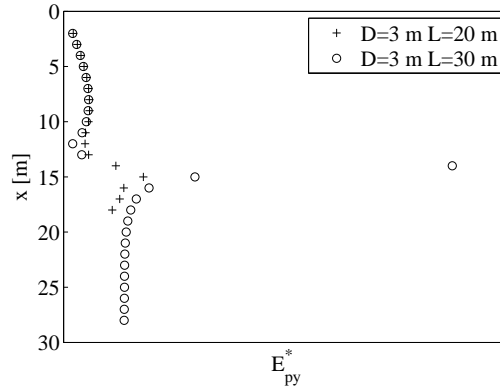


Figure 3: Effect of embedded length on E_{py}^* for $D = 3$ m, $\varphi_{tr} = 40^\circ$ determined by means of *Plaxis 3D Foundations*.

5.1.7 Improved Winkler model approach

Based on the validated numerical model in $FLAC^{3D}$ it was found that the initial stiffness of the p - y curves should increase with depth by means of a power function, cf. section 5.1.4, rather than being proportional to depth as recommended in API (1993) and DNV (1992). The non-linear variation of initial stiffness with depth were implemented in the Winkler model approach. In fig. 4 the load-displacement relationship for $D = 3$ m computed by means of $FLAC^{3D}$ is compared with results based on the Winkler model approach. The power function with the initial modulus of subgrade reaction determined by means of $FLAC^{3D}$, and the recommendations in API (1993), respectively have in turn been implemented in the Winkler model approach. The expression employed in API (1993) highly overestimates the strength of the soil at all displacements, cf. fig. 4, compared to the results obtained by means of $FLAC^{3D}$. When incorporating the power function, in the Winkler model approach the initial part of the load-displacement relationship fits the results obtained by $FLAC^{3D}$ very well until a deflection of 0.2 m.

For modern wind turbine foundations only small pile-head rotations are acceptable. Furthermore, the strict demands to the total stiffness of the system due to resonance in the serviceability mode increase the significance of the p - y curves initial slope and hereby the initial stiffness of the soil-pile system. On basis of this it is recommended to employ the power function in future design of large-diameter offshore monopile foundations in sand.

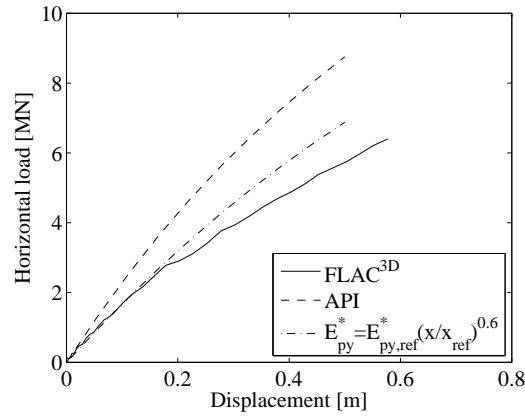


Figure 4: Load-displacement relationships at the pile-head obtained by means of $FLAC^{3D}$ compared to the Winkler model approach incorporating API (1993) p - y curves and the power function, cf. Lesny and Wiemann (2004), respectively. $D = 3$ m, $\varphi_{tr} = 40^\circ$

5.2 Directions for future research

The assessment of p - y curves presented in this thesis considers only offshore wind turbine monopile foundations in homogenous, dense cohesionless sands. Similar analyses are to be performed on different types of soils including sands with varying Young's modulus of elasticity and angles of internal friction. The effects of layered soil on the soil-pile interaction is also of a high interest. In order to validate the effects of diameter on the p - y curves more analyses are to be performed including a large range of different pile diameters, and load cases. Wind turbines and their support structures are highly subjected to cyclic loads why the effects of this must be evaluated in close concordance with an evaluation of the stiffness of the entire wind turbine system. Due to cyclic loading scour holes develops and the effects of these on the soil-pile interaction are to be analysed.

5.2.1 Experimental work

Large-scale tests are expensive and time consuming, which is why the described tests are performed at small-scale. However, large-scale tests will be needed in order to extend the current recommended p - y curve method to large-diameter non-slender monopiles. Until well-documented large-scale tests are available, small-scale tests at varying stress levels are of high importance in order to predict the soil-pile interaction of non-slender monopiles subjected to lateral loads. Several factors that might affect the soil-pile system are omitted in the present laboratory tests in order to isolate the effects

of the diameter. Among these are the disturbance of the soil when driving the pile, the effect of vertical load, and the effect of the compaction of the sand. Moreover, the pile tests are conducted on closed-ended piles in order to protect the strain gauges, which is in contrast to the open-ended piles employed for monopile foundations for offshore wind turbines. Due to the rigid pile behaviour shear forces along the pile-toe might contribute significantly to the net soil resistance. Future tests in the pressure tank must contain tests at higher stress levels in order to simulate a stress level comparable to a typical offshore monopile foundation. Further, more measurement levels along the test piles is preferable in order to obtain p - y curves of high quality.

5.2.2 Numerical work

The three-dimensional models employed in this project considers only massive piles or closed-ended piles in order to calibrate to the laboratory tests. Future models should include open-ended pipe piles, in order to analyse the effect of plugging, skin friction on the inside of the pile and shear forces along the pile-toe. A Mohr-Coulomb material model were employed in the numerical studies. The effects of a more accurate material model on the soil-pile interaction are to be investigated. The soil resistances in the present models are calculated by double differentiation of the moment distribution in the pile. Using this procedure small errors in the moment distribution is amplified which might affect the calculated p - y curves. In future work the soil resistance could be calculated by integrating the stresses in the interface elements along the circumference of the pile.

CHAPTER 6

References

- Abbas J. M., Chik Z. H., and Taha M. R., 2008. Single Pile Simulation and Analysis Subjected to Lateral Load. *Electronic Journal of Geotechnical Engineering*, **13E**, pp. 1-15.
- Abdel-Rahman K., and Achmus M., 2005. Finite element modelling of horizontally loaded Monopile Foundations for Offshore Wind Energy Converters in Germany. *International Symposium on Frontiers in Offshore Geotechnics*, Perth, Australia, Sept. 2005. Balkerna.
- API, 1993. Recommended practice for planning, designing, and constructing fixed offshore platforms - Working stress design, *API RP2A-WSD*, American Petroleum Institute, Washington, D.C., 21. edition.
- Ashford S. A., and Juirnarongrit T., March 2003. Evaluation of Pile Diameter Effect on Initial Modulus of Subgrade Reaction. *Journal of Geotechnical and Geoenvironmental Engineering*, **129**(3), pp. 234-242.
- Ashford S. A., and Juirnarongrit T., 2005. Effect of Pile Diameter on the Modulus of Subgrade Reaction. *Report No. SSRP-2001/22, Department of Structural Engineering, University of California, San Diego*.
- Ashour M., Norris G., and Pilling P., April 1998. Lateral loading of a pile in layered soil using the strain wedge model. *Journal of Geotechnical and Geoenvironmental Engineering*, **124**(4), paper no. 16004, pp. 303-315.
- Ashour M., and Norris G., May 2000. Modeling lateral soil-pile response based on soil-pile interaction. *Journal of Geotechnical and Geoenvironmental Engineering*, **126**(5), paper no. 19113, pp. 420-428.

Ashour M., Norris G., and Pilling P., August 2002. Strain wedge model capability of analyzing behavior of laterally loaded isolated piles, drilled shafts and pile groups. *Journal of Bridge Engineering*, **7**(4), pp. 245-254.

Augustesen A. H, Brødbæk K. T., Møller M., Sørensen S. P. H., Ibsen L. B., Pedersen T. S., and Andersen L., 2009. Numerical Modelling of Large-Diameter Steel Pile at Horns Rev. In *Proceedings of the Twelfth International Conference on Civil, Structural and Environmental Engineering Computing*, Portugal.

Austrell P. E., Dahlblom O., Lindemann J., Olsson A., Olsson K. G., Persson K., Petersson H., Ristinmaa M., Sandberg G., and Wernberg P. A., 2004. *CALFEM - A Finite Element Toolbox - Version 3.4*, Structural Mechanics, LTH, Sweden. ISBN: 91-8855823-1.

Banerjee P. K., and Davis T. G., 1978. The behavior of axially and laterally loaded single piles embedded in non-homogeneous soils. *Geotechnique*, **28**(3), pp. 309-326.

Barton Y. O., and Finn W. D. L., 1983. Lateral pile response and p - y curves from centrifuge tests. *Proceedings of the 15th Annual Offshore Technology Conference*, Houston, Texas, paper no. OTC 4502, pp. 503-508.

Belkhir S., Mezazigh S., and Levacher, D., December 1999. Non-Linear Behavior of Lateral-Loaded Pile Taking into Account the Shear Stress at the Sand. *Geotechnical Testing Journal*, GTJODJ, **22**(4), pp. 308-316.

Briaud J. L., Smith T. D., and Meyer, B. J., 1984. Using pressuremeter curve to design laterally loaded piles. In *Proceedings of the 15th Annual Offshore Technology Conference*, Houston, Texas, paper no. OTC 4501.

Broms B. B., 1964. Lateral resistance of piles in cohesionless soils. *Journal of Soil Mechanics and Foundation Div.*, **90**(3), pp. 123-156.

Brødbæk K. T., Møller M., and Sørensen S. P. H., 2009. Review of p - y Relationships in Cohesionless Soil. *DCE Technical Report no. 57*, Department of Civil Engineering, Aalborg University, Denmark.

Budhu M., and Davies T., 1987. Nonlinear Analysis of Laterally loaded piles in cohesionless Soils. *Canadian geotechnical journal*, **24**(2), pp. 289-296.

Carter D. P., 1984. A Non-Linear Soil Model for Predicting Lateral Pile Response. *Rep. No. 359, Civil Engineering Dept., Univ. of Auckland, New Zealand*.

Comodromos E. M., 2003. Response prediction for horizontally loaded pile groups. *Journal of the Southeast Asian Geotechnical Society*, **34**(2), pp. 123-133.

- Cox W. R., Reese L. C., and Grubbs B. R., 1974. Field Testing of Laterally Loaded Piles in Sand. *Proceedings of the Sixth Annual Offshore Technology Conference*, Houston, Texas, paper no. OTC 2079.
- Desai C. S., Sharma K. G., Wathugala G. W., and Rigby D. B., 1991. Implementation of hierarchical single surface δ_0 and δ_1 models in finite element procedure. *International Journal for Numerical & Analytical Methods in Geomechanics*, **15**(9), pp. 649-680.
- DNV, 1992. Foundations - Classification Notes No 30.4, Det Norske Veritas, Det Norske Veritas Classification A/S.
- Dobry R., Vincente E., O'Rourke M., and Roesset J., 1982. Stiffness and Damping of Single Piles. *Journal of geotechnical engineering*, **108**(3), pp. 439-458.
- Dunnivant T. W., and O'Neill M. W., 1985. Performance analysis and interpretation of a lateral load test of a 72-inch-diameter bored pile in overconsolidated clay. *Report UHCE 85-4*, Dept. of Civil Engineering, University of Houston, Texas, p. 57.
- Fan C. C., and Long J. H., 2005. Assessment of existing methods for predicting soil response of laterally loaded piles in sand. *Computers and Geotechnics* **32**, pp. 274-289.
- FLAC^{3D} 3.1 manual*, 2006. Fast Lagrangian Analysis of Continua in 3 Dimensions, Itasca Consulting Group Inc., Minneapolis, Minnesota, USA.
- Georgiadis M., 1983. Development of p - y curves for layered soils. *Proceedings of the Geotechnical Practice in Offshore Engineering*, ASCE, pp. 536-545.
- Hansen B. J., 1961. *The ultimate resistance of rigid piles against transversal forces*. Danish Geotechnical Institute, Bull. No. 12, Copenhagen, Denmark, 5-9.
- Harremoës P., Ovesen N. K., and Jacobsen H. M., 1984. *Lærebog i geoteknik 2*, 4. edition, 7. printing. Polyteknisk Forlag, Lyngby, Danmark.
- Hetenyi M., 1946. *Beams on Elastic Foundation*. Ann Arbor: The University of Michigan Press.
- Ibsen, L. B., Hanson, M., Hjort, T. H., Thaarup, M., 2009. MC-Parameter Calibration for Baskarp Sand No. 15. *DCE Technical Report No. 62*, Department of Civil Engineering, Aalborg University, Denmark.
- Ibsen L. B., Liingaard M., and Nielsen S. A., 2005. Bucket foundation, a status. *Proceedings of Copenhagen Offshore Wind*.

- Jacobsen M., and Gwizdala K., 1992. *Bearing Capacity and Settlements of Piles*. Centertrykkeriet, Aalborg University, Denmark.
- Karasev O. V., Talanov G. P., and Benda S. F., 1977. Investigation of the work of single situ-cast piles under different load combinations. *Journal of Soil Mechanics and Foundation Engineering*, translated from Russian, **14**(3), pp. 173-177.
- Karthigeyan S., Ramakrishna V. V. G. S. T., and Rajagopal K., May 2006. Influence of vertical load on the lateral response of piles in sand. *Computers and Geotechnics* **33**, pp. 121-131.
- Kellezi L., and Hansen P. B., 2003. Static and dynamic analysis of an off-shore mono-pile windmill foundation. *Proceedings of the BGA International Conference on Foundations: Innovations, observations, design and practice*, Dundee, UK, pp. 401-410.
- Kristensen L. K., and Pedersen T. S., 2007. Strength and deformation abilities of suction caissons subjected to cyclic loading. *Master thesis*, Department of Civil Engineering, Aalborg University, Denmark.
- Larsen K. A., 2008. Static Behaviour of Bucket Foundations. *DCE Thesis no. 7*, Department of Civil Engineering, Aalborg University, Denmark.
- LeBlanc C., Houlsby G. T., and Byrne B. W., 2007. Response of Stiff Piles to Long-term Cyclic Loading.
- Lesny K., and Wiemann J., 2006. Finite-Element-Modelling of Large Diameter Monopiles for Offshore Wind Energy Converters. *Geo Congress 2006, February 26 to March 1*, Atlanta, GA, USA.
- Lesny K., Paikowsky S. G., and Gurbuz A., 2007. Scale effects in lateral load response of large diameter monopiles. *GeoDenver 2007 February 18 to 21*, Denver, USA.
- Liingaard M., 2006. Dynamic Behaviour of Suction Caissons. *DCE Thesis no. 3*, Department of Civil Engineering, Aalborg University, Denmark.
- Ling L. F., 1988. Back Analysis of Lateral Load Test on Piles. *Rep. No. 460, Civil Engineering Dept., Univ. of Auckland, New Zealand*.
- Matlock H., and Reese L. C., 1960. Generalized Solutions for Laterally Loaded Piles. *Journal of the Soil Mechanics and Foundations Division*, **86**(5), pp. 63-91.
- Matlock H., 1970. Correlations for Design of Laterally Loaded Piles in Soft Clay. *Proceedings, Second Annual Offshore Technology Conference*, Houston, Texas, paper no. OTC 1204, pp. 577-594.

- McClelland B., and Focht J. A. Jr., 1958. Soil Modulus for Laterally Loaded Piles. *Transactions*. ASCE 123: pp. 1049-1086.
- Murchison J. M., and O'Neill M. W., 1984. Evaluation of p - y relationships in cohesionless soils. *Analysis and Design of Pile Foundations. Proceedings of a Symposium in conjunction with the ASCE National Convention*, pp. 174-191.
- Norris G. M., 1986. Theoretically based BEF laterally loaded pile analysis. *Proceedings, Third Int. Conf. on Numerical Methods in offshore piling*, Editions Technip, Paris, France, pp. 361-386.
- O'Neill M. W., and Dunnivant T. W., 1984. A study of effect of scale, velocity, and cyclic degradability on laterally loaded single piles in overconsolidated clay. *Report UHCE 84-7*, Dept. of Civ. Engrg., University of Houston, Texas, p. 368.
- Pasternak P. L., 1954. On a New Method of Analysis of an Elastic Foundation by Means of Two Foundation Constants, *Gosudarstvennoe Izdatelstvo Liberatuni po Stroitelstvui Arkhitekture*, Moskow, pp. 355-421.
- Peck R. B., Hanson W. E., and Thornburn T. H., 1953. *Foundation Engineering*, John Wiley and Sons, Inc. New York.
- Pender M. J., 1993. Aseismic Pile Foundation Design Analysis. *Bull. NZ Nat. Soc. Earthquake Engineering.*, **26**(1), pp. 49-160.
- Plaxis 2D Version 9.0, Brinkgreve R. B. J., Broere W., and Waterman D. (edt.), 2008. Material Models Manual.
- Plaxis 3D Foundation Version 2, Brinkgreve R. B. J., and Swolfs W. M. (edt.), 2007. Material Models.
- Plaxis 3D Foundation Version 2, Brinkgreve R. B. J., and Swolfs W. M. (edt.), 2007. Reference Manual.
- Plaxis 3D Foundation Version 2, Brinkgreve R. B. J., and Swolfs W. M. (edt.), 2007. Scientific Manual.
- Plaxis 3D Foundation Version 2, Brinkgreve R. B. J., and Swolfs W. M. (edt.), 2007. Tutorial Manual.
- Plaxis 3D Foundation Version 2, Brinkgreve R. B. J., and Swolfs W. M. (edt.), 2007. Validation Manual.
- Poulos H. G., 1971. Behavior of laterally loaded piles: I - Single piles. *Journal of the Soil Mechanics and Foundations Division*, **97**(5), pp. 711-731.

- Poulos H. G., and Davis E. H., 1980. *Pile foundation analysis and design*, John Wiley & Sons.
- Poulos H., and Hull T., 1989. The Role of Analytical Geomechanics in Foundation Engineering. in *Foundation Eng.: Current principles and Practices*, **2**, pp. 1578-1606.
- Reese L. C., and Matlock H., 1956. Non-dimensional Solutions for Laterally Loaded Piles with Soil Modulus Assumed Proportional to Depth. *Proceedings of the eighth Texas conference on soil mechanics and foundation engineering*. Special publication no. 29.
- Reese L. C., Cox W. R., and Koop, F. D., 1974. Analysis of Laterally Loaded Piles in Sand. *Proceedings of the Sixth Annual Offshore Technology Conference*, Houston, Texas, **2**, paper no. OTC 2080.
- Reese L. C., and Welch R. C., 1975. Lateral loading of deep foundation in stiff clay. *Journal of Geotechnic Engineering*, Div., **101**(7), pp. 633-649.
- Reese L. C., and Van Impe W. F., 2001. *Single Piles and Pile Groups Under Lateral Loading*, Taylor & Francis Group plc, London.
- Stevens J. B., and Audibert J. M. E., 1979. Re-examination of p-y curve formulation. *Proceedings Of the XI Annual Offshore Technology Conference*, Houston, Texas, OTC 3402, pp. 397-403.
- Terzaghi K., 1956. Evaluation of coefficients of subgrade reaction. *Geotechnique*, **5**(4), pp. 297-326.
- Timoshenko S. P., 1941. Strength of materials, part II, advanced theory and problems, 2nd edition, 10th printing. New York: D. Van Nostrand.
- United Nations, 1998. Kyoto protocol. *United Nations framework convention on climate change*.
- Ubilla J., Abdoun T., and Zimmie T., 2006. Application of in-flight robot in centrifuge modeling of laterally loaded stiff pile foundations. *Physical Modelling in Geotechnics*, Taylor & Francis Group, London, ISBN 0-41-41586-1, pp. 259-264.
- Vesic A. S., 1961. Beam on Elastic Subgrade and the Winkler's Hypothesis. *Proceedings of the 5th International Conference on Soil Mechanics and Foundation Engineering*, Paris, **1**, pp. 845-850.
- Winkler E., 1867. Die lehre von elasticzitat and festigkeit (on elasticity and fixity), Prague, 182 p.

Yang K., Liang R., 2006. Methods for Deriving p - y Curves from Instrumented Lateral Load Tests. *Geotechnical Testing Journal*, **30**(1), paper ID GTJ100317, pp. 31-38.

Zhang L., Silva F., and Grismala R., January 2005. Ultimate Lateral Resistance to Piles in Cohesionless Soils. *Journal of Geotechnical and Geoenvironmental Engineering*, **131**(1), pp. 78-83.

Appendices

- Appendix A: Test setup
- Appendix B: Soil preparation and derivation of soil parameters
- Appendix C: Material properties employed in the numerical analyses
- Appendix D: Winkler model approach
- Appendix E: *FLAC^{3D}*
- Appendix F: *Plaxis 3D Foundation*
- Appendix G: Mohr–Coulomb failure criterion
- Appendix H: Calibration of test piles
- Appendix I: Test 1: $D = 0.08$ m, $L = 0.4$ m, $P_0 = 0$ kPa
- Appendix J: Test 2: $D = 0.08$ m, $L = 0.4$ m, $P_0 = 100$ kPa
- Appendix K: Test 3: $D = 0.08$ m, $L = 0.4$ m, $P_0 = 50$ kPa
- Appendix L: Test 4: $D = 0.06$ m, $L = 0.3$ m, $P_0 = 0$ kPa
- Appendix M: Test 5: $D = 0.06$ m, $L = 0.3$ m, $P_0 = 50$ kPa
- Appendix N: Test 6: $D = 0.06$ m, $L = 0.3$ m, $P_0 = 100$ kPa
- Appendix O: Calibration of *FLAC^{3D}* to laboratory test results
- Appendix P: Evaluation of the Load-Displacement Relationships for Large-Diameter Piles in Sand

APPENDIX A

Test setup

This appendix gives an overview of the test setup used in the Laboratory of Geotechnical Engineering at Aalborg University. In appendix B the preparation of the soil, installation of the piles, and determination of material properties are described. The appendices, I–N, contains the test results.

A.1 Pressure tank

The objective of the tests is to investigate the effect of pile diameter on the soil response in sand for non-slender piles. Furthermore, the tests are conducted to calibrate numerical models by means of the commercial programs *Plaxis 3D Foundation* and *FLAC^{3D}*. Two instrumented aluminium pipe piles with outer diameters of 60 and 80 mm, respectively, are subjected to a horizontal load applied approximately 370 mm above soil surface. Both piles have a slenderness ratio, $L/D = 5$, and a wall thickness of 5 mm. The tests are carried out in the pressure tank shown in fig. A.1.

The pressure tank is manufactured by Bergla Maskinfabrik in Brønderslev, Denmark. The diameter and height of the pressure tank are approximately 2.1 m and 2.5 m, respectively. The pressure tank is installed in a load-frame resting on a reinforced foundation independent of the remaining floor in the laboratory. On top of the pressure tank a platform is constructed in order to make the access to the top of the pressure tank and hereby the preparation for the tests more comfortable. The pressure tank has trap doors, so the test setup can be prepared prior to the testing. One of the trap doors is indicated in fig. A.1. Furthermore, the tank contains openings, cf. fig. A.2,

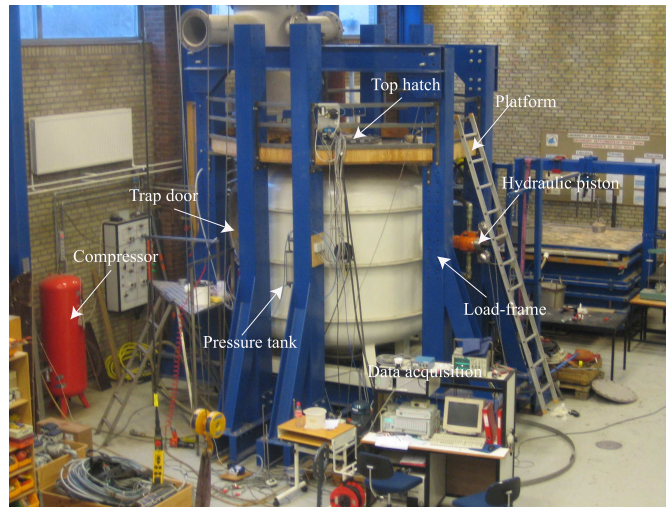


Figure A.1: Pressure tank installed in a load-frame.

where the measurement devices are lead out. At the top hatch, cf. fig. A.1, a hydraulic piston is mounted in order to install the test piles. The pressure tank contains 0.69 m of fully saturated sand. A highly permeable layer of gravel is located underneath the sand.



Figure A.2: Openings for the measurement devices.

The purpose of testing in the pressure tank is the possibility of increasing the effective stress level. Thereby more realistic soil parameters including the angle of internal friction are obtained. According to the Mohr–Coulomb failure criterion the failure is given by a straight line in the meridian plane. This is not the case at small stress levels, where the criteria overestimates the

angle of internal friction. This problem is minimised when working at higher stress levels. The pressure tank is approved for air pressures up to 2 bar corresponding to the effective vertical stresses at a depth of approximately 20 m. The test setup is shown in fig. A.3. The pile is actuated by a hydraulic piston, cf. fig. A.4, and by means of displacement transducers and a force transducer the load displacement relationship at three levels above soil surface is obtained.

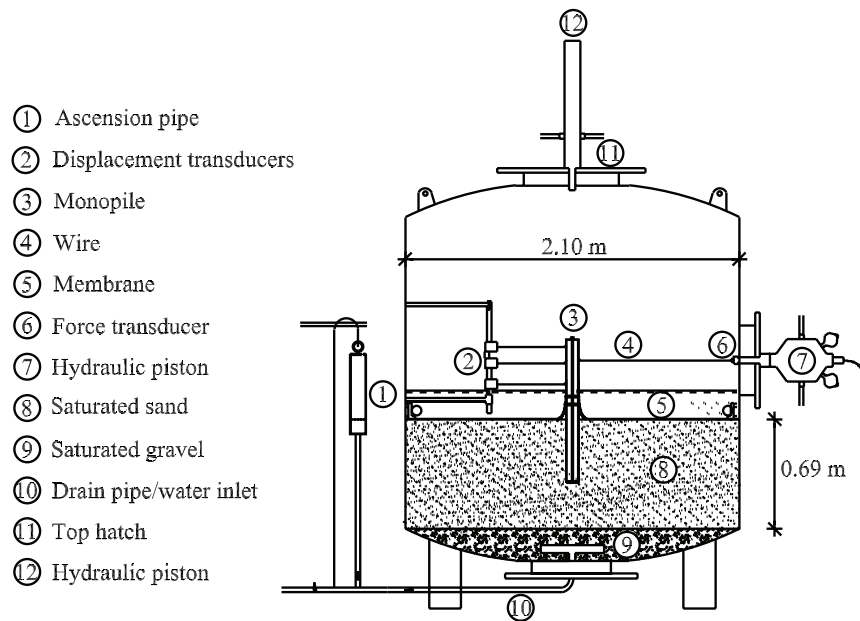


Figure A.3: Test setup.



Figure A.4: Hydraulic piston employed to actuate the test piles.

In order to obtain an increase in the effective vertical stresses corresponding to the applied air pressure a membrane is placed on the soil surface. The membrane, which prevents the air from inducing a higher pore pressure, is

shown in fig. A.5. The pile is lead through a sealing in the elastic membrane allowing the pile to be extended above the soil surface. At the outer perimeter of the membrane a vertical rubber band is attached to it. On the outside of this vertical rubber band two mouldings are attached, cf. fig. A.6. The purpose of these mouldings, is to make the joint between the membrane and the pressure tank more elastic in order to minimise small gaps due to imperfections of the pressure tank and membrane. The rubber band and mouldings are pressed against the tank wall by a coil as shown in A.6. The coil is made up from a fire hose and has the exact same diameter as the pressure tank. When inflated, the coil provides an equal pressure at the rubber band through the whole perimeter of the membrane.

Above the membrane approximately 16 cm of water is poured in. The dynamic viscosity of water is around 55 times higher than for air, which prevents or at least minimises the flow through potential gaps between the membrane and the pressure tank wall. During the tests a water volume of around 20-30 liter/hour passes through gaps between the membrane and the pressure tank. In addition to this the pore pressure in the soil will increase, due to volumetric strains when applying the overburden pressure. In order to maintain a hydrostatic pore pressure in the soil, corresponding to a water table at the soil surface, an ascension pipe outside the tank is connected as shown in fig. A.3 and fig. A.7. Through this, it is possible to control the pore pressure. If the water column in the ascension pipe increases, water is lead out of the tank through a drain in the bottom of the tank securing hydrostatic pore pressures. The water is lead out to the sewer.



(a) Membrane.

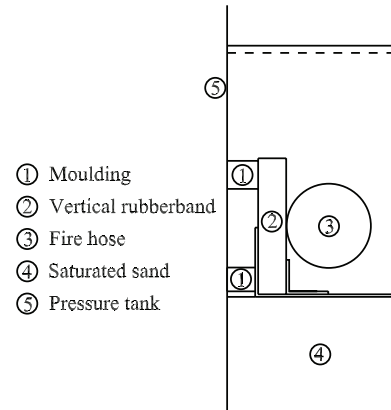


(b) Joint between tank wall and membrane.

Figure A.5: Membrane preventing the air pressure from inducing a excessive pore pressure. The membrane is pressed against the pressure tank wall by a fire hose under high pressure.



(a) Mouldings mounted on the outside of the membrane.



(b) Cross-section of the joint between the membrane and the pressure tank.

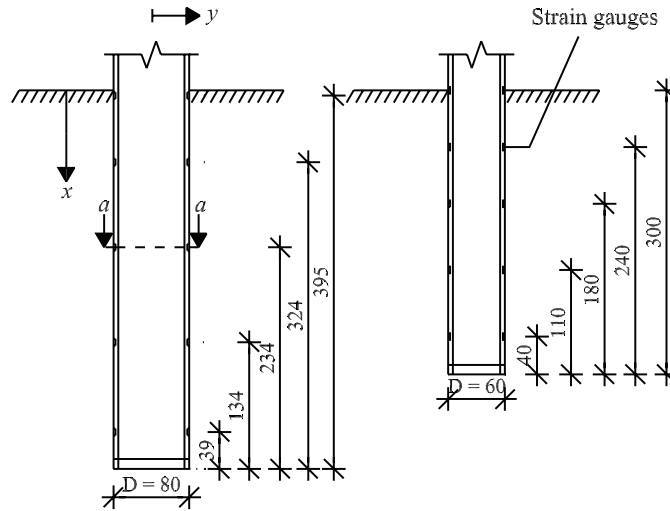
Figure A.6: Details of the joint between the membrane and the pressure tank wall.



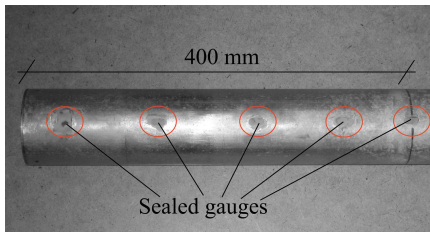
Figure A.7: Ascension pipe.

A.2 Measuring system

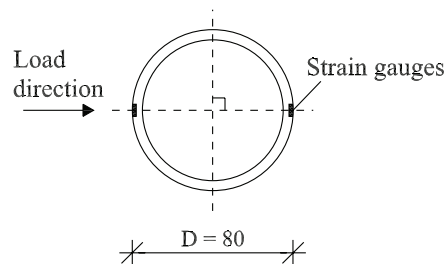
The piles employed in the tests are made from aluminium pipes with a wall thickness of 5 mm. The piles are instrumented with aluminium strain gauges from HBM of the type K-LY43-3/120 placed in five levels, as illustrated in fig. A.8a, for the two different pile diameters, respectively. The strain gauges are installed in milled grooves as shown in fig. A.8b and fig. A.8c. The gauges are sealed with a protective coating in order to protect them from water. The depth, width, and length of the mill outs are approximately 2, 6, and 10 mm, respectively at each gauge. The wiring for the gauges is drawn inside the piles. The piles are closed-ended in order to prevent from water inside the piles.



(a) Distance between strain gauges for the two different pile diameters.



(b) Sealed gauges for the pile with an outer diameter of 80 mm.



(c) Cross section at a measurement level.

Figure A.8: (a) Strain gauges installed at five different levels. (b) Picture of pile, $D = 80$ mm, with sealed strain gauges. (c) Section a-a. All five measurement levels are identical. Measures are in mm.

Each strain gauge is installed as a half bridge where the second active resis-

tance in the circuit is a gauge installed in a compensation box as illustrated in fig. A.9. The gauges are mounted with a mutual angle of 180° aligned in the plane of the horizontal load as shown in fig. A.8c. The strain gauges are mounted in the vertical direction implying that the curvature strains in the axial direction of the pile are measured.

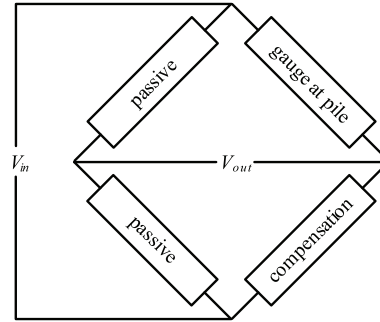


Figure A.9: Schematic strain gauge setup. V_{in} and V_{out} denotes the input and output voltage of the Wheatstone bridge, respectively.

The horizontal pile displacement is measured at three different levels, as illustrated in fig. A.3 and fig. A.11. The pile is pulled out by a hydraulic piston. A 4 mm wire rope consisting of seven strands laid connects the hydraulic piston to the pile. In order to measure the force acting on the pile a force transducer of the type HBM U2B 10 KN connects in series the hydraulic piston and the wire. Displacements are measured by wire transducers of the type WS10-1000-R1K-L10 from ASM GmbH.

The vertical displacement of the pile during the tests is also measured at the pile with an outer diameter of 60 mm. To measure the vertical displacement a wire transducer is attached to the side of the pile. Hereby, the rotation and the horizontal displacement of the pile will affect the measured vertical displacement as illustrated in fig. A.12. The effects of the rotation and horizontal displacement of the pile is deducted by use of the laws of trigonometry.

For specific details about the collection of data, see Kristensen and Pedersen (2007), where all details about the electronics and the data acquisition are specified.

A.3 Soil characteristics

The experiments are conducted on fully saturated Baskarp Sand No. 15, a graded sand from Sweden. A representative distribution of grain size determined from sieve analysis is shown in fig. A.13. The shape of the largest

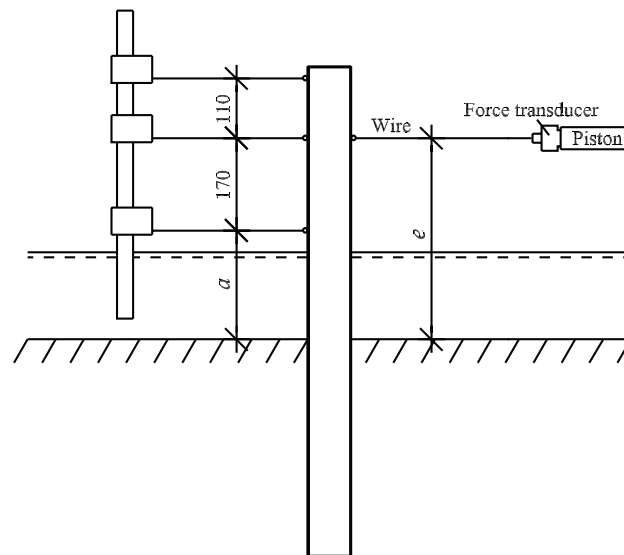


Figure A.10: Measurement of horizontal displacement at three different levels. The distance a is 205 and 200 mm for the pile with an outer diameter of 60 and 80 mm, respectively. e denotes the load eccentricity. Measures are in mm.



Figure A.11: The employed displacement transducers and force transducer.

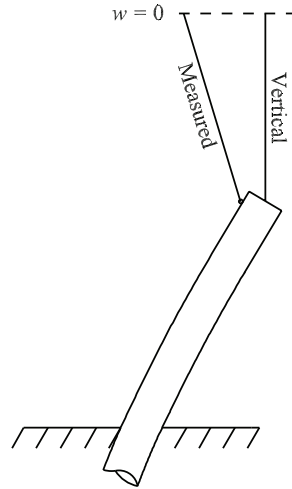


Figure A.12: Measuring of vertical displacement. $w = 0$ denote the level of the displacement transducer.

grains are round while the small grains have sharp edges. The main part of the sand is quartz, but it also contains feldspar and biotite. The properties of Baskarp Sand No. 15 are well-known due to previous laboratory tests at Aalborg University, cf. Larsen (2008). The properties are summarised in tab. A.1.

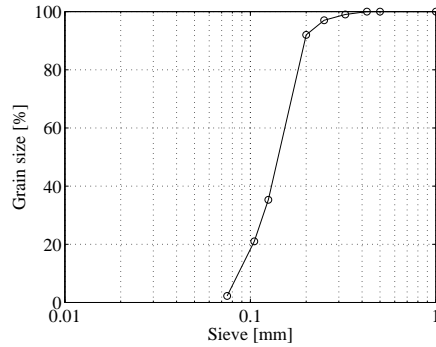


Figure A.13: Distribution of grains for Baskarp Sand no. 15, after Larsen (2008).

Table A.1: Material properties for Baskarp Sand No. 15, after Larsen (2008).

Specific grain density d_s	2.64
Maximum void ratio e_{\max}	0.858
Minimum void ratio e_{\min}	0.549
$d_{50} = 50\%$ - quantile	0.14 mm
$U = d_{60}/d_{10}$	1.78

A.4 Interpretation of strain gauge measurements

The piles are each instrumented with five pairs of strain gauges aligned in the plane of the horizontal load but at different levels of the piles, cf. fig. A.8a. At each time step the average strain, $\bar{\varepsilon}$, is computed for each pair of strain gauges:

$$\bar{\varepsilon} = \frac{\text{abs}(\varepsilon_1 - \varepsilon_2)}{2} \quad (\text{A.1})$$

where ε_1 and ε_2 are the single strain gauge measurement at the same level of the pile.

The curvature of the pile, κ , is determined by:

$$\sigma = \frac{M}{I_p} y \Leftrightarrow \quad (\text{A.2})$$

$$E_p \bar{\varepsilon} = \frac{M}{I_p} r^* \Leftrightarrow \quad (\text{A.3})$$

$$E_p \bar{\varepsilon} = \frac{E_p I_p \kappa}{I_p} r^* \Leftrightarrow \quad (\text{A.4})$$

$$\kappa = \frac{\bar{\varepsilon}}{r^*} \quad (\text{A.5})$$

where E_p is the Young's modulus of elasticity for the pile, I_p is the second moment of inertia, and r^* denotes the distance from the centre of the pile to the strain gauges.

The discrete values of κ are fitted by three different approaches. When fitting to the results from the five strain gauge levels along the pile a 4. order polynomial is used. By implementing the assumption that the curvature at the pile-toe is zero, a 5. order polynomial is fitted to the discrete values of curvature. The curvature above the soil surface will vary linearly from the curvature at the soil surface, κ_0 , to zero at the height of the hydraulic piston. Using this assumption and adding two extra curvature levels to the fit at the straight line, a 5. order polynomial is fitted to the eight levels. The extra points of curvature are shown in fig. A.14.

Based on the bending moment distribution with depth the p - y curves can be obtained by integrating and differentiating the distribution of moment along the length of the pile. The deflection of the pile wall, y , and the soil resistance, p , can be obtained by:

$$y(x) = \int \int \frac{M(x)}{E_p I_p} dx dx \quad (\text{A.6})$$

$$p(x) = \frac{d^2 M(x)}{dx^2} \quad (\text{A.7})$$

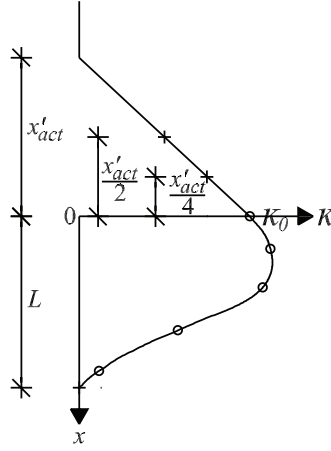


Figure A.14: Fitting of discrete values of curvature. (○) indicate levels where the curvature is calculated from strain gauge measurements. Points marked with (+) indicate levels where the curvature has been assumed. x'_{act} denotes the vertical distance from the strain gauge located near ground level to the height of the hydraulic piston.

where $E_p I_p$ denotes the pile bending stiffness.

Boundary conditions at the soil surface must be known in order to determine the integration constants, cf. (A.6). During the tests it is not possible to measure the rotation and deflection at the soil surface due to the water filled in above the membrane. However, by including the measured displacement at the height of the hydraulic piston, the displacement at the transducer above the hydraulic piston and the well-known curvature at the soil surface the boundary conditions are obtained.

Above the soil surface a linear distribution of moment and hereby curvature will occur between the height of the hydraulic piston and the soil surface. The curvature at the soil surface, κ_0 , is determined by the fitting procedure. Incorporating the lateral displacement and the rotation at the level of the hydraulic piston the boundary conditions at the soil surface are determined. The determination is as follows, where the applied variables are shown in fig. A.15:

$$\kappa = \frac{d^2 y(x^*)}{dx^{*2}} = \kappa_0 - \frac{\kappa_0}{x_{act}} x^* \Rightarrow \quad (\text{A.8})$$

$$\frac{dy(x^*)}{dx^*} = \kappa_0 x^* - \frac{\kappa_0}{2x_{act}} x^{*2} + C_1 \Rightarrow \quad (\text{A.9})$$

$$y(x^*) = \frac{\kappa_0}{2} x^{*2} - \frac{\kappa_0}{6x_{act}} x^{*3} + C_1 x^* + C_2 \quad (\text{A.10})$$

The constants C_1 and C_2 corresponding to $\frac{dy(0)}{dx^*}$ and $y(0)$ respectively can then be determined on the basis of the rotation, Θ , and displacement, u_1 , at $x^* = x_{act}$.

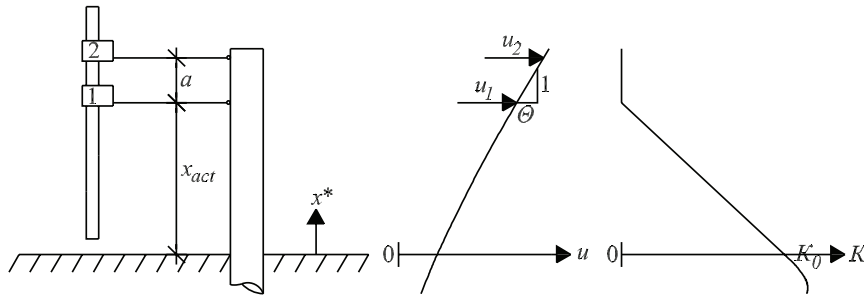


Figure A.15: Definitions to determine the boundary conditions at the soil surface.

When determining the soil resistance, p , the moment distribution is differentiated twice, cf. (A.6). However, according to Yang and Liang (2006) the measurement errors are amplified when differentiating, leading to an inaccurate distribution of p . They therefore suggest the use of the piecewise polynomial curve fitting method. When using this method five successive moment data points are fitted to a 3. order polynomial by using the least square method. The 3. order polynomial is then differentiated twice and the soil response, p , is evaluated at the centre point. The soil response for the upper and lower three points are obtained from 3. order polynomials fitted to the upper and lower five points, respectively. In fig. A.16 the piecewise polynomial fitting curve method is illustrated for the situation where three extra points of known curvature are assumed.

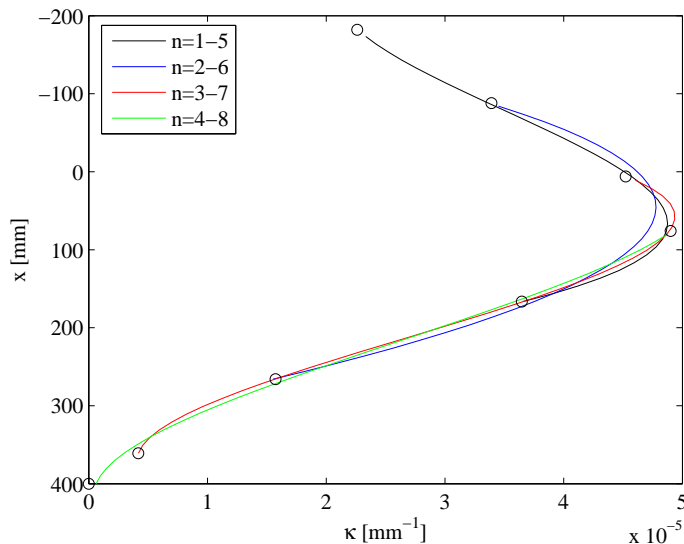


Figure A.16: Example of eight curvature points fitted by the piecewise polynomial curve fitting method. n denotes the point number starting from the top.

A.5 Calibration of test piles

In order to ensure a proper relation between the strain gauge output and bending moment distribution, calibrations of the test piles have been performed. The test setup for the calibrations is shown in fig. A.17. In order to eliminate effects of stress concentrations, load is applied at four different locations as shown in fig. A.18 and fig. A.19 for the two employed piles, respectively. At each location a load series consisting of seven load steps of 20 kg, from 0–120 kg are conducted. The piles are carefully orientated so that the loads are applied in the plane of the strain gauges. An example of the calibration results are shown in fig. A.20 for the pile with an outer diameter of 80 mm. The slope of a linear regression to the points shown in A.20 is multiplied with the distance from the centre of the pile to the strain gauge, r^* , where as the bending stiffness, $E_p I_p$, is obtained. Similar interpretations are made for each of the remaining four strain gauge levels, cf. appendix H. Due to the small strains obtained at strain gauge level 1, SG_1 , large uncertainties are introduced, why the results obtained at this level are omitted in the calculation of the total pile bending stiffness. By taking the average of the bending stiffness' obtained at each strain gauge level the bending stiffness of the pile is determined to $EI_{80,calibrated} = 52.4 \text{ kNm}^2$ with $\sigma_{80,calibrated} = 0.874$. Using the same calibration procedure for the pile with an outer diameter of 60 mm, the bending stiffness is determined to $EI_{60,calibrated} = 24.9 \text{ kNm}^2$ and $\sigma_{60,calibrated} = 0.585$. It is emphasized that Bernoulli–Euler beam theory is employed to describe the kinematic relations though an error is introduced due to the shear force distribution over the cross section.

A.6 Test programme

The test programme is designed to investigate the initial stiffness of the load-displacement relationships and its dependency on pile diameter. In order to reach a proper stress level the tests are conducted with varying overburden pressures, P_0 . The test programme and references to the succeeding appendices are shown in tab. A.2.

When conducting the tests, the soil is brought to failure, unloaded, and reloaded in order to get an estimate of the ultimate resistance and the amount of elastic behaviour in the soil. The displacement inputs applied are of varying magnitudes due to different overburden pressures, and pile diameters.



Figure A.17: Test setup for calibration of pile bending stiffness, $E_p I_p$.

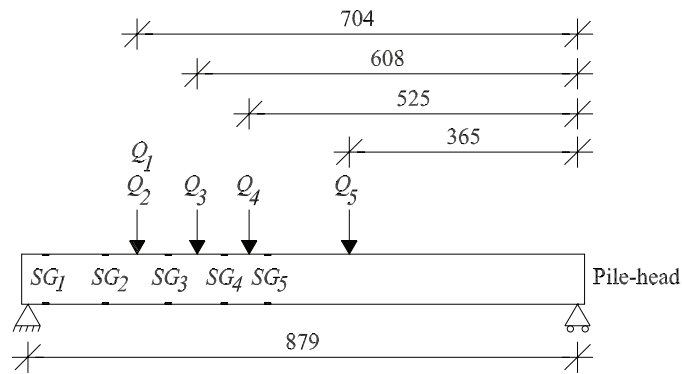


Figure A.18: Location of loads, Q_i , applied at pile with $D = 80$ mm. Measures are in mm.

Table A.2: Test programme.

	D [mm]	L/D	P_0 [kPa]	e [m]	Reference
Test 1	80	5	0	0.370	Appendix I
Test 2	80	5	100	0.370	Appendix J
Test 3	80	5	50	0.370	Appendix K
Test 4	60	5	0	0.375	Appendix L
Test 5	60	5	50	0.375	Appendix M
Test 6	60	5	100	0.375	Appendix N

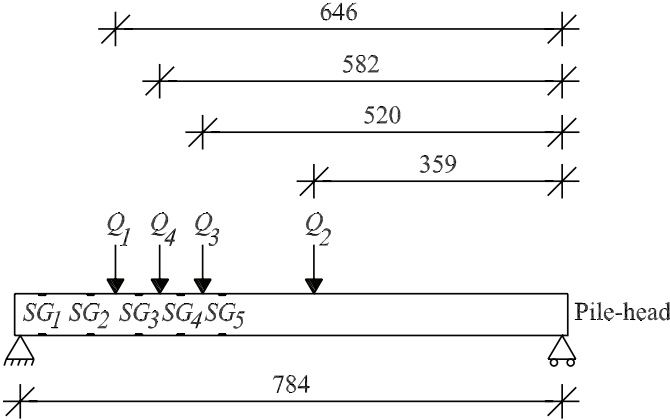


Figure A.19: Location of loads, Q_i , applied at pile with $D = 60$ mm. Measures are in mm.

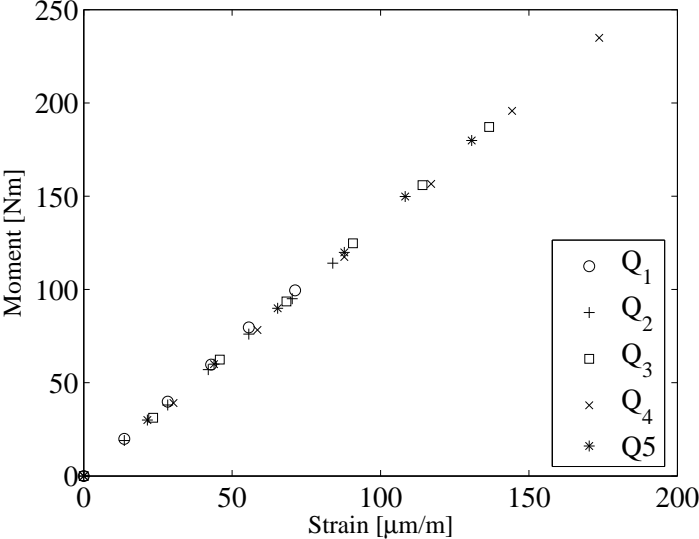


Figure A.20: Measured strain versus applied moment for pile with $D = 80$ mm at strain gauge level 5, SG_5 .

References

Kristensen L. K., and Pedersen T. S., 2007. Strength and deformation abilities of suction caissons subjected to cyclic loading. *Master thesis*, Department of Civil Engineering, Aalborg University, Denmark.

Yang K., Liang R., 2006. Methods for Deriving p - y Curves from Instrumented Lateral Load Tests. *Geotechnical Testing Journal*, **30**(1), paper ID GTJ100317, pp. 31-38.

Larsen K. A., 2008. Static Behaviour of Bucket Foundations. *DCE Thesis no. 7*, Department of Civil Engineering, Aalborg University, Denmark.

APPENDIX B

Soil preparation and derivation of soil parameters

Before conducting tests in the pressure tank the sand is prepared by mechanical vibration. The purpose of this preparation is to ensure that the sand is fully saturated, i.e. no air captions in the sand, and to ensure a homogeneous compaction of the material. The compaction is controlled by the conduction of cone penetration tests (CPT), which is also used to determine the material parameters of the sand. In the following the procedures for preparing the material, installation of the pile, and execution of CPT's are treated.

B.1 Pile installation

The piles are closed-ended with dimensions as given in appendix A. The piles are installed in one continuous motion by use of a hydraulic piston mounted on the top of the pressure tank, cf. fig. A.3. During installation an upward gradient of a magnitude of 0.9 is applied in order to minimize the pressure at the closed pile-end and to protect the strain gauges. In this way the toe resistance and the skin friction along the pile are minimised.

B.2 Preparation of soil

Overall the preparation of the soil is divided into four stages corresponding to the stage of the laboratory work:

- Preparation prior to all testing.

- Re-compaction of soil near the pile after installation.
- Re-compaction of the material between two tests without removing the pile.
- Re-compaction of the material between two tests after removing the pile.

In all four stages the sand is loosened up by use of an upward gradient and compacted by vibration. A gradient of magnitude 0.9 is employed as suggested by Kristensen and Pedersen (2007). A higher gradient might cause water channels to be formed. With a sand depth of 0.69 m, cf. fig. A.3, this corresponds to a pressure difference in pressure head of 0.63 m. To ensure homogeneous vibration a plate as shown in fig. B.1 with holes fitting the mechanical vibrator is placed above the soil surface.

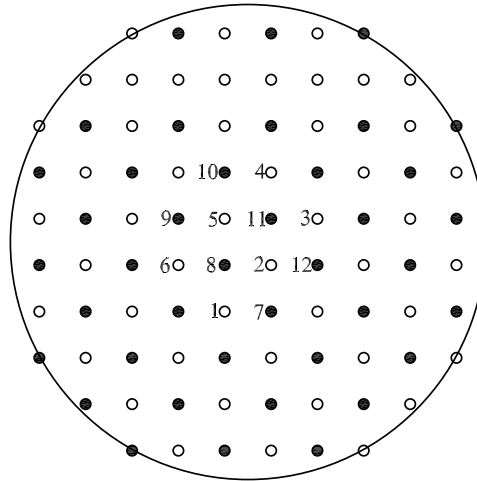


Figure B.1: Plate with holes to ensure a homogeneous vibration. The solid circles (●) indicate the holes vibrated first and the non-solid circles (○) indicate the holes vibrated secondly. The numbers indicate the holes used for extra vibration after pile installation and between each tests.

The general procedure for preparation of the sand is as follows: After Kristensen and Pedersen (2007).

- The soil is loosened up by an upward gradient for at least 5 minutes.
- Vibration in the solid circles (●), cf. fig. B.1.
- Vibration in the non-solid circles (○), cf. fig. B.1.
- The soil is loosened up again by an upward gradient for at least 5 minutes.

- Vibration in the solid circles (\bullet), cf. fig. B.1.
- Vibration in the non-solid circles (\circ), cf. fig. B.1.

This general six-point procedure is used, in some cases with small modifications, at each of the four preparation stages. During the vibration of the sand the water surface should be situated at least 5 cm above the soil surface, in order to prevent air coming into the soil.

B.2.1 Preparation prior to all testing

When initiating the laboratory work the sand in the pressure tank had been dry for several months. An extensive vibration, to free the air captured in the sand and to eliminate effects from previous test setups, have therefore been needed before any tests were carried out. After each run of the six-point procedure at this stage, CPT's have been carried out to verify the compaction. After this, the sand had reached the desired compaction and homogeneity and was ready for installation of a pile. The test results from the CPT's prior to installation of a pile have been employed as references. Hereby, the soil conditions before each test, cf. appendices I–N, has the desired compaction and homogeneity.

B.2.2 Re-compaction of soil near the pile after installation

After installation of a pile a mechanical vibration of the sand in the 12 holes nearest the pile is performed in a pattern as shown in fig. B.1. This extra vibration serves to minimise the effects from the failure created in the soil when installing the pile. In this way the coefficient of horizontal earth pressure, and the compaction of the grains near the pile are all as close as possible to the parameters for the rest of the soil in the pressure tank. In order to prevent the pile from deforming from its upright position when vibrating, it is fixed by the same hydraulic piston, cf. $\textcircled{2}$ in fig. A.3, as used for installation of the pile. After this extra vibration the soil is compacted after the general six-point procedure and CPT's are conducted to verify the compaction. A total of six CPT's are carried out at this stage, cf. fig. B.2. Four with a distance of 0.5 m from the centre of the pile and two at the neutral sides of the pile in relation to the direction of pile actuation. The two CPT's on the neutral sides are conducted with a distance of 0.16 m from the centre of the pile.

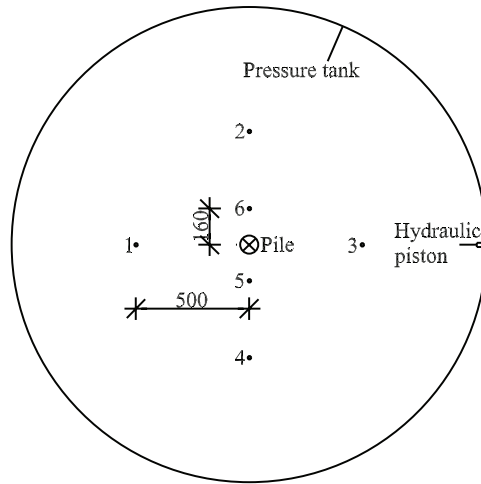


Figure B.2: Location of the CPT's conducted in the tank prior to each test. Measures are in mm.

B.2.3 Re-compaction of the material between two tests

After running a pile test the soil must be re-compacted. If the same pile is to be used in the following test the pile is brought back to its upright position and fixed by the hydraulic piston while the soil is compacted. The procedure for compaction at this stage is first a vibration in the 12 holes near the pile as shown in fig. B.1, followed by the general six-point procedure. Once again CPT's, cf. fig. B.2, are conducted to verify the compaction. On the contrary, when a new pile with another diameter is to be installed the compaction of the soil is started over again as described in section B.2.1.

B.3 Cone penetration tests

The CPT equipment used in the laboratory is shown in fig. B.3. The dimensions of the cone is given in fig. B.4. As shown, the tip resistance is measured by strain gauges installed in a full bridge and attached to a steel pipe behind the cone head. In order to measure the total resistance, given as the sum of the tip resistance and the friction on the sides of the cone, three additional weight cells are installed in the opposite end of the CPT-probe. As the sidefriction is negligible in the cohesionless sand these weight cells are not employed in this project.

The hydraulic piston at the top of the pressure tank, cf. ⑫ in fig. A.3, is used for pressing the CPT into the soil. The test setup is shown in fig. B.5. The penetration velocity is approximately 5 mm/s.



Figure B.3: Laboratory CPT.

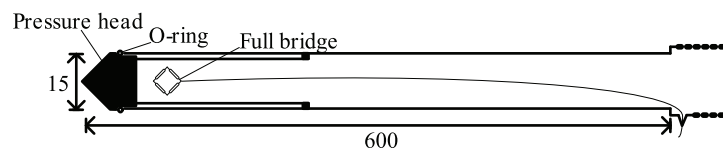


Figure B.4: Sectional view of the CPT-cone. Measures are in mm.



Figure B.5: CPT-setup.

Prior to testing, the strain gauges in the pressure head are calibrated by applying known loads as shown in fig. B.6. The maximum load applied in the calibration is 120 kg. This is partly due to the size of yoke and weights and partly to protect the CPT from failure caused by instability of the setup. The gauge output is linear as shown in fig. B.7.



Figure B.6: Setup for CPT-calibration.

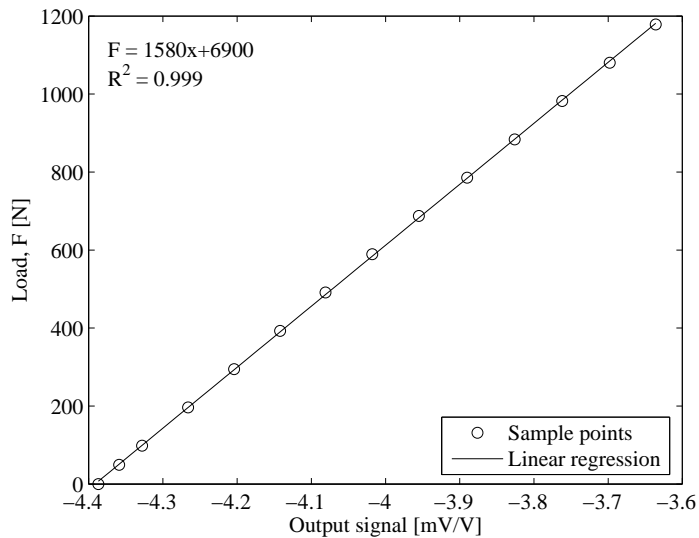


Figure B.7: Example of calibration output.

B.4 Interpretation of CPT's

The objective of conducting CPT's is partly to verify a homogeneous compaction of the soil and partly to determine the material properties of the soil. Control of a homogeneous compaction is made by graphic interpretation of the tip resistance, q_c , plotted against the depth, x . Determination of the angle of internal friction, φ_{tr} , is however more complicated. Ibsen et al. (2009) investigated the relation between φ_{tr} , I_D , and σ'_3 for Baskarp sand No. 15 and found (B.1) to be applicable. Equation (B.1) is based on the linear regression shown in fig. B.8 displaying the results of triaxial tests conducted at stress levels varying from $\sigma'_3=5-800$ kPa where σ_3 denotes the minor principal stress. In the formula the relative density, I_D , is given in percent.

$$\varphi_{tr} = 0.152I_D + 27.39\sigma'_3^{-0.2807} + 23.21[^\circ] \quad (\text{B.1})$$

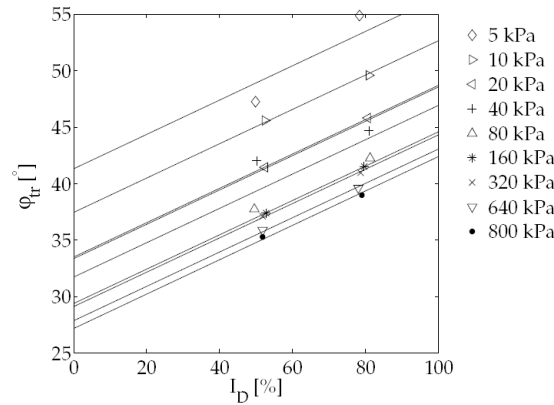


Figure B.8: Results of triaxial tests conducted on Baskarp Sand No. 15. The numbers in the legend corresponds to the σ'_3 stress level, after Ibsen et al. (2009).

To determine I_D an iteration is introduced using the following equations:

$$\gamma' = \frac{d_s - 1}{1 + e_{in\ situ}} \gamma_w \quad (\text{B.2})$$

$$\sigma'_1 = \gamma' x \quad (\text{B.3})$$

$$I_D = c_2 \left(\frac{\sigma'_1}{(q_c)^{c_1}} \right)^{c_3} \quad (\text{B.4})$$

$$I_D = \frac{e_{max} - e_{in\ situ}}{e_{max} - e_{min}} \quad (\text{B.5})$$

where $e_{in\ situ}$ is the in situ void ratio, $\gamma_w = 10.0 \text{ kN/m}^3$ is the unit weight of water, σ'_1 is the effective vertical stress, and q_c is the measured cone head resistance. The fitting constants are $c_1 = 0.75$, $c_2 = 0.0514$, and $c_3 = -0.42$. The remaining soil parameters are given in tab. A.1. It should be noticed that (B.4) is a function fitted by Ibsen et al. (2009) to Baskarp Sand No. 15 and the employed CPT-probe.

To begin the iteration procedure a void ratio of e_{min} is assumed. With use of (B.2)–(B.5) a new value of $e_{in\ situ}$ is calculated. Convergence is assumed reached when the difference between two successive values of $e_{in\ situ}$ is less than 10^{-4} .

The minor principal stress σ'_3 is dependent on the coefficient of horizontal earth pressure at rest, K_0 . However, K_0 can be expressed in terms of σ'_1 and φ_{tr} implying the only unknown in (B.1) is φ_{tr} , which is determined by iteration.

It is seen from (B.1) that $\varphi_{tr} \rightarrow \infty$ for $\sigma'_3 \rightarrow 0$. Furthermore, it is seen from fig. B.8 that the (B.1) does not fit the triaxial tests very well for $\sigma'_3 = 5.0 \text{ kPa}$. When conducting CPT's the CPT-cone only reaches a depth of 0.35–0.55 m. This leads to stress levels in the σ'_3 direction varying from 0.0 kPa to approximately 2.5 kPa for the tests at atmospheric pressure which, according to the lowest applied horizontal stress in the triaxial test, is below the range of the formula. Therefore, when determining φ_{tr} for the sand at atmospheric pressure a lower bound of 5.0 kPa on the stress level is applied. This may lead to a lower value of φ_{tr} than the real value. The effect of this is however considered acceptable. When the sand is subjected to an additional pressure at the surface the effective stresses will increase. In these cases the actual stress level is used in the calculation of φ_{tr} .

Inserting I_D in percent, the dilatancy angle, ψ_{tr} , can likewise be determined by:

$$\psi_{tr} = 0.195I_D + 14.86\sigma'_3{}^{-0.09764} - 9.946[^\circ] \quad (\text{B.6})$$

For determining the initial stiffness of the soil, the tangential Young's modulus of elasticity is employed. E_0 is derived on the basis of the relative density, I_D . The following relations are employed for determining E_0 .

$$E_{50} = (0.6322 \cdot I_D^{2.507} + 10920) \left(\frac{c \cdot \cos(\varphi_{tr}) + \sigma'_3 \cdot \sin(\varphi_{tr})}{c \cdot \cos(\varphi_{tr}) + \sigma_3^{ref} \cdot \sin(\varphi_{tr})} \right)^{0.58} \quad (\text{B.7})$$

$$E_0 = \frac{2E_{50}}{2 - R_f} \quad (\text{B.8})$$

The outcome of (B.7) is given in kPa and is according to Ibsen et al. (2009) derived for Baskarp sand nr. 15, while (B.8) is the relation between the tangential stiffness and E_{50} employed in Plaxis 2D (2008). The parameter R_f is the ratio between q_f and q_a , denoting the ultimate deviatoric stress and the asymptotic value of the shear strength, respectively. The standard value $R_f = 0.9$ as given in *Plaxis 2D* is employed in the present derivation of E_0 . The derived soil parameters are given in tab. B.1 for the six tests. The results for E_0 for the tests without overburden pressure are neglected as the uncertainties of the employed formulas are high at this stress level.

Table B.1: Material properties calculated for the six tests.

	P_0 [kPa]	φ_{tr} [°]	ψ_{tr} [°]	I_D [-]	γ [kN/m ³]	E_0 [MPa]
Test 1	0	52.6	18.1	0.79	10.2	-
Test 2	100	45.9	16.2	0.79	10.2	41.1
Test 3	50	48.5	16.9	0.79	10.2	25.4
Test 4	0	52.2	17.5	0.76	10.1	-
Test 5	50	48.3	16.7	0.78	10.1	24.9
Test 6	100	45.1	15.3	0.75	10.1	37.4

References

Plaxis 2D Version 9.0, Brinkgreve R. B. J., Broere W., and Waterman D. (edt.), 2008. Material Models Manual.

Ibsen, L. B., Hanson, M., Hjort, T. H., Thaarup, M., 2009. MC-Parameter Calibration for Baskarp Sand No. 15. *DCE Technical Report No. 62*, Department of Civil Engineering, Aalborg University, Denmark.

Kristensen L. K., and Pedersen T. S., 2007. Strength and deformation abilities of suction caissons subjected to cyclic loading. *Master thesis*, Department of Civil Engineering, Aalborg University, Denmark.

APPENDIX C

Material properties employed in the numerical analyses

The test programme and material properties for the soil and piles are given in tab. C.1. For the tests without overburden pressures Young's modulus of elasticity of the soil is calibrated by means of the numerical models as the low horizontal stresses leads to large uncertainties. For all analyses the Poisson's ratio is $\nu_p = 0.33$ and $\nu_s = 0.23$, for the piles and soil, respectively. In *FLAC^{3D}* the interface shear stiffness and interface normal stiffness is set to $k_s = k_n = 100E_0$.

Table C.1: Test programme and material properties for the six tests. The listed material properties are employed in the numerical validation of the test results.

	Diameter	Overburden pressure	Angle of internal friction	Dilatancy angle
	D [m]	P_0 [kPa]	φ_{tr} [°]	ψ [°]
Test 1	0.8	0	52.6	10
Test 2	0.8	100	45.9	10
Test 3	0.8	50	48.5	10
Test 4	0.6	0	52.2	10
Test 5	0.6	50	48.3	10
Test 6	0.6	100	45.1	10
Cohesion	Relative density	Unit weight	Young's modulus of elasticity	Pile bending stiffness
c [kPa]	I_D [—]	γ' [kN/m ³]	E_0 [MPa]	$E_p I_p$ [kNm ²]
0.1	0.79	10.2	-	52.4
0.1	0.79	10.2	41.1	52.4
0.1	0.79	10.2	25.4	52.4
0.1	0.76	10.1	-	24.9
0.1	0.78	10.1	24.9	24.9
0.1	0.75	10.1	37.4	24.9

APPENDIX D

Winkler model approach

The Winkler model approach in which the pile is modelled as a beam on an elastic foundation is a widely used method incorporated in the design regulations, e.g. API (1993), and DNV (1992). The soil response and hereby the elastic foundation is represented by non-linear springs described by means of p - y curves. In order to calculate the pile deformation for piles exposed to lateral loading according to the p - y curve method a Winkler model has been produced. The p - y curves for sand presented in the design regulations, e.g. API (1993) and DNV (1992), are implemented in the model. Furthermore, it is possible to incorporate alternative models, e.g. the upper bound solution for the ultimate soil resistance, cf. Jacobsen and Gwizdala (1992), and the ultimate soil resistance according to Hansen (1961).

The Winkler model is made up in the program *MATLAB version 7.0* with use of the finite element toolbox *CALFEM version 3.4*, described in Austrell et al. (2004). *CALFEM* contains routines for several types of elements including beam elements. For the beam elements both traditionally Bernoulli-Euler and Timoshenko beam theory can be employed. The *Calfem* routines for calculating element stiffness matrices, global stiffness matrices, and for solving the set of equations, $\underline{Ka} = \underline{f}$, is used in the conducted model.

Systems with linear-elastic beam elements can be solved with use of *CALFEM*. However, as the p - y curves are non-linear an iterative procedure are incorporated in the model. The model is able to calculate the pile behaviour from both a prescribed deflection and an applied force. In order to compare pile deflections from the p - y curve method with the laboratory tests in the pressure tank the model is able to take the effect of overburden pressure into account.

D.1 Element geometry

The pile is modelled by means of 2-noded beam elements with three degrees of freedom at each node as illustrated in fig. D.1. The length of the beam elements are identical along the pile. In order to model the supporting soil along the pile, horizontal beam elements are employed. The joints between the pile and the supporting beam elements are made as hinges. Hence, no bending moments can be transferred and the supporting beam elements simulate the soil resistance according to the Winkler model approach, as only lateral resistance is transferred. The geometry is shown in fig. D.2.

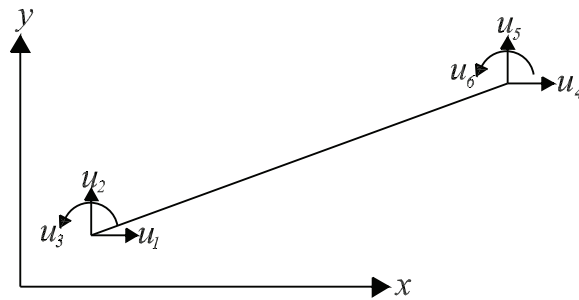


Figure D.1: 2-noded beam element with 3 degrees of freedom at each node, 2 translational and 1 rotational, respectively. u_1 – u_6 indicate the degrees of freedom. (x, y) specifies the global coordinate system.

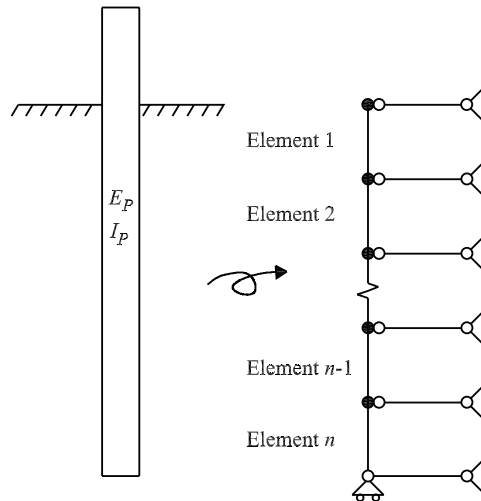


Figure D.2: Winkler model approach. The element geometry for a monopile divided into n elements with equal length is shown at the right. The circles specifies the nodes. A dot indicate that bending moment can be transferred and a circle indicate a hinge. E_p and I_p denotes the Young's modulus of elasticity and the second moment of inertia of the pile, respectively.

When approximating the stiffness of the elastic foundation, a distribution

of soil resistance as indicated by the hatched area, cf. fig. D.3, is assumed. Hereby, the stiffness is constant through out two times half the element height. This assumption is not correct as soil resistance varies nonlinearly with depth. Furthermore, the approximation of soil resistance is highly inaccurate for the element at the soil surface and at the element at the bottom of the pile. However, these errors approach zero for increasing number of elements.

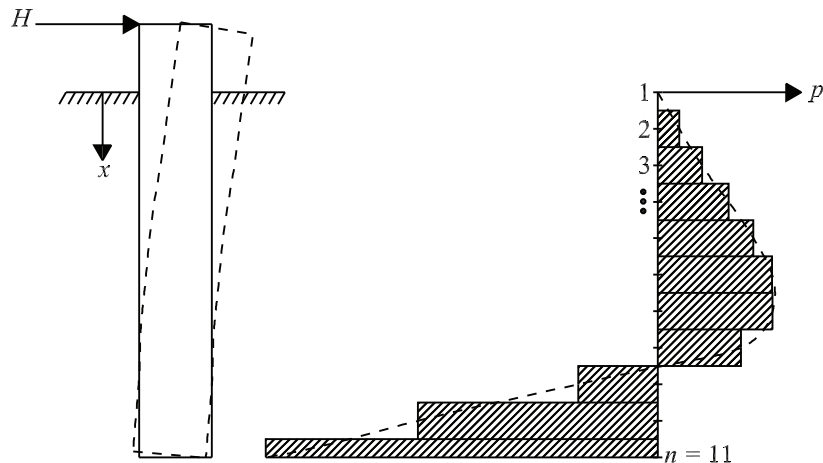


Figure D.3: The hatched area at the right is the assumed soil resistance when determining the stiffness of the elastic foundations for a monopile subjected to a lateral load, H . The soil resistance calculated by means of p - y curves are illustrated by the dashed line. In the illustration the numbers specify the node number. The pile is divided into a total number of ten elements corresponding to $n = 11$ nodes.

D.2 Iterative procedures for solving the non-linear set of equations

In the laboratory tests the horizontal load is applied as a prescribed displacement. However, when designing wind turbine foundations an estimated force is applied. It is therefore desirable to be able to switch between prescribed displacements and applied forces. To account for the non-linearity of the p - y curves an iterative procedure is therefore needed to determine the correct spring stiffness for the elastic foundations. Different iteration procedures are employed for the two methods for analysing the pile behaviour. For the displacement controlled solution a prescribed displacement Δy can be applied with the eccentricity e . However, horizontal load and bending moment respectively, are applied at the soil surface for the force controlled solution, cf. fig. D.4.

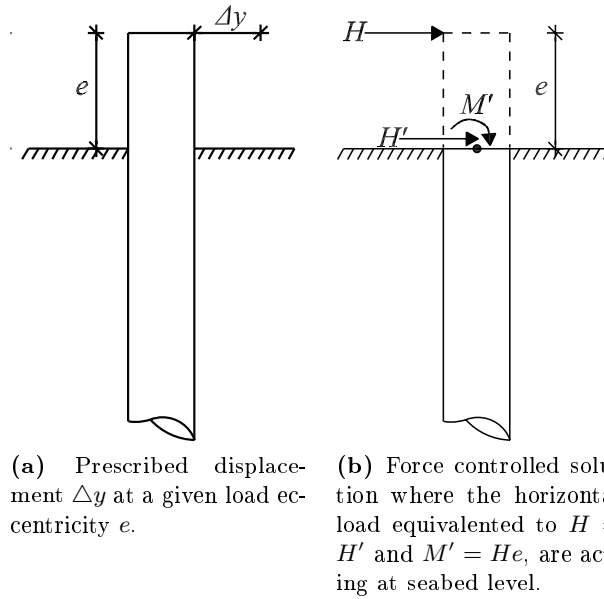


Figure D.4: The two approaches employed in the Winkler models.

D.2.1 Force controlled approach

In the force controlled approach the Newton-Raphson algorithm is employed as iteration procedure. The tangential stiffness of the p - y curves, $\frac{dp}{dy}$, is used to calculate the stiffness of the elastic foundations. After each iteration the soil response corresponding to the estimated pile deflection is calculated. Hereby, the residual, r_i , of the lateral force and bending moment can be calculated from the equations of equilibrium. New estimates of the pile deflection are conducted until the residual is lower than 0.001 ‰ of both the applied horizontal load and bending moment. The iteration procedure is illustrated in fig. D.5.

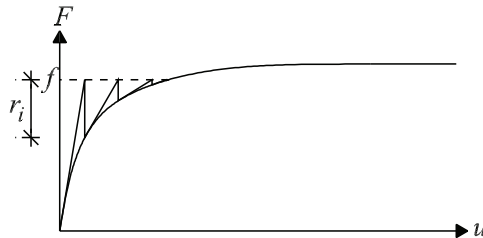


Figure D.5: Iteration procedure for the force controlled approach. F denotes the applied load and r_i is the residual at iteration step i .

D.2.2 Displacement controlled approach

In the displacement controlled approach the subgrade reaction modulus, E_{py} , is used to estimate the pile deflection. The first estimate of the pile deformation is made with spring stiffness' corresponding to the initial stiffness of the p - y curves, E_{py}^* . From the estimated pile deformation new values of E_{py} are calculated by use of p - y curves. The determined values of E_{py} are employed as spring stiffness' and hereby, a new estimate of the lateral pile deflection is obtained. This procedure is repeated until the difference between two estimates of the pile deflection for all nodes is less than 0.001 % of the prescribed displacement.

D.3 Overburden pressure

According to Georgiadis (1983) the effect of multiple soil layers can be incorporated in the Winkler model approach by introducing an equivalent system with a fictive depth x' . The equivalent system proposed by Georgiadis (1983) is employed to describe the effect of the overburden pressures, P_0 , applied at the laboratory tests, cf. appendix A. The two equivalent systems are illustrated in fig. D.6.

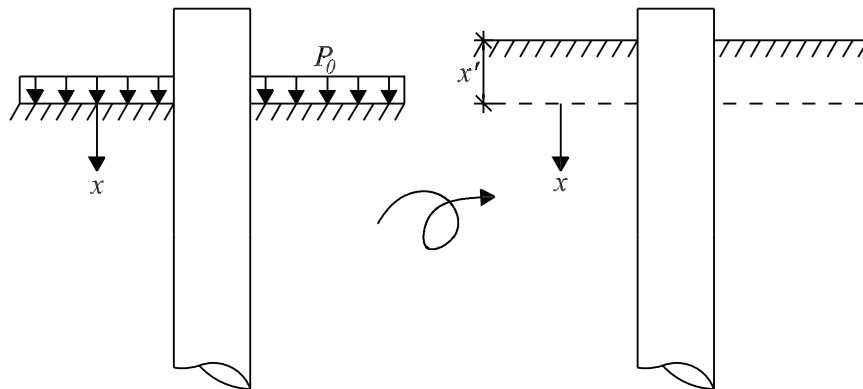


Figure D.6: The system with overburden pressure, P_0 , at the left and the equivalent system as proposed by Georgiadis (1983) at the right.

In order to estimate the soil resistance correctly for the two equivalent systems both the initial stiffness, E_{py}^* , and the ultimate soil resistance, p_u , needs to be equivalent. The fictive depth for the equivalent system to the system with overburden pressure is calculated by requiring similar ultimate resistances at soil surface for the two systems. As the ultimate resistance is compared at the soil surface the ultimate soil resistances at shallow depth are considered. This assumption leads to the following relation in which x'

can be determined:

$$p_{us}^p = p_{us}^{x'} \Rightarrow C_2DP_0 = (C_1x' + C_2D)\gamma'x' \quad (\text{D.1})$$

p_{us}^p and $p_{us}^{x'}$ indicates the ultimate soil resistance for the system with overburden pressure and the equivalent system, respectively. C_1 and C_2 are constants, cf. API (1993), D is the pile diameter and γ' is the effective unit weight. When determining the fictive depth from (D.1) no attention is attached to the equivalence of effective stresses. It should be noticed that the method proposed by Georgiadis (1983) is developed for layered soils. Furthermore, Georgiadis (1983) equivalences the ultimate soil resistance integrated with depth for the equivalent systems, which is in contrast to the employed method where the ultimate resistance at the soil surface is equivalented.

The ultimate soil resistance at the depth x can be approximated by insertion of $x + x'$ in the formula for the ultimate resistance recommended by API (1993):

$$p_u = \min \left(\begin{array}{l} p_{us} = (C_1(x + x') + C_2D)\gamma'(x + x') \\ p_{ud} = C_3D\gamma'(x + x') \end{array} \right) \quad (\text{D.2})$$

According to API (1993) the p - y curve for piles in sand is given by:

$$p(y) = Ap_u \tanh \left(\frac{k(x + x')}{Ap_u} y \right) \quad (\text{D.3})$$

The factor A is a factor accounting for cyclic or static loading conditions and y is the lateral pile deflection. The initial stiffness of the p - y curves, E_{py}^* , is estimated as:

$$E_{py}^* = k(x + x') \quad (\text{D.4})$$

where k is the initial modulus of subgrade reaction.

When applying overburden pressure in the pressure tank, the pile will, above the membrane, be subjected to an equally pressure at the circumference of the pile. Due to the stiffness of the pile material, this will not affect the soil-pile interaction. In contrast, the axial pressure component at the pile-head acts as an added mass to the pile-head which leads to an increase in effective stresses in the area close to the pile. The effect of the added mass is not incorporated in the p - y -curves recommended by API (1993). Due to this the effect of the added mass at the pile-head is not incorporated in the constructed Winkler model.

D.4 Convergence analysis

In order to find an appropriate number of nodes in the model a convergence analysis of the displacement controlled approach has been performed. The input listed in tab. D.1 is employed and the results are shown in fig. D.7. A number of 100 nodes along the pile are chosen as an appropriate number of nodes, given that the normalised error, cf. (D.5), for both the horizontal load, the pile-head deflection, and the pile-toe deflection, is less than 2×10^{-4} and the calculation time is reasonable. As shown the model converges at a small amounts of elements. When calculating the normalised error a number of $n = 320$ nodes is chosen as a reference value. The same number of elements are employed when considering the force controlled approach.

$$\text{normalised error} = \frac{\text{abs}(\text{value}_{320} - \text{value}_n)}{\text{value}_{320}} \quad (\text{D.5})$$

Table D.1: Input parameters for convergence analysis and comparison of Bernoulli-Euler and Timoshenko beam theory.

Outer pile diameter D	4.0 m
Embedded pile length L	20 m
Wall thickness t	0.05 m
Young's modulus of elasticity E_p	210 GPa
Poissons ratio ν_p	0.3
Angle of internal friction φ_{tr}	44°
Initial modulus of subgrade reaction k	40000 kN/m ³
Load eccentricity e	30 m
Prescribed displacement Δy	0.4 m

D.5 Choice of beam theory

In this section results obtained from Bernoulli-Euler and Timoshenko beam theory are compared. The comparison is made up for a displacement controlled large-diameter monopile with input parameters as listed in tab. D.1. The lateral pile deflection behaviour is shown in fig. D.8a for both Bernoulli-Euler and Timoshenko beam theory. The absolute difference between the two beam theories are shown in fig. D.8b. The maximum absolute difference between the two beam theories is found to be approximately 0.7 mm and is hereby small compared to the prescribed deflection (400 mm). However, it should be emphasised that the pile deflection consists of both a rotation as a rigid object and pile deformation due to bending moments. The relative difference for the two beam theories would therefore be larger for a

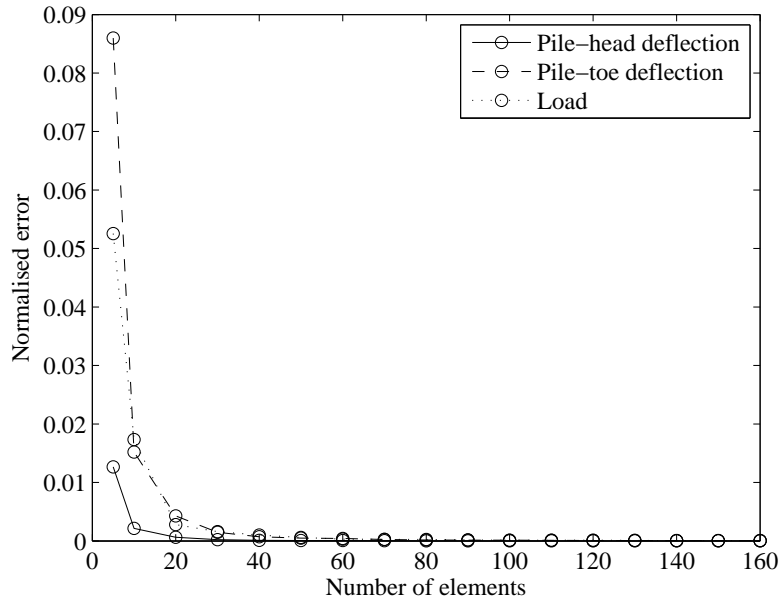
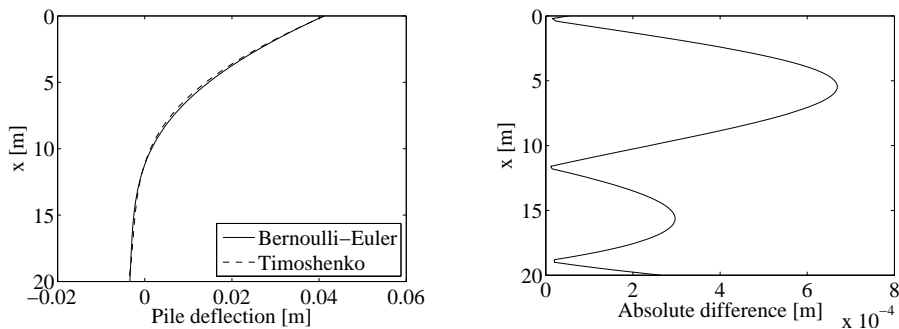


Figure D.7: Convergence analysis of the displacement controlled model. The input parameters are as listed in tab. D.1.

fixed beam with the same properties. Due to the small difference between Bernoulli-Euler and Timoshenko theory it is chosen to use Bernoulli-Euler beam theory in the calculations.



(a) Lateral pile deflection with depth.

(b) Absolute difference between the pile deflection calculated from Bernoulli-Euler and Timoshenko theory.

Figure D.8: Comparison of Bernoulli-Euler and Timoshenko beam theory. The input parameters are as listed in tab. D.1.

References

API, 1993. Recommended practice for planning, designing, and constructing fixed offshore platforms - Working stress design, *API RP2A-WSD*, American Petroleum Institute, Washington, D.C., 21. edition.

Austrell P. E., Dahlblom O., Lindemann J., Olsson A., Olsson K. G., Persson K., Petersson H., Ristinmaa M., Sandberg G., and Wernberg P. A, 2004. *CALFEM - A Finite Element Toolbox - Version 3.4*, Structural Mechanics, LTH, Sweden. ISBN: 91-8855823-1.

DNV, 1992. Foundations - Classification Notes No 30.4, Det Norske Veritas, Det Norske Veritas Classification A/S.

Georgiadis M., 1983. Development of p - y curves for layered soils. *Proceedings of the Geotechnical Practice in Offshore Engineering*, ASCE, pp. 536-545.

Hansen B. J., 1961. *The ultimate resistance of rigid piles against transversal forces*. Danish Geotechnical Institute, Bull. No. 12, Copenhagen, Denmark, 5-9.

Jacobsen M., and Gwizdala K., 1992. *Bearing Capacity and Settlements of Piles*. Centertrykkeriet, Aalborg University, Denmark.

APPENDIX E

FLAC^{3D}

The theoretical background for numerical modelling in *FLAC^{3D}* is presented in this appendix. *FLAC^{3D}* is a commercial program based on the explicit finite difference method. The program allows a numerical study of the mechanical behaviour of a continuous three-dimensional medium as it reaches equilibrium. There are 12 constitutive models provided in *FLAC^{3D}*. In this thesis the Mohr–Coulomb failure criterion is employed in the analyses of the laterally loaded monopiles. A brief description of the material model is outlined in appendix G. This appendix is based on the *FLAC^{3D}* 3.1 manual (2006).

The mechanical behaviour of the medium is derived from laws of motion, definitions of strain, and the use of a constitutive equation for the medium. Furthermore, the virtual work theorem is implemented in the derivation of the laws of motion. From these equations a set of partial differential equations are derived, relating mechanical (stress) and kinematic (strain rate and velocity) variables. All variables are time-dependent as a consequence of employing a dynamic solution approach to solve the set of equations. To solve the set of equations appropriate boundaries and initial conditions are to be specified.

The lagrange formulation is implemented in *FLAC^{3D}*. Furthermore, all components in the kinematic relations are determined at the current position. As a consequence of this the program provides a description of large-strain deformations in the medium, why the generated mesh is updated.

E.1 Numerical formulation

In order to produce a solution to the set of partial differential equations, *FLAC^{3D}* employs a method characterised by three approaches:

- The continuous medium is replaced by a number of discrete elements with all forces concentrated at the nodes in the mesh.
- In order to solve the set of equations the finite difference approach is employed. This means that all first-order space and time derivatives of the variables are approximated by finite differences. Linear variations of the variables over time and space are assumed.
- A dynamic solution approach is attached. Thus, the program steps forward until equilibrium is reached in the nodes.

E.1.1 Discretisation of medium

The medium is discretised into hexahedral zones consisting of elements of tetrahedral shape, cf. fig. E.1. A tetrahedon can be divided into two different configurations of five tetrahedra. In order to ensure a symmetric zone response for a zone loaded symmetrically, *FLAC^{3D}* takes the average of the nodal forces calculated from the two configurations of tetrahedra.

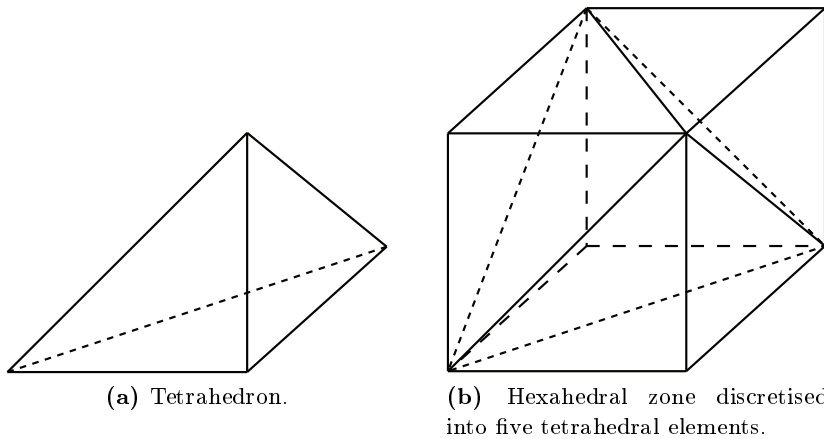


Figure E.1: Tetrahedron as employed zone elements in *FLAC^{3D}*, after *FLAC^{3D}* 3.1 manual (2006).

Each tetrahedral element has constant strain-rate, $\frac{\Delta \varepsilon_{ij}}{\Delta t}$, where the indices i and j takes the values of 1, 2, and 3. By employing elements of tetrahedral

shape deformation patterns producing no strain rate is prevented. However, the elements do not allow deformations without a change in volume. A so-called mixed discretisation is therefore performed. When using mixed discretisation the estimated stress- and strain-rate tensors for each tetrahedron are divided into deviatoric and volumetric parts, and an average value of the volumetric part is calculated for the hexahedral zone. The average values of the volumetric part of the zone stress- and strain-rate are then applied for each tetrahedron. A deformation mode for which mixed discretisation is efficient is shown in fig. E.2.

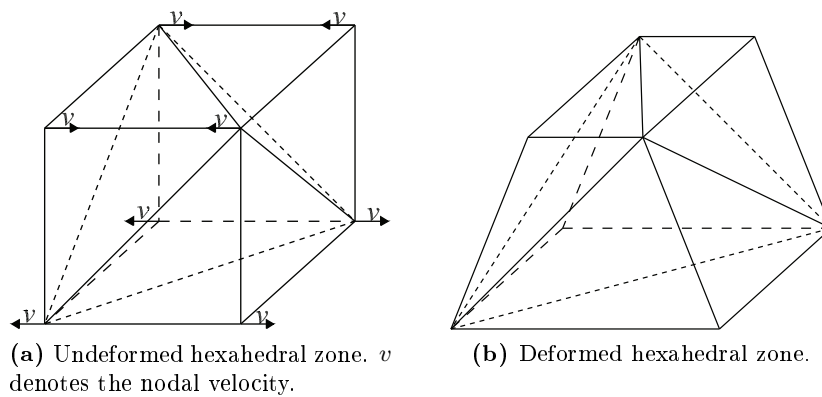


Figure E.2: Deformation mode where mixed discretisation is efficient, after *FLAC^{3D}* 3.1 manual (2006).

E.2 Interfaces

In *FLAC^{3D}* the standard interfaces consist of triangular elements. By default two triangular interface elements are created for each zone face. The interfaces are one-sided and are hereby attached to one surface. The interface is sensitive to interpenetration with the other surface, denoted as the target face. Each interface node is assigned a representative area and a shear and normal force for each individual node can hereby be calculated. The representative area assigned to an interface node is illustrated in fig. E.3.

A linear Coulomb shear-strength criterion is employed in the conducted models for the interfaces to limit the shear force acting on the interface nodes. Furthermore, the interfaces are applied normal and shear stiffnesses, shear and tensile bond strengths, and a dilatancy angle. The shear and tensile bond strengths are by default not activated. The components of the constitutive model employed for the interfaces are illustrated in fig. E.4.

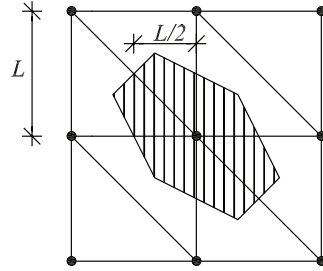


Figure E.3: Interface consisting of eight triangular interface elements where L is the length of the catheters, after *FLAC^{3D}* 3.1 manual (2006). The interface nodes are marked with (•). The hatched area indicate the representative area for the centre node.

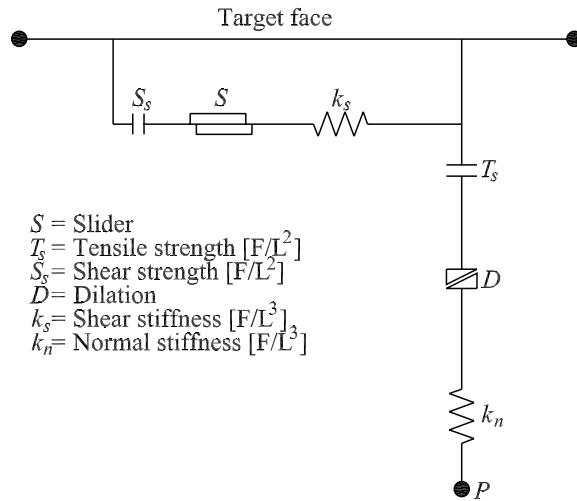


Figure E.4: Components acting on interface node P , in the constitutive model employed for the interfaces, after *FLAC^{3D}* 3.1 manual (2006). F and L denotes dimensions.

E.2.1 Interface properties

In order to calibrate the interface of the conducted numerical models the interface properties for friction, dilation, cohesion, and normal and shear stiffnesses are varied. The normal and shear stiffnesses should not be set too low as interpenetration can occur if the interface displacement is high compared to the zone size. The normal displacement, u , of the interface can be estimated by the normal stress, σ :

$$u = \frac{\sigma}{k_n} \quad (\text{E.1})$$

Furthermore, the normal and shear stiffnesses should not be set much higher than the stiffest surrounding zone as calculation time increases with large variations in stiffness. If the interface displacement is large the contact between target face and interface might not be established. This can however be controlled with the parameter *ctol* that specifies the maximum depth of interface penetration. If the penetration is larger than *ctol* no contact is established between the target face and the interface. The value is by default determined relatively to zone dimensions.

E.3 Numerical stability

To provide valid results the numerical scheme has to be stable. Let the three-dimensional medium be assembled by nodal point masses, m , connected by linear springs with the spring stiffness k . In order to make a stable numerical solution the employed timestep must be lower than a critical timestep corresponding to the minimum eigenperiod of the total system. However, in *FLAC^{3D}* a local numerical stability analysis is performed, as a global eigenvalue analysis is impractical. In *FLAC^{3D}* a unit timestep $\Delta t = 1$ is adopted and to ensure a local stable solution the local nodal masses are adjusted to fulfill a stable condition. For an infinite series of springs and nodal masses the criterion of a local stable solution, takes the form:

$$m = k(\Delta t)^2 \quad (\text{E.2})$$

Thereby, the solution is stable if the magnitude of the point mass is greater than or equal to the spring stiffness. This analysis could be extended to more general elements among these the tetrahedron.

E.4 Numerical damping

As mentioned the derivation of the set of partial differential equations includes the laws of motion. In order to provide a static solution the equations of motion must be damped. *FLAC^{3D}* provides two types of damping models, local and mechanical damping, respectively. Local damping generally dissipates energy faster than combined damping. However, local damping is only activated when the velocity changes sign. For a significantly uniform motion this type of damping is therefore not preferred, and instead combined damping is preferred for uniform motions. Damping forces are activated for sign-changes of both the velocity and the unbalanced force when using combined damping. Hereby, combined damping is able to damp objects exposed to uniform motions.

References

FLAC^{3D} 3.1 manual, 2006. Fast Lagrangian Analysis of Continua in 3 Dimensions, Itasca Consulting Group Inc., Minneapolis, Minnesota, USA.

APPENDIX F

Plaxis 3D Foundation

Plaxis 3D Foundation is a commercial finite element program developed to solve geotechnical problems. The objective of employing *Plaxis 3D Foundation* in this project is to verify the results obtained by means of *FLAC^{3D}* for large-diameter piles subjected to lateral loads. The program contains four predefined material models. In the simulations performed in this project the Mohr–Coulomb material model is employed. The model is outlined in appendix G. This appendix is based on the *Plaxis 3D Foundation* Version 2 manual (2007).

The program is a traditional implicit finite element solver relating forces and displacements by demanding equilibrium in every point in the model. From the equations of equilibrium the weak formulation of the continuum problem is obtained by means of virtual work. In contrast to *FLAC^{3D}*, *Plaxis 3D Foundation* is a static solver, meaning that inertial forces are omitted. The load is applied in increments, automatically determined by the program, assuring numerical stability at each step. The nodal forces and displacements are determined through a Gaussian integration over the stress points in each element.

Plaxis 3D Foundation allows only loads to be applied, i.e. it is not possible to prescribe displacements or velocities. The program allows pore pressures and creep relations to be time dependent. As the models in this project should simulate drained conditions only, and as creep is not considered, the models are independent of time.

F.1 Numerical formulation

Continuum mechanics is applied in order to obtain the forces and displacements in the model. The soil and the pile is divided into a finite number of elements as shown in fig. F.1. Each element contains a number of nodes with degrees of freedom shared with the surrounding elements. To describe the kinematic relations between the nodes, shape functions of second order is applied.

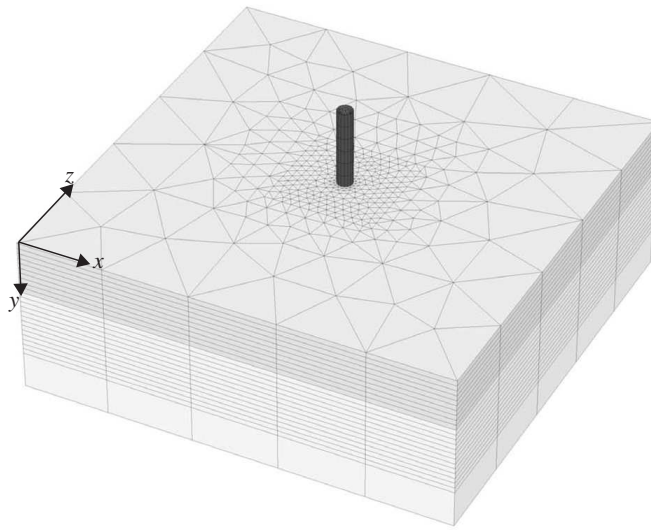


Figure F.1: Discretised model employed in *Plaxis 3D Foundation*.

F.1.1 Discretisation of medium

Various elements are used for discretisation of the model. The mesh generation is carried out by creating a 2D mesh from which the 3D mesh is generated. The soil is in 2D modelled by means of six node triangular elements corresponding to 15 node wedge elements in the 3D mesh. The wedge elements employed to the soil is shown in fig. F.2 with nodes and gauss integration points. The element has three translational degrees of freedom, u_x , u_y and u_z , at each node and six integration points.

The pile is created by means of three noded line elements in the 2D mesh giving eight noded wall elements in the 3D mesh as shown in fig. F.3. Each node has six degrees of freedom; three translational u_x , u_y and u_z and three rotational degrees of freedom ϕ_x , ϕ_y and ϕ_z . The number of integration points is four.

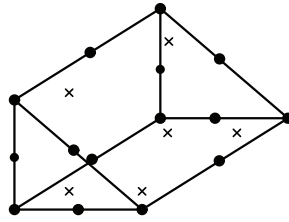


Figure F.2: Volume element with nodes (●) and stress points (x), after *Plaxis 3D Foundation* Version 2 manual (2007).

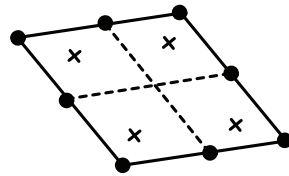


Figure F.3: Wall element with nodes (●) and stress points (x), after *Plaxis 3D Foundation* Version 2 manual (2007).

In the simulations of the laterally loaded piles, floor elements are employed to close the pile-ends. The floor elements, cf. fig. F.4, are plate elements which can only be oriented in the x - z plane. The elements are six noded triangular elements with six degrees of freedom at each node, three translational and three rotational. The number of integration points are three.

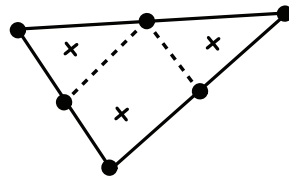


Figure F.4: Floor element with nodes (●) and stress points (x), after *Plaxis 3D Foundation* Version 2 manual (2007).

F.2 Interfaces

To model the soil-pile interaction 16 noded quadrilateral interface elements, as shown in fig. F.5, are employed. Each node has three translational degrees of freedom. The volume of the quadrilateral interface elements is zero. The objective of employing node pairs with the distance zero is to allow the interface to simulate slipping and gapping between soil and structure. As the thickness of the interface elements are zero a virtual thickness is employed to calculate the stiffness. The virtual thickness is calculated automatically and can not be modified by the user.

The stiffness and strength of the soil-structure interface is determined by the parameter R_{inter} . The R_{inter} parameter scales the interface friction angle, φ_i , and the interface stiffness parameters, E_i and G_i , by means of the following relations:

$$\tan(\varphi_i) = R_{inter} \tan(\varphi_s) \quad (\text{F.1})$$

$$E_i = R_{inter}^2 E_s \quad (\text{F.2})$$

$$G_i = R_{inter}^2 G_s \quad (\text{F.3})$$

$$(\text{F.4})$$

where subscripts s and i denotes the soil and the interface parameters, respectively. The Poisson's ratio of the interfaces is by default set to $\nu_i = 0.45$.

For a perfectly rough soil-structure interface $R_{inter} = 1.0$. As the transition between a soil and a structure is normally weaker and more flexible than the associated soil layer, values lower than one should be applied. The value of R_{inter} depends on both soil and structure and should therefore be calibrated for each case.

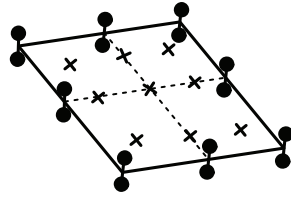


Figure F.5: Interface element with nodes (●) and stress points (×), after *Plaxis 3D Foundation* Version 2 manual (2007).

F.3 Numerical stability

The numerical stability of *Plaxis 3D Foundation* is ensured implicitly by several error control algorithms. At first the applied loads are automatically divided into appropriate increments. The increment size is determined from the calculation control parameters *desired maximum* (des. max.) and *desired minimum* (des. min.) parameters.

Plaxis 3D Foundation will continue applying load increments until reaching the fully prescribed load or until one of the error controlling procedures terminates the calculation. These error controlling processes are governed by the following parameters:

- *additional steps*

- *tolerated error*
- *maximum iterations*

The *additional steps* (add. steps) parameter states the maximum number of load steps. If the fully prescribed load is not reached before reaching the maximum number of load steps the *additional steps* parameter should be increased. This parameter ensures that the user is warned if the step size is too small. The *tolerated error* (tol. error) parameter specifies the size of the local and global error tolerated at each iteration while the *maximum iterations* (max. iterations) parameter specifies the maximum number of iterations allowed. If the maximum number of iterations are reached before the error is converged below the maximum tolerated error the calculations are terminated. In this way the user is warned if convergence is not within the limits. The global error is in the *Plaxis 3D Foundation* solver related to the out-of-balance nodal forces. These out-of-balance nodal forces refers to the difference between the external loads and the forces that are in equilibrium with the current stresses. The local error however, refers to the error at each individual integration point.

In addition to these above mentioned parameters, the iterative procedure is optimised by running an over-relaxation procedure controlled by the factor *degree of over-relaxation* (over-relax). The procedure is illustrated in fig. F.6 with a relaxation factor of one and two, respectively.

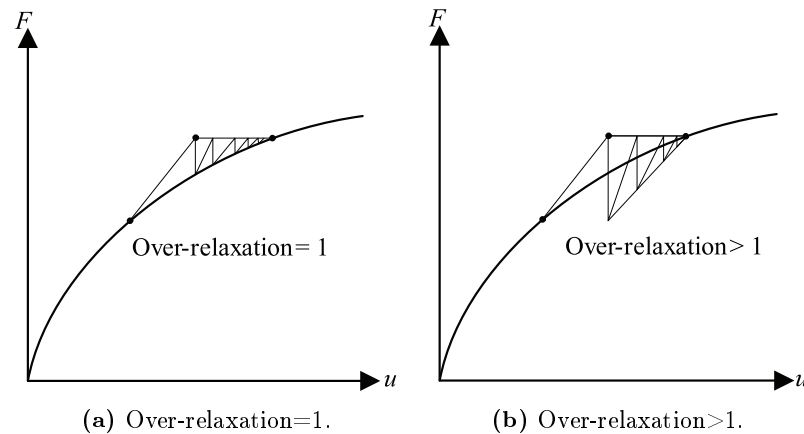


Figure F.6: Principle of over-relaxation, after *Plaxis 3D Foundation* Version 2 manual (2007).

By default *Plaxis 3D Foundation* uses an arc-length control algorithm to ensure the model to converge near the point of collapse. The principle behind arc-length control is illustrated in fig. F.7. If the arc-length control is de-selected a modified Newton-Raphson algorithm is employed. As shown

in fig. F.7 the modified Newton-Raphson algorithm will not converge at the prescribed load increment. The arc-length control procedure might in some cases give rise to numerical instability, and might in these cases with advantage be de-selected. However, this could influence the convergence near the point of collapse.

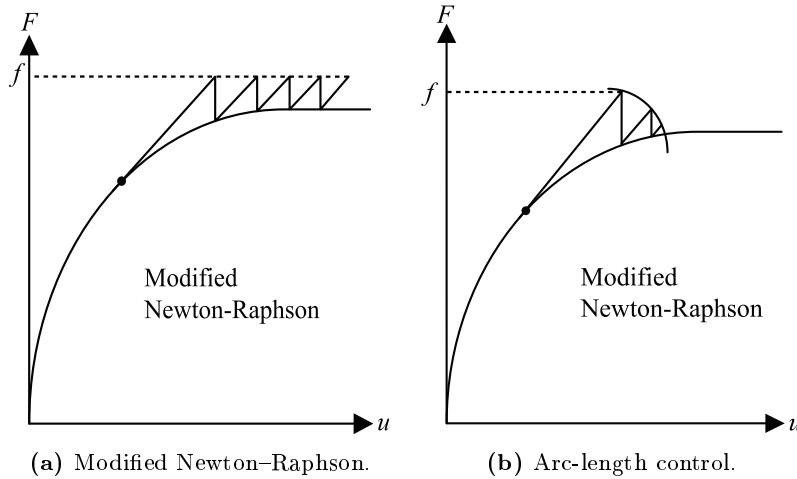


Figure F.7: Principle of arc-length control compared to a modified Newton-Raphson control algorithm, after *Plaxis 3D Foundation* Version 2 manual (2007).

In all simulations performed in this project the default calculation control settings are employed. The values are listed in tab. F.1.

Table F.1: Calculation control parameters employed in the simulations conducted by means of *Plaxis 3D Foundation*.

Des. max.	Des. min.	Add. steps	Tol. error	Max. iterations	Over-relax.	Arc-length control
10	4	250	0.01	50	1.2	yes

References

Plaxis 3D Foundation Version 2, Brinkgreve R. B. J., and Swolfs W. M. (edt.), 2007. Material Models.

Plaxis 3D Foundation Version 2, Brinkgreve R. B. J., and Swolfs W. M. (edt.), 2007. Reference Manual.

Plaxis 3D Foundation Version 2, Brinkgreve R. B. J., and Swolfs W. M. (edt.), 2007. Scientific Manual.

Plaxis 3D Foundation Version 2, Brinkgreve R. B. J., and Swolfs W. M. (edt.), 2007. Tutorial Manual.

Plaxis 3D Foundation Version 2, Brinkgreve R. B. J., and Swolfs W. M. (edt.), 2007. Validation Manual.

Mohr-Coulomb failure criterion

The Mohr–Coulomb model is the traditionally used model to represent shear failure in soil and rock, as the model match laboratory tests well even though the model is simple. A brief introduction is outlined in the following, based on the FLAC 3D 3.1 manual (2006).

The Mohr–Coulomb model is an elasto-plastic model. The model is based on the association between Mohr’s circles of stress and the Coulomb failure criterion. The model is based on a linear elastic-perfect plastic stress-strain curve, as shown in fig. G.1. The total strain increment during loading could be expressed as the sum of the elastic and plastic response. The elastic response is expressed by Hooke’s law.

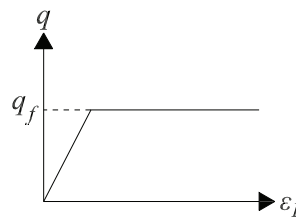


Figure G.1: Assumed stress-strain curve in the Mohr–Coulomb model. Deviatoric stress, q , as function of uniaxial strain, ε_1 . Note that $-\sigma_1 \geq -\sigma_2 \geq -\sigma_3$.

To estimate yielding, q_f , of the material a yield function dependent on the stresses and strains in the soil, f , is introduced. The yield function for a cohesionless material in the principal stress space is shown in fig. G.2.

If the given stress state is not in contact with the yield surface the material behaves linear elastic ($f < 0$) while yielding occurs when the shear stresses

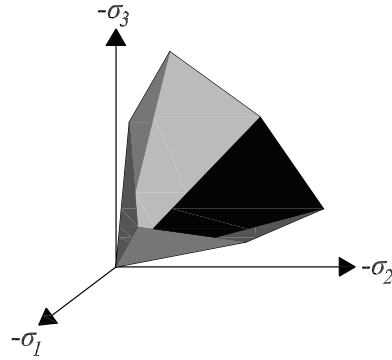


Figure G.2: Mohr–Coulomb yield surface in principal stress space. Note that compressive stresses are negative in *FLAC^{3D}* and *Plaxis 3D Foundation*.

reaches the yield surface ($f = 0$). The yield surface is controlled by a non-associated flow rule.

It is possible in the model to implement tension cutoff (tension yield function). Hereby, it is possible to control the amount of tension in the material. When working with cohesionless materials no tensile forces are transferred. The yield function in tension is controlled by a associated flow rule with an angle of internal friction of 90° .

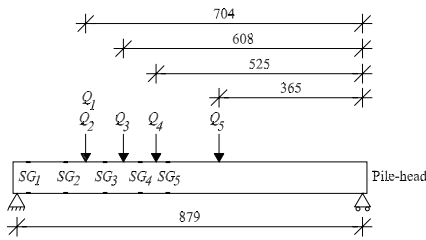
The input parameters when employing the Mohr–Coulomb model are cohesion, friction, dilation and tensile strength. The properties are assumed to remain constant although material hardening or softening may occur after the onset of yielding and effect the material properties. As the initial stiffness of the p – y curves for sand is the main focus of this project the material properties after yielding are not of high importance.

References

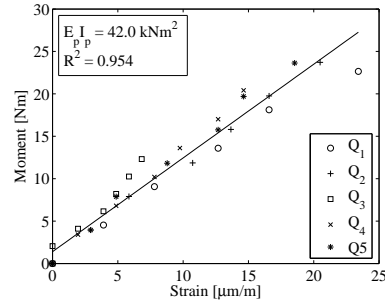
FLAC^{3D} 3.1 manual, 2006. Fast Lagrangian Analysis of Continua in 3 Dimensions, Itasca Consulting Group Inc., Minneapolis, Minnesota, USA.

APPENDIX H

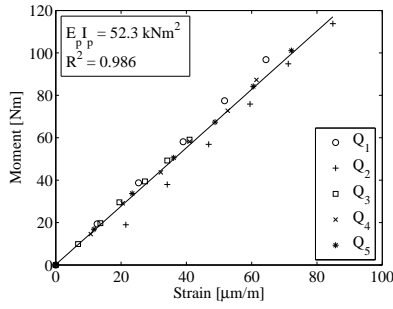
Calibration of test piles



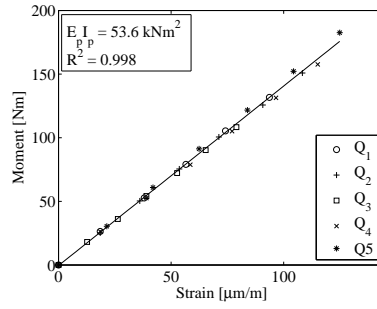
(a) Location of loads, Q_i . Measures are in mm.



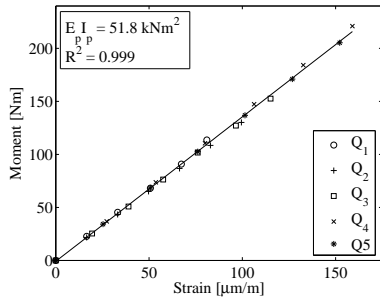
(b) Measured strain versus applied moment at strain gauge level 1, SG_1 .



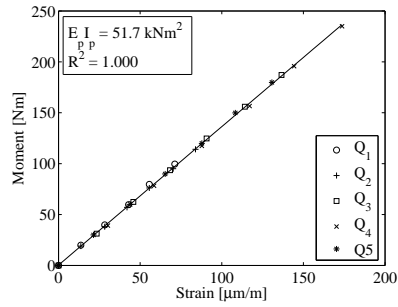
(c) Measured strain versus applied moment at strain gauge level 2, SG_2 .



(d) Measured strain versus applied moment at strain gauge level 3, SG_3 .



(e) Measured strain versus applied moment at strain gauge level 4, SG_4 .



(f) Measured strain versus applied moment at strain gauge level 5, SG_5 .

Figure H.1: Calibration of pile with an outer diameter of 80 mm.

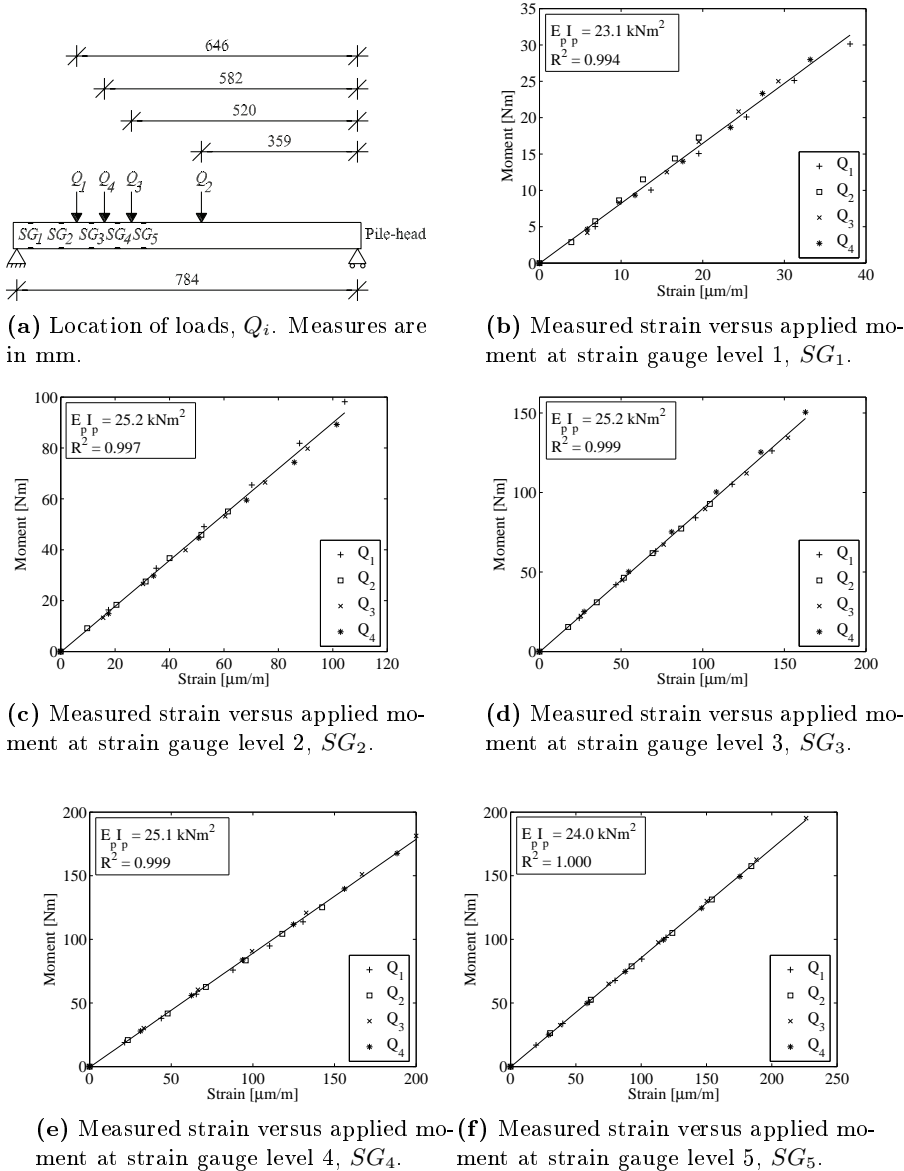


Figure H.2: Calibration of pile with an outer diameter of 60 mm.

APPENDIX I

Test 1: $D = 0.08$ m, $L = 0.4$ m, $P_0 = 0$ kPa

Initiated: 22.01.09	Completed: 23.01.09
Pile diameter (m): 0.08	Load eccentricity (m): 0.37
Embedded length (m): 0.40	Overburden pressure (kPa): 0
Wall thickness (m): 0.005	By: KTB, MM, SPHS
Comments:	

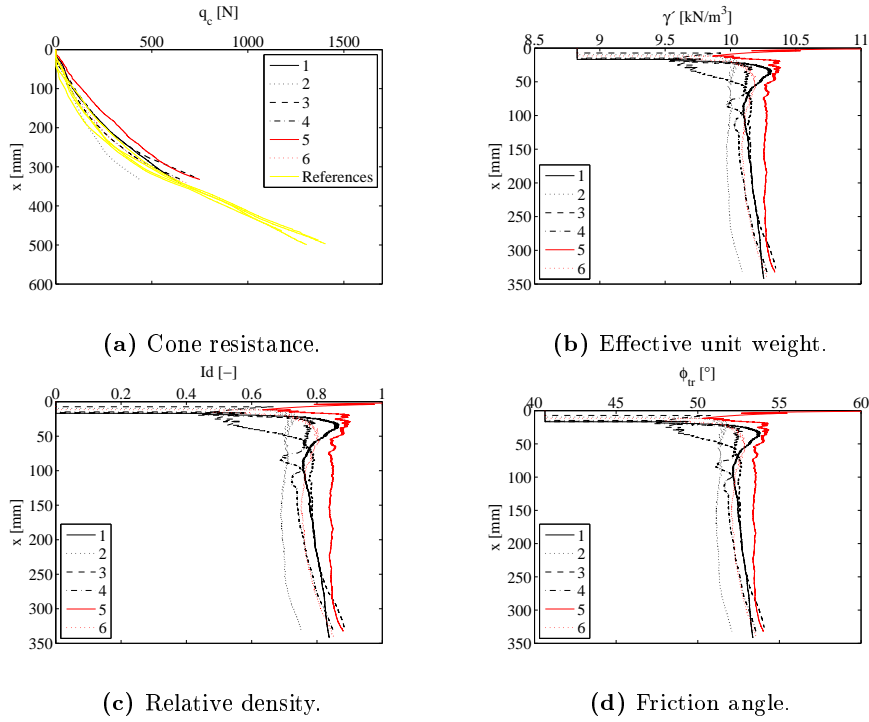


Figure I.1: CPT-results.

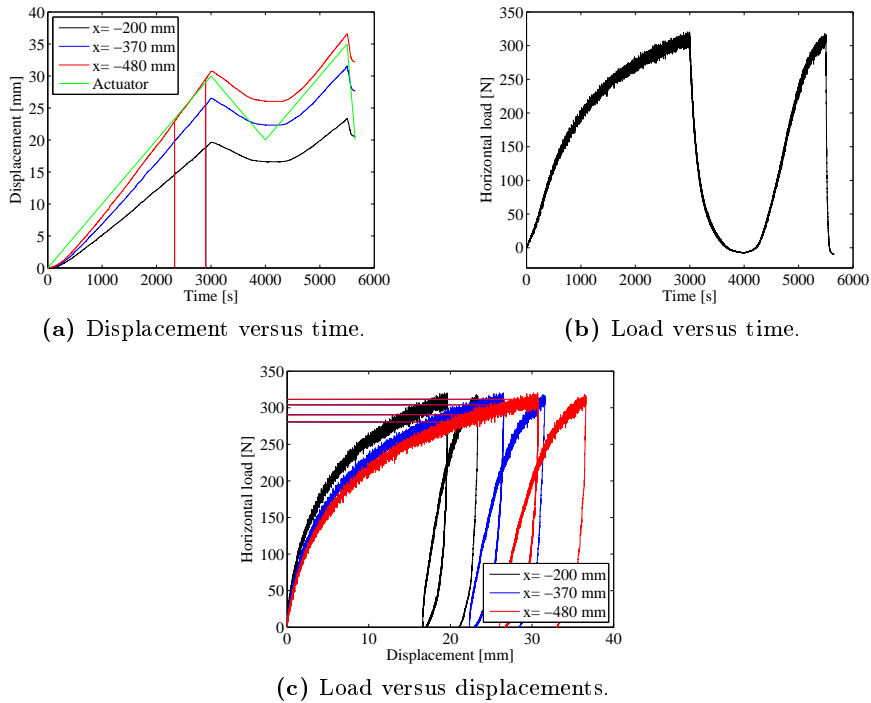
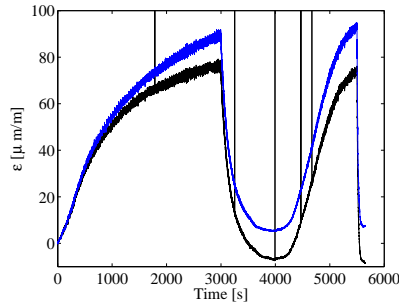
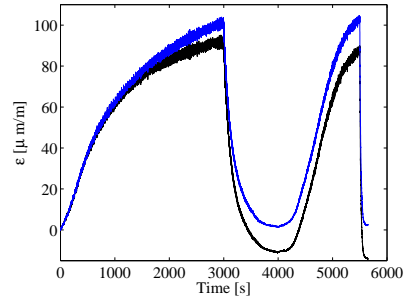


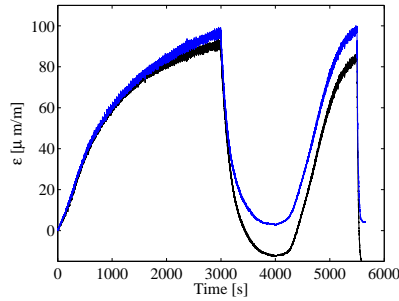
Figure I.2: Lateral loading of pile with $D = 80$ mm. The sampling frequency is 10 Hz.



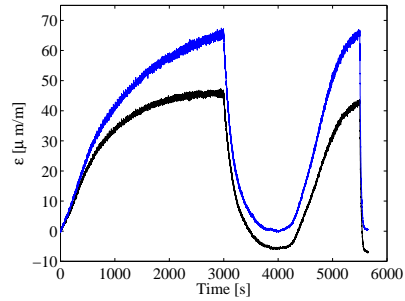
(a) Absolute value of strains at $x = 5.5$ mm. The black curve denotes compression.



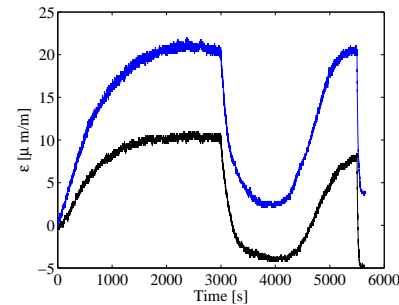
(b) Absolute value of strains at $x = 76$ mm. The black curve denotes compression.



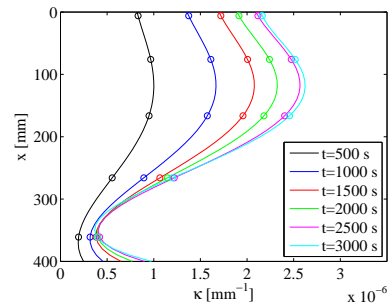
(c) Absolute value of strains at $x = 166$ mm. The black curve denotes compression.



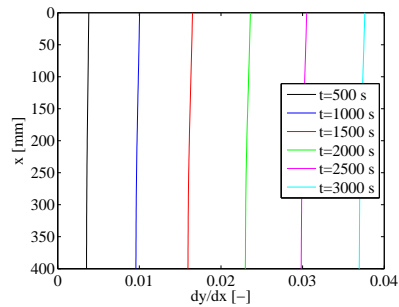
(d) Absolute value of strains at $x = 266$ mm. The black curve denotes compression.



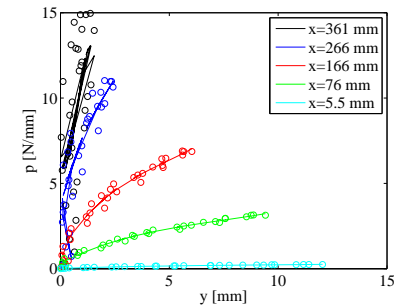
(e) Absolute value of strains at $x = 361$ mm. The black curve denotes compression.



(f) Curvature versus depth.



(g) Rotation versus depth.



(h) p - y curves fitted by a 5. order polynomial.

Figure I.3: Fig. (a)–(e) test output. Fig. (f)–(h) strain gauge interpretation.

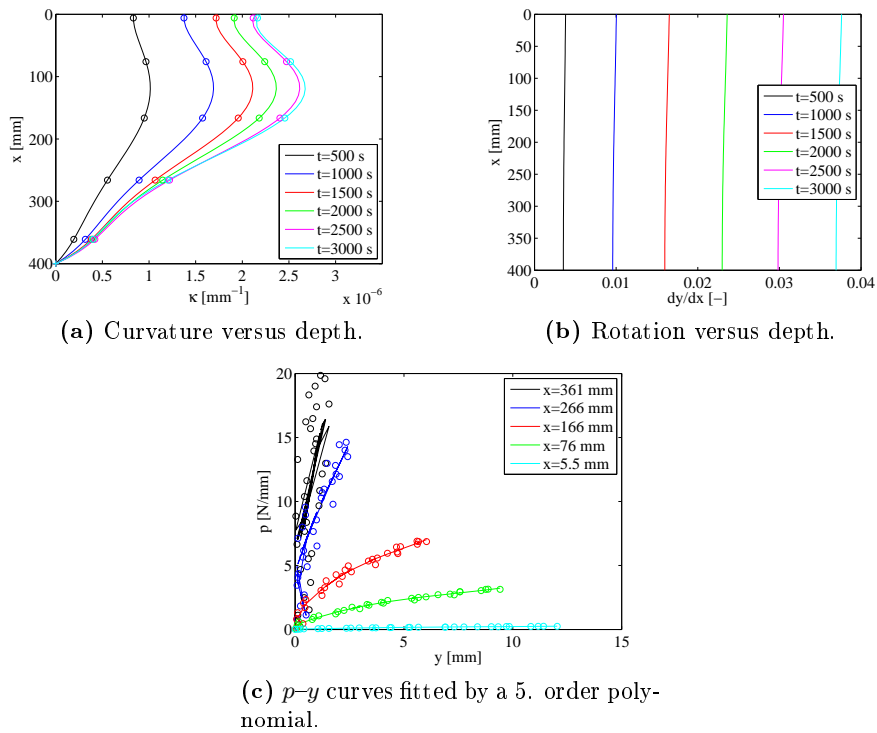


Figure I.4: Strain gauge interpretation assuming zero curvature at pile toe marked with (+).

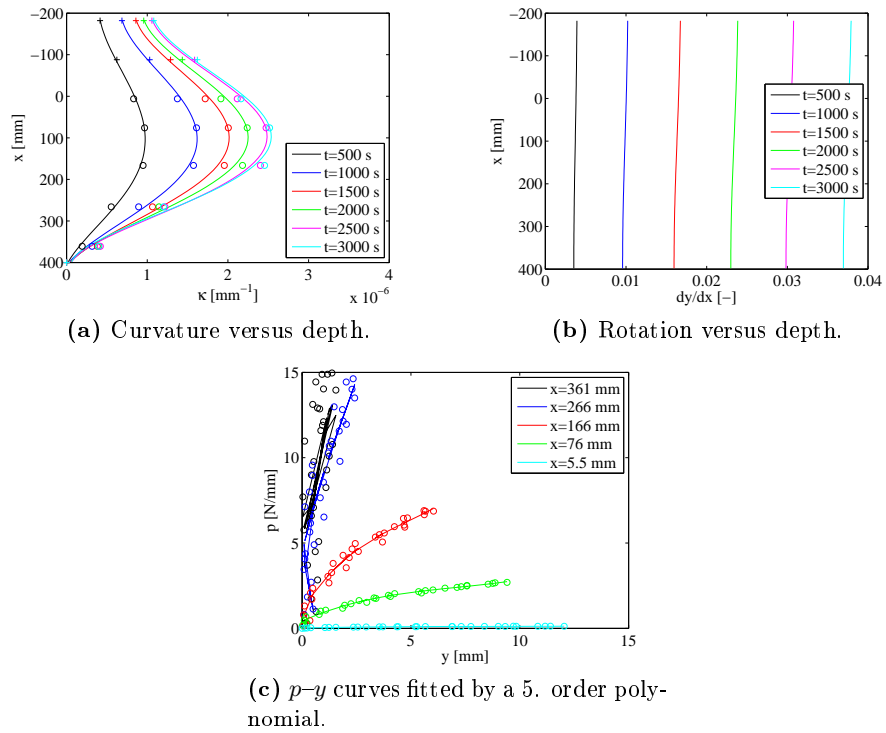


Figure I.5: Strain gauge interpretation assuming known curvature in three extra levels marked with (+).

APPENDIX J

Test 2: $D = 0.08$ m, $L = 0.4$ m, $P_o = 100$ kPa

Initiated: 27.01.09	Completed: 28.01.09
Pile diameter (m): 0.08	Load eccentricity (m): 0.37
Embedded length (m): 0.40	Overburden pressure (kPa): 100
Wall thickness (m): 0.005	By: KTB, MM, SPHS
Comments: The strain gauges exposed to tension at depths of 5.5, 76, and 266 mm, respectively do not work properly at strains larger than 1230, 1720, and 220 $\mu m/m$, respectively. In the interpretation of the strain gauge measurements the strain gauge located at a depth of 266 mm exposed to tension is not considered. At depths of 5.5 mm and 76 mm both the strain gauges exposed to compression and tension are taken into consideration until the gauges exposed to tension fails.	

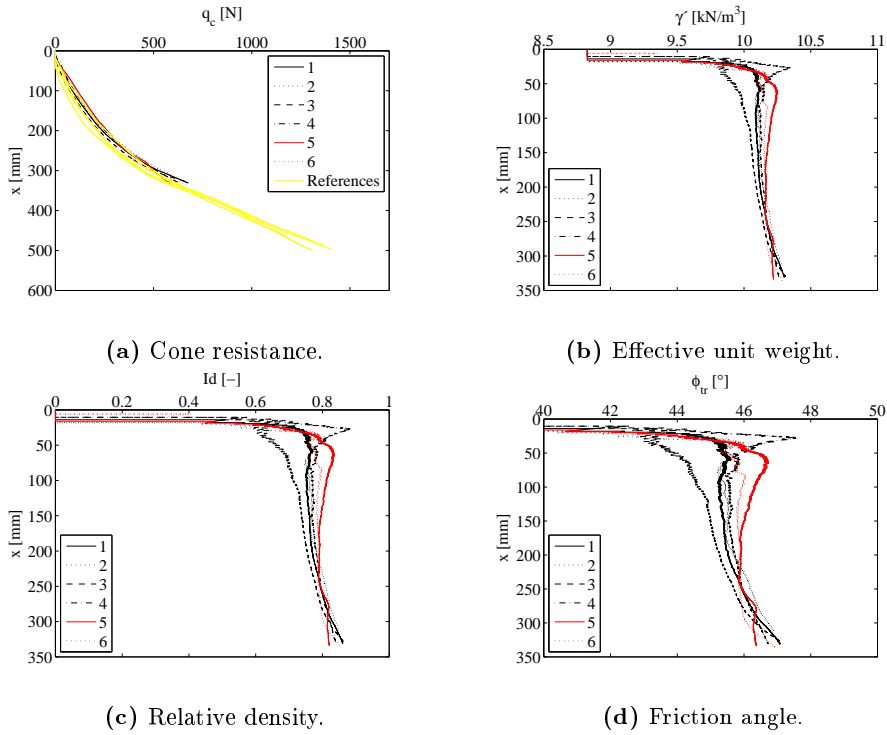


Figure J.1: CPT-results.

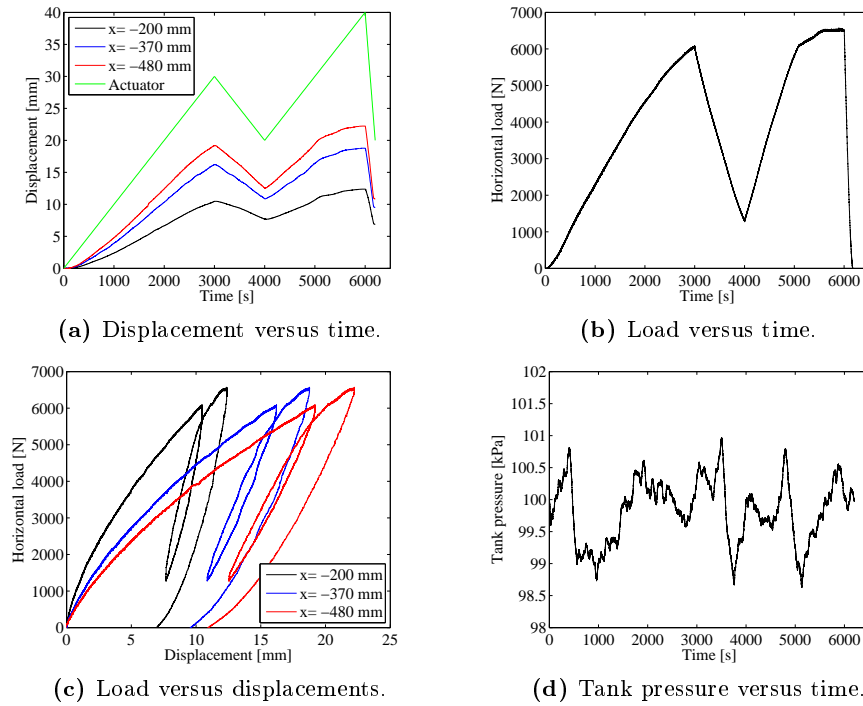
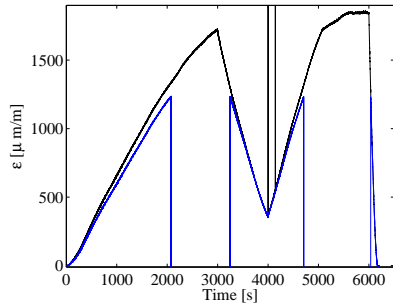
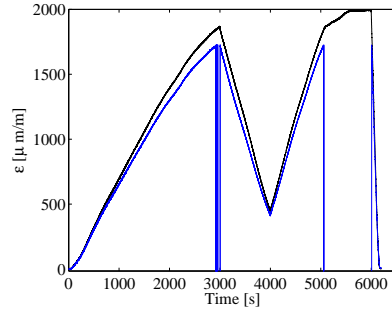


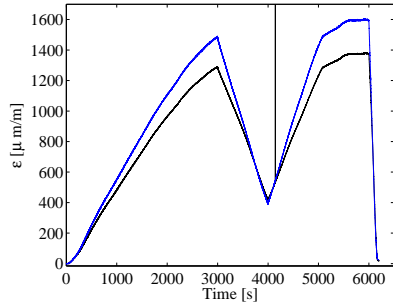
Figure J.2: Lateral loading of pile with $D = 80$ mm. The sampling frequency is 10 Hz.



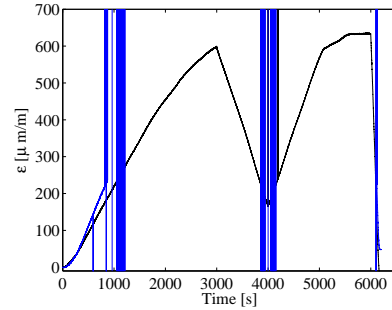
(a) Absolute value of strains at $x = 5.5$ mm. The black curve denotes compression.



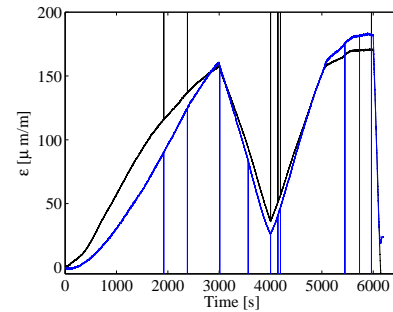
(b) Absolute value of strains at $x = 76$ mm. The black curve denotes compression.



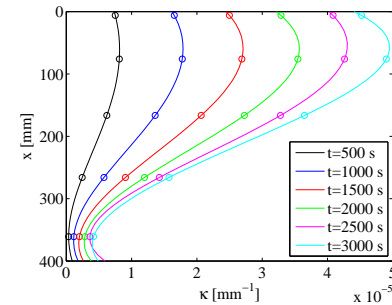
(c) Absolute value of strains at $x = 166$ mm. The black curve denotes compression.



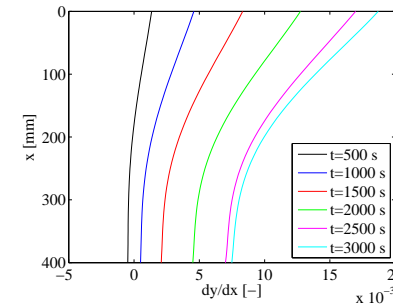
(d) Absolute value of strains at $x = 266$ mm. The black curve denotes compression.



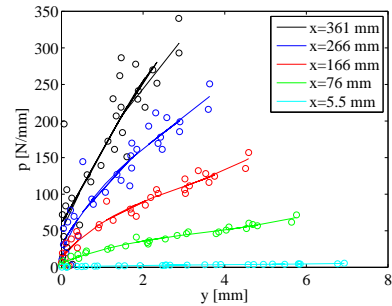
(e) Absolute value of strains at $x = 361$ mm. The black curve denotes compression.



(f) Curvature versus depth.



(g) Rotation versus depth.



(h) p - y curves fitted by a 5. order polynomial.

Figure J.3: Fig. (a)–(e) test output. Fig. (f)–(h) strain gauge interpretation.

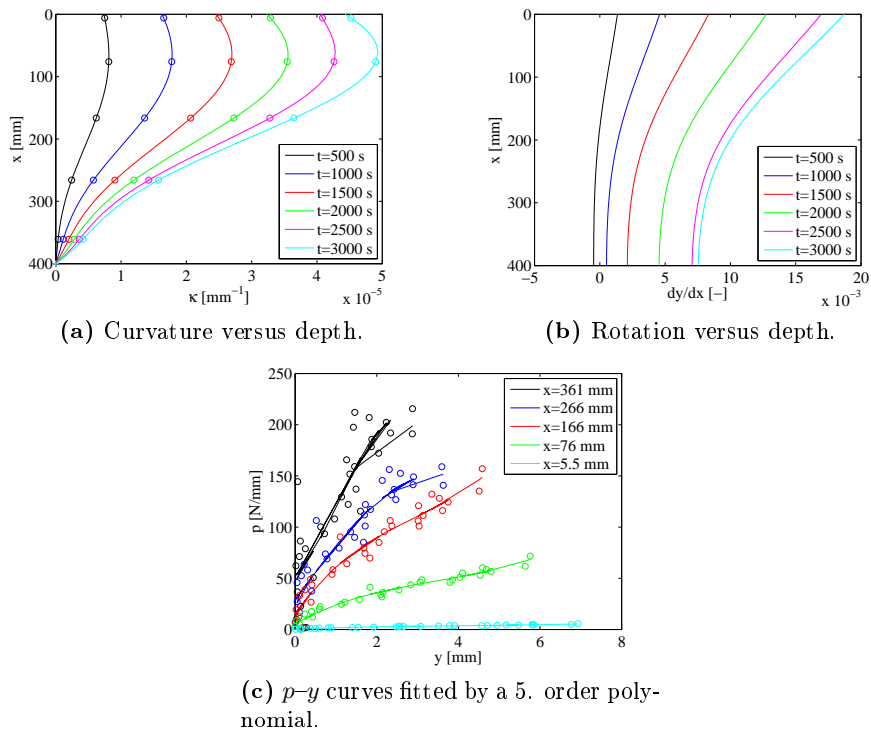


Figure J.4: Strain gauge interpretation assuming zero curvature at pile toe marked with (+).

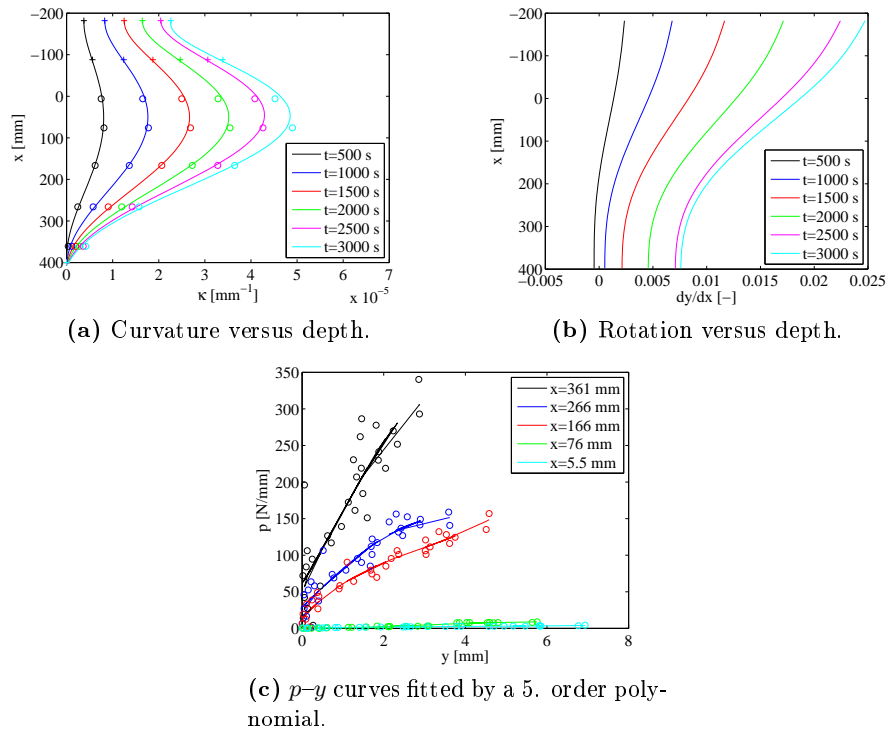


Figure J.5: Strain gauge interpretation assuming known curvature in three extra levels marked with (+).

APPENDIX K

Test 3: $D = 0.08$ m, $L = 0.4$ m, $P_0 = 50$ kPa

Initiated: 29.01.09	Completed: 30.01.09
Pile diameter (m): 0.08	Load eccentricity (m): 0.37
Embedded length (m): 0.40	Overburden pressure (kPa): 50
Wall thickness (m): 0.005	By: KTB, MM, SPHS
Comments: The strain gauges exposed to tension at depths of 5.5, 76, and 266 mm, respectively do not work properly at strains larger than 1260, 1740, and 110 $\mu m/m$, respectively. In the interpretation of the strain gauge measurements the strain gauge located at a depth of 266 mm exposed to tension is not considered. At depths of 5.5 mm and 76 mm both the strain gauges exposed to compression and tension are taken into consideration until the gauges exposed to tension fails. Furthermore, large variations in tank pressure is observed after 2500 s. Test results after 2500 s are therefore not analysed.	

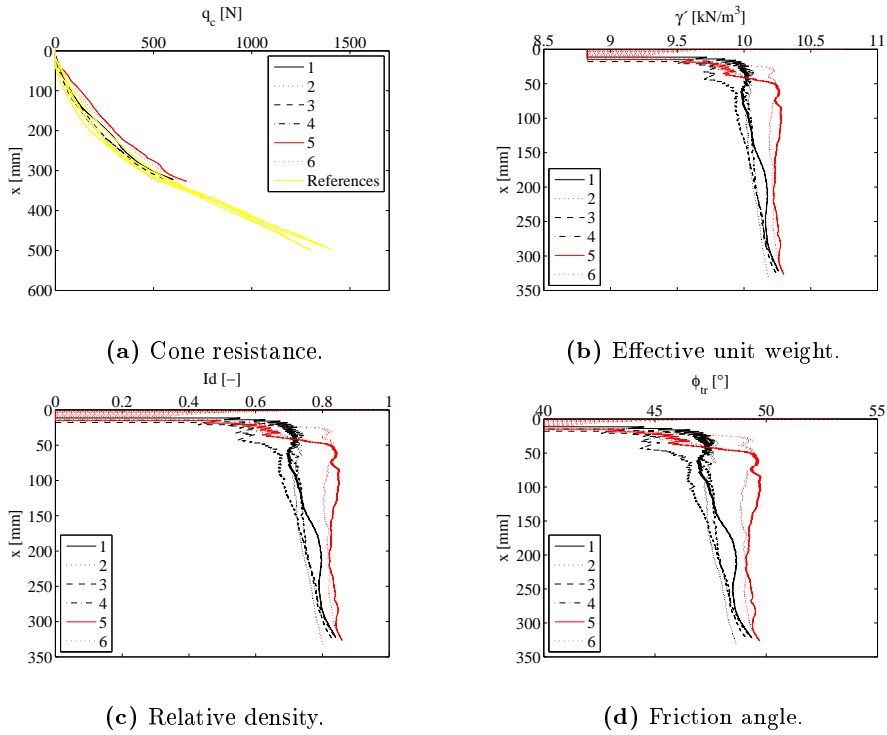


Figure K.1: CPT-results.

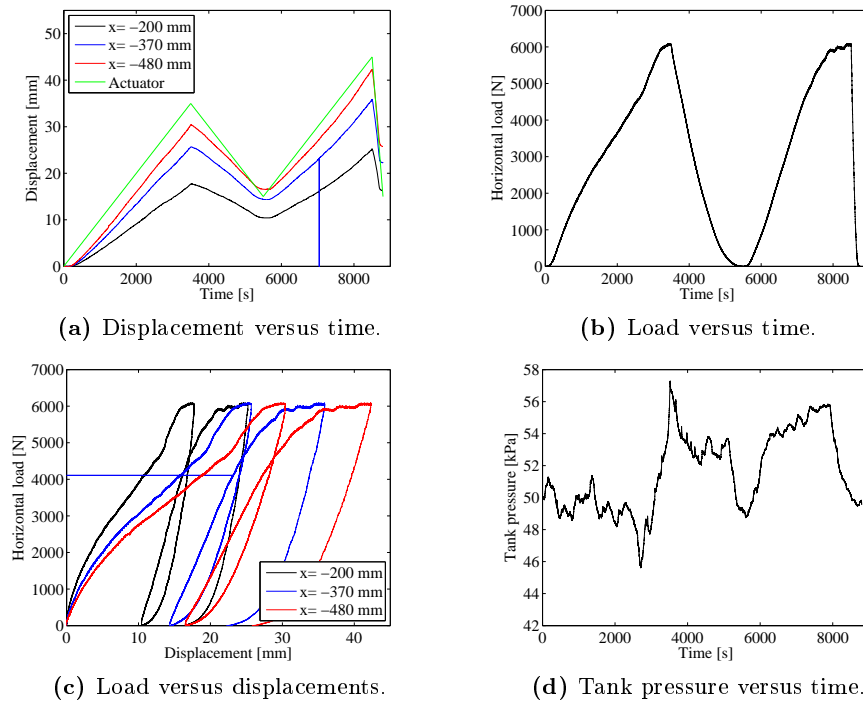
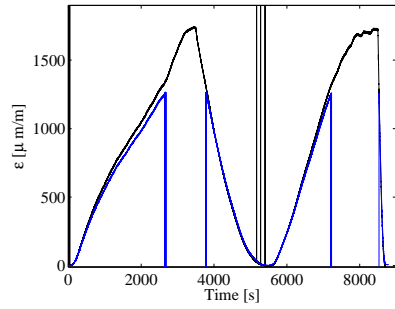
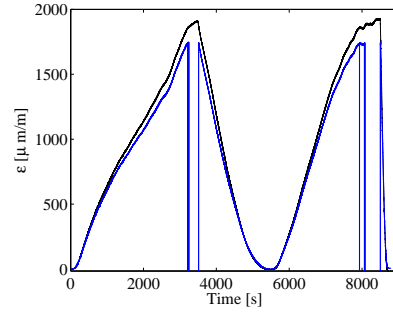


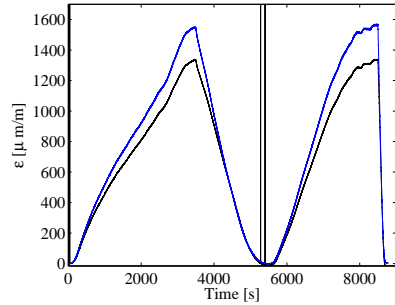
Figure K.2: Lateral loading of pile with $D = 80\text{mm}$. The sampling frequency is 10 Hz.



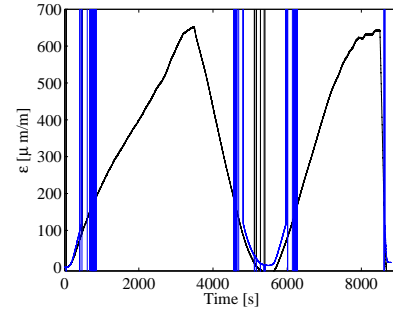
(a) Absolute value of strains at $x = 5.5$ mm. The black curve denotes compression.



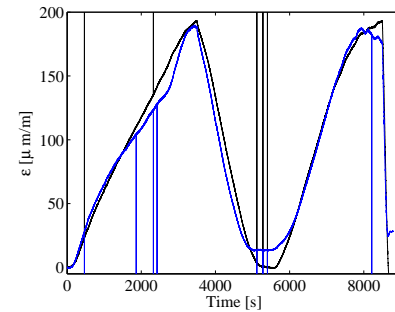
(b) Absolute value of strains at $x = 76$ mm. The black curve denotes compression.



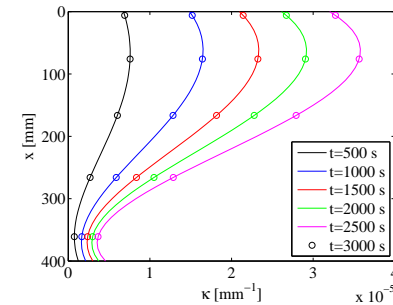
(c) Absolute value of strains at $x = 166$ mm. The black curve denotes compression.



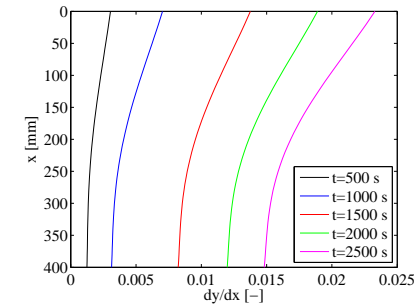
(d) Absolute value of strains at $x = 266$ mm. The black curve denotes compression.



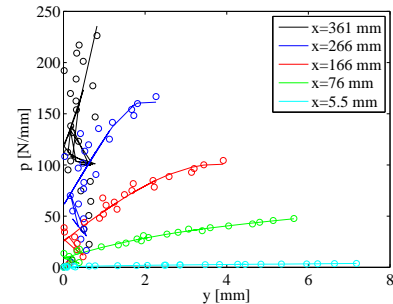
(e) Absolute value of strains at $x = 361$ mm. The black curve denotes compression.



(f) Curvature versus depth.



(g) Rotation versus depth.



(h) p - y curves fitted by a 5. order polynomial.

Figure K.3: Fig. (a)–(e) test output. Fig. (f)–(h) strain gauge interpretation.

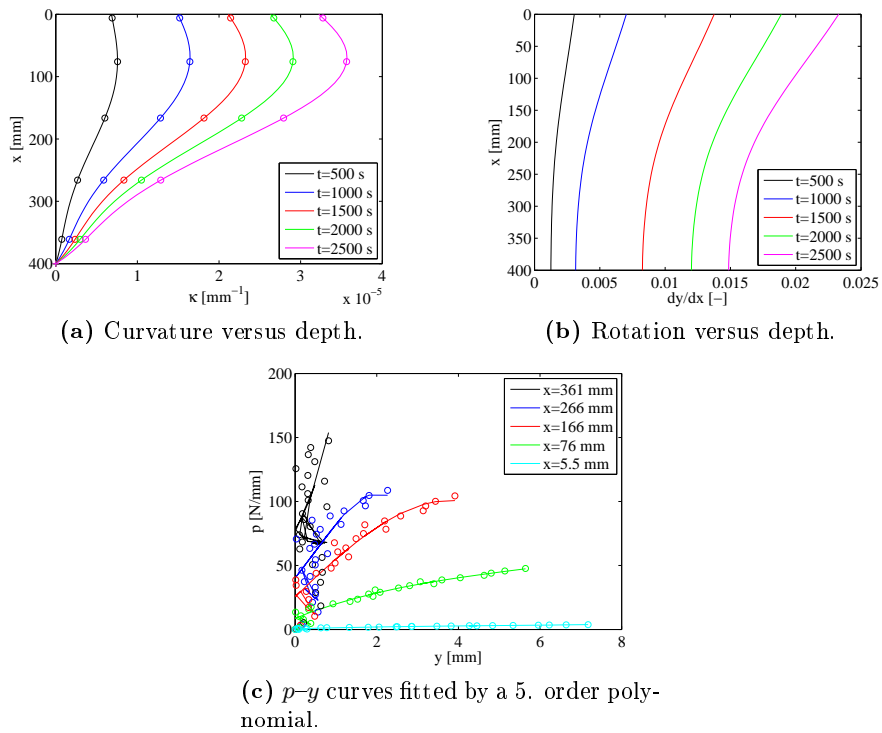


Figure K.4: Strain gauge interpretation assuming zero curvature at pile toe marked with (+).

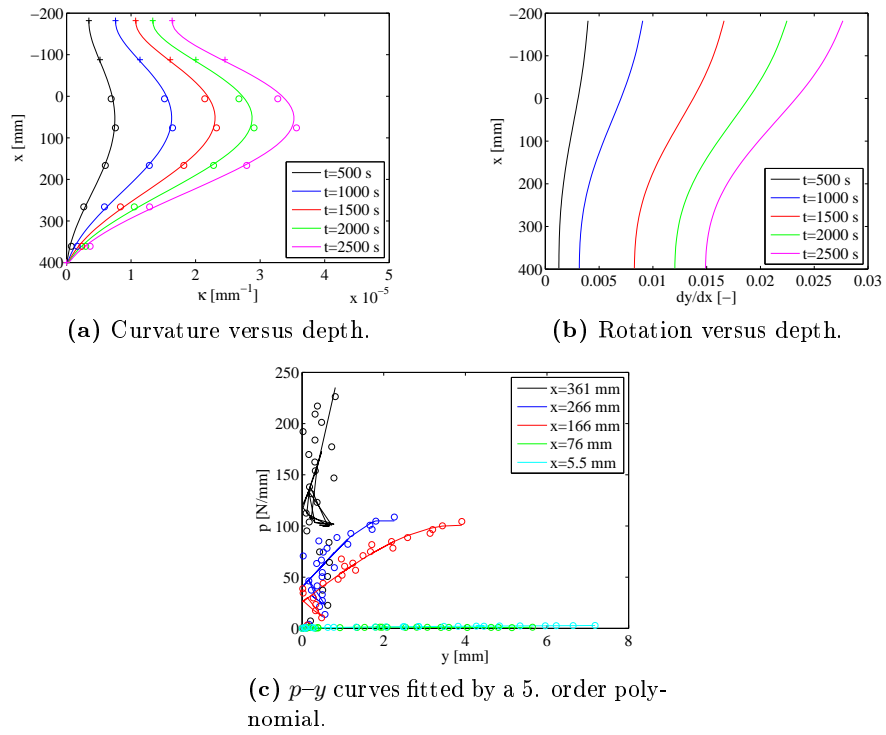


Figure K.5: Strain gauge interpretation assuming known curvature in three extra levels marked with (+).

APPENDIX L

Test 4: $D = 0.06$ m, $L = 0.3$ m, $P_0 = 0$ kPa

Initiated: 19.02.09	Completed: 20.02.09
Pile diameter (m): 0.06	Load eccentricity (m): 0.375
Embedded length (m): 0.30	Overburden pressure (kPa): 0
Wall thickness (m): 0.005	By: KTB, MM, SPHS
Comments: The strain gauge exposed to compression at a depth of 120 mm does not produce reliable results. This strain gauge is therefore not included in the strain gauge interpretation.	

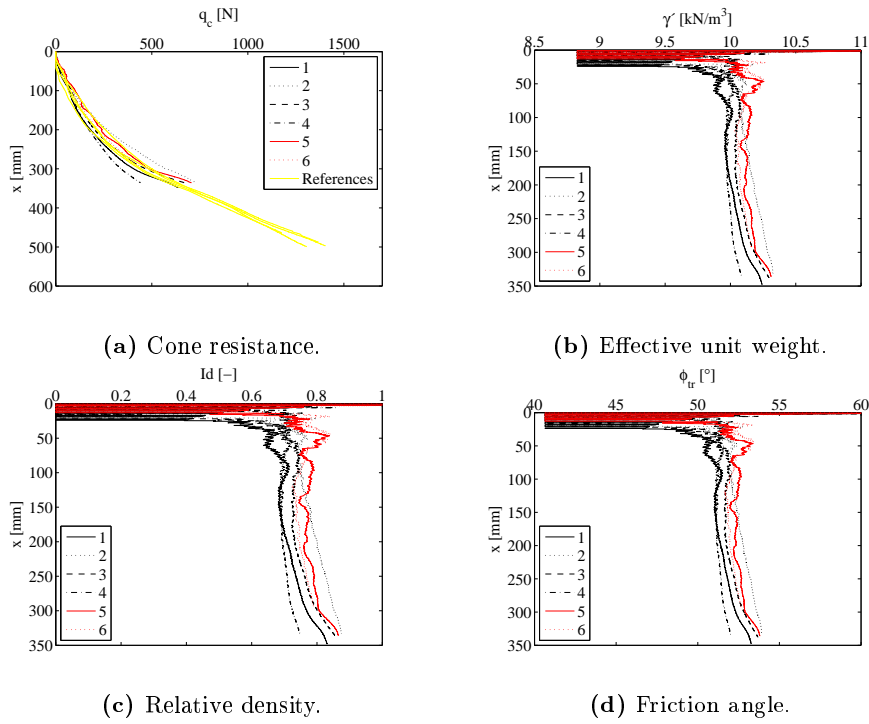


Figure L.1: CPT-results.

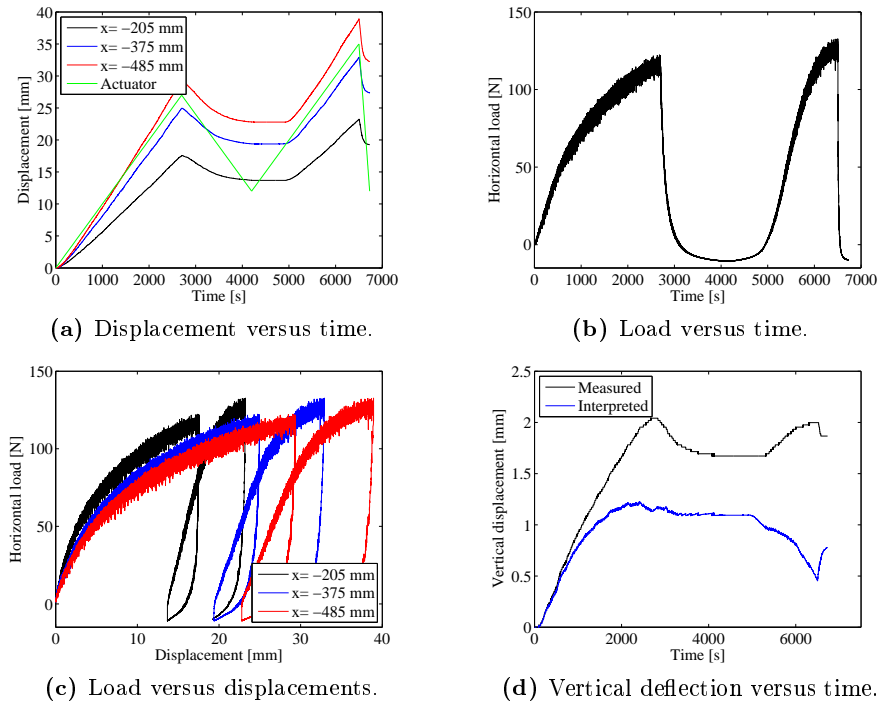
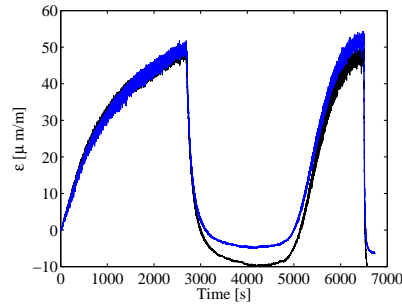
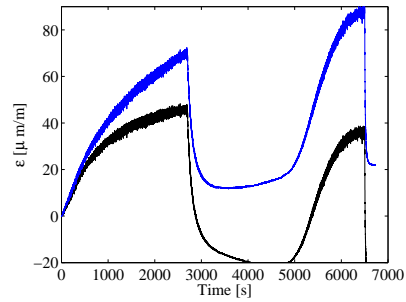


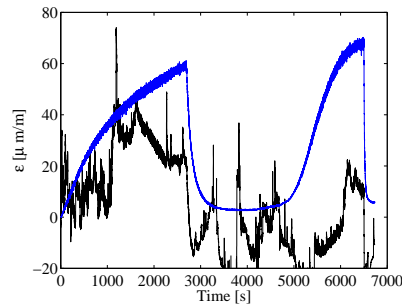
Figure L.2: Lateral loading of pile with $D = 60$ mm. The sampling frequency is 10 Hz.



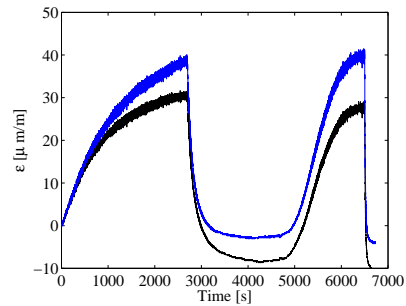
(a) Absolute value of strains at $x = 0$ mm. The black curve denotes compression.



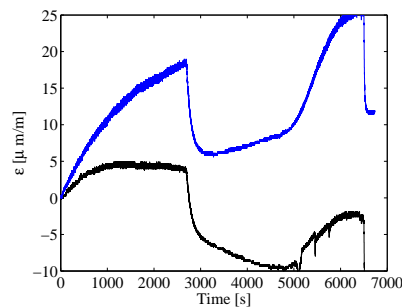
(b) Absolute value of strains at $x = 60$ mm. The black curve denotes compression.



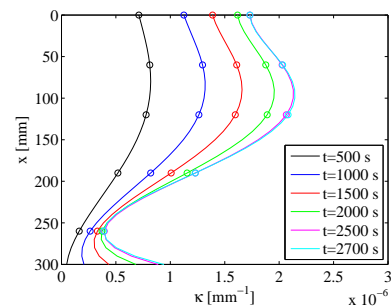
(c) Absolute value of strains at $x = 120$ mm. The black curve denotes compression.



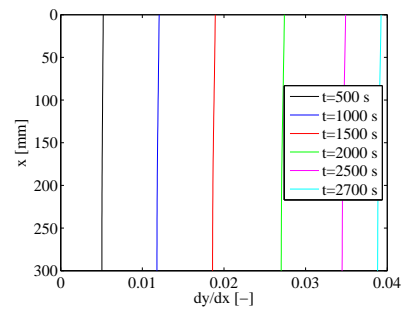
(d) Absolute value of strains at $x = 190$ mm. The black curve denotes compression.



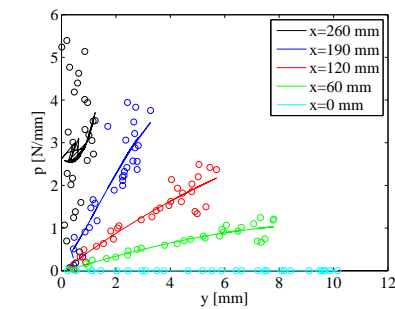
(e) Absolute value of strains at $x = 260$ mm. The black curve denotes compression.



(f) Curvature versus depth.



(g) Rotation versus depth.



(h) p - y curves fitted by a 5. order polynomial.

Figure L.3: Fig. (a)–(e) test output. Fig. (f)–(h) strain gauge interpretation.

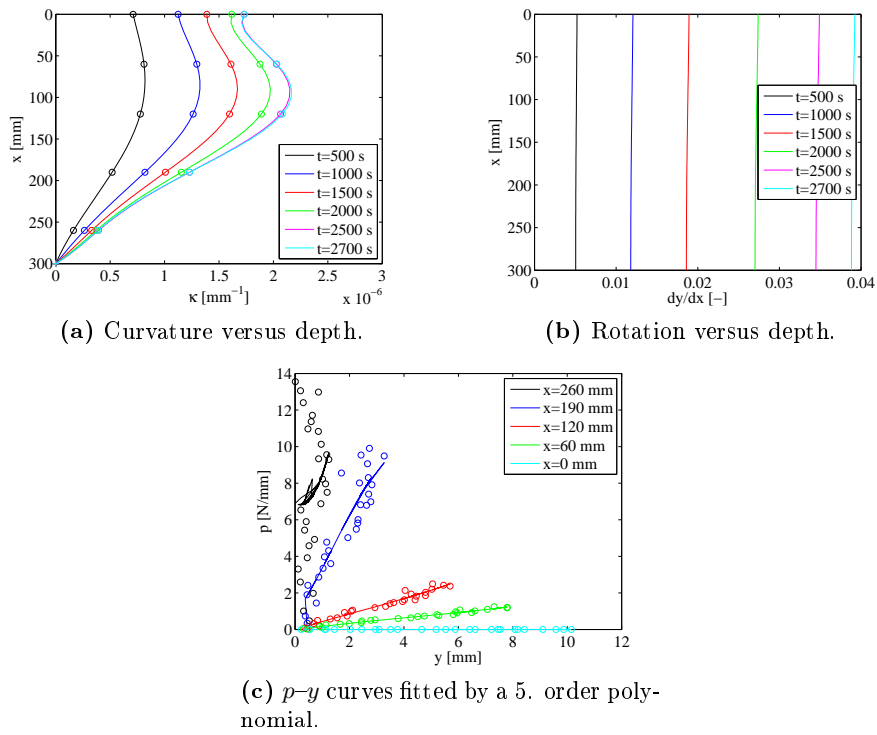


Figure L.4: Strain gauge interpretation assuming zero curvature at pile toe marked with (+).

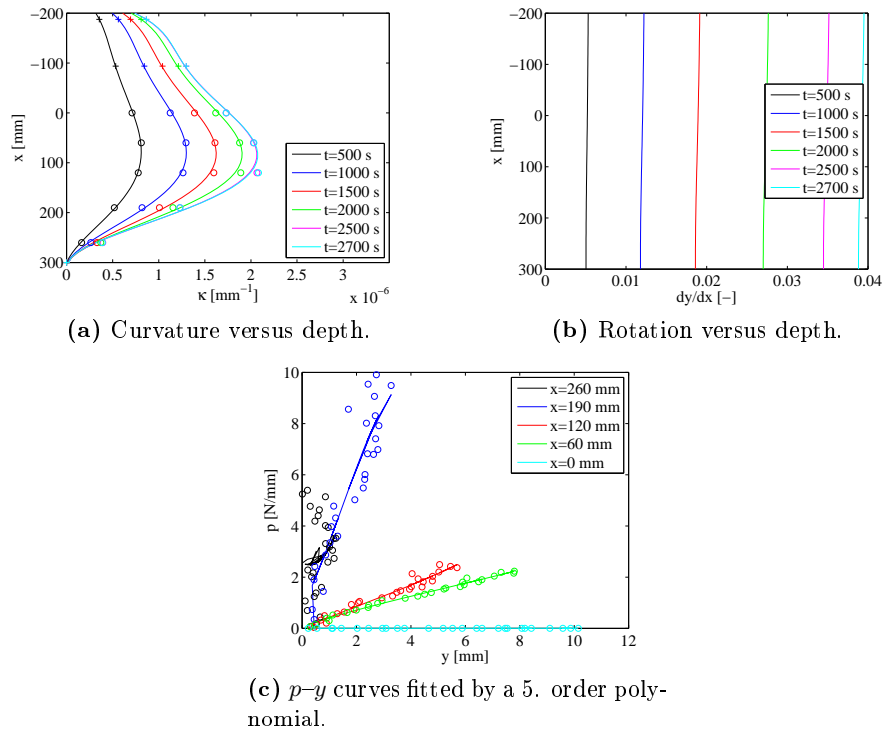
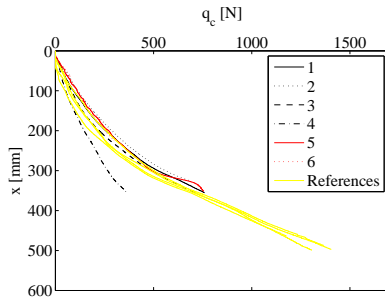


Figure L.5: Strain gauge interpretation assuming known curvature in three extra levels marked with (+).

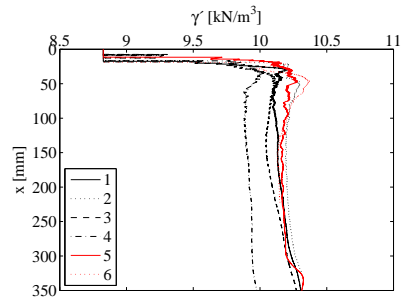
APPENDIX M

Test 5: $D = 0.06$ m, $L = 0.3$ m, $P_0 = 50$ kPa

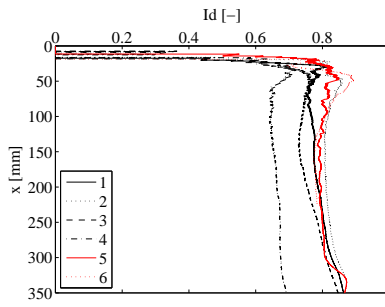
Initiated: 21.02.09	Completed: 22.02.09
Pile diameter (m): 0.06	Load eccentricity (m): 0.375
Embedded length (m): 0.30	Overburden pressure (kPa): 50
Wall thickness (m): 0.005	By: KTB, MM, SPHS
Comments:	



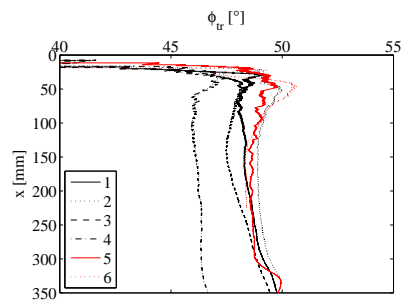
(a) Cone resistance.



(b) Effective unit weight.

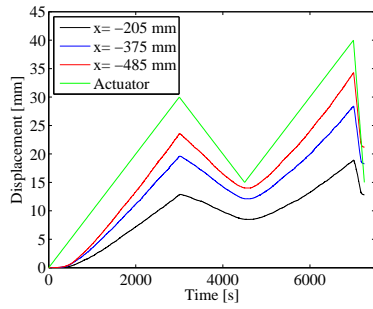


(c) Relative density.

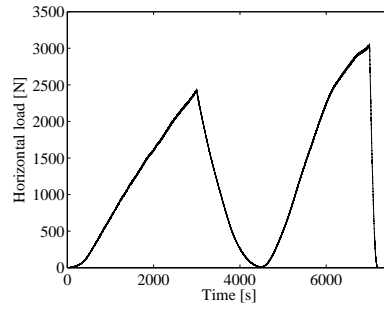


(d) Friction angle.

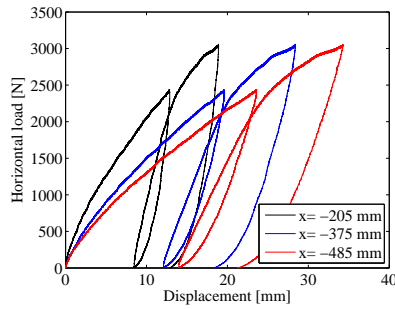
Figure M.1: CPT-results.



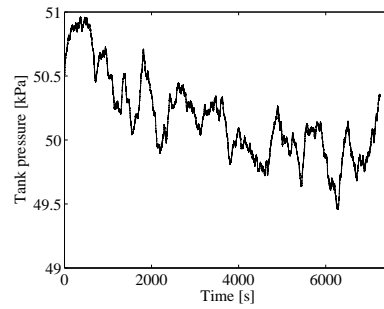
(a) Displacement versus time.



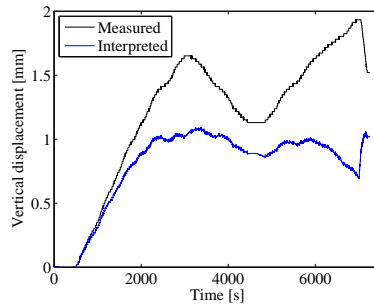
(b) Load versus time.



(c) Load versus displacements.

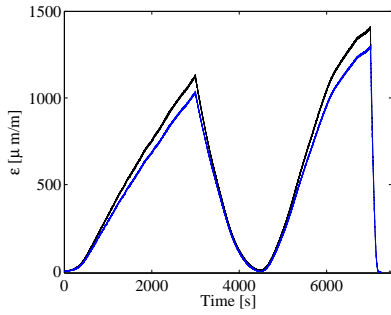


(d) Tank pressure versus time.

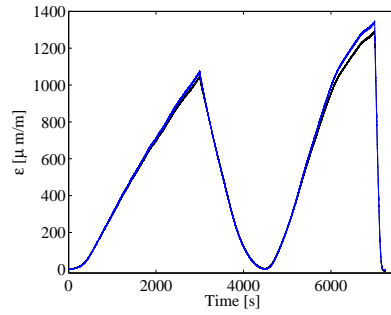


(e) Vertical displacement versus time.

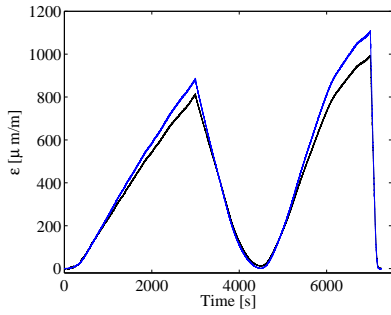
Figure M.2: Lateral loading of pile with $D = 60$ mm. The sampling frequency is 10 Hz.



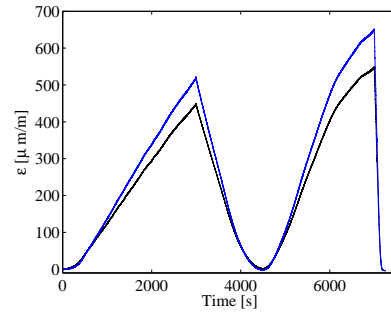
(a) Absolute value of strains at $x = 0$ mm. The black curve denotes compression.



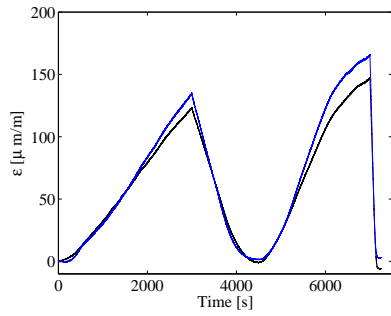
(b) Absolute value of strains at $x = 60$ mm. The black curve denotes compression.



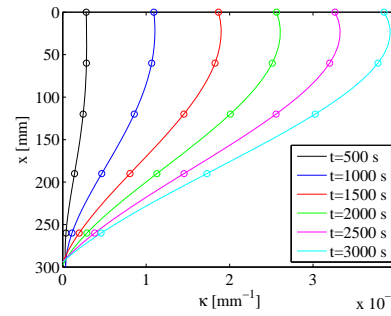
(c) Absolute value of strains at $x = 120$ mm. The black curve denotes compression.



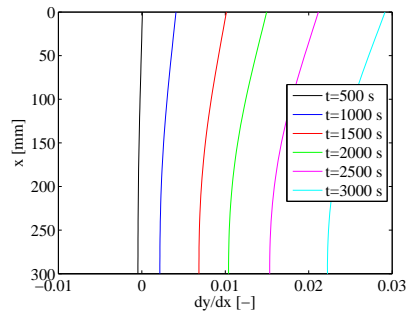
(d) Absolute value of strains at $x = 190$ mm. The black curve denotes compression.



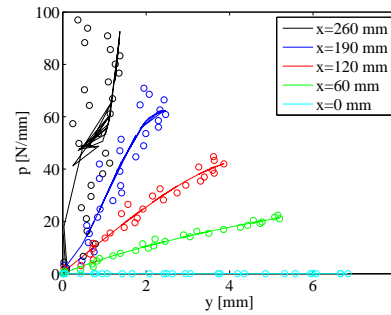
(e) Absolute value of strains at $x = 260$ mm. The black curve denotes compression.



(f) Curvature versus depth.



(g) Rotation versus depth.



(h) p - y curves fitted by a 5. order polynomial.

Figure M.3: Fig. (a)–(e) test output. Fig. (f)–(h) strain gauge interpretation.

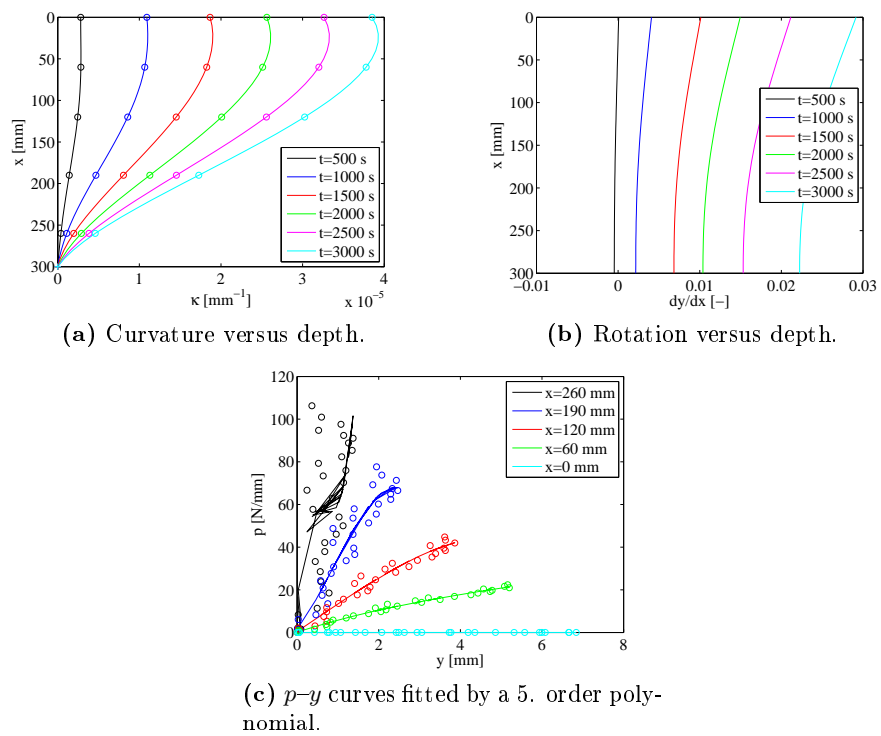


Figure M.4: Strain gauge interpretation assuming zero curvature at pile toe marked with (+).

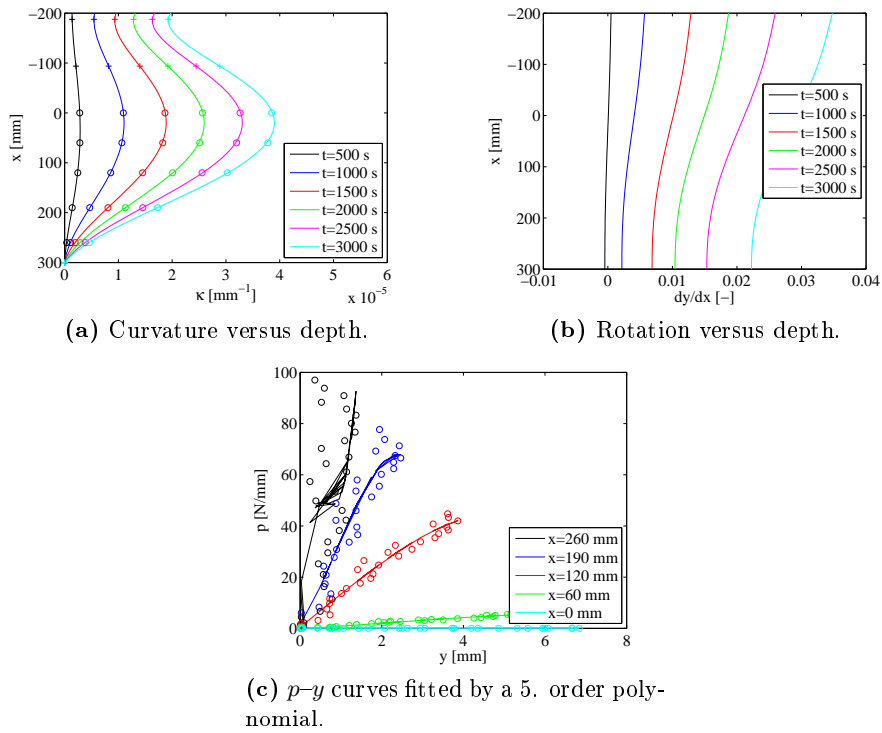
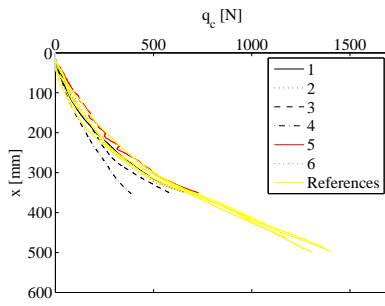


Figure M.5: Strain gauge interpretation assuming known curvature in three extra levels marked with (+).

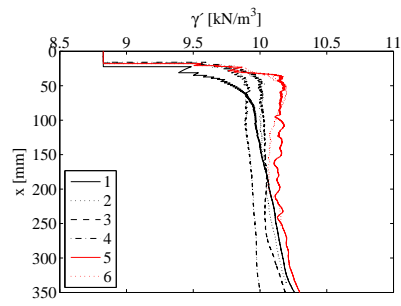
APPENDIX N

Test 6: $D = 0.06$ m, $L = 0.3$ m, $P_o = 100$ kPa

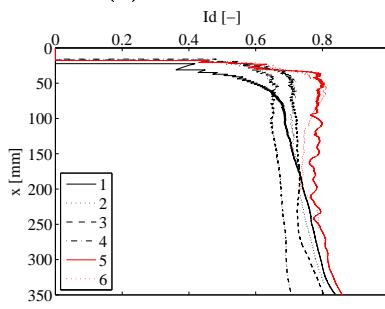
Initiated: 24.02.09	Completed: 26.02.09
Pile diameter (m): 0.06	Load eccentricity (m): 0.375
Embedded length (m): 0.30	Overburden pressure (kPa): 100
Wall thickness (m): 0.005	By: KTB, MM, SPHS
Comments: The strain gauge exposed to tension at a depth of 60 mm does not work properly at strains larger than $1270 \mu m/m$. Both strain gauges at a depth of 60 mm are taken into consideration when interpreting the strain gauge measurements until the gauge exposed to tension fails.	



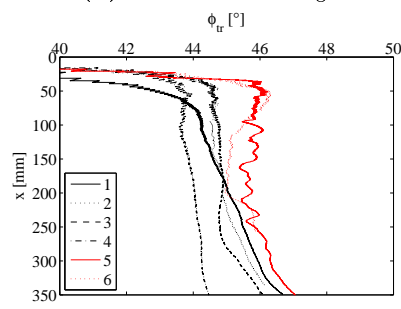
(a) Cone resistance.



(b) Effective unit weight.

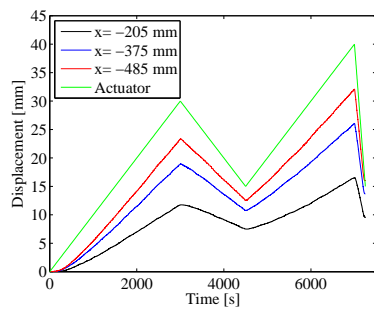


(c) Relative density.

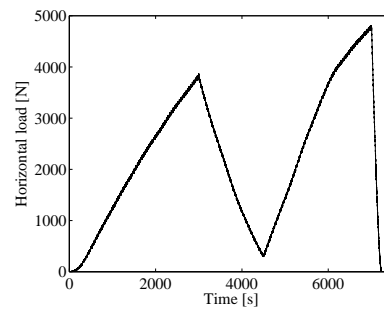


(d) Friction angle.

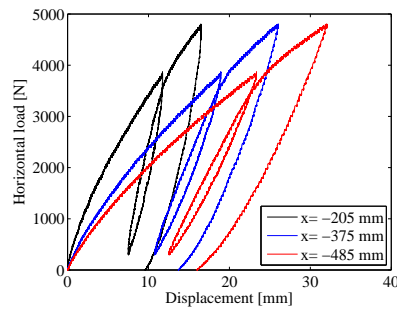
Figure N.1: CPT-results.



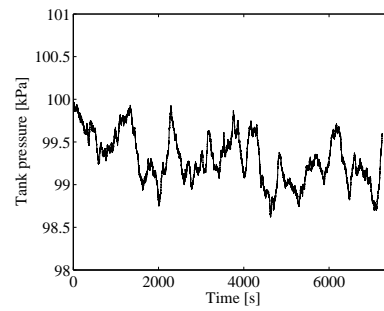
(a) Displacement versus time.



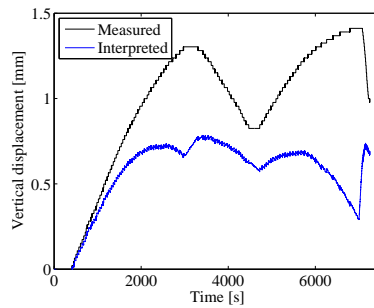
(b) Load versus time.



(c) Load versus displacements.

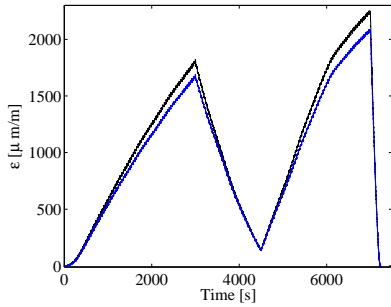


(d) Tank pressure versus time.

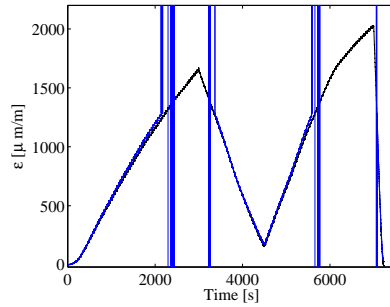


(e) Vertical displacement versus time.

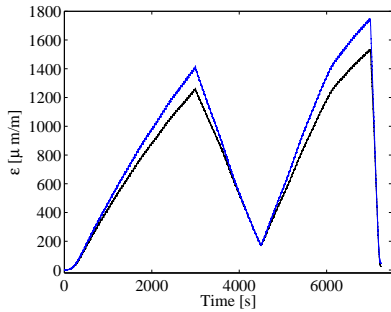
Figure N.2: Lateral loading of 60 mm pile. The sampling frequency is 10 Hz.



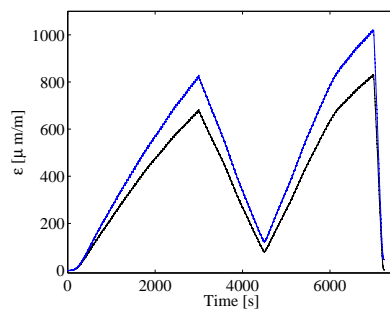
(a) Absolute value of strains at $x = 0$ mm. The black curve denotes compression.



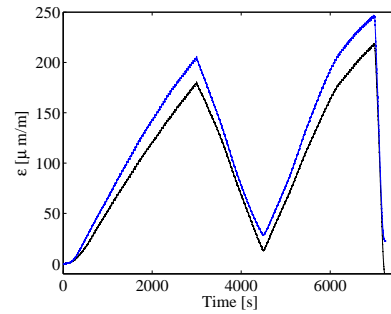
(b) Absolute value of strains at $x = 60$ mm. The black curve denotes compression.



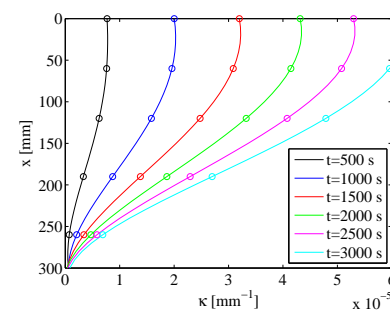
(c) Absolute value of strains at $x = 120$ mm. The black curve denotes compression.



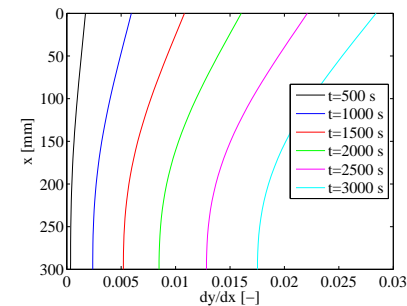
(d) Absolute value of strains at $x = 190$ mm. The black curve denotes compression.



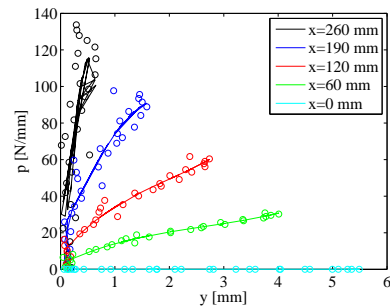
(e) Absolute value of strains at $x = 260$ mm. The black curve denotes compression.



(f) Curvature versus depth.



(g) Rotation versus depth.



(h) p - y curves fitted by a 5. order polynomial.

Figure N.3: Fig. (a)–(e) test output. Fig. (f)–(h) strain gauge interpretation.

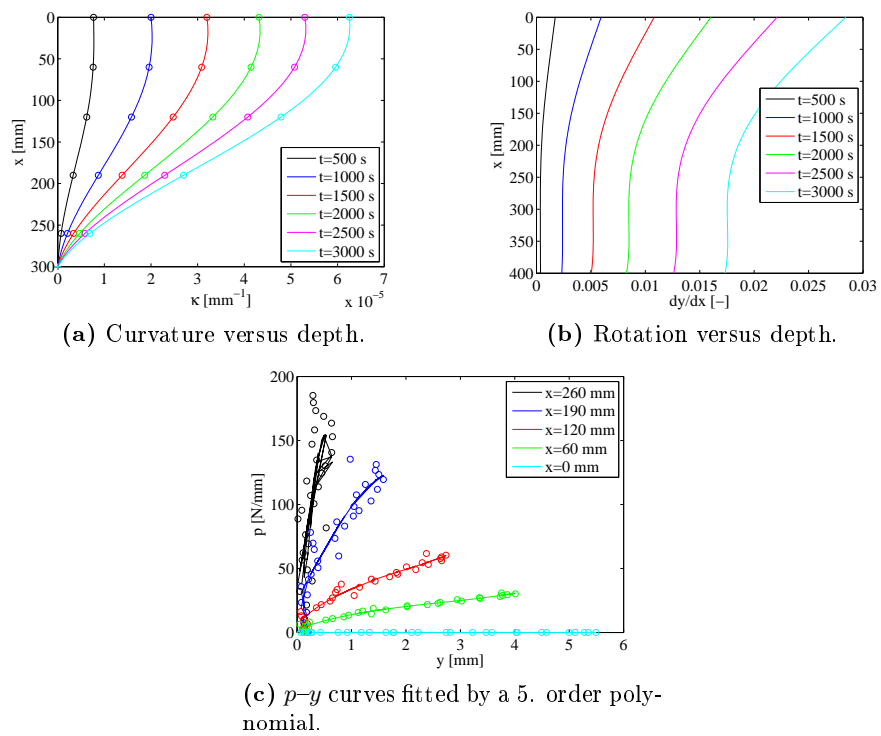


Figure N.4: Strain gauge interpretation assuming zero curvature at pile toe marked with (+).

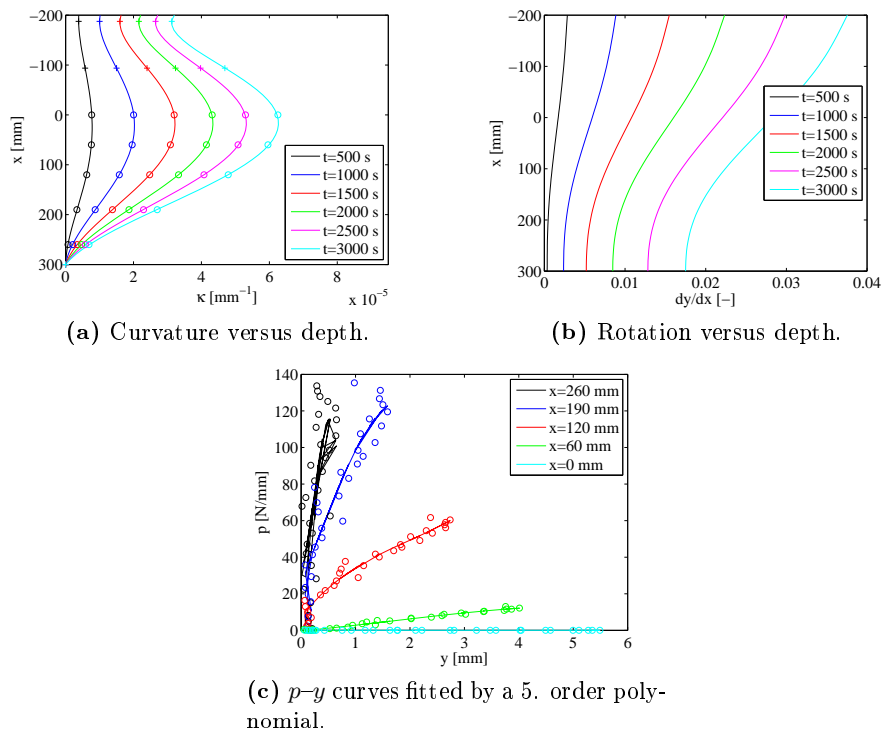
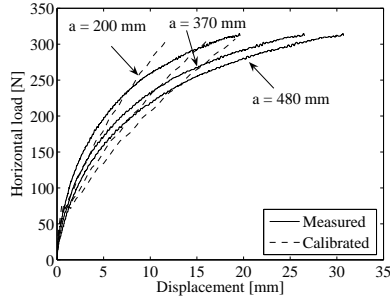


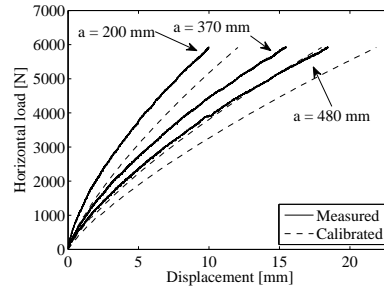
Figure N.5: Strain gauge interpretation assuming known curvature in three extra levels marked with (+).

APPENDIX O

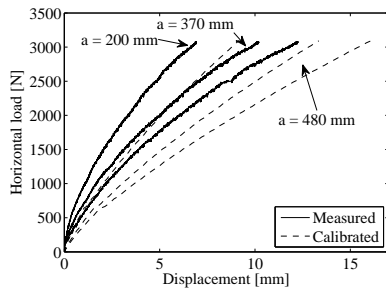
Calibration of $FLAC^{3D}$ to laboratory test results



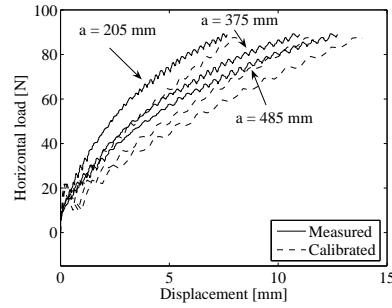
(a) Test 1: $D = 0.08$ m, $L = 0.4$ m, $P_0 = 0$ kPa - $E_0 = 3.5$ MPa.



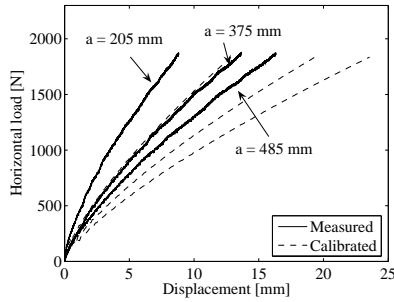
(b) Test 2: $D = 0.08$ m, $L = 0.4$ m, $P_0 = 100$ kPa.



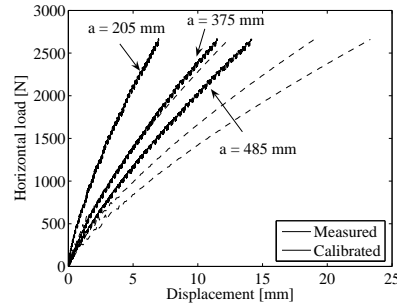
(c) Test 3: $D = 0.08$ m, $L = 0.4$ m, $P_0 = 50$ kPa.



(d) Test 4: $D = 0.06$ m, $L = 0.3$ m, $P_0 = 0$ kPa - $E_0 = 2.5$ MPa.



(e) Test 5: $D = 0.06$ m, $L = 0.3$ m, $P_0 = 50$ kPa.



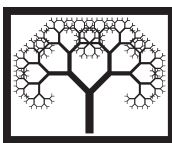
(f) Test 6: $D = 0.06$ m, $L = 0.3$ m, $P_0 = 100$ kPa.

Figure O.1: Calibration of three-dimensional model employed in $FLAC^{3D}$ to the six laboratory tests. The material properties employed in the numerical analyses are as listed in appendix C.

APPENDIX P

Evaluation of the Load-Displacement Relationships for Large-Diameter Piles in Sand

*Accepted at The Twelfth International Conference on Civil, Structural
and Environmental Engineering Computing, Portugal, 2009.*



©Civil-Comp Press, 2009

Proceedings of the Twelfth International Conference on Civil, Structural and Environmental Engineering Computing, B.H.V. Topping, L.F. Costa Neves and R.C. Barros, (Editors), Civil-Comp Press, Stirlingshire, Scotland, paper 1, 2009.

Paper 1

Evaluation of the Load-Displacement Relationships for Large-Diameter Piles in Sand

S.P.H. Sorensen, K.T. Brodback, M. Moller, A.H. Augustesen and L.B. Ibsen

Department of Civil Engineering, Aalborg University, Denmark

Keywords: monopile, sand, $p-y$ curves, Winkler model approach, geotechnical engineering, FLAC^{3D}, laboratory tests.

For laterally loaded piles in sand with diameters up to 6m, for example monopiles used as foundations of offshore wind turbines, there is no approved design procedure. The $p-y$ curve method, given in offshore design regulations, is usually employed for the design of monopiles. However, this method was developed for slender piles with diameters much less than 6m and it is based on a limited number of tests.

The aim of the present work is to extend the $p-y$ curve method to large-diameter non-slender piles by considering the effects of the pile diameter on the soil response. The main focus is the initial stiffness of the $p-y$ curves. The evaluation is based on experimental work as well as three-dimensional numerical analyses. The numerical analyses are made by means of the commercial programme FLAC^{3D}. A Mohr-Coulomb material model is employed. The numerical model is calibrated using six small-scale tests conducted on heavily instrumented piles with diameters varying from 60-80 mm subjected to a horizontal load. The tests are carried out in a pressure tank at different effective stress levels in order to simulate realistic effective vertical stresses for a typical monopile. After calibrating the model using small-scale tests the numerical model is extended to full-scale wind turbine foundations. The results are compared with results obtained from a traditional $p-y$ curve design based on a Winkler model approach.

Major findings of this paper are:

1. The initial stiffness of the $p-y$ curves increases for increasing pile diameter.
2. The initial modulus of subgrade reaction given by the offshore design regulations is overestimated for large diameter non-slender piles.
3. A linear variation of the initial stiffness with depth is a non-conservative estimation at large depths
4. The power function proposed by Lesny and Wiemann [1] describing the variation of initial stiffness with depth provides reasonable results compared with the three-dimensional numerical model.

References

- [1] K. Lesny, J. Wiemann, "Finite-Element-Modelling of Large Diameter Monopiles for Offshore Wind Energy Converters", Geo Congress 2006, February 26 to March 1, Atlanta, GA, USA, 2006.

Abstract

For laterally loaded piles in sand with diameters up to 6 m, e.g. monopiles used as foundations for offshore wind turbines, there is no approved design procedure. The p - y curve method, given in offshore design regulations, is usually employed for the design of monopiles. However, this method was developed for slender piles with diameters much less than 6 m and it is based on a limited number of tests. The aim of the present work is to extend the p - y curve method to large-diameter non-slender piles by considering the effects of the pile diameter on the soil response. The main focus is the initial stiffness of the p - y curves. The evaluation is based on experimental work as well as three-dimensional numerical analyses in the commercial programme *FLAC*^{3D}.

Keywords: monopile, sand, p - y curves, Winkler model approach, geotechnical engineering, *FLAC*^{3D}, laboratory tests.

1 Introduction

Several concepts for offshore wind turbine foundations exist. The choice of foundation concept primarily depends on site conditions and the dominant type of loading. At great water depths the most common foundation concept is monopiles, which are single steel pipe piles driven open-ended. Recently installed monopiles have diameters around 4 to 6 m and a pile slenderness ratio (L/D) around 5 where L is the embedded length and D is the outer pile diameter. The maximum forces acting on a 3.5 MW offshore wind turbine foundation at the mudline is, according to Ubilla et al. [1], in the order of 4 MN in horizontal load, 6 MN in vertical load, and 120 MNm in overturning moment. Hence, a monopile foundation for an offshore wind turbine is highly subjected to lateral loading.

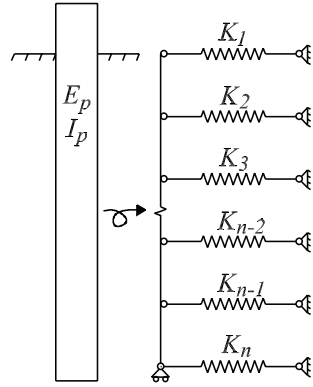


Figure 1: Winkler model approach. K denotes the stiffness of the elastic foundation while E_p and I_p are the Young's modulus of elasticity and second moment of inertia for the pile, respectively. The circles indicate hinges.

In current design of laterally loaded offshore monopiles, p - y curves are normally employed. A p - y curve describe the non-linear relationship between the soil resistance acting against the pile wall, p , and the lateral deflection of the pile, y . Several formulations of p - y curves exist depending on the type of soil. These formulations are originally formulated to be employed in the offshore oil and gas sector. However, they are also used for offshore wind turbine foundations, although piles with significantly larger diameter and significantly smaller slenderness ratio are employed for this type of foundation. In traditional design a Winkler approach is often employed in which the pile is modelled as a beam on an elastic foundation, cf. Figure 1. The elastic foundation consists of a number of springs with spring stiffness, K_i , given by means of p - y curves. When using the Winkler approach the soil continuity is not taken into account as the springs are considered uncoupled.

The p - y curve for sand employed in the offshore design regulations, e.g. DNV [2] and API [3], are given in Equation (1).

$$p(y) = Ap_u \tanh\left(\frac{kx}{Ap_u}y\right) \quad (1)$$

in which A is a factor corresponding to static or cyclic analyses, p_u is the ultimate soil resistance, k is the initial modulus of subgrade reaction and x is the depth measured from soil surface. k is determined in terms of the angle of internal friction or the relative density and governs the initial slope of the p - y curves. Hereby, the initial stiffness of the p - y curves is assumed independent of the pile properties.

The hyperbolic expression is based on the testing of two identical, instrumented piles installed at Mustang Island, Texas as described by Cox et al. [4]. The tests included a total of seven load cases. Furthermore, the tests were conducted for only one pile diameter, one type of sand, and for circular pipe piles. A change in any of these factors might affect the behaviour of a laterally loaded pile. Due to the very limited number of full-scale tests performed to validate the method, the influence of

a broad spectra of parameters on the p - y curves are still to be clarified. Especially when considering offshore wind turbine foundations a validation of stiff piles with a slenderness ratio of $L/D < 10$ is needed as the Mustang Island test piles had a slenderness ratio of $L/D = 34.4$. Briaud et al. [5] postulate that the soil response depends on the flexibility of the pile. Criteria for stiff versus flexible behaviour of piles have been proposed by various authors, e.g. Dobry et al. [6]; Budhu and Davies [7]; and Poulos and Hull [8]. A pile behaves rigidly according to the following criterion, cf. [8]:

$$L < 1.48 \left(\frac{E_p I_p}{E_s} \right)^{0.25} \quad (2)$$

in which L is the embedded length, I_p is the second moment of inertia of the pile, and E_p and E_s is Young's modulus of elasticity of the pile and the soil, respectively. Similarly, the criterion for a flexible pile behaviour is:

$$L > 4.44 \left(\frac{E_p I_p}{E_s} \right)^{0.25} \quad (3)$$

According to Equation (2) a steel monopile with an outer diameter of 4 m, an embedded length of 20 m and a wall thickness of 0.05 m behaves rigidly if $E_s < 7.6$ MPa. In contrast, the pile exhibits a flexible behaviour if $E_s > 617$ MPa. Even dense sands have $E_s < 100$ MPa, so in accordance to Equation (2) the recently installed monopiles for offshore foundations behaves more rigidly than flexible.

For modern wind turbine foundations only small pile head rotations are acceptable. Furthermore, the strict demands to the total stiffness of the system due to resonance in the serviceability mode increase the significance of the p - y curve's initial slope and hereby the initial stiffness of the soil-pile system. It seems questionable that the initial stiffness of the p - y curves are independent of the pile properties among these the pile diameter. The research within the field of diameter effects gives contradictory conclusions. Most researchers, cf. Terzaghi [9]; Ashford and Juirnarongrit [10]; and Fan and Long [11], conclude that the effect of the diameter on the initial stiffness of the p - y curves are insignificant. In contradiction to this Carter [12] and Ling [13] postulate that the initial stiffness of the p - y curves has a linear relation with the pile diameter. However, as well as the research is based on a very limited number of tests, most research considers only relatively slender piles, which is rarely the case for offshore wind turbine foundations.

In the present paper the effects of diameter on static p - y curves for piles in homogeneous sand are assessed in two ways. Firstly in terms of six small-scale tests carried out in a pressure tank at varying effective stress levels in the Laboratory of Foundation at Aalborg University, Denmark. Secondly a numerical model, calibrated to the laboratory tests, is extended to simulation of large-scale offshore wind turbine foundations. The numerical model is made by means of the commercial programme *FLAC^{3D}*. The main focus in the assessment of the p - y curves is the initial stiffness.



Figure 2: Pressure tank at Aalborg University, Denmark.

2 Laboratory test

2.1 Setup

When conducting small-scale tests in sand at 1-g an often introduced source of error is the low stress levels causing the angle of internal friction to vary strongly with stresses. Hence, it is an advantage to increase the effective stresses to a level where the angle of internal friction, φ_{tr} , is independent of a possible stress variation during the tests. This is possible in the pressure tank at Aalborg University, cf. Figure 2. The pressure tank is furnished with trap doors in order to enable preparation of the test setup prior to each test.

The increase in effective stress level is created by separating the lower part of the pressure tank, containing saturated soil, from the upper part by use of an elastic membrane. In this way the saturated soil is sealed from the air above. By increasing the air pressure in the upper part, a homogenous increase in stresses is introduced at the soil surface via the elastic membrane. To ensure limited excessive pore pressure, the soil is connected to an ascension pipe, leaving the soil fully saturated but with stresses applied as effective stresses only. A cross sectional view of the test setup is shown in Figure 3.

A total number of six tests have been conducted at overburden pressures, $P_0 = 0$ kPa, $P_0 = 50$ kPa and $P_0 = 100$ kPa. The overburden pressure is equal to the pressure at the elastic membrane. The conducted tests are quasi-static tests on two instrumented aluminium pipe piles with outer diameters of $D = 60$ mm and $D = 80$ mm, respectively. Both piles have a slenderness ratio of $L/D = 5$ corresponding to an embedded length of 0.3 m and 0.4 m, respectively. Both piles have a wall thickness of 5 mm and are closed-ended in order to protect the strain gauges and their corresponding cords against water. The piles are installed in one continuous motion by means of a hydraulic piston mounted vertically on the top of the pressure tank. After installation the

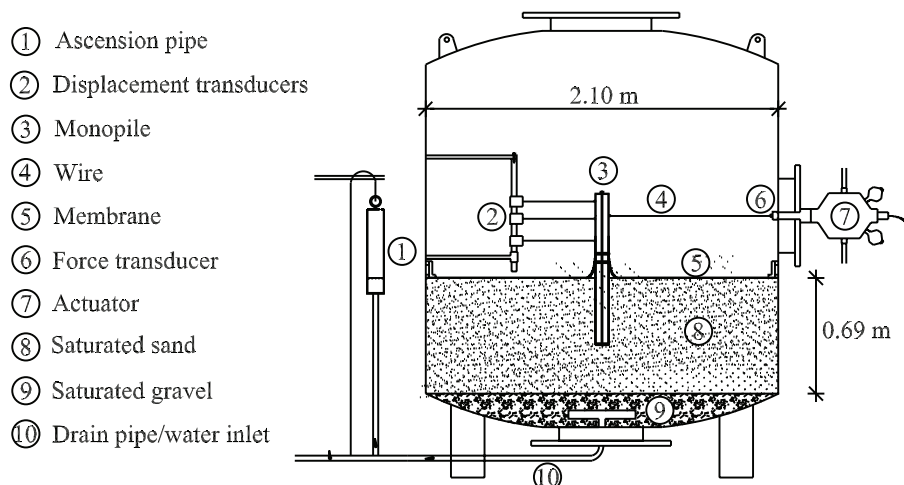


Figure 3: Pressure tank - test setup.

sand is mechanically vibrated. In this way a homogenous compaction of the soil is ensured.

A hydraulic piston, cf. 7 in Figure 3, is employed horizontally at the pressure tank to actuate the test piles with a vertical load eccentricity of 0.37 m above the soil surface. The pile and the hydraulic piston is connected by means of a steel wire. In order to measure the force acting on the pile a force transducer is connected in series of the hydraulic piston and the wire. Lateral deflections are measured at three levels (0.2, 0.37 and 0.48 m) above the soil surface by means of wire transducers. A total number of 10 strain gauges are mounted on the pile beneath the soil surface. The strain gauges are located at five levels as shown in Figure 4. At each level two foil strain gauges are mounted in grooves milled on the outside of the pile with a mutual angle of 180° oriented in the plane of the horizontal load. The grooves are sealed to protect the strain gauges.

The two employed piles have been calibrated prior to the testing and have the following pile bending stiffness': $EI_{p,80} = 52.4 \text{ kNm}^2$; $EI_{p,60} = 24.9 \text{ kNm}^2$. The Poisson's ratio of the aluminium piles is considered to be $\nu = 0.33$.

The soil in the pressure tank consists of 0.69 m fully saturated Baskarp Sand no. 15 which is a graded sand from Sweden, with the characteristics given in Table 1.

Specific grain density d_s	2.64
Maximum void ratio e_{\max}	0.858
Minimum void ratio e_{\min}	0.549
$d_{50} = 50\%$ - quantile	0.14 mm
$U = d_{60}/d_{10}$	1.78

Table 1: Material properties for Baskarp Sand No. 15, after Larsen [14].

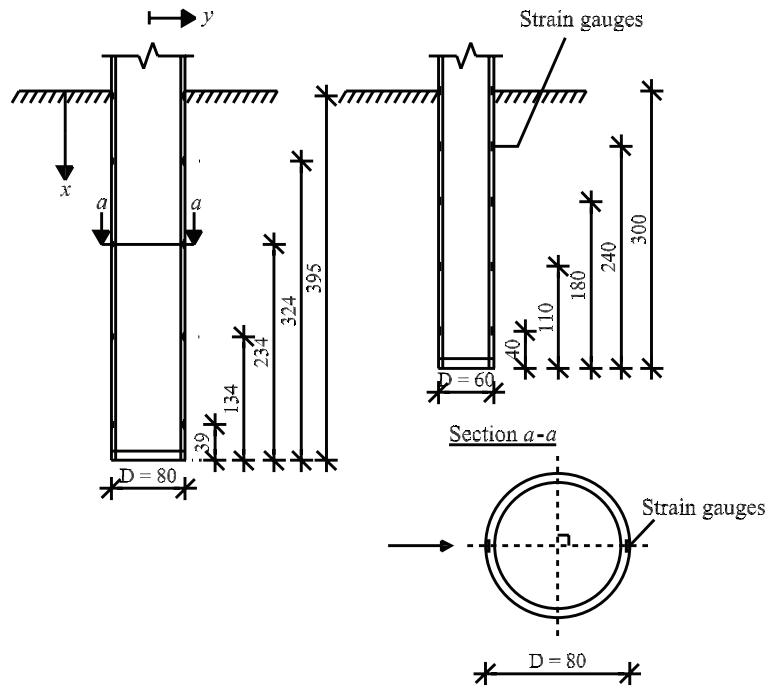


Figure 4: Strain gauge levels. All measurement levels are identical. Measures are in mm.

The homogeneous compaction before each test is controlled by conducting cone penetration tests (CPT). Four CPT's with a distance of 0.5 m from the center of the pile and two 0.16 m from the neutral sides of the pile, i.e. the sides perpendicular to the load direction, are conducted. The employed CPT is a prototype probe with a diameter of 15 mm. Based on the measured cone resistance, q_c , as function of depth the material properties of the sand have been derived. The derived parameters are given in Table 2 for the six tests. The parameters are derived in accordance to Ibsen et al. [15] where the angle of internal friction, ϕ_{tr} , and the tangential Young's modulus of elasticity, E_0 , is related to the stress level. Due to the high angles of internal friction the sand is considered as very dense. For the tests without overburden pressure E_0 is calibrated against the numerical models as the employed formulas produce large uncertainties at low stress levels.

2.2 Analysis of the tests results

Figure 5 presents the load-displacement relationships at different overburden pressures measured at the height of the hydraulic piston. As shown in the figure the ultimate resistance is strongly dependent on the vertical stresses.

The p - y curves are traditionally derived on basis of the bending moment distribu-

	D [mm]	P_0 [kPa]	φ_{tr} [°]	Relative density I_D [-]	Unit weight γ' [kN/m ³]	E_0 [MPa]
Test 1	80	0	52.6	0.79	10.2	-
Test 2	80	100	45.9	0.79	10.2	41.1
Test 3	80	50	48.5	0.79	10.2	25.4
Test 4	60	0	52.2	0.76	10.1	-
Test 5	60	50	48.3	0.78	10.1	24.9
Test 6	60	100	45.1	0.75	10.1	37.4

Table 2: Test programme and material properties calculated for the six tests.

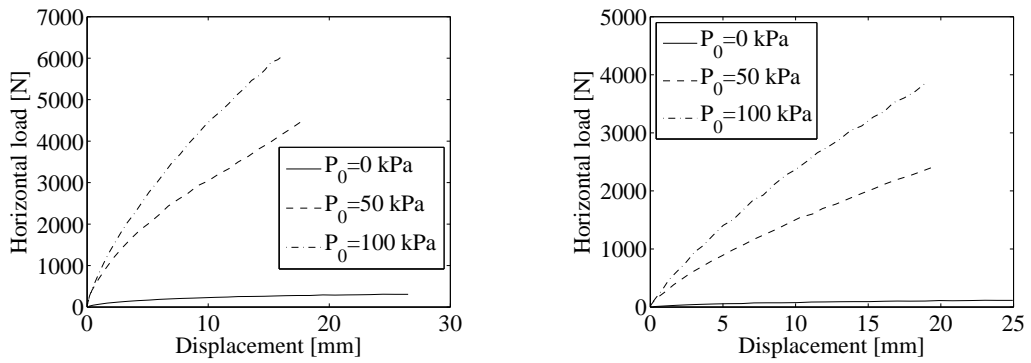


Figure 5: Load-displacement for different pressures at the height of the hydraulic piston. Left: $D = 0.08$ m, $L = 0.4$ m. Right: $D = 0.06$ m, $L = 0.3$ m.

tion along the pile, $M(x)$, and the pile bending stiffness, $E_p I_p$:

$$y(x) = \int \int \frac{M(x)}{E_p I_p} dx dx \quad (4)$$

$$p(x) = \frac{d^2 M(x)}{dx^2} \quad (5)$$

The double integration of the discrete data points with respect to depth does not implement significant errors. However, double differentiation of the discrete signal gives an amplification of measurement errors. In order to minimise these errors the piecewise polynomial curve fitting method described by Yang and Liang [16] is employed in this paper. When using this method the moment distribution is estimated by fitting five successive moment data points to 3. order polynomials.

Figure 6 presents the lateral pile displacements with depth at the three different stress levels for the two pile diameters. A prescribed deflection of 10 mm at the level of the hydraulic piston are outlined. The lateral displacement can be separated into two components: deformation of the pile due to bending moments and rotation of the pile as a rigid object. The pile deformation due to bending moments is calculated according to Equation (4). The pile rotation is obtained by the displacement trans-

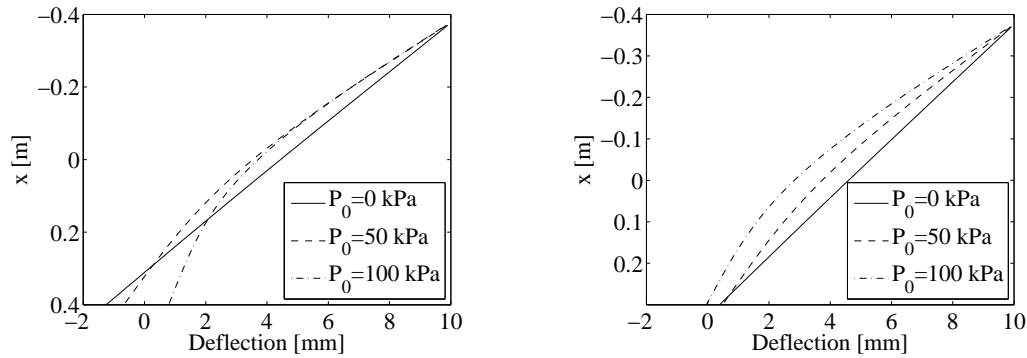


Figure 6: Lateral pile displacement at different stress levels. Left: $D = 0.08$ m, $L = 0.4$ m. Right: $D = 0.06$ m, $L = 0.3$ m.

ducers at the top of the pile and at the height of the hydraulic piston. Based on the known vertical distance between the two displacement transducers and the measured horizontal displacements the rotation of the pile at the height of the hydraulic piston is obtained. As shown the piles behave almost as rigid objects when $P_0 = 0$ kPa. When applying overburden pressure the pile deformation caused by bending is more significant, but still with a pile deflection primarily depending on the rotation. Due to the rigid behaviour of the pile, the deflection at the pile toe must be negative which is not the case for most of the tests. This could be caused by the relatively small vertical distance between the displacement transducers which could lead to large uncertainties when determining the rotation.

Figure 7 presents normalised p - y curves at two depths. The observations lead to the conclusion that the initial stiffness of the p - y curve is highly dependent on the pile diameter with the highest stiffness relating to the largest pile diameter. When $P_0 = 0$ kPa the initial stiffness of the pile with an outer diameter of 80 mm is in the range of 3–4 times higher than the stiffness for the pile with an outer diameter of 60 mm.

3 Numerical modeling of monopile under static lateral loading

A three-dimensional numerical model has been constructed in the commercial programme $FLAC^{3D}$ with the objective to examine the behaviour of laterally loaded, large-diameter piles in cohesionless soil. $FLAC^{3D}$ is a dynamic, explicit finite difference solver based on the finite difference method. A Mohr–Coulomb material model with tension cut-off has been employed.

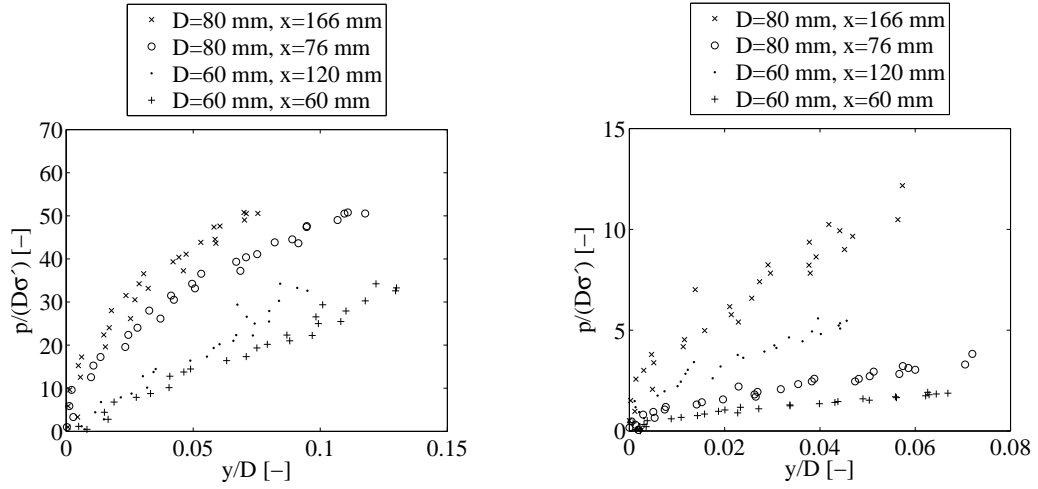


Figure 7: Relationship between normalised soil resistance and normalised displacement for the two pile diameters. Left: $P_0 = 0$ kPa. Right: $P_0 = 100$ kPa.

3.1 Construction of numerical model in $FLAC^{3D}$

Due to symmetric loading conditions only one half of the pile and surrounding soil are modelled. The pile is modelled as a solid cylinder, in contrast to the closed-ended pipe piles employed in the laboratory tests. The bending stiffness of the solid piles, EI_{flac} , is equivalent to the stiffness of the hollow test piles, $E_p I_p$, by reducing Young's modulus of elasticity. The weight of the hollow and the solid piles are in the same way equivalent. Both the laboratory test piles and the large-scale pipe piles are equivalent. The Poisson's ratio of the pile material is not scaled, which leads to an incorrect scaling of the shear modulus, G , and bulk modulus, K . The effect of this error is small as the pile primarily is subjected to bending.

The geometry of the model and the orientation of the coordinate system are shown in Figure 8. The grid is generated from zone elements. Each zone consist of five first order, constant rate of strain, tetrahedral subelements. The outer boundaries of the grid when calibrating are set to the inner diameter of the pressure tank. When simulating large-scale piles the outer boundaries, are set individually for each pile. The outer diameter of the soil mass is set to $40D$ based on the recommendations by Abbas et al. [17]. The height of the grid is set to $L + 15$ m. It has been observed that the zone of failure does not reach the outer boundaries.

The soil-pile interface is modelled by means of the standard $FLAC^{3D}$ interface. A linear Coulomb shear-strength criterion is employed for the interfaces to limit the shear forces acting on the interface nodes. The interface elements allows gapping and slipping between the soil and the pile.

The horizontal load is applied as a velocity at the nodes corresponding to $x = 0$ at the pile head. Hereby, no artificial bending moment is introduced at the pile head.

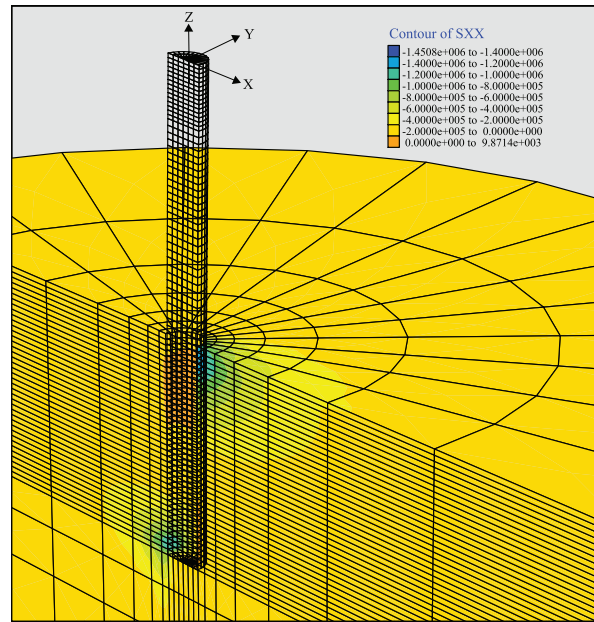


Figure 8: Three-dimensional mesh. The contour illustrates the horizontal stresses, s_{xx} , at a horizontal load of 5300 N, $D = 0.08$ m, $L = 0.4$ m, and $P_0 = 100$ kPa.

The calculations are executed in steps. Firstly, the initial stresses are generated for the whole model containing only soil properties. The horizontal stresses are determined by a K_0 -procedure. Secondly, the pile parameters are introduced. In order to take the overburden pressure into account for the test piles an initial load is applied in these cases. When applying the overburden pressure, the pile is at first assumed smooth. When equilibrium is reached for the smooth pile the correct interface properties are employed and a new equilibrium state is computed. After reaching equilibrium in the model, velocities are applied to the pile head in small increments in order to minimise inertial forces in the system. Further, damping is employed in the system.

3.2 Calibration of numerical model

On the basis of the derived soil parameters given in Table 2 the interface properties of the numerical model in $FLAC^{3D}$ have been calibrated. The soil parameters are assumed to remain constant with depth. An example of the calibration is shown in Figure 9 where the measured lateral displacement at three levels, symbolised by a , above the soil surface is compared with the results obtained from the numerical model. Figure 10 presents the calibrated and measured bending moment distribution at a horizontal load of 2100 N. The bending moment distribution along the pile is computed by means of Naviers formula correlating stresses and moments. The bending moment is calculated from two points ($y = 0$, $x = \pm D/2$) at each level of the pile. Hereby, the average vertical stress corresponding to the axial force is eliminated. As shown in Figure 9 and 10, the agreement between the experimental and computed values is

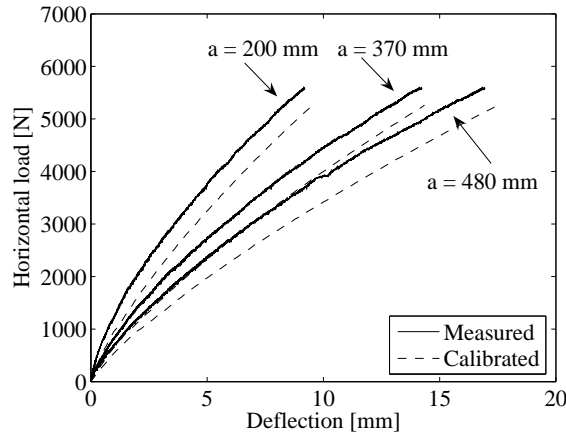


Figure 9: Load-displacement relationship at three levels above soil surface, for $D = 0.08$ m, $L = 0.4$ m, and $P_0 = 100$ kPa.

good, as the parameters listed in Table 2 have been employed in $FLAC^{3D}$. Similar analyses have been conducted for the remaining five tests with similar results. Based on these calibrations the wall friction angle, δ , is set to 30° .

3.3 Simulation of large-scale monopiles

Three steel pipe piles with pile diameters of 3 m, 5 m, and 7 m, respectively are simulated with the objective to examine the behaviour of large-diameter non-slender monopiles. The embedded length is 20 m, the wall thickness is 0.05 m and the vertical load eccentricity is 15 m.

The material parameters for the soil and pile employed in the large-scale analyses are listed in Table 3.

Effective unit weight of the soil γ'	10 kN/m ³
Angle of internal friction φ_{tr}	40°
Dilatancy angle ψ_{tr}	10°
Cohesion c	0.1 kN/m ²
Relative density I_D	80%
Poisson's ratio for the soil ν_s	0.23
Coefficient of horizontal earth pressure at rest K_0	$1 - \sin(\varphi_{tr})$
Young's modulus of elasticity for the pile E_p	210 GPa
Poisson's ratio for the pile ν_p	0.3
Unit weight of the pile γ_p	78.5 kN/m ³

Table 3: Material properties employed in the large-scale analyses.

The tangential Young's modulus of elasticity for the soil, E_0 , is varied with the mi-

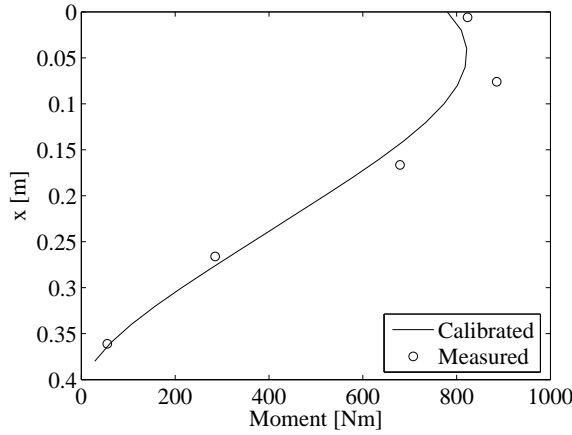


Figure 10: Distribution of bending moment with depth at a horizontal load of 2100 N, $D = 0.08$ m, $L = 0.4$ m, and $P_0 = 100$ kPa.

nor principal stress σ'_3 on basis of Equation (6) proposed by Ibsen et al. [15]. Equation (6) is valid for Baskarp Sand no. 15. The factor of 1.82 specifies, according to *Plaxis 2D* [18], the relation between E_0 and E_{50} .

$$E_0 = 1.82(0.6322I_D^{2.507} + 10920) \left(\frac{c \cdot \cos(\varphi_{tr}) + \sigma'_3 \cdot \sin(\varphi_{tr})}{c \cdot \cos(\varphi_{tr}) + \sigma_3^{ref} \cdot \sin(\varphi_{tr})} \right)^{0.58} \quad [\text{kN/m}^2] \quad (6)$$

In the empiric formula I_D should be implemented in percent and $\sigma_3^{ref} = 100$ kPa.

Figure 11 presents the lateral pile deflection with respect to depth. The applied displacements, corresponding lateral load, and depth of maximum moments are outlined in Table 4 for the three simulated piles. The deflection of the piles shows a rigid body motion which is most significant for $D = 7$ m. The more rigid pile behaviour for increasing diameters is in good accordance with Poulos and Hull [8] as the employed pile bending stiffness increases for increasing pile diameter. Due to the rigid pile behaviour, a significant negative deflection at the pile toe is observed. The point of zero deflection is located at a depth of approximately $x = 15$ m for all three piles.

Outer diameter [m]	Displacement [m]	Load [MN]	Depth of max. moment [m]
3	0.58	6.4	4.8
5	0.24	8.8	5.0
7	0.84	21.4	4.9

Table 4: Applied displacements, equivalent loads, and depth of maximum moments for the three pile diameters.

Figure 12 presents the distribution of bending moment along the piles. It is observed that the maximum bending moment is located at a depth of approximately 5

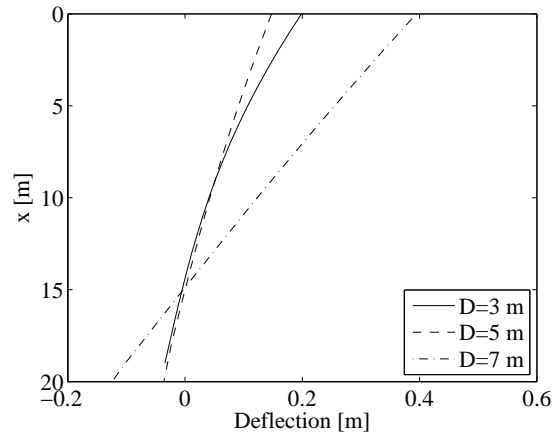


Figure 11: Lateral pile deflection for the three large-scale piles.

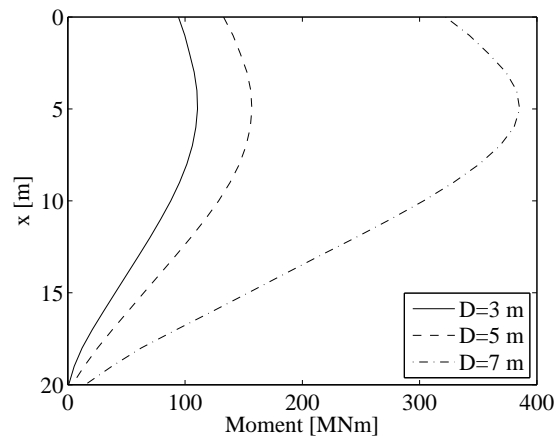


Figure 12: Bending moment distribution along the piles.

m for all the piles, cf. Table 4. As the point of zero deflection for the three piles are situated approximately at the same depth, the depth of maximum moment are as well. For the piles with $D = 5 - 7$ m the bending moment is non-zero at the pile toe. This may be due to a combination of large diameter, large rotations and the solid base.

Figure 13 shows the $p-y$ curves obtained at a depth of $x = 2$ m. Further, the $p-y$ curves according to API [3], cf. Equation (1), are outlined in the figures. As expected the ultimate soil resistance increases for increasing pile diameter. Further, the initial part of the curves, is stiffer for the API $p-y$ curves compared to the $p-y$ curves obtained by means of $FLAC^{3D}$. The ultimate soil resistance of the API $p-y$ curves has some degree of conservatism in the case of very large diameters. This is however, not observed for the pile with $D = 3$ m. Furthermore, the $p-y$ curves obtained from the three-dimensional numerical model do not reach a steady state at

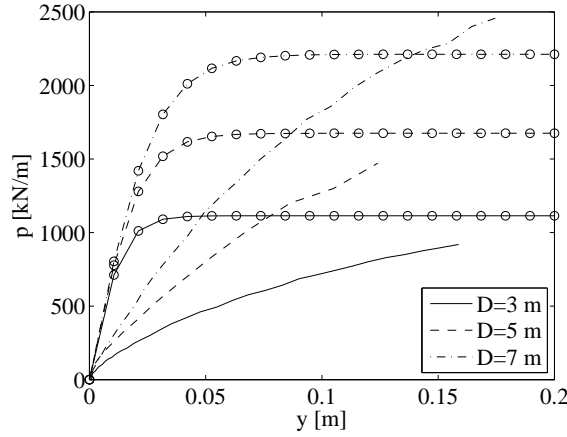


Figure 13: Comparison of API p - y curves marked with (o) and the p - y curves obtained by the numerical model for the three piles, respectively.

the applied displacements.

The variation of initial stiffness with depth, $E_{py}^* = \frac{\delta p}{\delta y}$, $y = 0$, is presented in Figure 14 for the three pile diameters. The initial stiffness is observed to increase for increasing pile diameters. The design regulations, e.g. DNV [2] and API [3], suggest that the initial modulus of subgrade reaction, k , and hereby also the initial stiffness E_{py}^* :

$$E_{py}^* = kx \quad (7)$$

is independent of the pile diameter, which is in contrast to the variation of initial stiffness shown in Figure 14. The p - y curves obtained near the point of zero deflection is characterised by a lot of scatter causing large uncertainties for the initial stiffness at large depths.

The magnitudes of k in Equation (7) are outlined in Table 5 at $x = 2 - 7$ m where this assumption is reasonable. As indicated in Table 5, k is highly dependent on the pile diameter; increasing diameter results in an increase in k . This observation is most significant when comparing the results for the piles with $D = 3$ m and $D = 5$ m. For dense sand ($\varphi_{tr} = 40^\circ$) the offshore design regulations recommend $k = 40000$ kN/m³. This cannot be validated based on the analyses since k ranges between 9700–29000 kN/m³. In order to validate the results in Table 5 more research is needed.

According to Figure 14 there is no linear variation of $E_{py}^* = kx$ with depth. Lesny and Wiemann [19] propose a power function for the variation of E_{py}^* with depth:

$$E_{py}^* = E_{py,ref}^* \left(\frac{x}{x_{ref}} \right)^a \quad (8)$$

where $E_{py,ref}^*$ denotes the initial stiffness at a reference depth, x_{ref} , and a is a factor depending on the relative density of the sand. According to [19] the factor a is to be set to 0.6 for medium dense sands.

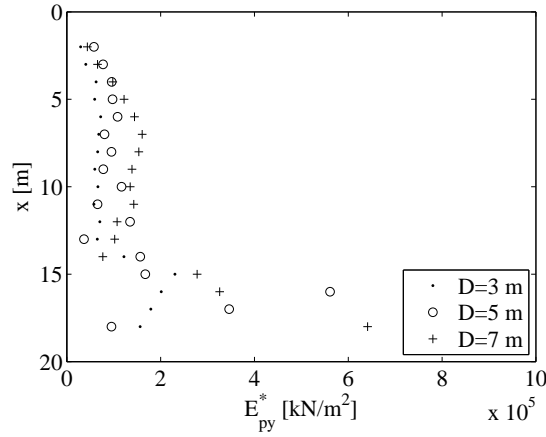


Figure 14: Initial stiffness versus depth.

	$D=3$ m	$D=5$ m	$D=7$ m
$x=2$ m	14799	28964	21891
$x=3$ m	13550	25798	21846
$x=4$ m	15663	23921	24547
$x=5$ m	11881	19532	24440
$x=6$ m	12045	18065	24077
$x=7$ m	9747	11475	22963

Table 5: Initial modulus of subgrade reaction, k . k are specified in $[\text{kN}/\text{m}^3]$.

Figure 15 presents the obtained initial stiffness' from the simulations and the variations based on Equation (7) and (8) for $D = 3$ m. The two expressions, cf. Equations (7) and (8), are identical when $a = 1$. As a reference initial stiffness, $E_{py,ref}^*$, the initial stiffness at $x_{ref} = 2$ m is employed. Figure 15 indicates that the linear expression employed in the design regulations fits the obtained E_{py}^* well until a depth of approximately 5 m. Beneath this depth the linear expression highly overestimates E_{py}^* , implying that the soil response is non-conservative at large depths. The power function fits the obtained E_{py}^* well until a depth of 13 m. The obtained by means of $FLAC^{3D}$ E_{py}^* beneath $x = 13$ m are influenced by the point of zero deflection. For the remaining pile diameters a similar variation of E_{py}^* with depth is found, giving that the expression in the offshore design regulations overestimates the soil-pile interaction for large-diameter monopiles en sand at large depth.

3.4 Comparison of the results with a Winkler model approach

A traditional Winkler model has been constructed in order to compare the results obtained from the three-dimensional numerical model with the recommendations in

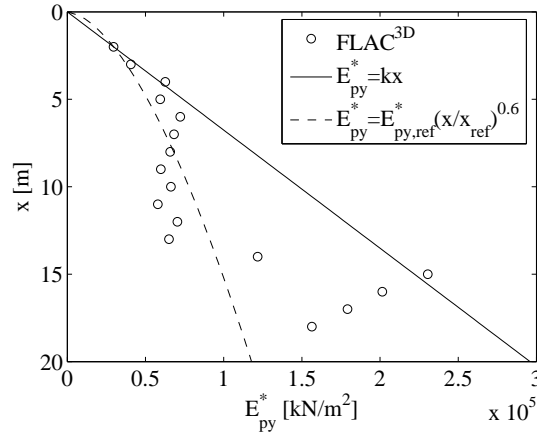


Figure 15: Variation of E_{py}^* as function of depth, $D = 3$ m, $x_{ref} = 2$ m, and $E_{py,ref}^* = 29598$ kN/m².

the design regulations. The nonlinear soil behaviour is modelled using the API [3] p - y curves, cf. Equation (1). The comparison between the three-dimensional numerical model and the Winkler model approach is performed, with the same pile geometry, and soil conditions as listed in Table 3. Figure 16 presents the load-displacement relationships at the pile top located 15 m above seabed ($D = 3$ m) obtained from $FLAC^{3D}$, and the Winkler model approach. The power function, cf. Equation (8), and the recommendations in API [3], with $k = 40000$ kN/m³ and $k = k_{ref}$ at $x = 2$ m, respectively have in turn been implemented in the Winkler model approach. Figure 16 indicates that the expression employed in API [3] highly overestimates the strength of the soil at all deflections compared to $FLAC^{3D}$. In accordance with Table 5 this is expected as the initial modulus of subgrade reaction, k , is overestimated compared to the values calculated by means of $FLAC^{3D}$. The linear expression, cf. Equation (7), with k_{ref} as the value obtained at $x_{ref} = 2$ m gives reasonable results until a deflection of approximately 0.1 m. At higher deflections there is a considerable difference between the deflections determined by $FLAC^{3D}$ and the linear expression. When employing the power function, cf. Equation (8), in the Winkler model approach the initial part of the load-displacement relationship fits very well until a deflection of 0.2 m. At higher deflections an overestimation of the horizontal load is observed compared to $FLAC^{3D}$. However, the difference is less than obtained by employing the linear expression in the Winkler model. Similar load-displacement behaviour has been observed for the piles with $D = 5$ m and $D = 7$ m.

For modern wind turbine foundations only small deformations/rotations are allowed. Therefore, it is desirable that the initial part of the curves fits the pile behaviour well, which is the case for the power function employed in the Winkler model approach. Hence, it can be concluded that the Winkler model approach is useful when a proper variation of the initial stiffness associated with the p - y curves is employed.

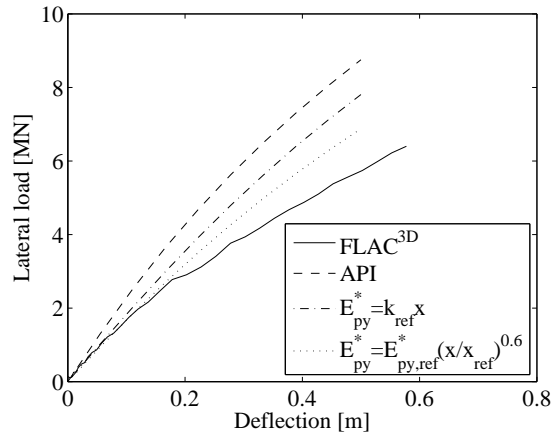


Figure 16: Load-displacement relationships at the pile top calculated by $FLAC^{3D}$ compared with the Winkler model approach incorporating API ($k = 40000 \text{ kN/m}^3$), API (k_{ref}), and the power function, cf. [19], respectively.

4 Conclusion

This paper presents the results of six quasi-static tests on two non-slender laterally loaded monopiles in a pressure tank. The tests are reproduced by means of a three-dimensional numerical model constructed in $FLAC^{3D}$ and extended to large-scale monopiles with pile diameters varying between $D = 3 - 7 \text{ m}$. This corresponds to slenderness ratios between $L/D = 2.9 - 6.7$. The conclusions that can be drawn are:

- The non-slender piles deflects as almost rigid objects given only one point of zero deflection. Hereby, negative deflections at the pile toe are observed.
- The initial modulus of subgrade reaction, k , is highly affected by the pile diameter; increasing diameter results in an increase in k . This is observed in connection with both the tests and the numerical analyses. This contradicts the recommendations in the offshore design regulations. k is varying between $9700\text{-}29000 \text{ kN/m}^3$ at small depths when increasing the diameter from $3\text{-}7 \text{ m}$.
- The design regulations recommends a linear variation of initial stiffness with depth. This recommendation is non-conservative at large depths. Here, the soil response is overestimated. A non-linear variation of initial stiffness with depth proposed by Lesny and Wiemann [19] provides a good agreement when compared to the results from the three-dimensional numerical model.
- More research is needed in order to update the $p\text{-}y$ curves recommended in the offshore design regulations to large diameter non-slender monopiles.

Acknowledgements

The project has only been possible with the financial support from the Energy Research Programme administered by the Danish Energy Authority. The project is associated with the ERP programme “Physical and numerical modelling of monopile for offshore wind turbines”, journal no. 033001/33033-0039. The funding is sincerely acknowledged. Appreciation is extended to Christian LeBlanc and Morten Liingaard, DONG Energy A/S, for fruitful discussions. Furthermore, the authors would like to thank the staff at the laboratory at the Dept. of Civil Engineering, Aalborg University, for their immeasurable help with the test setup.

References

- [1] J. Ubilla, T. Abdoun, T. Zimmie, “Application of in-flight robot in centrifuge modeling of laterally loaded stiff pile foundations”, *Physical Modelling in Geotechnics*, Taylor & Francis Group, London, ISBN 0-41-41586-1,259-264, 2006.
- [2] DNV, “Foundations - Classification Notes No 30.4”, Det Norske Veritas, Det Norske Veritas Classification A/S, 1992.
- [3] API, “Recommended practice for planning, designing, and constructing fixed offshore platforms - Working stress design”, API RP2A-WSD, American Petroleum Institute, Washington D.C., 21. edition, 1993.
- [4] W.R. Cox, L.C. Reese, B.R. Grubbs, “Field Testing of Laterally Loaded Piles in Sand”, *Proceedings of the Sixth Annual Offshore Technology Conference*, Houston, Texas, 2079, 1974.
- [5] J.L. Briaud, T.D. Smith, B.J. Meyer, “Using pressuremeter curve to design laterally loaded piles”, *Proceedings of the 15th Annual Offshore Technology Conference*, Houston, Texas, 495-502, 4501, 1984.
- [6] R. Dobry, E. Vincente, M. O’Rourke, J. Roesset, “Stiffness and Damping of Single Piles”, *Journal of geotechnical engineering*, 108, 3, 439-458, 1982.
- [7] M. Budhu, T. Davies, “Nonlinear Analysis of Laterally loaded piles in cohesionless Soils”, *Canadian geotechnical journal*, 24(2), 289-296, 1987.
- [8] H. Poulos, T. Hull, “The Role of Analytical Geomechanics in Foundation Engineering”, *Foundation Engineering: Current principles and Practices*, 2, 1578-1606, 1989.
- [9] K. Terzaghi, “Evaluation of coefficients of subgrade reaction”, *Geotechnique*, 5(4), 297-326, 1956.
- [10] S.A. Ashford, T. Juirnarongrit, “Evaluation of Pile Diameter Effect on Initial Modulus of Subgrade Reaction”, *Journal of Geotechnical and Geoenvironmental Engineering*, 129(3), 234-242, 2003.
- [11] C.C. Fan, J.H. Long, “Assessment of existing methods for predicting soil response of laterally loaded piles in sand”, *Computers and Geotechnics*, 32, 274-289, 2005.

- [12] D.P. Carter, “A Non-Linear Soil Model for Predicting Lateral Pile Response”, Rep. No. 359, Civil Engineering Dept., Univ. of Auckland, New Zealand, 1984.
- [13] L.F. Ling, “Back Analysis of Lateral Load Test on Piles”, Rep. No. 460, Civil Engineering Dept., Univ. of Auckland, New Zealand, 1988.
- [14] K. A. Larsen, “Static Behaviour of Bucket Foundations”, Department of Civil Engineering, Aalborg University, Denmark, 2008.
- [15] L. B. Ibsen, M. Hanson, T. H. Hjort, M. Thaarup, “MC-Parameter Calibration for Baskarp Sand No. 15”, DCE Technical Report No. 62, Department of Civil Engineering, Aalborg University, Denmark, 2009.
- [16] K. Yang, R. Liang, “Methods for Deriving $p-y$ Curves from Instrumented Lateral Load Tests”, Geotechnical Testing Journal, 30(1), Paper ID GTJ100317, 2006.
- [17] J. M. Abbas , Z. H. Chik, M. R. Taha, “Single Pile Simulation and Analysis Subjected to Lateral Load”, Electronic Journal of Geotechnical Engineering, 13E, 1-15, 2008.
- [18] Plaxis 2D, “Material Models Manual Version 9.0”.
- [19] K. Lesny, J. Wiemann, “Finite-Element-Modelling of Large Diameter Monopiles for Offshore Wind Energy Converters”, Geo Congress 2006, February 26 to March 1, Atlanta, GA, USA, 2006.

